UNIVERSITÄT
ZU KÖLN

CHARACTERIZATION OF ARCTIC LOW-LEVEL CLOUDS AND PRECIPITATION OVER THE FRAM STRAIT BY AIRBORNE RADAR OBSERVATIONS

INAUGURAL-DISSERTATION

ZUR

ERLANGUNG DES DOKORGRADES

DER MATHEMATISCH-NATURWISSENSCHAFTLICHEN FAKULTÄT

DER UNIVERSITÄT ZU KÖLN

VORGELEGT VON

IMKE SCHIRMACHER

AUS GRÄFELFING

KÖLN, DEZEMBER 2024

BERICHTERSTATTENDE:
Prof.in Dr.in Susanne Crewell
Prof.in Dr.in Heike Kalesse-Los

TAG DER MÜNDLICHEN PRÜFUNG:
13.02.2025

'*Prognose* war also ein überflüssiges Wort,
das Vater auch nicht aufschrieb,
während er die Wolkenformationen durchaus aufschrieb,
so dass ich neue Lieblingswörter erhielt,
Wörter wie
Zirruswolke, *Türmchenwolke*, oder *Quellwolke*.'

-HANS-JOSEPH ORTHEIL
DIE ERFINDUNG DES LEBENS

Piano Sonata No. 7
III. Precipitato

-SERGEI PROKOFIEV

ABSTRACT

Clouds are dominant features in the Earth's atmosphere, particularly in the Arctic. There, specifically, low-level clouds are common that frequently consist of both supercooled liquid and ice simultaneously and are thus called mixed-phase clouds. These clouds and their precipitation substantially impact the Earth's radiative budget by warming the surface and also affect the Earth's water cycle. However, limited observations of Arctic low-level clouds and precipitation lead to persistent uncertainties in their occurrence and the distribution of liquid and ice. The latter uncertainty has been indicated to cause a disagreement in the sign of the cloud feedback in the Arctic across climate models. To clarify the role of low-level clouds in the Arctic, accurate observations of their distribution, microphysics, and precipitation are required over ocean, sea ice, and land. An improved understanding of cloud microphysical processes enhances the understanding of cloud formation, evolution, and lifetime and is therefore necessary to improve weather and climate models.

This thesis uses the unique capabilities of airborne radar observations to characterize Arctic low-level clouds and their precipitation with a particular focus on mixed-phase clouds and their development over the Fram Strait, a critical region for Arctic climate change. Airborne down-looking radar observations are especially suitable because they can cover large areas over open ocean and sea ice with a high spatial resolution and can reach close to the surface. This way, they can detect clouds that are not detected by other observational techniques. The investigated airborne observations, which cover more than 25,000 km over the ocean, were conducted during four campaigns that took place within the ArctiC Amplification: Climate Relevant Atmospheric and SurfaCe Processes, and Feedback Mechanisms ((AC)^3) project in spring and summer between 2017 and 2022.

The first study presented in this thesis highlights the need for airborne radar observations to observe low-level clouds due to limitations in spaceborne radar observations. By simulating spaceborne radar observations using the airborne radar measurements, limitations of spaceborne radars are assessed concerning their coarse horizontal and vertical resolution and their blind zone that covers the lowest kilometer of the atmosphere. Overall, the spaceborne simulations overestimate the observed cloud fraction, particularly when cold and dry air is advected from the central Arctic over the ocean, i. e., marine cold air outbreaks that foster low-level cloud formation. The blind zone of the spaceborne radar simultaneously misses half of the precipitation amount coming mostly from light precipitation events.

The second study focuses on marine cold air outbreaks that offer unique conditions to study low-level mixed-phase clouds and their evolution. To characterize the clouds, metrics that describe the roll circulation, as well as cloud macro- and microphysics, are derived from radar observations and investigated along the fetch, i. e., the distance an air mass traveled over an open ocean. For two marine cold air outbreak cases of different strengths and with different microphysical preconditions, discrepancies in cloud and precipitation characteristics, including their evolution within cloud objects, are identified. In contrast, similarities are found regarding their evolution with fetch. Moreover, the study highlights that the evolution of snowfall is influenced by microphysical processes, i. e., riming, that are modified by the roll circulations.

The third study aims to constrain snowfall estimates that highly differ among existing data sets. The focus lies on a statistical assessment of snowfall from low-level clouds over the Fram Strait during marine cold air outbreaks. The retrieved snowfall estimates enable an evaluation of the representation of snowfall in reanalyses. Snowfall rates are retrieved from the airborne radar reflectivity observations by applying a power law, a so-called Z_e–S relation. An optimal relation has been derived from radar and precipitation gauge observations at Ny-Ålesund, Svalbard. The observed snowfall rates over the Fram Strait during marine cold air outbreaks are, on average, 330 mm year^{-1} and generally increase with the fetch. Reanalyses have different shortcomings in representing snowfall: the studied global reanalysis overestimates snowfall occurrence, particularly of light snowfall, resulting in a total overestimation of snow accumulation along the flight tracks. In contrast, the studied regional reanalysis underestimates snowfall occurrences and rates.

Overall, this thesis provides an improved assessment and process understanding of low-level clouds over the Fram Strait and related snowfall. The findings are a benchmark to evaluate models and further data sets, such as precipitation estimates from the recently launched satellite EarthCARE.

ZUSAMMENFASSUNG

Wolken bedecken große Teile der Erde, insbesondere in der Arktis. Dort treten vor allem niedrige Wolken auf, die häufig gleichzeitig aus unterkühltem Wasser und Eis bestehen. Solche Wolken werden Mischphasenwolken genannt. Sie erwärmen die Erdoberfläche und bilden Niederschlag, weshalb sie einen erheblichen Einfluss auf den Strahlungshaushalt und den Wasserkreislauf der Erde haben. Beobachtungen dieser niedrigen arktischen Wolken sind jedoch begrenzt, weshalb es erhebliche Unsicherheiten bezüglich der Häufigkeits- und Phasenverteilung von Wolken und Niederschlag gibt. Ungenauigkeiten in der Phasenverteilung von Wolkenpartikeln sind sehr wahrscheinlich der Grund für widersprüchliche Wolkenrückkopplungen in der Arktis zwischen verschiedenen Klimamodellen. Um die Rolle der niedrigen Wolken im arktischen Klimasystem besser verstehen zu können, sind genauere Beobachtungen ihres Auftretens, ihrer Mikrophysik und ihres Niederschlags über dem Meer, dem Meereis und dem Land notwendig. Ein detaillierterer Einblick in mikrophysikalische Prozesse verbessert das Verständnis der Wolkenentstehung, -entwicklung und -lebensdauer. Dies ist essenziell, um Wetter- und Klimamodelle verbessern zu können.

In dieser Dissertation werden die einzigartigen Möglichkeiten flugzeuggestützter Radarbeobachtungen genutzt, um niedrige Wolken und deren Niederschlag über der Framstraße, einer Region, die stark vom Klimawandel betroffen ist, zu charakterisieren. Dabei liegt ein besonderer Schwerpunkt auf Mischphasenwolken und deren Entwicklung. Flugzeuggestützte Radarbeobachtungen sind dafür besonders geeignet, weil sie weite Gebiete über dem offenen Meer und dem Meereis mit einer hohen räumlichen Auflösung abdecken können und Wolken bis wenige hundert Meter über der Erdoberfläche detektieren können. Dadurch können sie Wolken messen, welche mit anderen Messmethoden nicht detektierbar sind. Die untersuchten Messungen umfassen eine Strecke von mehr als 25,000 km über dem Meer. Sie wurden im Rahmen des (AC)³ Projektes während vier Kampagnen im Frühjahr und Sommer zwischen 2017 und 2022 aufgezeichnet.

Die erste Studie dieser Dissertation betont die Notwendigkeit flugzeuggestützter Radarbeobachtungen für die Erforschung niedriger Wolken, welche nur eingeschränkt durch satellitengestützte Radare detektiert werden. Mithilfe der flugzeuggestützten Radarmessungen werden satellitengestützte Radarbeobachtungen simuliert und Grenzen satellitengestützter Radare im Hinblick auf ihre grobe horizontale und vertikale Auflösung, sowie der Rückstreueffekte vom Erdboden, welche die Messungen im untersten Kilometer überlagern, bewertet.

Insgesamt überschätzen die Simulationen die beobachtete Wolkenhäufigkeit, insbesondere dann, wenn kalte und trockene Luft aus der zentralen Arktis über das Meer transportiert wird. Solche Situationen werden marine Kaltluftausbrüche genannt und tragen stark zur Bildung niedriger Wolken bei. Außerdem detektieren satellitengestützte Radare durch die Rückstreueffekte nahe des Erdbodens nur die Hälfte des meist leichten Niederschlags.

Die zweite Studie befasst sich mit marinen Kaltluftausbrüchen, die gute Bedingungen für die Untersuchung niedriger Mischphasenwolken und deren Entwicklung bieten. Es werden Metriken zur Beschreibung der mesoskaligen Zirkulation und der Wolkenmakrophysik und -mikrophysik aus Radarbeobachtungen abgeleitet und als Funktion der Entfernung, die eine Luftmasse über dem offenen Meer zurückgelegt hat, untersucht. Zwei unterschiedlich intensive marine Kaltluftausbrüche, die verschiedene mikrophysikalische Voraussetzungen aufweisen, zeigen unterschiedliche Wolken- und Niederschlagscharakteristika. Gerade die Entwicklung der Wolkeneigenschaften innerhalb der Wolkenobjekte ist unterschiedlich, während die Entwicklung mit der zurückgelegten Distanz über dem offenen Meer ähnlich ist. Die Studie zeigt außerdem, dass die Entwicklung des Schneefalls durch mikrophysikalische Prozesse beeinflusst wird, die durch die mesoskaligen Zirkulationen verändert werden.

Das Ziel der dritten Studie ist es, Abschätzungen von Schneefallraten zu verbessern, da diese zwischen verschiedenen Datensätzen stark variieren. Dies wird durch eine statistische Analyse des Schneefalls niedriger Wolken erreicht, die während mariner Kaltluftausbrüche über der Framstraße auftreten. Die abgeleiteten Schneefallraten ermöglichen eine Bewertung der Darstellung von Schneefall in Reanalysen. Die Schneefallraten werden von den flugzeuggestützten Beobachtungen der Radarreflektivität ermittelt, indem eine sogenannte Z_e–S Beziehung angewendet wird. Diese Beziehung wird aus bodengestützten Beobachtungen eines Radars und eines Niederschlagsmessers aus Ny-Ålesund, Spitzbergen, abgeleitet. Die beobachteten Schneefallraten während mariner Kaltluftausbrüche über der Framstraße betragen im Durchschnitt 330 mm Jahr^{-1} und nehmen im Allgemeinen mit dem Abstand zur Meereiskante zu. Reanalysen stellen diesen Schneefall unterschiedlich dar: Die untersuchte globale Reanalyse überschätzt das Auftreten von Schneefall, insbesondere der geringen Schneefallraten, und dadurch den akkumulierten Schneefall entlang der Flugrouten. Die untersuchte regionale Reanalyse hingegen unterschätzt das Auftreten von Schneefall sowie die Schneefallraten.

Diese Dissertation untersucht niedrige Wolken und deren Niederschlag über der Framstraße und verbessert damit das Prozessverständnis dieser Wolken. Die Ergebnisse können als Referenz für zukünftige Modellevaluierungen und Beobachtungsvalidierungen, wie zum Beispiel des kürzlich gestarteten Satelliten EarthCARE, dienen.

CONTENTS

ACRONYMS

ABL	Atmospheric Boundary Layer
$(AC)^3$	ArctiC Amplification: Climate Relevant Atmospheric and SurfaCe Processes, and Feedback Mechanisms
ACLOUD	Arctic CLoud Observations Using airborne measurements during polar Day
AFLUX	Airborne measurements of radiative and turbulent FLUXes of energy and momentum in the Arctic boundary layer
AWIPEV	research base operated by the German Alfred Wegener Institute for Polar and Marine Research (AWI) and the French Polar Institute Paul-Émile Victor (IPEV)
CARRA	Copernicus Arctic Regional ReAnalysis
CCN	Cloud Condensation Nuclei
CMIP5 and 6	Coupled Model Intercomparison Project Phase 5 and 6
CPR	Cloud Profiling Radar
CTH	Cloud Top Height
DGZ	Dendritic Growth Zone
ECMWF	European Centre for Medium-range Weather Forecast
ERA5	ECMWF ReAnalysis version 5
FMCW	Frequency-Modulated Continuous-Wave
GPCP	Global Precipitation Climatology Project
HALO	*High Altitude LOng range aircraft*
INP	Ice Nucleation Particle
LES	Large Eddy Simulation
LWP	Liquid Water Path
M	normalized rime mass fraction
MCAO	Marine Cold Air Outbreak
MiRAC	Microwave Radar/radiometer for Arctic Clouds
MIZ	Marginal Ice Zone
MOSAiC	Multidisciplinary drifting Observatory for the Study of Arctic Climate
MOSAiC-ACA	MOSAiC Airborne observations in the Central Arctic
MPC	Mixed-Phase Cloud
P5	*Polar 5*
P6	*Polar 6*
pp	percentage points
S	liquid-equivalent snowfall rate
SIP	Secondary Ice Production
TOA	Top Of the Atmosphere
WBF	Wegener-Bergeron-Findeisen
Z_e	equivalent radar reflectivity

1

INTRODUCTION

1.1 MOTIVATION

Arctic amplification

The Arctic climate system has changed profoundly within the past four decades: Arctic near-surface temperatures have increased nearly three times as much as the global average near-surface temperature (Zhou et al., 2024). This phenomenon is called Arctic amplification (Serreze and Barry, 2011; Wendisch et al., 2023). In turn, Arctic amplification affects further Arctic climate system components, e. g., late-summer sea ice cover halved over the past 40 years (Screen, 2021).

feedbacks

Generally, a perturbed climate component affects further climate components that simultaneously feed back on the original perturbation, which can be either amplified (positive feedback) or dampened (negative feedback). Feedbacks occur all over the globe, however, some feedbacks are strongest in the unique polar environments (Wendisch et al., 2023). In polar regions, the surface radiation budget is exceptional due to low solar zenith angles, polar day and night, and high surface albedo. Furthermore, the thermodynamic conditions are highly unique. The low solar radiation leads to extremely cold conditions, and meridional advection of air from the mid-latitudes evokes frequent near-surface temperature and moisture inversions. These Arctic thermodynamic processes provoke low-level clouds that are very persistent compared to other places on Earth (Morrison et al., 2012; Shupe et al., 2008a; Solomon et al., 2011). Finally, interactions with the cryosphere play an important role in polar regions.

cloud feedback

To date, Arctic clouds warm the surface (Curry et al., 1996; Intrieri et al., 2002; Shupe and Intrieri, 2004), i. e., by roughly $+10\,\mathrm{W\,m^{-2}}$ over the Arctic ocean (Kay and L'Ecuyer, 2013). Future warming and moistening of the Arctic atmosphere will likely affect cloud properties such as cloud frequency, height, and phase. These changes impact the Earth's radiative budget, quantified by the cloud height, cloud amount, and cloud phase feedback (Zelinka et al., 2017). Altogether, these mechanisms contribute to the cloud feedback. Nevertheless, the sign and magnitude of the cloud feedback are uncertain (Block et al., 2020; IPCC, 2013): first, the warming effect of low-level clouds obtained by models is not well understood nor constrained by observations yet. Second, the cloud-phase feedback is highly uncertain (Goosse et al., 2018; Storelvmo et al., 2015; Tan et al., 2016). Due to warming, the phase partitioning of clouds should change from ice to liquid-dominated. The higher liquid content increases the cloud optical thickness and cloud albedo (Curry, 1995; Sun and Shine, 1994).

On average, the cloud-phase feedback is thus negative (Storelvmo et al., 2015). However, the temperature at which the phase will shift significantly is highly uncertain, leading to a debate about the sign of the overall cloud feedback (Mitchell et al., 1989; Storelvmo et al., 2015; Tan and Storelvmo, 2016). Moreover, an increased cloud liquid fraction likely affects the precipitation amount, the mass loss, and thus the cloud amount feedback (Storelvmo et al., 2015). However, the cloud feedback is not independent, e. g., also the sea ice retreat causes more open ocean and likely increases the cloud amount, mainly of low-level liquid-bearing clouds (Cesana et al., 2024). It is of global relevance to constrain the current feedback of Arctic low-level clouds (IPCC, 2013), its implication on Arctic amplification, and its future changes because the Arctic affects the global climate and weather, including extreme events (Cohen et al., 2014; Francis and Vavrus, 2012, 2015).

model deficit

Yet, substantial uncertainty persists regarding the relevance of the various mechanisms contributing to Arctic amplification (Block et al., 2020) and the prediction of Arctic future warming, which is expected to accelerate (Overland et al., 2014; Pan et al., 2023). However, the coverage of low-level stratiform clouds, which is one of the most substantial sources of uncertainty in this context (Mioche et al., 2015), is underestimated by global and regional climate models (Fletcher et al., 2016a; Geerts et al., 2022). This is because models parameterize subgrid-scale processes (Roode et al., 2019; Tomassini et al., 2017). More accurate thermodynamic, cloud, and sea ice observations are vital to constrain the model output and foster the process understanding for enhanced parametrizations in global and regional climate model simulations (IPCC, 2013; Tan et al., 2016). Especially in the Arctic, the phase partitioning within clouds has to be represented more realistically (e. g., Curry et al., 2000; Field et al., 2014; Klein et al., 2009; Morrison and Pinto, 2006; Prenni et al., 2007; Sandvik et al., 2007). To achieve this, in particular, understanding cloud processes, which affect the cloud feedback and lifetime, must be facilitated.

aim of this thesis

The launch of satellites equipped with remote sensing instruments, such as CloudSat in 2006, improved cloud observations in the Arctic that, however, remain a challenge. CloudSat's active remote sensing instruments cover large parts of the Arctic and enable the investigation of the vertical cloud structure (Milani and Kidd, 2023). However, it is challenging to assess low-level hydrometeors from these spaceborne instruments (Liu, 2022; Palerme et al., 2019). This limitation can be overcome by high-resolution airborne radar observations that better resolve inhomogeneities of low-level clouds reaching closer to the ground (Mech et al., 2019). This study thus exploits airborne radar observations to characterize the micro- and macrophysics of low-level clouds and their precipitation over the Fram Strait.

1.2 CLOUD OBSERVATIONS IN THE ARCTIC

Sampling clouds in the Arctic is a challenge. Ideally, observations sample the three-dimensional structure of the atmosphere continuously in time, covering the entire Arctic with a high resolution in space and time. Only such observations would resolve temporal variations and spatial differences in cloud structures and microphysics that are provoked by, e. g., atmospheric dynamics, variations in surface properties, and topography (Shestakova et al., 2022; Walter and Overland, 1984; Wendisch et al., 2024). Currently, Arctic clouds are observed by in-situ (e. g., Moser et al., 2023; Vochezer et al., 2016) and remote sensing approaches (e. g., Chellini et al., 2023a; Griesche et al., 2020) from ground-based (e. g., Geerts et al., 2022; Gierens et al., 2020), airborne (e. g., Klingebiel et al., 2023; Maherndl et al., 2024a), or spaceborne (e. g., Mateling et al., 2023; Murray-Watson et al., 2023) instruments. However, all measurement techniques suffer limitations.

in-situ observations

In-situ instruments sample the air that surrounds the sensor. In-situ cloud observations are commonly taken on board an aircraft with a high temporal and spatial resolution (e. g., Morrison et al., 2011). However, their spatial and temporal coverages are limited because only one specific location can be sampled along flight tracks.

remote sensing observations

Contrarily to in-situ instruments, remote sensing instruments can be applied far off the location of interest, making ground-based (e. g., Mages et al., 2023; Shupe et al., 2008a), airborne (e. g., Ruiz-Donoso et al., 2020), and spaceborne (e. g., Mioche et al., 2015) applications possible. The application on various platforms allows the adaptation of the resolution and coverage of the observation to different needs. Remote sensing instruments retrieve information about the atmosphere by receiving radiation (Petty, 2006). A distinction is made between active and passive remote sensing.

active remote sensing

Active remote sensing instruments receive radiation that has been transmitted previously and is then backscattered by hydrometeors within the atmosphere. In doing so, active remote sensing resolves the atmosphere vertically. Here, lidars (short for LIght Detection And Ranging) and radars (RAdio Detection And Ranging) are essential instruments used within this thesis's framework (see Sect. 1.5). Lidars transmit radiation between 250 nm and eleven µm and are thus sensitive to small particles (Weitkamp, 2005). However, already a relatively small number of hydrometeors extincts the lidar signal and makes an assessment of the whole atmospheric column impossible. Radars transmit longer wavelengths within the milli- to micrometer range and are thus sensitive to larger particles (Doviak and Zrnić, 2006). Such microwave radars can penetrate the entire atmosphere because clouds are semitransparent within the microwave spectrum (Ulaby and Long, 2014).

passive remote sensing

Passive remote sensing instruments receive attenuated thermal emissions (Petty, 2006). In the microwave regime, they retrieve information over the entire atmospheric column (Ulaby and Long, 2014). However, the signals are column integrals that include numerous emission sources and cannot be directly assigned to hydrometeors at a specific location. For downward-looking instruments, the received microwave signal originates both from the atmosphere and the Earth's surface.

ground-based observations

Arctic ground-based supersites provide already long time series. Nevertheless, only a few land-based observatories exist, such as the research base operated by the German Alfred Wegener Institute for Polar and Marine Research (AWI) and the French Polar Institute Paul-Émile Victor (IPEV) (AWIPEV) (Neuber, 2006) at Ny-Ålesund, Svalbard, the Summit station (Shupe et al., 2013) in Greenland, the Barrow Atmospheric Baseline Observatory (Vasel et al., 2020) near Utqiagvik, Alaska, or the Eureka observatory (Shupe, 2011) in Canada. Over the ocean, observations obtained aboard research vessels during short-term cruises (e. g., Kanzow, 2023; Renfrew et al., 2019) or drifting campaigns (Shupe et al., 2022; Uttal et al., 2002), and buoy observations (Ignatius and Ortmeyer, 2004) expand the ground-based data set. Ground-based active remote sensing observations are especially interesting, as they accurately resolve the lower atmosphere. Nevertheless, the specific environmental conditions at each ground-based measurement site, e. g., land-sea contrast or orography, influence the observations and make a generalization of the observations over the entire Arctic impossible (Mioche et al., 2015).

spaceborne remote sensing

Cloud observations from above benefit from higher spatial coverage than ground-based observations. This applies, in particular, to remote sensing from satellites. So far, spaceborne active remote sensing is rare. Radar observations, for example, have been only retrieved aboard the CloudSat (since 2006; Stephens et al., 2002) and EarthCARE (since 2024; Illingworth et al., 2015; Wehr et al., 2023) satellites and provide just a cross section of the atmosphere. Unfortunately, spaceborne radars do not resolve cloud properties close to the ground due to strong backscatter signals from the surface, so-called ground clutter (Lamer et al., 2020; Liu, 2022; Maahn et al., 2014; Palerme et al., 2019). Spaceborne passive remote sensing instruments operating within the visible, infrared, or microwave spectrum cover a wider swath than active instruments, however, frequently fail to discriminate Arctic low-level cloud and surface signals. Within the microwave spectrum, the low-level cloud fraction is underestimated because of brightness temperature differences between the surface and clouds that are too small (Milani and Kidd, 2023; Mioche et al., 2015). In conclusion, satellite remote sensing experiences substantial limitations in observing clouds below 1 km height.

airborne remote sensing

As described above, remote sensing instruments can also be installed on aircraft. Compared to coarsely resolved spaceborne observations that suffer ground clutter over many heights, airborne remote sensing can better resolve inhomogeneities of low-level clouds reaching closer to the ground (Mech et al., 2019). However, airborne measurements are limited to campaigns. To generalize findings, multiple campaigns have to be conducted that cover different periods of the year and take place as long as possible (Wendisch et al., 2023). Such campaigns have been successfully performed within the framework of the project ArctiC Amplification: Climate Relevant Atmospheric and SurfaCe Processes, and Feedback Mechanisms ((AC)³) (Wendisch et al., 2023; Sect. 1.5).

cloud occurrence

Spaceborne active remote sensing observations indicate that clouds occur more frequently in the Arctic than over the entire Earth, for which the average cloud cover is roughly 70 % (Stubenrauch et al., 2013). Averaged over the Arctic, the cloud cover is lowest in winter (60–70 %) and highest in autumn (80–100 %; Mioche et al., 2015). At Ny-Ålesund, Svalbard, ground-based remote sensing observations that reach just above the ground confirm this annual cycle of cloud cover between the years 2016 and 2018 (Gierens et al., 2020). Over the Fram Strait west of the Svalbard archipelago, the cloud cover is roughly 70 % in summer and 90 % at other times and thus above the respective seasonal Arctic-wide averages (Mioche et al., 2015).

low-level cloud occurrence

Clouds at different heights contribute to this cloud cover. With 50 % of the observed clouds being low-level stratus, low-level clouds are very prominent in the Arctic, partly due to the advection of moist air above near surface inversions (Eastman and Warren, 2010; Liu et al., 2012; Mioche et al., 2015; Shupe et al., 2006). Over the Arctic Ocean, low-level clouds are even more dominant: active remote sensing observations indicate that roughly 80 % of the clouds observed between 2006 to 2011 occurred below 2 km altitude (Liu et al., 2012).

low-level mixed-phase cloud occurrence

Arctic low-level clouds frequently consist of supercooled liquid droplets and ice particles simultaneously – so-called Mixed-Phase Clouds (MPCs) (Sect. 2.2). From autumn until the beginning of summer more than 40 % of the clouds detected from space over the Svalbard region are MPCs with cloud top heights between 500 m and 3 km (see Table 1.1; Mioche et al., 2015). This low-level MPC occurrence depends on the surface cover and is thus even higher over open water such as the Fram Strait.

Over Ny-Ålesund, however, substantial discrepancies remain between MPC observations from ground-based (Gierens et al., 2020) and synergetic satellite radar and lidar remote sensing (Mioche et al., 2015; see Table 1.1): ground-based observations detect overall fewer low-level MPCs and the annual cycle of MPCs occurrence is reversed between the two data sets. Part of the differences can presumably be explained by the different considered time periods and cloud lifetimes

Table 1.1: Mean occurrence of low-level Mixed-Phase Clouds with cloud tops between 500 and 3000 m height in the region around the Svalbard archipelago between 2007 and 2010. The values are from Mioche et al. (2015).

Season	Over open water	Over sea ice	Over land
Winter	48 %	42 %	40 %
Spring	53 %	41 %	38 %
Summer	34 %	34 %	36 %
Autumn	44 %	40 %	42 %

in these two data sets. However, this is unlikely to explain the striking differences between ground-based and spaceborne observations. Instead, the two-year period covered by the ground-based observations might be too short to capture cloud variability accurately. Conversely, spaceborne instruments exhibit a number of limitations that might be responsible for the discrepancies: the spaceborne radar conceals spatial cloud patterns along the track due to its coarse resolution and stretches or fails to detect shallow clouds due to its pulse length (Lamer et al., 2020), it does not capture clouds due to ground clutter inside the lowest kilometer of the atmosphere (Lamer et al., 2020; Liu, 2022; Palerme et al., 2019), and it fails to detect clouds due to its limited sensitivity. In particular, the blind zone effect might reduce the observed cloud cover in summer, when clouds are often below 1 km height (Maahn et al., 2014). The spaceborne lidar can sample the entire atmospheric column, however, its signal might be attenuated by high clouds. Moreover, the low amount of ice within MPCs might be below the lidar's detection limit, leading to a misclassification of MPCs as liquid clouds (Gierens et al., 2020). For these reasons, airborne remote sensing is needed to reduce the uncertainty of low-level MPC observations and to solve the puzzle of why ground-based and spaceborne remote sensing MPC observations differ substantially.

1.3 MARINE COLD AIR OUTBREAKS

Marine Cold Air Outbreaks (MCAOs) might occur whenever cold air flows over warm water. Then, roll circulations develop perpendicular to the flow that form cloud streets (Fig. 1.1), which are well visible in satellite images. These clouds are often mixed-phase (e. g., Geerts et al., 2022; Kirschler et al., 2023; Tornow et al., 2021). Extreme surface heat fluxes (Brümmer, 1996) strengthen convection within the Atmospheric Boundary Layer (ABL) and deepen the ABL downstream. With distance over the open water, the low-level cloud streets thus deepen and transform into closed and open cellular convection, leading to a cloud breakup. MCAOs occur frequently in the cold air sector of extratropical cyclones (Afargan-Gerstman et al., 2020; Fletcher et

Figure 1.1: Cloud streets during a Marine Cold Air Outbreak on 4 April 2022 from an airborne perspective. The picture was taken by Mario Mech.

al., 2016b; Kolstad et al., 2009; Papritz and Grams, 2018). They have a lifetime of roughly a few days, a horizontal scale of 1,000 km (Fletcher et al., 2016b), and can occur worldwide. Nevertheless, they are more common and intense in the Northern than in the Southern Hemisphere, where they occur 70 % less frequently during winter (Fletcher et al., 2016b). The frequency of occurrence of MCAOs has a seasonal cycle: for the Northern Hemisphere, MCAOs occur most frequently in winter, by half less in spring and autumn, and not at all in summer, when temperature contrasts between the Arctic air and ocean are low (Fletcher et al., 2016b).

Arctic marine cold air outbreaks

Especially in the Arctic, MCAOs appear when cold and dry air flows from the ice-covered central Arctic southward over the open ocean. Over the Nordic Seas, European Centre for Medium-range Weather Forecast (ECMWF) ReAnalysis version 5 (ERA5) data and CloudSat observations reveal that most MCAOs are located over the Fram Strait year-round (Mateling et al., 2023), occurring two-thirds of the time during their primary season from December to March (Dahlke et al., 2022). The MCAO events over the Fram Strait are also the strongest Arctic MCAOs (Fletcher et al., 2016b; Papritz and Spengler, 2017). A persistent anticyclonic blocking over the North Atlantic or Greenland and anomalous low pressure over the Barents or Kara Seas often causes these long-lasting MCAOs (e. g., Dahlke et al., 2022; Kolstad et al., 2009; Terpstra et al., 2021). Then, the magnitude of the zonal pressure gradient over the Fram Strait determines the MCAO strength (Dahlke et al., 2022). Moreover, the passage of Arctic cyclones goes over the Fram Strait and increases the frequency of MCAO occurrences.

implications on climate

MCAOs are relevant for climate research as their cloud formation induces an above-average surface longwave warming (Sect. 2.1). Nevertheless, this warming is an order of magnitude smaller than the concurrent cooling by surface heat fluxes (Fletcher et al., 2016a). Arctic MCAOs have, moreover, enormous implications on Arctic and mid-latitudinal weather and climate as they are the dominant mechanism for energy exchange (Pithan et al., 2018) and air mass transformation between both regions (Papritz and Spengler, 2017; Pithan et al., 2018). The cold air advection is frequently responsible for severe weather in North America, Europe, and East Asia (Abel et al., 2017; Papritz and Grams, 2018; Papritz and Spengler, 2017; Turner and Marshall, 2011a). One example was the "Beast from the East" that brought heavy snowfall and freezing across Europe in February 2018. During this event, 88 % of the snowfall in Europe was attributed to evaporation over the Barents Sea, which was anomalously warm and ice-free (Bailey et al., 2021). Reanalysis data show that over the past 40 years, the decline in sea ice in the Barents Sea during autumn and winter increases evaporation (Bailey et al., 2021) and changes the circulation patterns by increasing the occurrence of blocking situations (Liu et al., 2012) and thus MCAOs. As a result, the maximum snowfall in Europe increases by 1.6 mm water equivalent per year (Bailey et al., 2021). In the future, the Arctic is predicted to be the major moisture source for Europe and to influence the mid-latitudinal weather even more than today (Bailey et al., 2021). Moreover, some Arctic MCAOs generate polar lows (Meyer et al., 2021; Terpstra et al., 2021) that can induce further severe weather (e. g., Abel et al., 2017; Kolstad et al., 2009; Landgren et al., 2019; Shapiro et al., 1987).

implications on the ocean

The intense surface heat fluxes during MCAOs and associated polar lows also modify the ocean. Thus, 60–80 % of the oceanic heat loss in the Nordic Seas during winter is due to MCAOs (Papritz and Spengler, 2017). This enhances the northward transport of heat, favors deepwater production, and strengthens the oceanic meridional overturning circulation (Condron and Renfrew, 2013; Dickson et al., 1996; Isachsen et al., 2013; Papritz and Spengler, 2017; Terpstra et al., 2021).

implications on precipitation

MCAOs additionally affect the evolution of precipitating clouds, enhance the precipitation rates, and shape the Earth's water cycle (Abel et al., 2017; Brümmer, 1997). Over the North Atlantic, snowfall occurs most often during MCAO conditions regardless of its intensity or season (Mateling et al., 2023). During these MCAOs, nevertheless, most snowfall is light ($<0.1\,\mathrm{mm\,h^{-1}}$), while heavy snowfall rates ($>0.1\,\mathrm{mm\,h^{-1}}$) are relatively more common during non-MCAO conditions (Mateling et al., 2023).

past trend

To assess the driving factors and the global impact of MCAOs, interconnections between meteorological parameters and MCAOs, as well as teleconnections between different regions, have been studied with monthly resolution (Dahlke et al., 2022). Over the past 40 years, the MCAO strength over the Fram Strait decreased in December and January (Dahlke et al., 2022) because the Arctic warmed strongest in the lower troposphere (Dahlke et al., 2020; Graversen et al., 2008; Serreze et al., 2009). Retreating sea ice in the Barents Sea during these months was typically associated with high pressure to the east and cyclones to the west of the Barents Sea (Crasemann et al., 2017). However, in March, the MCAO strength increased over the past 40 years. This is because sea ice retreat in the Barents Sea provoked more frequent cyclones in this region, inducing northerlies and thus MCAOs in the Fram Strait (Dahlke et al., 2022). Moreover, the region north of Svalbard indicates that sea ice loss (Onarheim et al., 2014) can strengthen MCAOs and convective boundary layers locally (Tetzlaff et al., 2014).

model representation

Accurate forecasts of MCAO events are important, but the interconnection with environmental conditions and worldwide teleconnections (Dahlke et al., 2022) likely increase the uncertainty of predictions. Different models that resolve different scales do not represent MCAOs well: the roll formation and thin ABL within the initial phase of MCAOs are roughly reproduced by idealized high-resolution models (e. g., Gryschka and Raasch, 2005; Liu et al., 2004). Nevertheless, Liu et al. (2004) did not explicitly resolve small-scale turbulence, while Gryschka and Raasch (2005) did not represent cloud ice. The MCAO low-level stratiform clouds over open water and the timing of their breakup are generally not well captured by many kinds of models, such as single-column models, cloud-resolving models (Klein et al., 2009), Large Eddy Simulations (LESs) (Roode et al., 2019), and regional and global numerical weather predictions (Field et al., 2017).

Regardless of their resolution, all models mentioned above parameterize cloud microphysics. In many models, the conversion from supercooled liquid water to ice particles is too strong (Field et al., 2014; Kiszler et al., 2023; Klein et al., 2009), which influences the timing of the transition (Roode et al., 2019). A discussion about possible model improvements can be found in Sect. 2.2.2.

1.4 ARCTIC PRECIPITATION

observation deficit

The spatial and temporal coverage of accurate in situ and remote sensing precipitation observations is poor in the Arctic increasing the uncertainty of precipitation estimates, especially over the Arctic sea ice and ocean (Vihma et al., 2016). Snowfall observations during MCAOs are particularly uncertain for two main reasons: first, the shallow snowfall is missed by spaceborne radars due to their blind zones (Lerber et al., 2022b). Second, light snowfall is missed by spaceborne passive remote sensing instruments because of too little snowfall signals compared to the highly variable background signal coming from the surface (Milani and Kidd, 2023). Within the framework of the Global Precipitation Climatology Project (GPCP), an observational precipitation data product is retrieved that covers the entire Arctic from 1979 onwards by merging gauges and satellite observations (Adler et al., 2018). However, even the merged data are highly uncertain and assumed to perform worse than reanalyses (Serreze et al., 2005). This is despite the fact that reanalyses are affected by model limitations and by the lack of reliable observations assimilated (Zhang et al., 2013). Since snowfall is highly variable in time and space, good data coverage is essential for accurate data assimilation. Therefore, despite their limitations, both the latest global reanalysis ERA5 (Hersbach et al., 2020) and the novel, higher-resolved Copernicus Arctic Regional ReAnalysis (CARRA) (Yang et al., 2023) are frequently used to study precipitation in the Arctic.

precipitation pattern

Mechanisms that provoke precipitation in the Arctic vary spatially, leading to a pronounced precipitation pattern. Over the North Atlantic, cyclones advect heat and moisture into the Arctic and thus enhance precipitation rates (Lerber et al., 2022b). Over Greenland, most precipitation falls during southerly winds (Castellani et al., 2015) that advect moist air from ice-free areas around Greenland. Thus, the annual cycle of precipitation over Greenland has a maximum in summer and a minimum in spring (Castellani et al., 2015). Furthermore, precipitation microphysics vary spatially: in contrast to over the North Atlantic, snowfall over the Greenland ice sheet has little to no Liquid Water Path (LWP) (Castellani et al., 2015), which indicates that ice processes dominate.

A similar large-scale pattern of Arctic precipitation is captured by ERA5, the Coupled Model Intercomparison Project Phase 5 and 6 (CMIP5 and 6), GPCP, and CloudSat data: the precipitation rates are lowest over central Greenland and highest along the coast of Greenland, over the Greenland Sea, Barents Sea, and Fram Strait (Edel et al., 2020; Lerber et al., 2022b; McCrystall et al., 2021). However, the strength of long-term precipitation rates varies, i. e., from 1 (CMIP5 and 6 and GPCP; McCrystall et al., 2021) to 2 mm day^{-1} (ERA5 and CloudSat; Lerber et al., 2022b; McCrystall et al., 2021) over the Fram Strait. This difference could be caused by MCAOs (Lerber et al., 2022b).

past precipitation trend

The variability in precipitation rates averaged over the entire Arctic is large among the different data sets: precipitation rates from ERA5 reanalysis data, CMIP5 and 6 model data, and GPCP observations show a yearly uncertainty of roughly 30 % since 1997 (McCrystall et al., 2021). The large uncertainties in Arctic precipitation estimates cause different long-term precipitation trends among the data sets: models and reanalyses capture an apparent increase in precipitation related to warming, which varies spatially and seasonally and is especially strong over the Arctic Ocean (Bintanja, 2018; IPCC, 2013; McCrystall et al., 2021; Vihma et al., 2016). Moreover, models and reanalyses show frequent shifts from solid to liquid precipitation over the past years (Bintanja and Andry, 2017; Vihma et al., 2016). CMIP5 and 6 simulations show a decreasing ratio of snowfall to the total precipitation occurrence over time reaching roughly 67 % in 2005, when the historical period for the CMIP5 model simulation ended (McCrystall et al., 2021). The trend in precipitation amount retrieved by models and reanalyses is in stark contrast to observations that show no clear trend (Boisvert and Stroeve, 2015; McCrystall et al., 2021; Vihma et al., 2016). Nevertheless, observations confirm a decrease in snowfall fraction for the Atlantic sector of the Arctic (Łupikasza and Cielecka-Nowak, 2020), e. g., ground-based observations at Ny-Ålesund reported several periods of heavy rain in recent winters (Maturilli et al., 2013).

future precipitation trend

In the future, precipitation rates are predicted to increase by 30 to 60 % until the year 2100 (Bintanja and Andry, 2017; Bintanja and Selten, 2014; Vihma et al., 2016). The Arctic is expected to become moister because warmer air contains more water (Bintanja, 2018; Mudryk et al., 2020; Screen and Simmonds, 2010). This increased humidity might originate from locations affected by future sea ice decline (Bintanja and Selten, 2014; Boisvert and Stroeve, 2015; Serreze et al., 2012; Vihma et al., 2016) or might be advected by frequent poleward moisture transports (Hao et al., 2019; Wang et al., 2024; Woods et al., 2013; Zhang et al., 2013). Compared to past climate projections, more recent projections predict an even stronger increase in Arctic precipitation and an Arctic that is sooner rainfall-dominated during summer and autumn (McCrystall et al., 2021). However, uncertainties in the models, the moisture transport, and the sea ice distribution exist (Cai et al., 2024).

implications on climate

Improving the knowledge on present and future Arctic precipitation is essential because increased Arctic rainfall will have tremendous implications for the Arctic climate system. Rain that falls on snow and ice influences the surface properties and reduces the surface albedo. The decrease in surface albedo leads to an increase in near-surface air temperature, causing further (sea) ice and snow decline, known as the sea-ice albedo and snow-albedo feedback (Perovich et al., 2002). The Greenland ice sheet mass balance will decrease, which will cause the global sea level to rise (Fettweis et al., 2013; Oltmanns et al., 2019). More meltwater will increase the river discharge (Wu et al., 2005; Zhang et al., 2013), which in turn will increase the freshwater and heat content of the Arctic Ocean, particularly at the shelves where the ice volume shrinks (Park et al., 2020). Moreover, permafrost will melt, which increases the risk of slush avalanches (Hansen et al., 2014). In conclusion, rain in the Arctic represents a major hazard for wildlife and society (Hansen et al., 2014).

1.5 OPPORTUNITIES PROVIDED BY THE (AC)^3 PROJECT

Improving the understanding of Arctic amplification is tackled within the framework of the Transregional Collaborative Research Centre TR 172 "ArctiC Amplification: Climate Relevant Atmospheric and SurfaCe Processes, and Feedback Mechanisms ((AC)^3)" funded by the German Research Foundation (Wendisch et al., 2023). The aim of (AC)^3 is to identify, investigate, evaluate, and quantify the contribution of the critical processes to Arctic amplification. To do so, observations obtained at ground stations, on land and vessels, from balloons, aircraft, and satellites, as well as model data, are analyzed and developed (Wendisch et al., 2023).

ground station

The land station from which data are investigated within (AC)^3 and within this thesis is the French-German AWIPEV (Neuber, 2006). It is located at Ny-Ålesund, Svalbard, close to the coast of the Kongsfjorden, surrounded by 500–1,000 m high mountains. For Ny-Ålesund, a long-term data record of radiosondes is available since 1992 (Maturilli et al., 2013). Meteorological observations are obtained at the atmospheric observatory that hosts a 94 GHz cloud radar and a Humidity And Temperature PROfiler (HATPRO) microwave radiometer, among other instruments, on its roof. The radar was first installed in 2016 (Gierens et al., 2020; Maturilli and Ebell, 2018). On a nearby field, 180 m apart, a measurement tower that obtains wind, humidity, and temperature measurements, a precipitation gauge, and a Video In Situ Snowfall Sensor (VISSS; Maahn et al., 2024) that characterizes hydrometeor shapes and sizes are installed.

airborne campaigns

This thesis is centered around airborne field campaigns conducted within the (AC)^3 project that cover periods from 2017 to 2022 and seasons between March and September (Fig. 1.2). In total, three different aircraft were operated during these field studies, namely the *Polar 5* (P5), the *Polar 6* (P6) (Wesche et al., 2016), and the *High Altitude LOng range aircraft* (HALO) (Ziereis and Gläßer, 2006). The polar aircraft belong to the Alfred-Wegener-Institut and were operated from Longyearbyen, Svalbard. They are well suited for the Arctic environment, and observations benefit from their slow flight speed of around 80 m s^{-1}. However, their range is with a maximum of 2,300 km relatively small (Wendisch et al., 2024) and thick clouds hinder starting and landing. Most of the time, P5 performed remote sensing flights at an altitude of around 3 km height, i. e., above the low-level clouds. P6 was equipped with in situ instruments and flew different patterns below and inside the clouds (Mech et al., 2022). The HALO research aircraft was operated by the German aerospace center. HALO started from Kiruna, Sweden, to measure large-scale conditions with remote sensing instruments. Generally, it is operated at around 12 km height and can cover distances of more than 8,000 km (Ziereis and Gläßer, 2006). For each campaign, different aircraft were combined to study

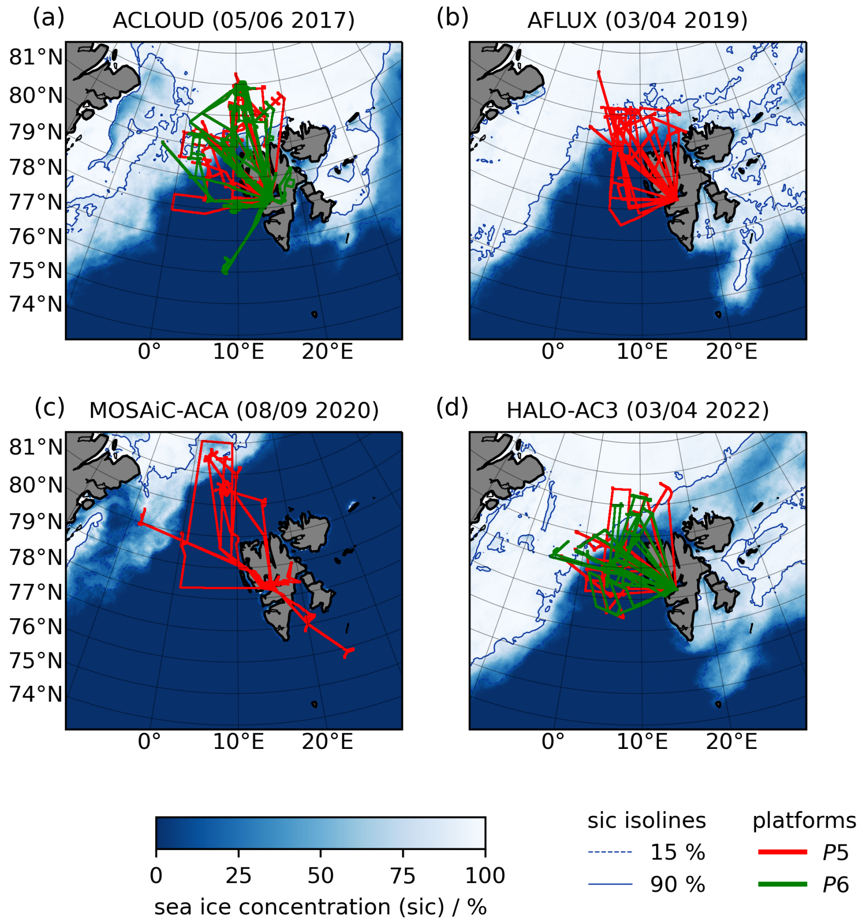

Figure 1.2: Flight tracks of *Polar 5* (P5) (red) and *Polar 6* (P6) (green), as well as sea ice concentration (sic) during the airborne campaigns Arctic CLoud Observations Using airborne measurements during polar Day (ACLOUD) (a), Airborne measurements of radiative and turbulent FLUXes of energy and momentum in the Arctic boundary layer (AFLUX) (b), Multidisciplinary drifting Observatory for the Study of Arctic Climate Airborne observations in the Central Arctic (MOSAiC-ACA) (c), and *High Altitude LOng range aircraft* (HALO)–ArctiC Amplification: Climate Relevant Atmospheric and SurfaCe Processes, and Feedback Mechanisms ((AC)³) (d).

the same region in synergy. The comprehensive data set helps to estimate the role Arctic clouds play in Arctic amplification. Airborne campaigns, whose data are analyzed within this thesis, are summarized in the following. The respective flight tracks of P5 and P6 are displayed in Fig. 1.2.

ACLOUD

In May and June 2017, Arctic CLoud Observations Using airborne measurements during polar Day (ACLOUD) were carried out (Ehrlich et al., 2019b; Wendisch et al., 2019). During this airborne campaign, both polar aircraft have been operated.

Figure 1.3: Microwave Radar/radiometer for Arctic Clouds (MiRAC) mounted within the belly pod under the research aircraft *Polar 5*. The picture was taken by Pavel Krobot.

AFLUX

Airborne measurements of radiative and turbulent FLUXes of energy and momentum in the Arctic boundary layer (AFLUX) followed in March and April 2019 (Mech et al., 2022). P5 was the only aircraft operating and obtained in situ and remote sensing measurements simultaneously. With these data, surface heterogeneity in the sea ice and its effect on Arctic cloud formation was especially targeted.

MOSAiC-ACA

From September 2019 to 2020, *RV Polarstern* drifted through the central Arctic during the Multidisciplinary drifting Observatory for the Study of Arctic Climate (MOSAiC) campaign (Shupe et al., 2022). (AC)^3 contributed with remote sensing measurements on board *RV Polarstern*, and balloon and ice measurements on the ice floe. From August until September 2020, the shipborne campaign was coordinated with an airborne campaign called MOSAiC Airborne observations in the Central Arctic (MOSAiC-ACA) (Mech et al., 2022). During MOSAiC-ACA, the aircraft P5 conducted remote sensing measurements.

HALO-*(AC)^3*

Lately, the HALO-(AC)^3 campaign was performed in March and April 2022, when all three research aircraft were operated synergetically (Wendisch et al., 2024). In particular, air mass transformations into and out of the Arctic have been studied. For the first time in the Arctic, a quasi-Lagrangian approach was conducted meaning that the same air masses were traced and observed several times. This strategy was achieved by modeling air mass trajectories with the help of wind fields from reanalyses during the flight planning.

Microwave Radar/radiometer for Arctic Clouds

This thesis specifically focuses on analyzing radar data obtained by the Microwave Radar/radiometer for Arctic Clouds (MiRAC). MiRAC has been mounted with a down-looking orientation in a belly pod under P5 throughout all the aforementioned campaigns (Fig. 1.3; Mech et al., 2019). The active component of the instrument (MiRAC-A) consists of a radar and an extra 89 GHz passive channel, from which LWP can be derived (Ruiz-Donoso et al., 2020).

auxiliary instruments

Within the framework of this thesis, the study of low-level clouds is supported by measurements from Vaisala RD94 dropsondes (George et al., 2021; Vaisala, 2010) released from HALO and P5 and by observations from the Airborne Mobile Aerosol Lidar (AMALi; Stachlewska et al., 2010) obtained on board P5. AMALi measures profiles of backscattered intensities at 532 nm (parallel and perpendicular polarized) and 355 nm (not polarized), and is used to calculate the Cloud Top Height (CTH) (Mech et al., 2022).

1.6 OBJECTIVES

Because of their predominance (Sect. 1.2) and their unresolved implications on the highly uncertain cloud feedback, this thesis aims to improve the understanding of Arctic low-level clouds, which are frequently MPCs (Sect. 1.2). This thesis makes use of the unique capabilities of airborne radar observations to study Arctic low-level clouds (Sect. 1.2). These observations were obtained during 56 research flights that were conducted within the $(AC)^3$ project (Sect. 1.5). The overarching aim of this thesis is to characterize low-level clouds and precipitation (Sect. 1.4) over the Fram Strait with a particular focus on MPCs (Sect. 2.2) and their development over the open ocean during MCAOs (Sect. 1.3). To do so, the thesis addresses three main research questions in separate Chapters. Finally, all findings are discussed in a broader context, conclusions are drawn, and future perspectives are given (Ch. 6). In the following, the research questions are motivated and contextualized.

1.6.1 *Study I: Arctic low-level clouds observed by space- and airborne radar*

The first study (Chapter 3), which was published in Atmospheric Measurement Techniques as Schirmacher et al. (2023), focuses on the limitations of spaceborne active remote sensing. In particular, CloudSat Cloud Profiling Radar (CPR) observations are often used to investigate the vertical cloud structure over the Arctic and provide the only Arctic-wide snowfall observations. However, it is still unclear how much of the cloud fraction is missed by CloudSat's blind zone and how well CloudSat CPR captures the cloud fraction over the remaining profile.

These questions are answered in the first study using airborne radar observations to retrieve the cloud fraction within the lowest 2.5 km height over the Fram Strait as a reference. This observed cloud fraction, which also includes precipitation, is assumed to represent the 'true' cloud fraction due to the higher resolution, higher sensitivity, and smaller blind zone compared with spaceborne observations (Sect. 1.2). To quantify CloudSat CPR limitations, differences between the airborne and spaceborne radar observations are investigated in two different ways. In direct comparisons, airborne satellite underflights are exploited. For more extensive and indirect comparisons, forward simulations that mimic the CloudSat CPR are performed and analyzed using airborne radar observations.

The first study's findings provide important context about the limitations of CloudSat CPR, which is relevant for studies that use these observations. This way, the study underlines the value of high-resolution airborne observations for remote places.

First research question

How large is the low-level cloud fraction over the Fram Strait, and how well can it be derived from satellite observations?

1.6.2 *Study II: Initial development of marine cold air outbreaks*

The formation of cloud streets during MCAOs induces an increased low-level cloud cover that is not well captured by spaceborne active remote sensing observations, as motivated by the first study. Moreover, spaceborne passive remote sensing instruments cannot retrieve cloud characteristics above the sea ice and close to its edge, in case of microwave passive remote sensing due to the unknown emissivity of the sea ice. However, the initial cloud development during MCAOs over open water close to the sea ice particularly presets further cloud evolution, such as cloud cover and precipitation characteristics downstream. Thus, the first study, already highlighted the need for high-resolution airborne active remote sensing observations.

In the second study, which was published in Atmospheric Chemistry and Physics under Schirmacher et al. (2024a), a novel method links radar observations to roll circulations that evoke cloud streets. This enables a synergetic analysis of high-resolution macro- and microphysical cloud and precipitation observations and circulation observations in the initial MCAO transformation phase. Observations of two MCAO cases of different strengths and with different microphysical preconditions are analyzed within roll cloud objects and as a function of fetch, i. e., the distance air traveled over open water before being assessed by the radar, which is computed from back trajectories. The detailed observations described in this study provide a benchmark for future model intercomparison studies.

Second research question

Do environmental conditions precondition MCAO evolution, and how do roll circulation and cloud properties change with fetch in the initial state of MCAOs?

1.6.3 *Study III: Snowfall over the Fram Strait*

Snowfall estimates during MCAOs are highly uncertain in the Arctic due to a limited number of observations. The first study concluded that low-level clouds and their precipitation that form during MCAOs are not resolved by spaceborne active remote sensing observations. The sparse observations also limit the performance of reanalyses. Within the framework of the second study, estimates of the liquid-equivalent snowfall rate (S) have been obtained from equivalent radar reflectivity (Z_e) observations over the Fram Strait using a relation that solely holds for a specific crystal habit. Nevertheless, crystal habits vary during MCAO snowfall, which increases the uncertainty of the retrieved snowfall estimates.

Within the third study, which is prepared for publication, a more precise snowfall statistic is derived for MCAOs over the Fram Strait. It is based on airborne radar observations using a Z_e–S relation derived from ground-based low-level MPC observations obtained at Ny-Ålesund. The retrieved snowfall rates over the Fram Strait are used to evaluate the representation of snowfall in reanalysis products.

The third study provides valuable snowfall estimates over the Fram Strait during MCAOs that reduce the snowfall uncertainty for the current climate and serve as a benchmark for the evaluation of the representation of snowfall in models, reanalyses, and further observations.

Third research question

How much snow falls over the Fram Strait during MCAOs, and how well do current reanalyses capture the observed snowfall rates?

2

BACKGROUND

This chapter provides background information on the three studies included in this thesis. The radiative effect of Arctic clouds, especially low-level Mixed-Phase Clouds (MPCs), was mentioned frequently in Chapter 1 and is explained in depth in Sect. 2.1. More information on Arctic low-level MPCs follows in Sect. 2.2, where the focus lies on microphysical processes (Sect. 2.2.1) and the implications of the presence of two phases (Sect. 2.2.2). Section 2.2 is relevant for all presented studies: first, Arctic low-level clouds are often mixed-phase (Sect. 1.2); second, cloud microphysics determine cloud occurrence and precipitation processes. Section 2.3 presents the theory about downward-looking microwave radar observations that are used throughout all studies.

2.1 CLOUD RADIATIVE EFFECT

Clouds have a longwave and shortwave radiative effect at the surface and Top Of the Atmosphere (TOA), leading to a net warming or cooling of Earth's atmosphere (Ramanathan et al., 1989). In the current climate, clouds, especially low-level clouds, on average, cool both at TOA and at the surface (Henderson et al., 2013). This is because the cooling effect of clouds reflecting shortwave radiation dominates over the warming effect of clouds absorbing and re-emitting longwave radiation. In the Arctic, however, clouds warm the surface (Curry et al., 1996; Intrieri et al., 2002; Shupe and Intrieri, 2004). One reason for this surface warming is the low solar elevation during the polar day and the absence of solar radiation during the polar night that both strongly reduce the reflection of shortwave radiation and thus lead to a dominant longwave effect (Lubin and Vogelmann, 2006; Stapf et al., 2021). Moreover, the high Arctic low-level cloud fraction substantially increases the amount of longwave radiation emitted to the surface (Fletcher et al., 2016a). Even though less dominant, the shortwave effect is sensitive to the surface albedo (Wendisch et al., 2019) and might offset the longwave warming at the surface in summer (Ebell et al., 2020; Shupe and Intrieri, 2004).

marine cold air outbreaks

During Marine Cold Air Outbreaks (MCAOs), the low-level cloud fraction and thus the surface longwave warming are above the marine average (Fletcher et al., 2016a; Narizhnaya and Chernokulsky, 2024). Simultaneously, the rare occurrence of MCAOs during summer limits their shortwave cooling effect at the surface (Fletcher et al., 2016a). In total, the annual surface warming of MCAOs is strongest in the Arctic

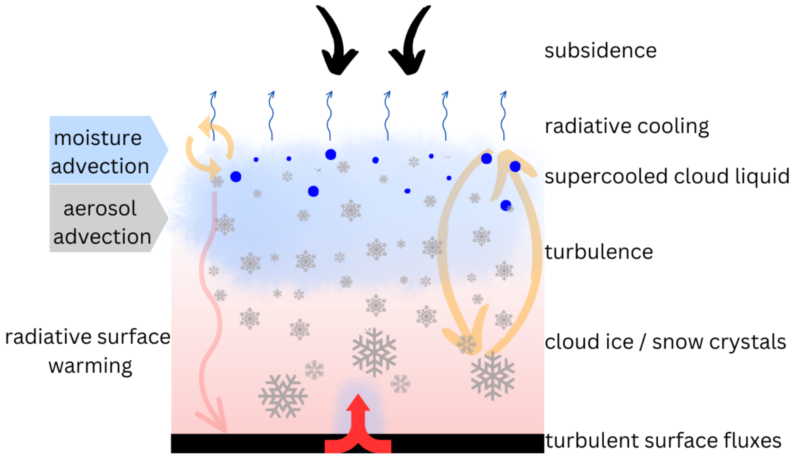

Figure 2.1: Processes maintaining Mixed-Phase Clouds. The Figure is adapted from Morrison et al. (2012).

(Fletcher et al., 2016a). Compared to the marine average, MCAO clouds have a smaller optical thickness, which slightly increases the outgoing longwave radiation at TOA and reduces the longwave warming at TOA that is already small due to the low cloud tops (Fletcher et al., 2016a).

mixed-phase clouds

The surface warming is particularly pronounced when low-level MPCs occur: Even though liquid-topped MPCs (Sect. 2.2) have a higher albedo, they emit more downward longwave radiation than ice clouds (Curry, 1995; Sun and Shine, 1994). This is because the longwave emission of a cloud scales with the amount of liquid water until saturation is reached at a Liquid Water Path (LWP) of roughly $30\,\mathrm{g\,m^{-2}}$ (Bennartz et al., 2013; Shupe and Intrieri, 2004).

2.2 MIXED-PHASE CLOUDS

2.2.1 *Microphysics*

The following information on microphysics in MPCs is taken from Lohmann et al. (2016), Pruppacher and Klett (1997), and Yau and Rogers (1996) unless stated otherwise. MPCs consist of supercooled liquid droplets and ice particles. The different phases are not homogeneously distributed but often occur in clusters and interact via microphysical processes (Shupe, 2011).

heterogeneous nucleation

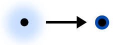

Under supersaturation with respect to water, i. e., within turbulent updrafts or the inversion layer at the top of MPCs (Sect. 2.2.2; Morrison et al., 2012), liquid cloud droplets nucleate heterogeneously on aerosols, so-called Cloud Condensation Nuclei (CCN), whose surfaces reduce the activation energy barrier. After being activated, liquid droplets grow by condensation. The rate of condensation is driven by vapor and heat diffusion as the latent heat released during the *condensational growth*

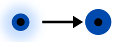

phase change has to propagate away from the droplet to maintain its growth. Negative condensation rates are called evaporation and lead to negative growth of the liquid droplets. In cloud-resolving model simulations of low-level MPCs over Svalbard, evaporation is a crucial phase-changing process (Kiszler et al., 2024). Generally, the liquid droplets are distributed within a layer at the cloud top (Fig. 2.1). However, sometimes, several liquid layers exist within a cloud.

homogenous/ heterogenous ice nucleation

Ice crystals can be formed either by homogeneous freezing of water and solution droplets at temperatures below about -35°C or by heterogeneous ice nucleation processes induced by Ice Nucleation Particles (INPs). As the newly formed ice particles grow and sediment (see below), most ice particles are distributed below the liquid layers (Morrison et al., 2012). Heterogeneous ice nucleation can occur at temperatures warmer than -35°C depending on INP type (see below) and supersaturation with respect to ice. Arctic INPs, such as soil dust or local sea spray aerosols, originate from land and ocean (Ansmann et al., 2023; Hartmann et al., 2020; Kanji et al., 2017; Zeppenfeld et al., 2023). However, INPs are rare in the atmosphere compared to CCN: they need to satisfy a specific surface structure since they are not dissolved during the freezing process and they are activated at a particle-specific temperature above which they cannot act as INPs. The concentration of activated INPs is roughly one per liter at -20 °C and increases exponentially with decreasing temperature (Fletcher, 1962b), resulting in observed concentrations between 10^{-5} and more than $10\,l^{-1}$ (Wex et al., 2019).

immersion freezing

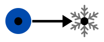

contact freezing

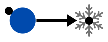

In MPCs, water vapor rarely deposits on INPs directly because the air is usually not simultaneously supersaturated with respect to ice and subsaturated with respect to water. Instead, water molecules frequently deposit on INPs and change their phase from liquid to solid (heterogeneous freezing nucleation) via two pathways (Ansmann et al., 2008; Prenni et al., 2009): During immersion freezing, the most dominant nucleation process in MPCs (Boer et al., 2011), an INP is immersed in a cloud droplet at higher temperatures and freezes after cooling. During contact freezing, an INP and a supercooled water droplet collide and freeze immediately.

secondary ice production

However, observations show that the ice crystal number concentration is more than one order of magnitude higher than the INP concentration (e. g., Crosier et al., 2011; Henneberger et al., 2013; Hobbs and Rangno, 1985, 1998; Korolev et al., 2020). This difference might be explained by Secondary Ice Production (SIP), i. e., the multiplication of already existing ice crystals (Field et al., 2017; Hallett and Mossop, 1974; Korolev and Leisner, 2020; Takahashi et al., 1995), by ice crystals that fall from a cloud aloft into the investigated cloud (Oue et al., 2016; Ramelli et al., 2021), or by blowing snow (Beck et al., 2018). In-situ measurements indicate that SIP is a necessary process for ice crystal formation at Ny-Ålesund, Svalbard (40 % frequency of occurrence; Pasquier et al., 2022), and for MPCs in general (Korolev et al., 2020; Korolev and Leisner, 2020).

depositional growth

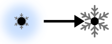

Under supersaturation with respect to ice, activated ice crystals grow through diffusion by the deposition of water molecules from the vapor phase on the crystal surface. The growth rate and ice crystal morphology depend on temperature and ice supersaturation. The three main ice crystal shapes are columns, plates, and dendrites. With increased supersaturation, more complex structures grow. The saturation vapor pressure of water exceeds that of ice the most at temperatures around -15°C, setting the temperature for maximum depositional growth. Here, dendritic structures experience rapid diffusional growth. Cloud-resolving model simulations show that deposition is an important ice growth process within low-level MPCs over Svalbard (Kiszler et al., 2024). Negative deposition rates are called sublimation and lead to negative growth of the ice crystals. Observations at Ny-Ålesund show that sublimation of snowfall reduces the snowfall amount on average by 19 percentage points (pp) within the lowermost 600 m of the atmosphere and thus is a crucial near-surface process (Maahn et al., 2014).

Wegener-Bergeron-Findeisen process

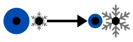

If the vapor pressure lies between the saturation pressures of water and ice, ice crystals grow by deposition at the expense of liquid droplets that evaporate, known as the Wegener-Bergeron-Findeisen (WBF) process (Bergeron, 1928; Findeisen, 1938; Wegener, 1911), which can lead to cloud glaciation. The WBF process is assumed to be small in MPCs, consistent with the resilience of MPCs (Sect. 2.2.2): First, the WBF process is less effective if the supercooled liquid and ice occur in clusters (Korolev et al., 2017). Second, the vapor pressure is mostly higher than the saturation pressures of ice and water (Korolev, 2007).

collision

Cloud particles within MPCs might also grow through collisions. Note that the collision efficiency is reduced for small hydrometeors because they are often deflected by the flow's streamlines around other hydrometeors. Collisions are induced mainly by differences in terminal velocities or turbulence (Chellini and Kneifel, 2024). Due to their low densities and thus large cross-section areas, ice particles have small terminal velocities and thus a lot of time to collide, which is essential for precipitation formation.

aggregation

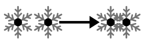

If the collision involves two ice particles, it is called aggregation. For sticking together, the sticking efficiency has to be high enough. This efficiency is enhanced within the so-called Dendritic Growth Zone (DGZ) between -20 and -10°C (Connolly et al., 2012; Karrer et al., 2021; Mitchell, 1988) when dendrites occur frequently and stick together by wedging their branches, and at temperatures just below 0°C (Cotton et al., 1986; Karrer et al., 2021; Lin et al., 1983) that foster a quasi-liquid layer formation around ice crystals (Fabry and Zawadzki, 1995; Faraday, 1850; Fletcher, 1962a).

riming

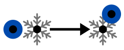

During riming, a droplet collides with and freezes on an ice crystal surface, mainly under a maximal sticking efficiency (Lamb and Verlinde, 2011). However, ice crystals and particularly water droplets must be sufficiently large for riming to occur, i. e., 35 µm for columns and up to 200 µm for dendrites (Wang and Ji, 2000). Different approaches exist to quantify riming; one is the normalized rime mass fraction (M), defined as the ratio of rime mass to the mass of a spherical, equally large graupel particle (Seifert et al., 2019). Riming occurs frequently in Arctic MPCs (Maherndl et al., 2024a; McFarquhar et al., 2007; Mioche et al., 2017), especially around -7°C (Waitz et al., 2022), even when the LWP is low ($<50\,\mathrm{g\,m^{-2}}$; Fitch and Garrett, 2022). Within MPCs, riming can be enhanced in updrafts that lift ice particles and expose them to supercooled liquid water at the cloud top over a more extended period before precipitating (Fitch and Garrett, 2022).

sedimentation

Hydrometeors experience gravitational and drag forces that determine their terminal velocities. The small supercooled liquid droplets within MPCs have a negligible mass and terminal velocity. The terminal velocity of ice crystals is small; it increases with particle size for small ice crystals and stays constant for large ice particles such as aggregates. In contrast, the enhanced density of rimed particles increases their terminal velocity compared to aggregates.

If the terminal velocity exceeds the updraft velocity, particles sediment. The resulting volume flux of ice particles through a unit horizontal surface per unit of time is defined as the snowfall rate or intensity, expressed by the liquid-equivalent snowfall rate (S) in mm water equivalent $\mathrm{h^{-1}}$:

$$S = \frac{\pi}{6}\int_0^\infty N(D)D^3u(D)dD. \tag{2.1}$$

Here, D is the equivolume diameter, the diameter of a liquid water sphere with the same mass as the actual hydrometeor; $u(D)$ is the fall velocity of particles of diameter D; and $N(D)$ is the ice particle size distribution, i. e., the number density of hydrometeors with diameters between D and $D + dD$. The many ways ice crystals and snowflakes form and interact broaden their $N(D)$ compared to rain, making a general formulation of $N(D)$ impossible. As for rain, the ice particle size distribution can be approximated by an exponential function with the intercept parameter N_0 and slope parameter Λ:

$$N(D) = N_0 exp(-\Lambda D). \tag{2.2}$$

The variety of ice crystal habits during a single snowfall event leads to a dependency of N_0 and Λ on microphysical characteristics. In summary, the microphysical processes discussed above and environmental meteorological conditions directly shape the distributions of particle sizes and terminal velocities within clouds and precipitation (e. g., Campbell and Shiobara, 2008; Clough and Franks, 1991).

2.2.2 *Implications due to phase partitioning*

cloud resilience

Low-level MPCs often persist over extended periods ranging from several hours to days (Morrison et al., 2012; Shupe et al., 2008a; Solomon et al., 2011). At Ny-Ålesund, low-level MPCs with a minimum lifetime of 1 h covered 23 % of the time between 2016 and 2018 (Gierens et al., 2020). Many interacting processes provoke the longevity of low-level MPCs (Morrison et al., 2012), summarized in Fig. 2.1. Even under conditions that lack small-scale convection or synoptic-scale forcing, i. e., subsidence, MPCs are maintained by an interaction among numerous local processes. One critical process is the longwave radiative cooling due to liquid droplets at the cloud top that induces an inversion layer at the cloud top and turbulence throughout the cloud layer, where cloud droplets grow by condensation and preserve the liquid within MPCs (Sect. 2.2.1). Moreover, large-scale advection of moisture frequently results in a moisture inversion at cloud top feeding the cloud from above by entrainment. Supercooled liquid water can induce surface longwave radiative warming. This decreases static stability, increases surface heat and moisture fluxes, and additionally maintains the cloud. Surface warming is even more pronounced under enhanced aerosol loading, associated with an advection of air from the mid-latitudes that increases the cloud droplet concentration.

radiative budget

Their persistence allows MPCs to feed back on the climate system over a longer time than pure ice clouds, which typically have shorter lifetimes due to their extensive mass loss induced by precipitation. Thus, Arctic low-level MPCs and their phase partitioning strongly affect the Arctic surface radiative budget (Tan et al., 2016) and amplify Arctic amplification (Tan and Storelvmo, 2019; Sect. 2.1).

model limitation

The phase partitioning of Arctic low-level MPCs complicates climate model simulations. These simulations frequently overestimate the ratio of ice particles compared to liquid droplets in MPCs (Cesana et al., 2015; Huang et al., 2021; Kiszler et al., 2023; Komurcu et al., 2014), likely due to a lack of microphysical subgrid-scale variability (Tan and Storelvmo, 2016) and simplified microphysical schemes. As a result, both simplifications enhance the glaciation rate (Barrett et al., 2017; Xie et al., 2008). The underestimation of the cloud liquid within Arctic low-level MPCs over Svalbard might be reduced by reducing the magnitude of the WBF process (Kiszler et al., 2024).

2.3 RADAR THEORY

Remote sensing exploits the interaction of radiation with atmospheric compounds to study properties such as temperature, water vapor, and cloud characteristics. As already introduced in Sect. 1.2, passive and active remote sensing exist. In the following, the focus is on active cloud remote sensing by so-called radars because this thesis is mainly dedicated to the radar of the airborne Microwave Radar/radiometer for Arctic Clouds (MiRAC) (Sect. 1.5). MiRAC is a customized version of the RPG–FMCW–94–SP Doppler cloud radar (Küchler et al., 2017), which has been tailored for the operation on *Polar 5* (P5) by Radiometer Physics GmbH (RPG). The general radar theory behind vertical profiling of hydrometeors is explained with a focus on MiRAC. The description follows the textbooks by Doviak and Zrnić (2006), Petty (2006), Ulaby and Long (2014), and Yau and Rogers (1996).

Radar antennas transmit directed radiation at a specific wavelength λ that has the power P_t at the output port. The power P_r that is received by the same or, in the case of MiRAC (Mech et al., 2019), by a closeby antenna after being backscattered by a point target such as a hydrometeor at the range r is described by the radar equation

$$P_r = \frac{P_t g^2 \lambda^2 \sigma_b f^4}{(4\pi)^3 r^4 l^2}, \tag{2.3}$$

where g is the antenna gain, f is the normalized power gain, l is the one-way transmission loss due to hydrometeors and atmospheric gasses, and σ_b is the backscattering cross-section. The backscattering cross-section is an apparent area that would produce a power density at the receiver equal to that scattered by the actual hydrometeor if it scattered isotropically. For a spherical drop with the equivolume diameter D (see Sect. 2.2.1) much smaller than λ, i. e., $D \leqslant \frac{\lambda}{16}$, σ_b can be approximated by Rayleigh scattering:

$$\sigma_b \approx \frac{\pi^5}{\lambda^4} |K_m|^2 D^6. \tag{2.4}$$

$K_m = \frac{m^2-1}{m^2+2}$ is a function of the complex refractive index m, which is the root mean square of the complex relative permittivity ϵ. The complex refractive index depends on λ and temperature and is roughly 0.91–0.93 for water droplets and 0.18–0.21 for ice particles.

Moving from a point scatterer to a volume containing several scatterers, e. g., a cloud volume that consists of many hydrometeors, the backscattering cross-section per unit volume at location $\vec{r}$ is also known as the reflectivity $\eta(\vec{r})$ in $\mathrm{mm}^2\,\mathrm{m}^{-3}$. $\eta(\vec{r})$ can be calculated using the particle size distribution $N(D, \vec{r})$ (see Sect. 2.2.1):

$$\eta(\vec{r}) = \int_0^\infty \sigma_b(D) N(D, \vec{r}) dD. \tag{2.5}$$

When focusing on liquid Rayleigh scatterer only and substituting Eq. 2.4, Eq. 2.5 becomes

$$\eta = \frac{\pi^5}{\lambda^4} |K_w|^2 Z \tag{2.6}$$

with the dielectric factor of liquid water $|K_w|$, and the reflectivity factor

$$Z = \frac{1}{\Delta V} \sum_i D_i^6 = \int_0^\infty N(D, \vec{r}) D^6 dD. \tag{2.7}$$

However, it is not always guaranteed that all scatterers within the target volume are liquid and have the same dielectric constant. To not have to account for the various dielectric constants of the scatterer, the equivalent radar reflectivity (Z_e) is defined using the dielectric factor of liquid water $|K_w|$ only:

$$Z_e(\lambda) = \frac{\lambda^4}{\pi^5 |K_w|^2} \int_0^\infty N(D, \vec{r}) \sigma_b(D, \lambda) dD. \tag{2.8}$$

For rain in the Rayleigh scattering regime, Z_e equals Z. Both radar reflectivities are given in $\mathrm{mm}^6\,\mathrm{m}^{-3}$; however, since they span many orders of magnitudes, they are often given on a logarithmic scale ($10 \log_{10} \frac{Z}{\mathrm{mm}^6 \mathrm{m}^{-3}}$) with units of dBZ.

Z_e can be calculated using the radar equation for volume scattering. For a Gaussian radar beam pattern, which is with an overlap of 95 % a valid assumption for the MiRAC beam (Rose, 2022), this results in

$$P_r = \frac{\pi^3}{1024 \ln[2]} \frac{P_t h g^2 f^4 \theta^2}{l^2 \lambda^2} \frac{|K_w|^2 Ze}{r^2}. \tag{2.9}$$

The second term of Eq. 2.9 includes all radar parameters, such as the pulse length h and the beamwidth θ, while the third term comprises the scattering characteristics. θ is defined as the half-power beamwidth and has an inverse relation with the antenna size. The antenna of the airborne MiRAC is shortened compared to the RPG–FMCW–94 Doppler cloud radar, which is installed at Ny-Ålesund (Sect. 1.5), to fit into the aircraft. This implies an increase in the beamwidth.

The radar pulse determines the spatial resolution of a radar. The beamwidth specifies the angular resolution that is higher for smaller θ. The pulse length defines the radial range resolution that is higher for shorter h. A high range resolution reduces the received signal (Eq. 2.9) and thus the minimum detectable reflectivity, especially at large distances r.

Radars are operated within wavelength ranges where the absorption by atmospheric gases is at a minimum, in so-called window re-

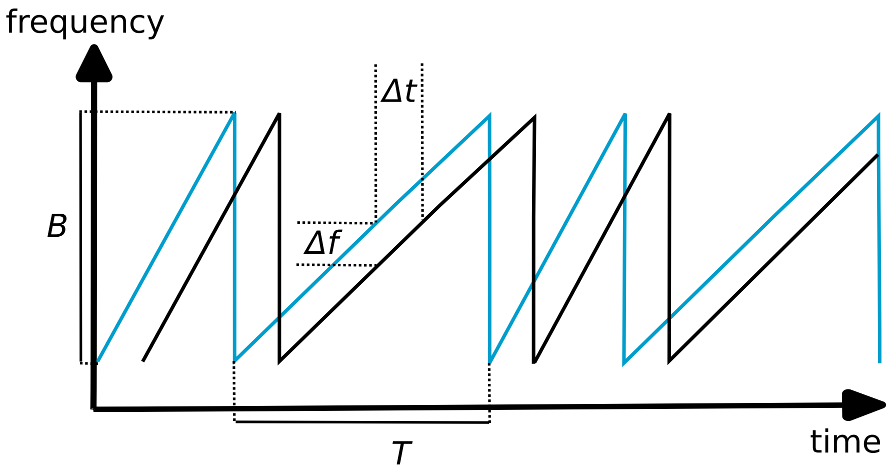

Figure 2.2: Sketch of a radar sawtooth chirp with two different chirp settings executed consecutively. The black line is the transmitted and the blue line is the backscattered signal. B indicates the bandwidth, T the chirp duration, Δt the time delay between the transmitted and received signal, and Δf the difference in frequency between both signals.

gions. The backscattering cross-section and the sensitivity to smaller particles increase with increasing operation frequency while keeping the transmission power constant. However, window regions at high frequencies are less transparent because of enhanced absorption by the water vapor continuum, liquid water, and atmospheric gases such as oxygen and water vapor. For the lower microwave spectrum below 100 GHz and thus for the operation frequency of MiRAC (94 GHz), absorption is relatively weak.

2.3.1 *Frequency-modulated continuous-wave radars*

Radars might transmit power in pulses or as continuous waves. The latter radars, which also include MiRAC (Mech et al., 2019), are so-called Frequency-Modulated Continuous-Wave (FMCW) radars. FMCW radars with a solid-state technology have a much lower power consumption than radars with a high-power source and are thus well suited for airborne operation. The transmitted frequency changes with time with a specific pattern such as a sawtooth, triangular, rectangular, or staircase pattern. MiRAC operates with a sawtooth pattern (Mech et al., 2019). A period of the pattern is called chirp. It is repeated throughout the measurement period (Fig. 2.2). The frequency increases linearly with time over a bandwidth B and a time called chirp duration T. The transmitted signal (Fig. 2.2, black) is backscattered by a stationary target (blue). Because the emitted signal travels at the speed of light c, it needs the time Δt to travel the distance to the target R and back:

$$R = \frac{c\Delta t}{2}. \tag{2.10}$$

For a specific time, Δt can be rewritten by the difference between the frequency of the received and transmitted signal, i. e., the so-called intermediate frequency difference Δf, and the gradient in frequency of the chirp. The intermediate frequency difference is generated by mixing the received and transmitted signals. Eq. 2.10 then becomes

$$R = \frac{c\Delta f}{2(\frac{df}{dt})} = \frac{c\Delta f}{2(\frac{B}{T})}. \tag{2.11}$$

FMCW radars can achieve a high radial range resolution through a large bandwidth. However, FMCW radars have to make certain compromises. To determine distances with high accuracy, it is possible to reach the bandwidth by a steep chirp gradient over a small chirp duration. In contrast, large maximum detectable distances are achieved by long chirp durations and small bandwidths, reducing accuracy. Multiple chirp settings can be consecutively executed to obtain accurate observations close to the radar and long-distance observations, as depicted in Figure 2.2. MiRAC makes use of alternating chirp settings. For further information about the applied chirp settings, see Mech et al. (2019) and their Table 1 and Fig. 1.

2.3.2 Z_e-S *relation*

Radars provide a radial distribution of Z_e. It is desirable to retrieve precipitation intensity from these observations. However, Z_e can be converted to the liquid-equivalent snowfall rate (S) only indirectly using an empiric equation that is typically a power law with the intercept parameter a and exponent parameter b (Doviak and Zrnić, 2006):

$$S = (\frac{1}{a} Z_e)^{\frac{1}{b}}. \tag{2.12}$$

S and Z_e are both functions of the snow particle size distribution. Retrieving S by one specific Z_e–S relation is only valid under the assumption of a constant particle size distribution for the application period. However, the crystals that fall during a snowfall event have substantial variations in their habits, orientations, terminal velocities, sizes, rime fractions, and scattering properties (Fujiyoshi et al., 1990; Macke et al., 1996; Matrosov, 1992), which leads to substantial variations in the snow particle size distribution (Castellani et al., 2015) and

Table 2.1: Selected Z_e–S relations from the literature with the intercept parameter a and exponent parameter b (Eq. 2.12).

name	conditions	a	b	source
Mds	dry snow: horizontally orientated oblate spheroids with an aspect ratio of 0.6	10.00	0.80	Matrosov (2007)
Lds	dry snow: randomly oriented three, four, and six bullet rosettes, sectors, and dendrites	11.50	1.25	Liu (2008b)
LR3	unrimed, dry snow: three bullet rosettes	13.16	1.40	Liu (2008a) Kulie and Bennartz (2009)
HA	unrimed, dry snow: aggregates	56.43	1.52	Hong (2007); Kulie and Bennartz (2009)
SS	unrimed, dry snow: low density, spherical particles	2.19	1.20	Surussavadee and Staelin (2006); Surussavadee and Staelin (2008); Kulie and Bennartz (2009)
Smix	single crystals, low-density snow, and rimed aggregates	18.18	0.98	Schoger et al. (2021)

thus raises the uncertainty of S retrieved by Eq. 2.12 (Liu, 2008b). Compared to relations for the rain rate, the uncertainty of Z_e–S relations is much higher because the dependence on terminal fall velocity or particle mass is poorly constrained (Matrosov, 2007; Matrosov et al., 2009). Hence, several Z_e–S relations exist for different snow and ice microphysics (Doviak and Zrnić, 2006). For example, Kulie and Bennartz (2009), Liu (2008b), Matrosov (2007), and Schoger et al. (2021) already derived Z_e–S relations for different locations, times of the year, and crystal habits (Table 2.1, Fig. 2.3). For these Z_e–S relations, a varies between 2 and 56 and is thus more variable than b (0.8–1.5). This uncertainty causes a large spread: a measured Z_e of 0 dBZ can be caused by a S between 0.03 and 0.3 mm h^{-1}. For the retrieval of the relations, the radar measurement of the range gate closest to the ground that is not affected by ground clutter is used, even though this height might be a few hundred meters above ground. Note that crystal habits might change below this height, e. g., particles might grow, sublimate, or multiply (Sect. 2.2.1), leading to a different S at the surface.

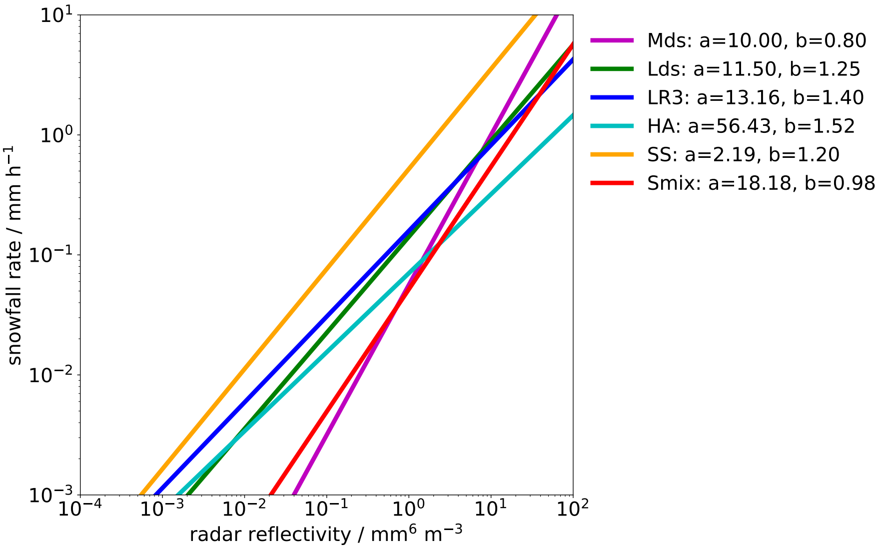

Figure 2.3: Selected equivalent radar reflectivity (Z_e)-liquid-equivalent snowfall rate (S) relations from the literature. a is the intercept parameter, and b is the exponent parameter of the respective relation (see Eq. 2.12). Further information on the equivalent radar reflectivity (Z_e)-liquid-equivalent snowfall rate (S) relations can be found in Table 2.1.

3

ARCTIC LOW-LEVEL CLOUDS OBSERVED BY SPACE- AND AIRBORNE RADAR

This study focuses on the first research question (Sect. 1.6.1) regarding the assessment of the low-level cloud and precipitation fraction over the Fram Strait from airborne observations and CloudSat Cloud Profiling Radar (CPR) observations with its respective limitations.

Schirmacher, I., P. Kollias, K. Lamer, M. Mech, L. Pfitzenmaier, M. Wendisch, and S. Crewell (2023). "Assessing Arctic low-level clouds and precipitation from above – a radar perspective." In: *Atmospheric Measurement Techniques* 16.17, pp. 4081–4100. DOI: `10.5194/amt-16-4081-2023`

AUTHOR CONTRIBUTION

IS performed the analysis, visualization, and writing and developed and conducted the methodology. IS, SC, and MM conceptualized the paper. PK, KL, and LP provided CloudSat expertise and contributed to the algorithm that simulates the CloudSat observations. All authors contributed to manuscript revisions.

ASSESSING ARCTIC LOW-LEVEL CLOUDS AND PRECIPITATION FROM ABOVE – A RADAR PERSPECTIVE

ABSTRACT

Most Arctic clouds occur below 2 km altitude, as revealed by CloudSat satellite observations. However, recent studies suggest that the relatively coarse spatial resolution, low sensitivity, and blind zone of the radar installed on CloudSat may not enable it to comprehensively document low-level clouds. We investigate the impact of these limitations on the Arctic low-level cloud fraction, which is the number of cloudy points with respect to all points as a function of height, derived from CloudSat radar observations. For this purpose, we leverage highly resolved vertical profiles of low-level cloud fraction derived from down-looking Microwave Radar/radiometer for Arctic Clouds (MiRAC) radar reflectivity measurements. MiRAC was operated during four aircraft campaigns that took place in the vicinity of Svalbard during different times of the year, covering more than 25 000 km. This allows us to study the dependence of CloudSat limitations on different synoptic and surface conditions.

A forward simulator converts MiRAC measurements to synthetic CloudSat radar reflectivities. These forward simulations are compared with the original CloudSat observations for four satellite underflights to prove the suitability of our forward-simulation approach. Above CloudSat's blind zone of 1 km and below 2.5 km, the forward simulations reveal that CloudSat would overestimate the MiRAC cloud fraction over all campaigns by about 6 percentage points (pp) due to its horizontal resolution and by 12 pp due to its range resolution and underestimate it by 10 pp due to its sensitivity. Especially during cold-air outbreaks over open water, high-reflectivity clouds appear below 1.5 km, which are stretched by CloudSat's pulse length causing the forward-simulated cloud fraction to be 16 pp higher than that observed by MiRAC. The pulse length merges multilayer clouds, whereas thin low-reflectivity clouds remain undetected. Consequently, 48 % of clouds observed by MiRAC belong to multilayer clouds, which reduces by a factor of 4 for the forward-simulated CloudSat counterpart. Despite the overestimation between 1 and 2.5 km, the overall low-level cloud fraction is strongly reduced due to CloudSat's blind zone that misses a cloud fraction of 32 % and half of the total (mainly light) precipitation amount.

3.1 INTRODUCTION

Low-level clouds are prominent features of the Arctic climate (Liu et al., 2012; Mioche et al., 2015; Shupe et al., 2006) and have a large impact on the radiative energy budget of the Arctic surface (e.g., Curry et al., 1996; Shupe and Intrieri, 2004; Wendisch et al., 2019). In contrast to the global cooling effect of low clouds, between 70 and 82° N they may create a positive (warming) cloud radiative forcing (CRF) of $\sim 10\,\mathrm{W\,m^{-2}}$ (Kay and L'Ecuyer, 2013). The terrestrial CRF dominates and warms the near-surface air due to low solar elevation during polar day and absent solar radiation during polar night (Lubin and Vogelmann, 2006; Stapf et al., 2021). Within the last 4 decades, the near-surface warming in the Arctic increased more strongly than the global average, which is referred to as Arctic amplification (Serreze and Barry, 2011; Wendisch et al., 2019). Diverse processes and interacting feedback mechanisms lead to Arctic amplification. An increased cloud cover and amount of water vapor and the lapse rate feedback from persistent clouds (Graversen et al., 2008) would enhance the terrestrial downward radiation (Francis and Hunter, 2006) and contribute more strongly to Arctic amplification than the sea ice–albedo feedback (Winton, 2006). Thus, there is high interest in accurate observations of Arctic low-level cloud properties and their changes.

Detailed ground-based remote sensing observations that measure the vertical distribution and variability in low-level clouds are available from very few stations in the Arctic (e.g., Gierens et al., 2020; Liu et al., 2017). They allow us to study the temporal variability over long time periods but at a specific place. In contrast, ship campaigns in the High Arctic (Intrieri and Shupe, 2004; Shupe et al., 2022) assess the spatial variability only over short time periods but over a larger yet still limited area. As recently highlighted by Griesche et al. (2021) using measurements from the RV *Polarstern* in the marginal sea ice zone (MIZ), however, the frequent occurrence of low-level stratus around 100 m is often missed by ground-based observations. On larger spatial scales, active satellite measurements resolve vertical cloud structures for long time periods. CloudSat (Stephens et al., 2002) has been frequently used for studies of Arctic clouds for example to investigate the correlation between low-level cloud occurrence and sea ice concentration (Mioche et al., 2015; Zygmuntowska et al., 2012). For the years 2006 to 2011, Liu et al. (2012) find that roughly 80 % of clouds over the Arctic Ocean occur below 2 km altitude.

CloudSat and ground-based observations at the Eureka site, in Canada, revealed different cloud occurrences below 2 km altitude (Blanchard et al., 2014; Mioche et al., 2015). Thus, it remains to be determined if CloudSat captures all low-level Arctic clouds due to its limitations. First, CloudSat's along-track sampling conceals spatial cloud patterns. Second, according to Lamer et al. (2020), the pulse length either stretches or fails to detect shallow clouds. Third, the lowest levels from CloudSat's vertical profiles suffer from ground clutter due to reflections at the surface called the blind zone. This blind zone prevents the cloud assessment roughly below the first kilometer (Lamer et al., 2020; Liu, 2022; Palerme et al., 2019). Using ground-based radar measurements for reference, Maahn et al. (2014) showed that CloudSat underestimates the total precipitation by 9 percentage points (pp) over Ny-Ålesund, Svalbard. The representation of Arctic low-level clouds in climate models is of high relevance to investigate, for example, its correlation with sea ice concentration (Morrison et al., 2019). To fully exploit CloudSat for improving climate models it is necessary to know its limitations and thus to evaluate CloudSat measurements with more finely resolved observations that ideally cover broad areas over land and ocean. These measurements should ultimately address how low-level cloud occurrence varies close to the surface, depends on surface characteristics and meteorological situation, and thus affects Arctic amplification.

CloudSat observations have been compared with airborne remote sensing (e.g., Gayet et al., 2009; Painemal et al., 2019) for relatively homogeneous clouds at higher altitudes to calibrate airborne instruments (Barker et al., 2008; Protat et al., 2009, 2011). For the first time, Liu (2022) investigates synthetic CloudSat cloud masks in the Arctic region. These data are based on radar reflectivities from QuickBeam radar forward simulations (Haynes et al., 2007) that used vertical profiles of retrieved cloud properties from ground-based radar and lidar during the SHEBA (Surface Heat Budget of the Arctic Ocean) experiment. Compared to ground-based observations, the forward-simulated data detected all clouds with heights above 1 km, but 25 pp less below 600 m. Nevertheless, in this study the synthetic data were generated under several assumptions and by low-temporal-resolution measurements that had a different viewing geometry.

In this study, we investigate vertical profiles of low-level cloud occurrences over the Fram Strait using CloudSat observations and measurements by the airborne Microwave Radar/radiometer for Arctic Clouds (MiRAC; Mech et al., 2019) operating at the same radar wavelength as CloudSat. MiRAC measured highly resolved profiles with a lower blind zone of about 150 m on board the *Polar 5* (Wesche et al., 2016) research aircraft during four airborne campaigns conducted in the vicinity of Svalbard within the framework of the German Research Foundation (DFG) project TRR 172, "ArctiC Amplification: Climate Relevant Atmospheric and SurfaCe Processes, and Feedback Mechanisms" ((AC)^3; Wendisch et al., 2023). The Svalbard region is of particular interest because the steady heat and moisture flux of the North Atlantic Ocean enhances cloud fraction and precipitation compared to the entire Arctic (McCrystall et al., 2021; Mioche et al., 2015). The campaigns, namely ACLOUD (Arctic CLoud Observa-

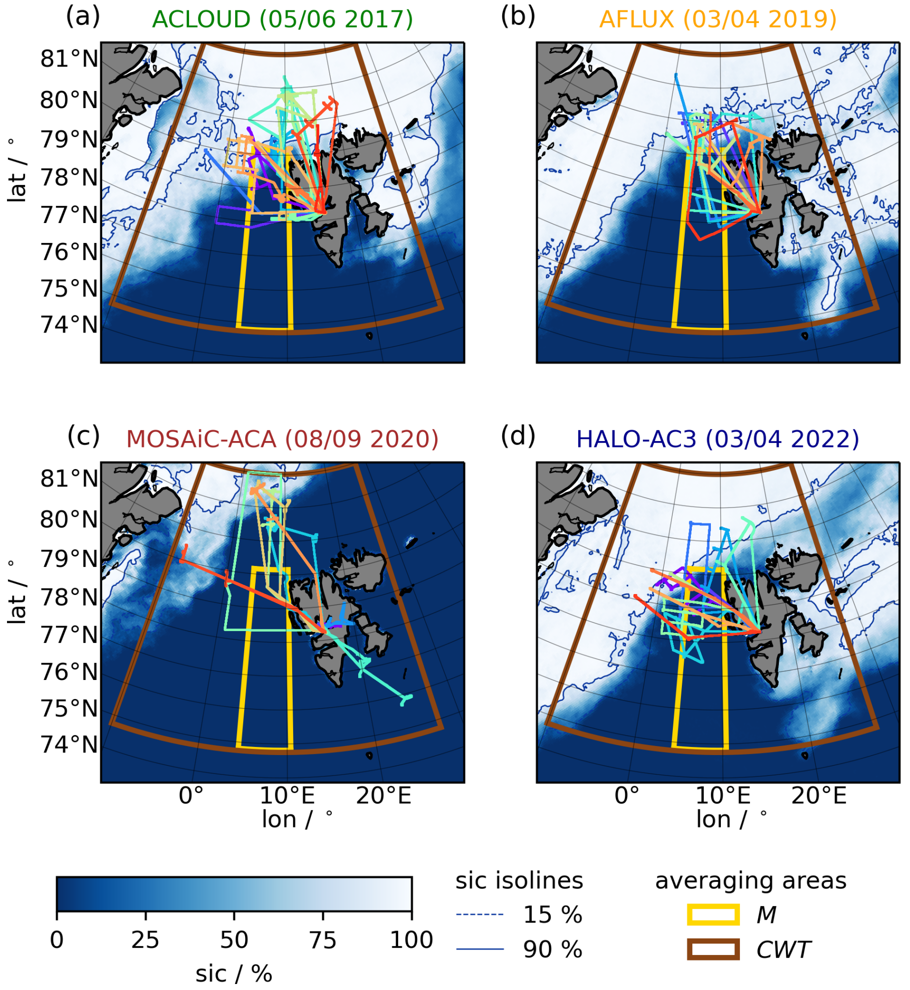

Figure 3.1: Flight tracks and sea ice concentration (sic) during the airborne campaigns ACLOUD **(a)**, AFLUX **(b)**, MOSAiC-ACA **(c)**, and HALO–(AC)^3 **(d)**. The indicated areas highlight the regions over which we calculate the marine cold-air-outbreak index (*M*; yellow) and determine the circulation weather type (CWT; brown).

tions Using airborne measurements during polar Day; Ehrlich et al., 2019b; Wendisch et al., 2019), AFLUX (Airborne measurements of radiative and turbulent FLUXes of energy and momentum in the Arctic boundary layer; Mech et al., 2022), MOSAiC-ACA (Multidisciplinary drifting Observatory for the Study of Arctic Climate-Airborne observations in the Central Arctic; Mech et al., 2022), and HALO–(AC)^3 (High Altitude and LOng range research aircraft–(AC)^3), covered periods from 2017 to 2022 between March and September. Since *Polar 5* flies relatively slowly, a unique database has been gathered that covers more than 25 000 km and includes four underflights of *Polar 5* below CloudSat. The larger spatial coverage of the airborne observations compared to observations from land stations allows for new insights into the cloud variability over open ocean and sea ice.

Table 3.1: Flight hours over several surfaces and covered distances during the analyzed flights of the four *Polar 5* campaigns. Sea ice concentrations below 15 % and above 90 % represent open water and sea ice.

Campaign	Start	End	Year	All (h)	Sea ice (h)	Open water (h)	Distance (km)
ACLOUD	22 May	28 June	2017	22	8	10	7016
AFLUX	20 March	15 April	2019	13	2	9	4134
MOSAiC-ACA	27 August	17 September	2020	15	1	13	4761
HALO–(AC)³	5 March	15 April	2022	31	6	22	9803
Sum				82	17	53	25 714

Table 3.2: Specifications of the Cloud Profiling Radar (CPR) on CloudSat and the airborne radar MiRAC, which are illustrated in Fig. 3.2.

Parameter	CPR	MiRAC
Flight altitude	730 km	3.09 km
Flight speed	$7000\,\mathrm{m\,s^{-1}}$	$87\,\mathrm{m\,s^{-1}}$
Frequency	94 GHz	94 GHz
Integration time	0.16 s	1 s
Pulse width	3.3×10^{-6} s	–
Range resolution	480 m	4.5–27 m
Across-track resolution	1320–1380 m	460 m
Half-power beam width	< 0.12°	0.85°
Footprint radius (r)	688 m	23 m
Distance between two measurement center points (d)	1093 m	87 m
Effective along-track resolution (res)	1780 m	110 m

The paper is organized as follows. First, we present the CloudSat and airborne remote sensing data and describe how CloudSat's radar reflectivities are forward-simulated from MiRAC observations (Sect. 3.2). Second, we outline the meteorological situation encountered during the campaigns (Sect. 3.3). Section 3.4 evaluates the forward simulations for four underflights and investigates the effects of CloudSat's spatial resolution, blind zone, and sensitivity on its performance in detecting low-level clouds. Afterwards, Sect. 3.5 compares the fraction of the MiRAC and forward-simulated radar reflectivities across the entire data with height to analyze the variability in low-level Arctic cloud occurrence with respect to meteorological and surface conditions and to identify states that limit CloudSat's cloud detection the most. Section 3.6 concludes the study and discusses future steps.

3.2 DATA AND METHODS

All four airborne campaigns were based in Longyearbyen, Svalbard, and included various flights focusing on the Fram Strait area with varying sea ice conditions during the different campaigns (Fig. 3.1, Table 3.1). This study uses only measurements with flight altitude above 2 km and omits measurements over land due to the complex topography. By using the daily sea ice concentration (sic) dataset (version 5.4) obtained by the second Advanced Microwave Scanning Radiometer (AMSR2), we differentiate between open water (sic $< 15\,\%$) and sea ice (sic $> 90\,\%$). This assumption is more strict than in previous studies (80 %; Strong and Rigor, 2013) to avoid cloud formation associated with leads. In total, 82 h of flight time corresponding to a distance exceeding 25 000 km is analyzed, with the majority (64 %) over open ocean.

CloudSat's Cloud Profiling Radar (CPR) and MiRAC are both down-looking W-band radars operating at 94 GHz. We focus on the measurements of the equivalent radar reflectivity factor Z from MiRAC (Z_M) and CPR (Z_C). The fraction of Z signals in the measurement period with height is also called hydrometeor fraction and hereafter referred to as cloud fraction (CF).

Note that attenuation by supercooled liquid layers and precipitation affects the downward-looking observations of both instruments the same way. While dry air negligibly attenuates Z at 94 GHz, atmospheric water vapor and hydrometeors can significantly attenuate Z. In the dry Arctic, nonetheless, this attenuation is assumed small. With a total column water vapor amount of $15\,\mathrm{kg\,m^{-2}}$, which is relatively high for the Arctic, a two-way attenuation below 1 dBZ would occur (Kneifel et al., 2015). A 500 m thick cloud with a liquid water path of $100\,\mathrm{g\,m^{-2}}$ would weaken Z by less than 0.6 dBZ (Stephens et al., 2002). Note that unlike the CPR, MiRAC does not suffer from atmospheric attenuation by hydrometeors above *Polar 5* flight altitude, which is mostly around 3 km.

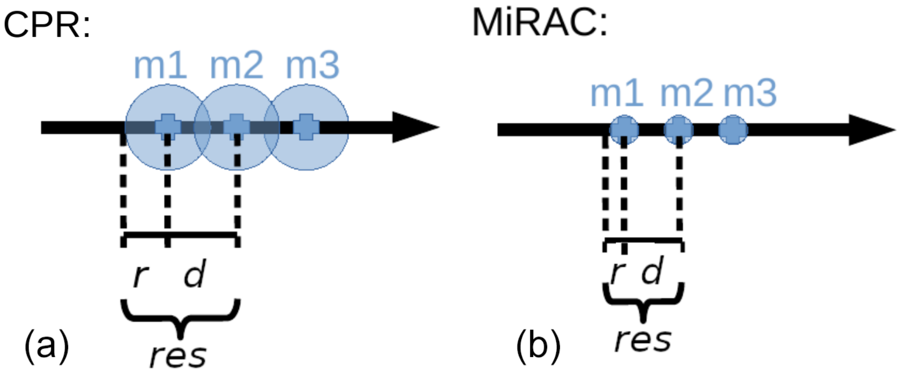

Figure 3.2: Sketch of the horizontal resolution of the radar on CloudSat (CPR; **a**) and airborne radar MiRAC **(b)**. The individual measurement center positions (m1, m2, and m3) are indicated by blue crosses and each footprint by blue circles; r is the radius of the footprint, d the distance between two measurements, and res the effective along-track resolution. For better illustration, MiRAC is scaled up by a factor of 10.

3.2.1 *Spaceborne CloudSat Cloud Profiling Radar (CPR)*

The CloudSat satellite orbit reaches up to 82.5° latitude and provides the only domain-wide vertically resolved satellite observations sensitive to clouds, light precipitation, and snow in the Arctic region (Kulie and Bennartz, 2009; Liu, 2008b; Palerme et al., 2014). The CPR (Table 3.2 for a list of specifications) is a pulsed radar, and the pulse width results in a range resolution of 480 m (Stephens et al., 2002; Tanelli et al., 2008).

The antenna half-power beam width and flight altitude cause a latitude-dependent across-track resolution of 1320 to 1380 m, which is 1375 m particularly around Svalbard (Fig. 3.2, Table 3.2). Due to the integration time, the distance between two adjacent measurement center points (d) is 1090 ± 10 m, which again depends slightly on latitude (Tanelli et al., 2008). As a result of the instantaneous footprint and the integration time, the effective along-track CloudSat resolution (res) during the campaigns is close to 1780 m. In 2006, the CPR sensitivity was close to −30 dBZ and was supposed to stay at least close to −26 dBZ (Stephens et al., 2002, 2008; Tanelli et al., 2008). Due to ground clutter, CloudSat likely overestimates low-level cloud occurrences below 0.5 height over ocean and 1 km over land and sea ice, respectively (Lamer et al., 2020; Maahn et al., 2014; Marchand, 2018; Mioche et al., 2015).

We analyze CPR data from the "2B-Geoprof" product version 5 (Marchand, 2018) over four underflights of *Polar 5* below CloudSat (Table 3.3) following Blanchard et al. (2014) and Lamer et al. (2020). This product contains Z and a CPR cloud mask, which assigns a value for the cloud detection probability every 240 m in height and 1 km along-track. The 2B-Geoprof product hereby oversamples the re-

Table 3.3: Specifications of the four underflights of *Polar 5* below CloudSat.

Case	Flight segment	Date	Start time (UTC)	End time (UTC)	Space between platforms at crossing (m)	Time difference between platforms (min)	
						Start	End
1	ACLOUD RF06_hl03	27 May 2017	09:48:36	10:44:27	1208	38.7	17.8
2	ACLOUD RRF11_hl02	2 June 2017	09:40:39	09:56:59	1047	7.0	8.4
3	AFLUX RF09_hl03	1 April 2019	09:35:50	10:11:59	1031	16.6	20.1
4	AFLUX RF13_hl03	7 April 2019	08:23:35	08:49:59	802	5.0	21.1

turn power by a factor of 2. The altitudes of the CloudSat range bins are slightly variable over time. For the analysis, the data are mapped to a constant grid with a grid size of 240 m by selecting the nearest neighbor. For the cloud mask, we settle for a given confidence value of 20 or higher following Lamer et al. (2020). This means that all range gates with lower values are considered to be cloud-free, filtering ground clutter and very weak signals (Marchand, 2018). Furthermore, only Z_C values larger than −27 dBZ are considered to be cloud signals. This threshold is in accordance with the one applied by the CPR cloud mask above the blind zone (Marchand, 2018). Contrary to this study, Mioche et al. (2015) investigate the combined radar–lidar product DARDAR that might more successfully identify low-level cloud structures compared to the 2B-Geoprof product. However, DARDAR interpolates the CPR data in the vertical to the finer resolution of the lidar (Winker et al., 2003), still detects ground clutter erroneously as near-surface supercooled droplets, and thus overestimates near-surface cloud fraction (Blanchard et al., 2014).

3.2.2 *Airborne*

MiRAC is a frequency-modulated continuous-wave (FMCW) radar and operates at the same frequency (94 GHz) as CloudSat (Table 3.2 for list of specifications). Its sensitivity and vertical resolution depend on the chirp settings. During the campaigns the settings were such that the detection limit mostly reached below −40 dBZ (Mech et al., 2019). The vertical resolution is 4.5 m close to the aircraft and at most 27 m (Mech et al., 2019). During the processing, the vertical resolution of all flights is interpolated to 5 m. Considering the beam

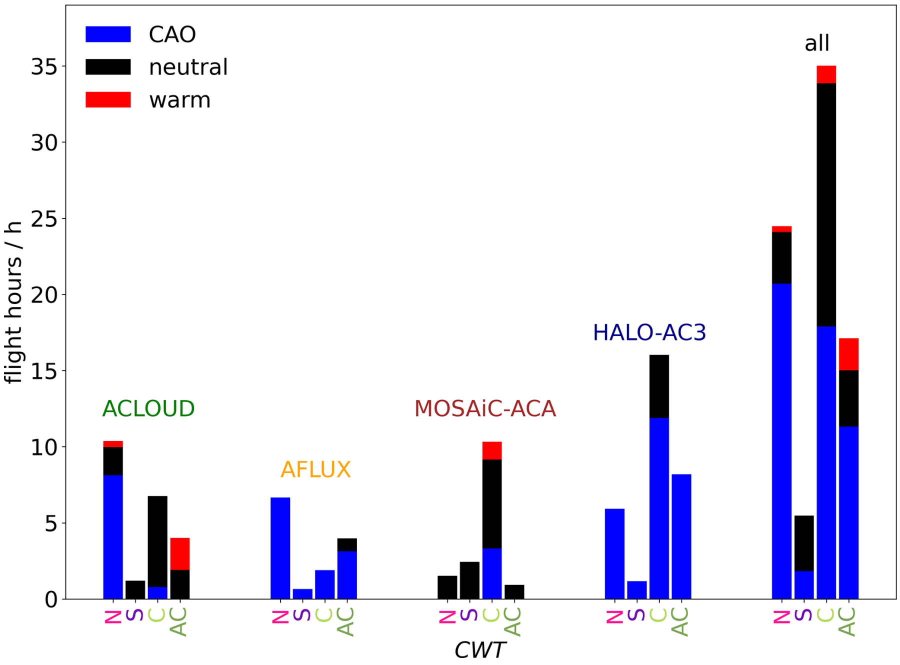

Figure 3.3: Analyzed flight hours during the different circulation weather types (CWTs) for each campaign and over all campaigns. N, S, C, and AC stand for northerly, southerly, cyclonic, and anticyclonic flow, respectively. Each CWT class is divided into the occurrence of the marine cold-air-outbreak index (M): warm periods (red), neutral periods (black), and cold-air outbreaks (CAOs; blue).

width, the radius of the beam's footprint at the surface is 23 m for the average flight altitude of about 3 km (Fig. 3.2). Due to the aircraft speed and temporal resolution of roughly 1 s, each measurement covers about 110 m. Hence, res of MiRAC is roughly 16 times higher than that of CPR. Z_M is not investigated inside the lowest 150 m of the atmosphere due to surface-type-dependent ground clutter (Mech et al., 2019) and is linearly interpolated to a temporal resolution of 1 s. This study only accounts for measurements along straight flight segments over ocean that exceed a flight altitude of 2 km (Risse et al., 2022).

The Airborne Mobile Aerosol Lidar (AMALi; Stachlewska et al., 2010) also operated on *Polar 5* is used to assess the cloud situation during the four underflights. It measures profiles of backscattered intensities at 532 (polarized parallel and perpendicularly) and 355 nm (not polarized). After averaging these profiles over 5 s and correcting them for the background signal and a drift, the attenuated backscatter coefficient is calculated (Ehrlich et al., 2019b). By determining the highest altitude of consecutive heights that exceed the backscatter coefficient of a cloud-free section, the cloud top height is obtained with a vertical resolution of 7.5 m and a horizontal resolution of 375 m (Kulla et al., 2021; Kulla et al., 2021b). For this study, we accessed all airborne data via the ac3airborne module that, among other things, stores all links to the data (Mech et al., 2022).

3.2.3 *Forward-simulation methodology*

This section summarizes the steps applied to convert the more finely resolved and more sensitive MiRAC to CloudSat radar reflectivities.

Along-track convolution. We calculate a moving time average over 13 profiles, which represent the number of MiRAC along-track bins (res of 110 m) within the CloudSat footprint (1375 m), and consider an along-track weighting function that imitates the antenna pattern by a symmetrical Gaussian distribution covering the CloudSat footprint (Lamer et al., 2020).

Along-track integration. Here, the integration distance of CloudSat (1093 m) is considered by calculating an arithmetic mean over all convoluted profiles within the integration distance. For the underflights (Sect. 3.2.1), we assign to every CloudSat observation the averaged profile that best resembles the distance between CloudSat and the location where *Polar 5* and CloudSat are closest (crossing location). For the statistical assessment over all campaigns, a profile is selected every 1093 m.

Along-range convolution. The range resolution of the Z_C and Z_M product is 240 m (Sect. 3.2.1) and 5 m (Sect. 3.2.2), respectively. To account for the pulse-limited range resolution of CloudSat, we average the convoluted observations from the previous step by applying a running mean with a symmetrical, 960 m long range-weighting function following Lamer et al. (2020). The range-weighting function is modeled with the help of a Gaussian distribution that produces a surface clutter echo profile similar to that observed by the CloudSat CPR postlaunch. The distribution spans 2 times the range resolution of CloudSat, i.e., 960 m, and thereby simulates ground clutter even more realistically, since the weight of signals far away from the center is tiny. Afterwards, we select Z values for every 240 m to mimic the digitization of CloudSat.

Sensitivity threshold. To obtain the fully forward-simulated equivalent radar reflectivities (Z_{sim}), we apply a sensitivity threshold of −27 dBZ to eliminate signals that fall below the CloudSat sensitivity due to averaging over cloudy and cloud-free bins (i.e., partial beam filling).

3.3 METEOROLOGICAL CONDITIONS DURING AIRBORNE CAMPAIGNS

The flights during the four campaigns (Fig. 3.1) span a range of meteorological conditions. We characterize and relate cloud occurrence to these conditions by determining the daily marine cold-air-outbreak index (M; Papritz et al., 2015) and the circulation weather type (CWT; Akkermans et al., 2012) from ERA5 reanalysis data provided for pressure levels (Hersbach et al., 2020).

3.3.1 *Marine cold-air-outbreak index (M)*

Following Papritz et al. (2015) and Kolstad (2017), M is defined as the difference between potential temperatures (θ) at the surface and 850 hPa altitude for each grid point over water:

$$M = \theta_{\mathrm{surf}} - \theta_{850\,\mathrm{hPa}}. \tag{3.1}$$

For a more robust estimate, daily M values are averaged for the Fram Straight area (Fig. 3.1, yellow). A M below -8 K classifies a warm period, whereas a M above 0 K identifies cold-air outbreaks (CAOs) following Knudsen et al. (2018). CAOs typically occur when cold air masses form over the central Arctic ice and move southward over the warm open ocean, where they quickly saturate. Over the open water, cloud streets evolve, which grow in the vertical and horizontal directions with distance to the ice edge until they form convective cells. The heat release from the ocean enhances turbulence that deepens the cloud layer with time (Atkinson and Wu Zhang, 1996; Brümmer, 1999; Etling and Brown, 1993). Air-mass transformation during a CAO still poses many questions, requiring detailed measurements for testing high-resolution modeling.

In total, 63 % of the analyzed measurements were taken during CAOs, 32 % under neutral conditions, and 5 % under warm conditions (Fig. 3.3). Note that the sampling is affected by weather conditions suitable for flying. During warm conditions, a thick, continuous, low cloud layer often hinders *Polar 5*'s take-off and landing at Longyearbyen airport (Svalbard). Therefore, warm periods do not appear representative.

ACLOUD (early summer) includes frequent CAO events and fewer warm periods (Fig. 3.3). During AFLUX and HALO–(AC)³, both taking place in early spring, CAO occurrences clearly dominate the analyzed flights. Conversely, neutral conditions ($-8\,\mathrm{K} < M < 0\,\mathrm{K}$) dominate MOSAiC-ACA, which was conducted in autumn. Only twice as much flight time was conducted during CAOs as during warm periods in this autumn campaign.

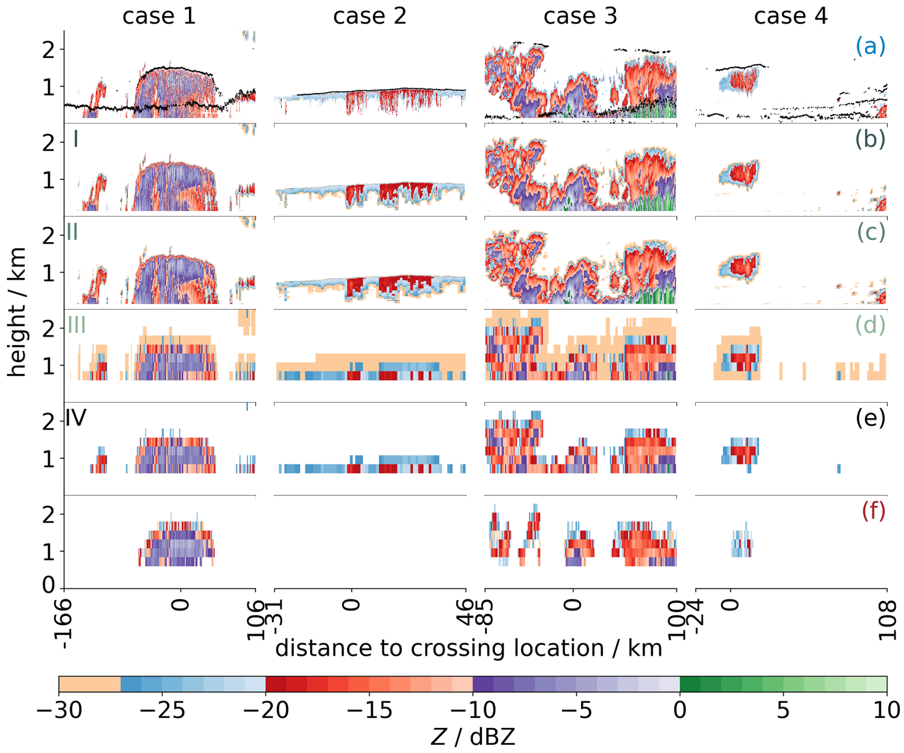

Figure 3.4: Profiles of the equivalent radar reflectivity (Z) during the four underflights of *Polar 5* below CloudSat (columns) as obtained from the airborne radar MiRAC (Z_M; **a**), after along-track convolution (I; **b**), after additional along-track integration (II; **c**), after further along-range convolution (III; **d**), and after applying a sensitivity threshold of −27 dBZ (Z_{sim}, IV; **e**). The CloudSat observations (Z_C; **f**) are filtered by the CPR cloud mask. In addition, the cloud top height derived by the airborne lidar AMALi (**a**; black dots) is shown.

3.3.2 *Circulation weather type (CWT)*

Several approaches to categorizing synoptic situations into CWTs by their large-scale atmospheric circulation exist, e.g., by analyzing the areal average of the vorticity, strength, and direction of the geostrophic flow. We follow Akkermans et al. (2012) and use the Jenkinson–Collison classification, which comprises eight directional classes (N, NE, E, SE, S, SW, W, and NW) and two vorticity regimes (cyclonic, C, and anticyclonic, AC; Philipp et al., 2016). For a representative assessment, the CWT is calculated from the geopotential height at 850 hPa over a larger area (Fig. 3.1, brown).

In general, the flow is directed in the meridional direction and flow directions W and E do not occur during the analyzed flights. Thus, the main flow directions are S, N, C, and AC, and classes in between are assigned to the neighboring main direction following Lerber et al. (2022b). In total, there was 0.6 h of flight time during NE and NW flows and 1.8 h during SE and SW conditions; thus, they contribute less than 1 %.

During all campaigns, northerly (30 %) and cyclonic (43 %) flows dominate, whereas southerly winds appear rarely, making up only 7 % of the analyzed flight time (Fig. 3.3). The fewest northerly winds occurred during the MOSAiC-ACA campaign (autumn). With 1.9 h, the amount of cyclonal flow is lowest during AFLUX. For AFLUX and HALO–(AC)^3 (both early spring), the primary difference in the synoptic situation is the main flow type, being northern and cyclonic during AFLUX and HALO–(AC)^3, respectively. Northerly winds generally implicate CAOs, except for MOSAiC-ACA, during which the number of CAOs is in general low. Cyclonic conditions frequently include CAOs during the spring campaigns AFLUX and HALO–(AC)^3, while they are less frequent ($<$ 30 %) during MOSAiC-ACA and ACLOUD (early summer).

3.4 CLOUDSAT UNDERFLIGHTS

Four CloudSat underflights (Table 3.3) were performed in the vicinity of Svalbard (Fig. 3.13) during ACLOUD and AFLUX, lasting about 35 min each. Z_M time series resolve the fine structures inside the clouds (Fig. 3.4a) and demonstrate that the cloud conditions during the underflights differ significantly. The clouds during cases 1 and 3 reach altitudes of up to more than 2 km and show light precipitation, as evidenced by reflectivities in the lowest range gate. During case 2, a thin cloud layer with virga and Z_M below −20 dBZ appears below 1 km. Case 4 is mostly cloud-free and exhibits only one small non-precipitating cloud below 2 km. During all cases, CloudSat observes no additional clouds at higher levels (not shown). Hence, no attenuation occurs through high clouds. The cloud top heights obtained from the AMALi lidar and MiRAC measurements generally agree well. Exceptions occur at very low levels when the lidar likely detects a thin supercooled layer, which is even beyond the sensitivity limit of MiRAC.

The horizontal cloud cover from the MiRAC observations during all underflights is 74 %, and 45 % of the cloud tops fall within the lowest kilometer. Z_M ranges from −31 to 8 dBZ (Fig. 3.5a). Precipitation, which is hereafter defined as Z larger than −5 dBZ (Maahn et al., 2014), is rare. The vertically resolved Z_M distribution (Fig. 3.5g) reveals that precipitation is confined to below 750 m height. Z_M is most frequent at −15 dBZ due to signals between 0.15 and 1.2 km height that are mainly observed during case 1.

The mean CF profile of MiRAC (CF_M; Fig. 3.6a, MiRAC) over all underflights shows almost no clouds above 2 km; the CF of clouds between 1.5 and 2 km height is on average 15 % and increases up to 40 % between 1.5 and 1 km height. At around 750 m, CF_M maximizes,

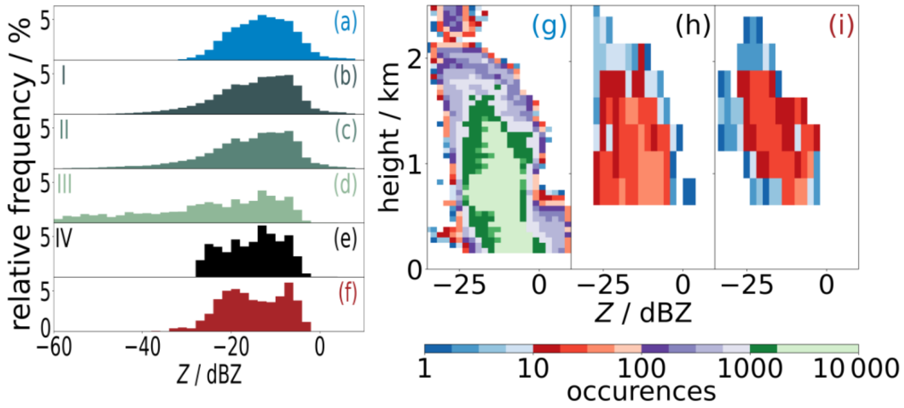

Figure 3.5: Histogram **(a–f)** and contoured frequency by altitude diagram (CFAD; **g–i**) of the equivalent radar reflectivity (Z) over four underflights of *Polar 5* below CloudSat. Histograms display the original MiRAC (Z_M; **a**) and CloudSat data (Z_C; **f**) and forward-simulated data obtained after each processing step (I–IV; Sect. 3.2.3). CFADs show Z_M **(g)**, the completely forward-simulated data (Z_{sim}; **h**), and Z_C **(i)**. The color coding of the labels is equivalent to Fig. 3.4. The size of the bins equals 2 dBZ.

with 53 % over less than 500 m mainly due to the cloud layer captured during case 2.

3.4.1 *Effect of the forward simulation*

At first, we illustrate how the different processing steps (Sect. 3.2.3) change the radar reflectivities when converting the MiRAC measurements (Z_M) to those that would be observed by CloudSat (Z_{sim}):

I. The along-track convolution (Fig. 3.4b) is independent of height and smooths hydrometeor-related signals in the horizontal. Therefore, especially broken cloud fields with small gaps are combined into clouds with larger horizontal extent. Furthermore, isolated reflectivities, such as during case 4 at altitudes below 200 m, become visible by smearing over a larger distance. The occurrence of very low-level clouds is confirmed by the lidar; however, they mostly fall even below the sensitivity limit of MiRAC. Note that at cloud boundaries, Z often declines below the sensitivity threshold of −27 dBZ (Fig. 3.5b). Compared to the original Z_M distribution, which has its maximum at −15 dBZ (Fig. 3.5a), the distribution becomes bimodal (Fig. 3.5b).

II. The along-track integration (Fig. 3.4c) broadens and smears cloud structures in the horizontal; e.g., cloud gaps clearly shrink during case 1. The bimodality of Fig. 3.4b strengthens, and the distribution now has a global maximum at −8 dBZ and a local maximum at −20 dBZ (Fig. 3.5c).

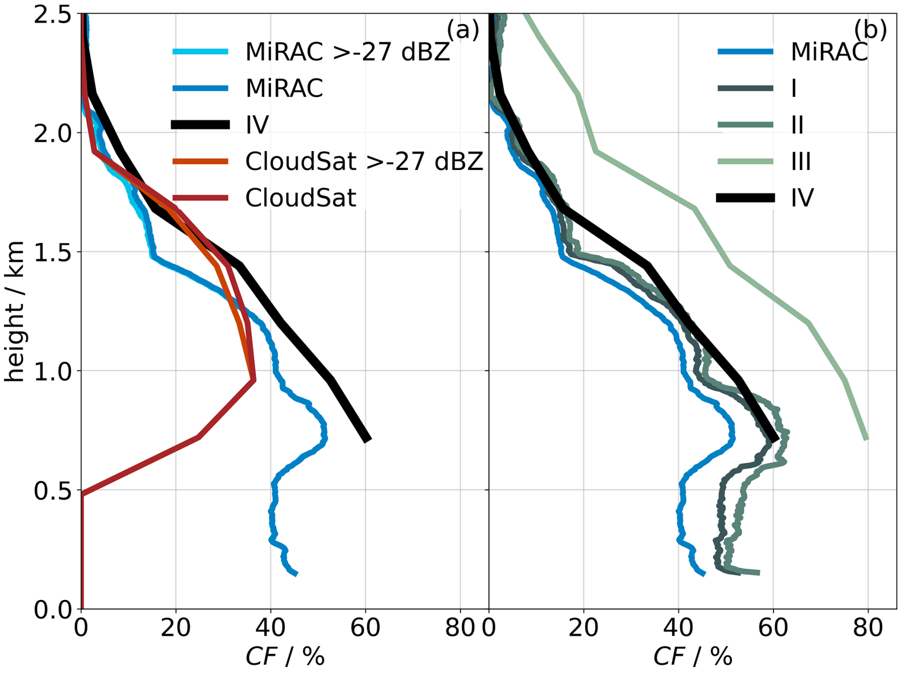

Figure 3.6: Cloud fraction (CF) profiles over four underflights of *Polar 5* below CloudSat. Original and completely forward-simulated (IV) profiles are displayed in **(a)**. The effect of each processing step (I–IV; Sect. 3.2.3) on CF is illustrated in **(b)**. The color coding is equivalent to Fig. 3.4.

III. After the along-range convolution (Fig. 3.4d), the coarser vertical resolution displays less fine cloud structures, stretches clouds in the vertical, and hence increases cloud top heights. To illustrate this in detail, the range-weighting function averages Z at the cloud top over a range of ±480 m. Thus, cloud-free conditions above the cloud top now show a non-negligible radar reflectivity moving the cloud top upwards. Similar to the along-track averaging, Z decreases drastically even below −60 dBZ (Fig. 3.5d).

IV. The sensitivity threshold (Fig. 3.4e compared to c) reduces the number of signals along cloud boundaries and the number of whole clusters during case 4 and enlarges cloud gaps.

The lower resolution and sensitivity of Z_{sim} do not change the contoured frequency by altitude diagram (CFAD) compared to Z_{M} at the most frequented regions between −15 and −8 dBZ (Fig. 3.5g and h). However, the forward simulations decrease the number of Z_{sim} values above 2.25 km and increase the number of Z_{sim} values smaller than 22 dBZ below 960 m height. Z_{sim} does not resolve the lowest 720 m and hence resolves almost no precipitation.

In a second step, we analyze how the mean CF profile averaged over all underflights changes in each processing step:

I. The along-track convolution (Fig. 3.6b, MiRAC compared to I) has no effect on CF above 1.5 km and increases CF by roughly 3 pp between 1 and 1.5 km and by 10 pp below. Near the surface, the overestimation of CF increases from 7 % to 25 % of CF_M. The change in CF due to along-track averaging depends on how many individual clouds are encountered. A larger number of clouds with short gaps in between, e.g., across cloud streets, favors more horizontal cloud stretching and thus increases CF more. The clouds in case 3 enhance CF over all heights, whereas the precipitation and virga in cases 1 and 2 intensify the low-layer CF increase.

II. The along-track integration (Fig. 3.6b, I compared to II) acts in the same way as the along-track convolution but with a smaller effect. An additional increase in CF occurs, which is strongest below 1 km but less than 3 pp.

III. The range convolution (Fig. 3.6b, II compared to III) shifts the CF profile up by about 480 m due to cloud top stretching as Z is averaged over hydrometeor-free areas. Below 1 km, CF increases additionally, by around 30 pp in total. Here, the effect of the range-weighting function (Sect. 3.2.3) spanning ± 480 m is evident. At 720 m, Z between 240 m and 1.2 km affects CF after the range convolution. Hence, the range-weighted signals from non-precipitating low-level clouds might reach the lowest level. As we do not explicitly model a surface reflection signal, this weighting is also the reason why CF_{sim} can only be calculated down to 720 m.

IV. CF after applying the sensitivity threshold (CF_{sim}; Fig. 3.6b, III compared to IV) reduces by 25 pp particularly just above 1.5 km. Most cloud tops are directly below 1.5 km, where the gradient of the CF_M profile is strongest. After cloud stretching, Z at the cloud tops is very small and often falls below the threshold. Thus, the effect of the threshold is predominant at 1.9 km, i.e., 480 m above the layer with most cloud tops. The sensitivity threshold reduces the cloud top height overestimation and leads to a net overshooting of about 240 m compared to CF_M. Note that close to 1.9 km, some Z_M values already fall below the threshold (Fig. 3.6a, MiRAC > -27 dBZ compared to MiRAC).

In summary, changes in sensitivity and resolution (Fig. 3.6a, MiRAC compared to IV) enhance CF_{sim} compared to CF_M most strongly below 1.5 km, i.e., 11 pp at 720 m, which is 25 % of CF_M.

3.4.2 *Evaluation of the forward simulation*

Can we use Z_{sim} as a proxy for Z_{C} and thereby expand the analysis period over all campaigns? A comparison of Z_{sim}, Z_{C}, and the corresponding CF profiles shall answer this question and detect measurement biases between MiRAC and CPR. Note that differences in the observed cloud fields can arise due to the time and location shifts between the two radars. The highly spatially and temporally variable clouds (Fig. 3.4) do not allow clouds to be projected in space and time as done by Gayet et al. (2009) for extended ice clouds.

Z_{sim} and Z_{C} agree well (Fig. 3.4e and f), though a lower number of signals is measured by CloudSat. This is most striking in case 2, when CloudSat detects no clouds. Note that in the raw CloudSat data, i.e., without applying the cloud mask, weak Z_{C} appears at 1 km height during case 2 (not shown). However, the mask attributes these signals to ground clutter and generally filters all signals below 720 m. The fact that MiRAC measurements for cases 1 and 3 evidence significant hydrometeor occurrence below 1 km demonstrates that the cloud mask is too strict, as pointed out in Lamer et al. (2020) (see their Fig. 1). Compared to the horizontal cloud cover from MiRAC, the one observed by CloudSat reduces by a factor of 2. Ground clutter could cause artificial echoes in the lower layers if the CPR mask is too gentle. In this case, ground clutter would enhance Z_{C} but not affect Z_{sim}, which is not dominant during the underflights (Fig. 3.7). Furthermore, CloudSat does not detect low Z_{M} and thus shows separate clouds instead of a continuous cloud layer during case 3.

We investigate the realism of the forward simulation by directly comparing Z_{sim} and Z_{C} for each pixel (Fig. 3.7). Z_{C} is on average 2 dB lower than Z_{sim} for times when both instruments measured a signal. This bias is in the same range (1–2 dB) as that found by Protat et al. (2009). They processed the airborne Z the same way we do but used a threshold of −29 dBZ. Note that they achieve a better matching of air- and spaceborne Z because they only analyze extended non-precipitating ice clouds and minimize the time and spatial lag between the measurements to below 10 min and a few hundred meters. Thus, the RMSE (5.5 dB) and standard deviation (5.17 dB) of our data, which is twice the value claimed by Protat et al. (2009) (2–3 dB), are larger. However, the highly variable low clouds that are observed by each instrument differ due to the time shift and location mismatch of the platforms; thus $Z_{\mathrm{C}} - Z_{\mathrm{sim}}$ (Fig. 3.14) is dependent on the distance to the underflight (time shift) and on the distance between both platforms (location shift). For measurements that are obtained within 30 km around the crossing location and when *Polar 5* and CloudSat are closer than 35 km, the bias and standard deviation decrease to −0.37 and 3.18 dB, respectively.

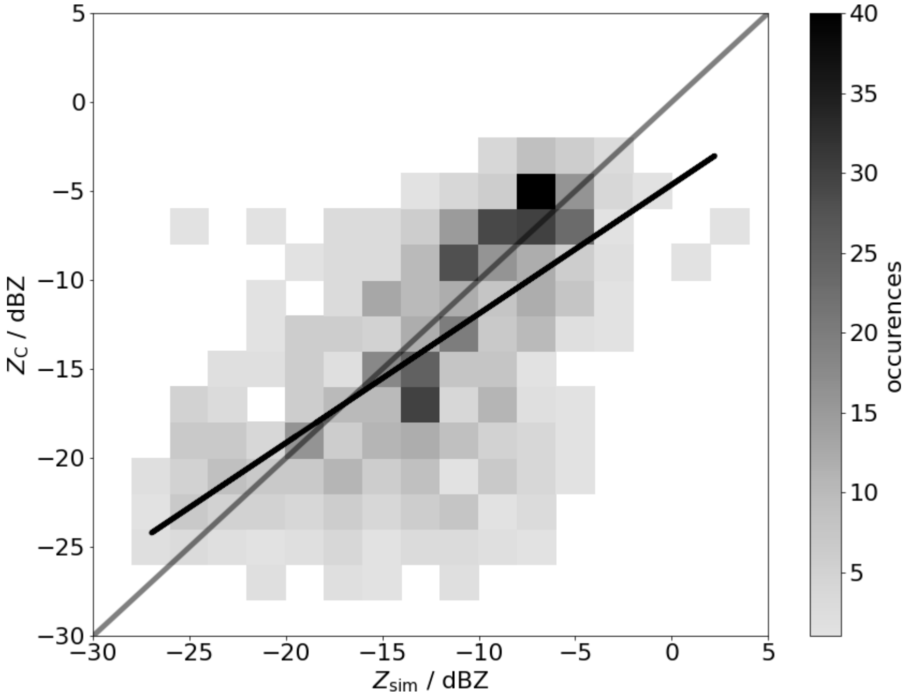

Figure 3.7: Comparison of the equivalent radar reflectivity obtained from forward simulation (Z_{sim}) and CloudSat (Z_C) over four underflights of *Polar 5* below CloudSat with the corresponding linear fit (black). The bin size equals 2 dBZ.

Having shown good agreement between forward-simulated and measured reflectivities, we now focus on the vertical cloud fraction profile. Above 1.5 km, the profiles agree very well; CF_C deviates from the CF_{sim} profile by less than 5 pp (Fig. 3.6a, IV compared to CloudSat). This agreement worsens for lower altitudes; CF_C is lower by 36 pp (16 pp) at 720 m (960 m) height, which is 60 % (31 %) of CF_{sim}. This is consistent with the omission of signals by CloudSat due to a too-aggressive cloud mask, as discussed above. In summary, the comparison demonstrates that Z_{sim} can be used as a good proxy for Z_C above 1.5 km but that care has to be taken below, especially in the blind zone. This holds particularly for the maximum CF_M of 50 % measured at 720 m, which CF_{sim} overestimates, but CloudSat observations strongly underestimate.

3.5 EVALUATION OF CLOUDSAT LIMITATIONS DURING CAMPAIGNS

Synthetic CloudSat reflectivity profiles (Z_{sim}) are generated from the MiRAC observations carried out over the four campaigns (Tables 3.1) and serve as a base for assessing CloudSat's limitations. We first investigate the effect of these limitations on cloud fraction profiles (Sect. 3.5.1) derived from Z_{sim} and specify the drivers for differences between forward simulations and "truth". Furthermore, we analyze how much multilayer clouds (Sect. 3.5.2) and precipitation (Sect. 3.5.3)

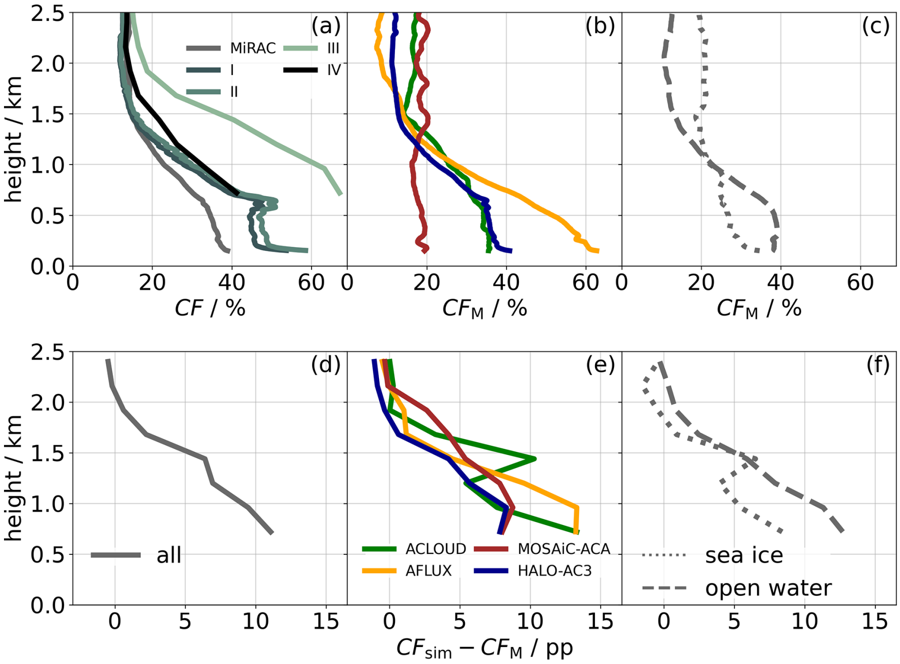

Figure 3.8: Cloud fraction profiles from the airborne radar MiRAC (CF_M) over four campaigns **(a–c)** and the difference compared to the forward-simulated profiles (CF_{sim}; **d–f**). Profiles are averaged over all data **(a, d)**, each campaign **(b, e)**, and different surface covers **(c, f)**. Sea ice concentrations below 15 % and above 90 % represent open water and sea ice. Moreover, the profiles after each processing step (I–IV; Sect. 3.2.3) are displayed in panel **(a)**.

are affected. Note that these campaign measurements cannot be considered as a climatology; however, they provide unique data and insights into Arctic low-level clouds.

3.5.1 *Cloud fraction profiles*

Averaged over the four campaigns, the observed vertical cloud fraction profile (CF_M) is 12 % for altitudes above 1.5 km and increases to 40 % towards the surface (Fig. 3.8a). The increase is strongest between 1.5 and 0.6 km, and the high values at MiRAC's lowest height of 150 m indicate frequent precipitation and probably very low clouds (Griesche et al., 2021). Excluding the blind zone, we average cloud fraction between 1 and 2.5 km and assess the impact of the different forward-simulation steps (Sect. 3.2.3). CF increases by 6 pp due to CloudSat's along-track convolution and integration (Fig. 3.8a, MiRAC compared to II), i.e., horizontal resolution; increases by 12 pp due to its range resolution (II compared to III); and decreases by 10 pp due to its sensitivity (III compared to IV). Vertically resolved, maximum effects of +25 pp (horizontal resolution), +20 pp (range resolution), and −30 pp (sensitivity) occur. The horizontal cloud cover between 1 and 2.5 km reduces by only 5 pp to 34 % during the forward simulation.

Mean $\mathrm{CF_M}$ over the lowest 2.5 km varies between 17 % during MOSAiC-ACA and 25 % during AFLUX (Fig. 3.8b). This is even more pronounced below 1.25 km, where $\mathrm{CF_M}$ differs between 20 % and 60 %, and might reflect a difference between autumn (MOSAiC-ACA) and spring (AFLUX). The profiles obtained during ACLOUD and HALO–(AC)^3 resemble the mean profile over all campaigns. The shape of the $\mathrm{CF_M}$ profile varies between the campaigns, again with the largest differences between AFLUX and MOSAiC-ACA. While MOSAiC-ACA features a roughly constant vertical $\mathrm{CF_M}$ of around 20 % in the lower troposphere, AFLUX has the lowest $\mathrm{CF_M}$ of about 10 % at higher altitudes, which strongly increases to 65 % towards the surface.

The average vertical profiles of the forward-simulated $\mathrm{CF_{sim}}$ and measured $\mathrm{CF_M}$ profiles show a similar shape (Fig. 3.8a, MiRAC and IV). However, the absolute difference between $\mathrm{CF_{sim}}$ and $\mathrm{CF_M}$ (Fig. 3.8d) reveals that $\mathrm{CF_{sim}}$ is larger, and the difference increases towards the surface. At the lowest forward-simulated height (0.72 km), $\mathrm{CF_{sim}}$ overestimates $\mathrm{CF_M}$ by 11 pp; i.e., CloudSat would overestimate cloud fraction by one-third. The increasing overestimation towards the surface is evident for all campaigns (Fig. 3.8e), though differences of about 5 pp are evident. In particular, a peak in the overestimation at 1.5 km height occurs during ACLOUD (Fig. 3.8e) that might depend on differences in the cloud situation.

As already illustrated for the underflights (Sect. 3.4.1), CloudSat's lower vertical resolution shifts $\mathrm{CF_{sim}}$ upwards vertically by roughly 240 m and stretches the clouds. In conclusion, low-level clouds are overestimated above the blind zone, but the dominant hydrometeor layer below 750 m is completely missed by the blind zone. CloudSat's performance, i.e., $\mathrm{CF_{sim}} - \mathrm{CF_M}$, does not show clear differences between the campaigns performed in different seasons. This might depend on the probed cloud types, their connection to different synoptic situations, and the way they are probed. In the following, we assess the dependence of CloudSat's performance on various parameters.

3.5.1.1 *Surface cover*

We analyze dissimilarities between $\mathrm{CF_M}$ and $\mathrm{CF_{sim}}$ over open water and sea ice (Fig. 3.8c and f). In general, cloud fraction profiles appear differently over sea ice, where they are relatively constant with height, and over open water, where higher levels have fewer and the lowest kilometer has more clouds. Over sea ice, a slight increase in $\mathrm{CF_M}$ close to the surface occurs that might be related to very low-level clouds found by Griesche et al. (2021). $\mathrm{CF_{sim}}$ overestimates $\mathrm{CF_M}$, especially below 1.75 km, with stronger overestimations closer to the ground (Fig. 3.8f). This overestimation is more pronounced over open water than over sea ice. Over ice, a second maximum in overestimation occurs at 1.5 km, where the cloud fraction is discontinuous.

3.5.1.2 *Cold-air-outbreak index*

CF is investigated for different M classes (Sect. 3.3.1). We only focus on CAOs and neutral conditions as too few cases for warm conditions exist, which would not allow valid conclusions to be drawn. During CAOs, CF_M is close to 10 % above 1.5 km height (Fig. 3.9a) and increases linearly down to 1 km and more slowly until it reaches 50 %, close to the surface. In contrast, with about 18 %, CF_M is more constant over height for neutral conditions. Then, no significant differences between sea ice and open water are visible, while differences up to 20 pp occur during CAOs. The latter differences vary with height similar to the overall difference between sea ice and open water (Fig. 3.8c). Clearly, CAOs are responsible for the highest low-level cloud fractions, with significant differences between measurements over ice and open water, where air-mass transformation changes cloud characteristics along the trajectory. The atmospheric boundary layer height increases with distance to the ice edge due to strong surface fluxes. Evaporation supports the cloud development from roll cloud streets close to the ice edge to cellular convection further downstream. CF_{sim} overestimates CF_M by up to 16 pp mainly during CAOs (Fig. 3.9c), when the coarse vertical resolution deepens the low-level cloud rolls over water, and less during neutral situations, when CF_M is constant. The overestimation is strongest close to the surface, i.e., 14 and 9 pp during CAOs and neutral conditions, respectively. We speculate that the overestimation depends on cloud amount and orientation of the flight tracks in respect to the cloud streets as this influences the number of cloud gaps over which signals are averaged.

3.5.1.3 *Circulation weather type*

Cyclonic flows are the most frequent CWT (43 %) followed by northerly flows (Fig. 3.3). CF_M shows a strong dependence on CWT, though for all regimes the highest cloud fraction occurs in CloudSat's blind zone (Fig. 3.9b). Northerly flows exhibit the largest CF_M. During cyclonic conditions, the shape of the profile is similar, but CF_M is lower. Both flows, particularly the northerly one, favor CAOs (Fig. 3.3) and associated cloud rolls. During southerly winds, non-precipitating clouds exist at different heights. CF_M is generally lowest and often zero during anticyclonic conditions, which, however, are rare. Again CF_{sim} overestimates CF_M for all CWTs below 1.5 km. The effect is strongest during northerly conditions followed by cyclonic conditions. Although, CF_M and its overestimation by CloudSat are largest during northerly winds, both seem to not be directly related to CWT; i.e., CF_M is larger during AFLUX than HALO–(AC)^3 regardless of CWT (not shown). In fact, CF_M and the difference compared to the synthetic profiles are sorted in the same order, which implies a dependence on the amount of cloud fraction.

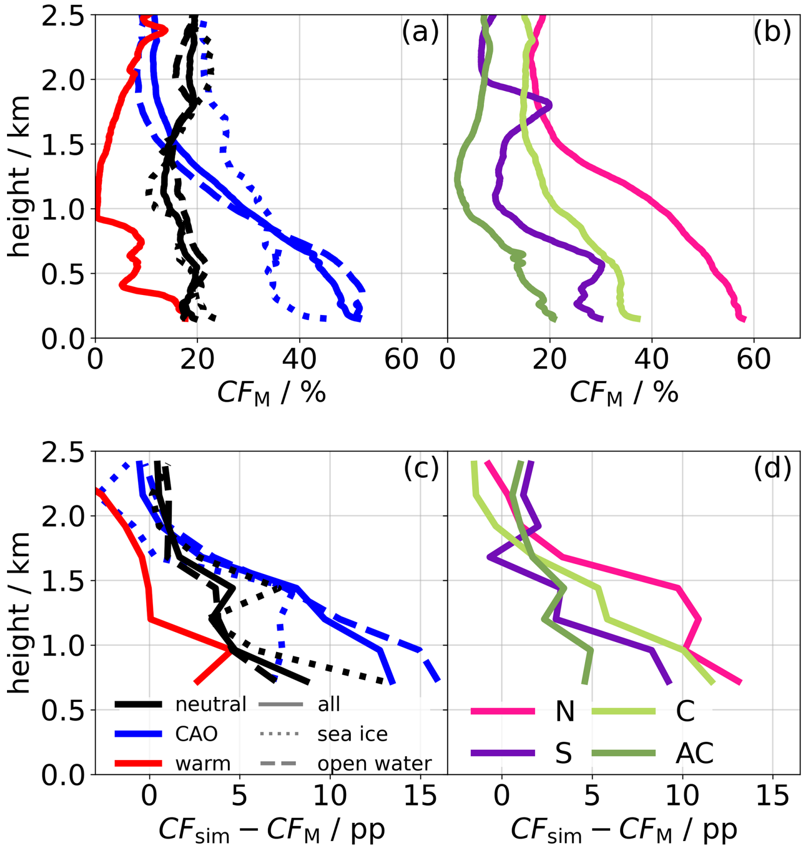

Figure 3.9: Cloud fraction profiles from the airborne radar MiRAC (CF_M) over four campaigns **(a, b)** and the difference compared to the forward-simulated profiles (CF_{sim}; **c, d**). Profiles are averaged for different marine cold-air indices (M; **a, c**; solid lines): warm period (red), neutral period (black), and cold-air-outbreak indices (CAO; blue). The data are additionally categorized as being observed over sea ice (sea ice concentration, sic, $< 15\,\%$; dotted) and open water (sic $> 90\,\%$; dashed). Moreover, profiles are separated into circulation weather types (CWTs; **b, d**). N, S, C, and AC stand for northerly, southerly, cyclonic, and anticyclonic flow, respectively.

In conclusion, the errors imposed by CloudSat's limitations ($CF_{sim} - CF_M$) do not show a clear dependence on the surface type, M, or CWT but rather on cloud fraction and the shape of the profile. Significant errors only occur for clouds below 1.5 km. For the low-level cloud fraction we thus propose a simple correction in the form of a linear regression: the overestimation is 5 pp at 30 % cloud fraction and increases linearly to 15 pp for a cloud fraction of 60 %. While such a correction would reduce the overestimation of the vertically resolved cloud fraction with a residual uncertainty of about 5 pp (not shown), it has to be stressed that the blind zone neglects low-level clouds, which are the most common clouds in the Arctic (Fig. 3.6).

3.5.2 *Multilayer clouds*

The radiative characteristics of multilayer and single-layer cloud conditions often differ (Li et al., 2011). During ACLOUD, Mech et al. (2019) identified 38 % of the cloudy scenes as being composed of multilayer clouds that have a median thickness of 205 m. CloudSat might miss individual clouds due to its sensitivity, and its coarse resolution might merge separate hydrometeor layers to a single layer (Sect. 3.4.1). We investigate the overall effect on the frequency of multilayer cloud occurrence by defining a profile as containing a multilayer cloud for CloudSat if a gap of at least one range gate (240 m) occurs in the Z_{sim} profile. For MiRAC a threshold of 90 m is used to take advantage of its finer resolution.

Averaged over all campaigns, 48 % of the cloud tops observed over all Z_{M} profiles belong to multilayer clouds that have a mean thickness of 347 m (single-layer clouds: 762 m). During the forward simulations these multilayer clouds might merge to single-layer clouds. For Z_{sim} only 12 % of the cloud tops belong to multilayer clouds, which have a mean thickness of 527 m. The coarse resolution deepens single-layer clouds by 140 m and multilayer clouds by 180 m. A total of 43 % of the observed multilayer cloud tops are below 1 km, which is less than for single-layer clouds (55 %); however, this implies that nearly every multilayer system has a layer with a cloud top below 1 km. With 48 % of all multilayer cloud tops, slightly more multilayer clouds are below 1 km for Z_{sim} than for Z_{M}.

The absolute number of cloudy Z_{M} profiles containing medium-thickness (0.24–1.92 km) clouds reduces by a factor of 15 during the forward simulation (Fig. 3.10a and b, gray). For 240 m thick clouds, the factor is 2.3 times larger. Z_{sim} does not detect more than twice as many shallow than medium-thickness clouds (Fig. 3.10b, gray). Furthermore, Z_{sim} misses the thickest clouds. Because of the low vertical resolution, Z_{sim} does not resolve the lowest 720 m of the atmosphere and thus thins the thickest clouds by 240 m to 2.16 km. The ratio between the number of clouds obtained by MiRAC and the forward simulations for clouds that are thicker than 1.92 km is 70 % of the averaged ratio due to cloud stretching.

For multilayer clouds only, the ratio between 480 and 240 m thick clouds increases for Z_{sim} (Fig. 3.10a and b, pink). First, shallow clouds might get stretched. Second, Z_{sim} might detect fewer thin clouds, which reduces the total number of cases. Furthermore, the absolute number of clouds over all cloud thicknesses excluding 240 m reduces by a factor of 68 during the forward simulation. The number of multilayer clouds diminishes 4 times as much as of all clouds due to the reduced resolution and sensitivity. Z_{sim} could either not detect thin, second cloud layers anymore or merge multilayer to single-layer clouds. For 240 m thick clouds, the reduction factor of the number of

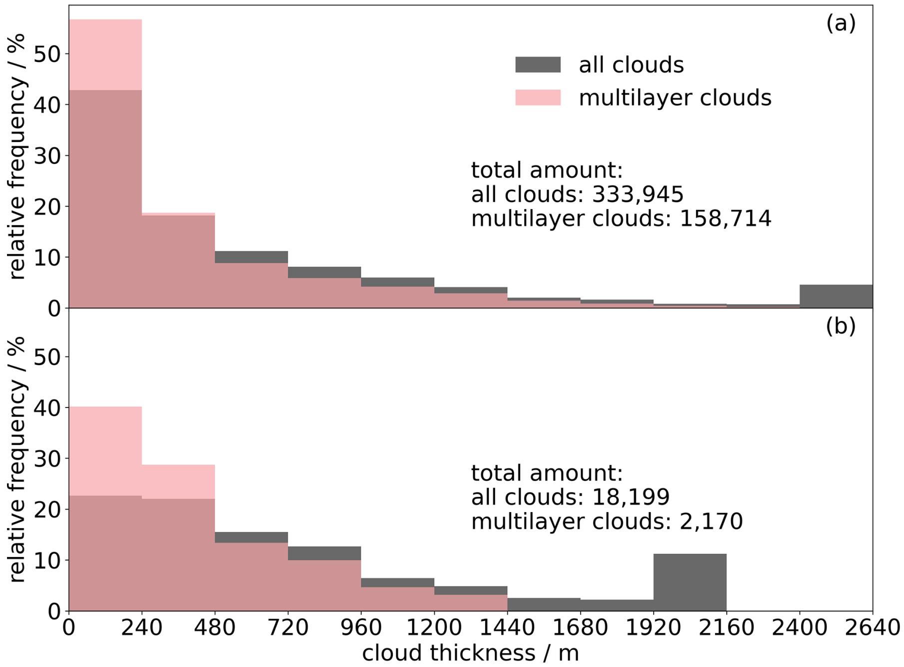

Figure 3.10: Relative frequency of occurrence for the thickness over all (gray) and multilayer clouds (pink) derived from the equivalent radar reflectivity of the airborne radar MiRAC (Z_M; **a**) and of the forward simulation (Z_{sim}; **b**) over four campaigns. Note that MiRAC resolution is much finer but binned to match the one of CloudSat. The total number of all and multilayer clouds is displayed, with each radar reflectivity profile counting as an additional cloud.

clouds observed by MiRAC and the forward simulations is twice the average over the remaining cloud thicknesses. The detection omission is larger for shallow than for deeper clouds but decreases compared to all clouds. Thus, the detection omission of forward-simulated shallow clouds is a general shortcoming rather than one attributed to multilayer clouds. Hence, the merging of multiple cloud layers results in the 4-times-larger reduction factor of the number of multilayer clouds.

3.5.3 *Precipitation*

One of the most important applications of CloudSat is the derivation of snowfall in the Arctic. The Fram Strait is of particular interest as precipitation is most intense in this area (McCrystall et al., 2021), and snowfall estimates between CloudSat and regional climate models differ highly (Lerber et al., 2022b). From the "2C-Snow-Profile", Edel et al. (2020) derived a mean snowfall rate (S_C) of 200 to 500 mm yr^{-1} around Svalbard. The snowfall rate of the 2C-Snow-Profile product is calculated for bins that contain snow or snow-producing clouds via optimal estimation from snow size distribution parameters and uncertainties that are obtained by optimal estimation as well (Wood and L'Ecuyer, 2018). To calculate these snow size distribution parameters, radar reflectivity profiles of the 2B-Geoprof product and temperatures from ECMWF-AUX (European Centre for Medium Range Forecasts-AUXiliary), i.e., state variable data interpolated to the CPR grid, as well as a priori snow microphysical properties, radar scattering properties, and size distribution parameters are required as input. These microphysical parameters represent dry snow, and the scattering properties hold for irregularly shaped particles (Wood, 2011). However, S_C, which is calculated for the near-surface bin at 1.2 km height, assumed to be the lowest bin not affected by ground clutter, deviates from the surface snowfall rate (S_{surf}). Moreover, resolution limitations (Sect. 3.2.1) might affect S_C.

We calculate snowfall rates from Z_M (S_M) and Z_{sim} (S_{sim}) for Z larger than -5 dBZ via the Z_e–S relation for three bullet rosettes following Maahn et al. (2014). Note that rosette habits might not capture the microphysical composition of oceanic snow-producing clouds under CAO conditions very well. We derive S_M for all heights above 150 m to avoid ground clutter contamination for MiRAC (Sect. 3.2.2).

First, the effect of CloudSat's resolution on the Z_{sim} and S_{sim} distributions is investigated at 1.2 km by comparing them with the respective Z_M and S_M distributions. Compared to Z_M, the relative number of Z_{sim} values between -5 and 3 dBZ is larger, and the number of stronger Z_{sim} values is lower (Fig. 3.11a); i.e., CloudSat would overestimate very light snowfall and underestimate stronger snowfall. Z decreases during the spatial convolution. Note that Z_M might fall below the threshold for precipitation ($Z > -5$ dBZ) during the forward simulation, reducing the number of S_{sim} values. The histogram of snowfall rates shows that the number of S_{sim} and S_M values decreases exponentially with their intensity (Fig. 3.11b). The relative number of S_{sim} values compared to S_M values is larger for S_{sim} below 0.2 mm h^{-1}, lower for S_{sim} between 0.2 and 2.0 mm h^{-1}, and comparable for S_{sim} above 2 mm h^{-1}. Due to its low resolution, CloudSat would overestimate low snowfall rates by 4 pp and underestimate higher rates by 4 pp.

We evaluate the influence of CloudSat's blind zone on its total precipitation amount (A_C), which is the integral of the snowfall rate at a specific height over measurement time, following Maahn et al. (2014) but for Z_M over ocean and sea ice. Over all campaigns, the total precipitation amount obtained from MiRAC (A_M) is 1.0 mm (S_M of 111 mm yr^{-1}) at 1.2 km and with 2.1 mm (S_M of 229 mm yr^{-1}) more than twice as much at 150 m (Fig. 3.12). For a 1-year period at Ny-Ålesund, Maahn et al. (2014) found a larger S_{surf} of 320 mm yr^{-1} using a ground-based radar, which might result from the choice of flight patterns that avoid storms and deep clouds. Due to its blind zone, CloudSat would underestimate A_M at 150 m by 51 pp (Fig. 3.12),

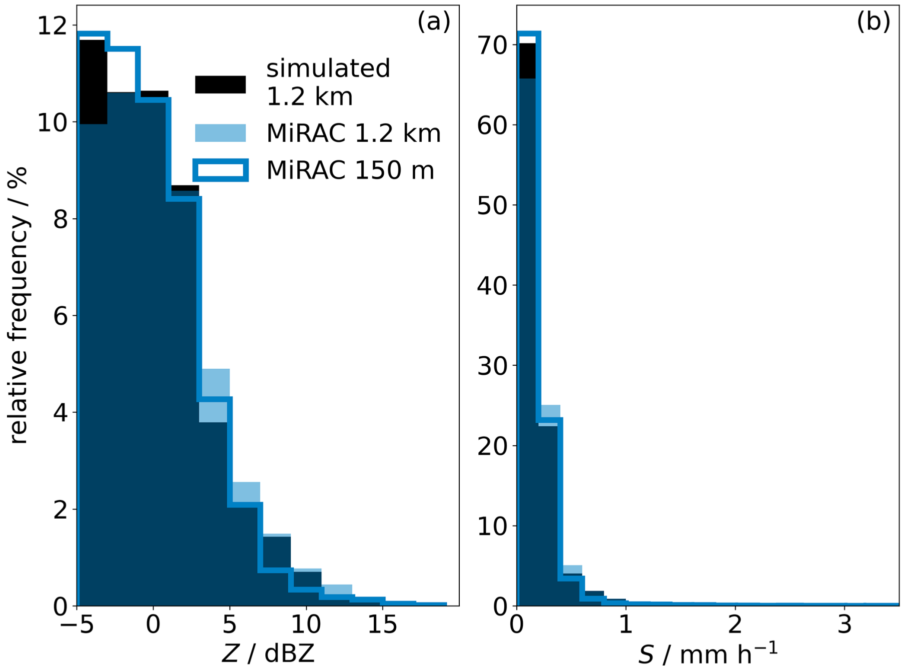

Figure 3.11: Relative frequency of occurrence of the equivalent radar reflectivity (Z; **a**) and precipitation rate (S; **b**) for Z larger than -5 dBZ observed by the airborne radar MiRAC at 1.2 km (blue shade) and 150 m (blue line) and by the forward simulations at 1.2 km height (black shade) over four campaigns. The size of the bins equals 2 dBZ and 0.2 mm h^{-1}.

which is much stronger than for Ny-Ålesund (9 pp; Maahn et al., 2014).

To identify the Z_M regime leading to the underestimation of A_M caused by CloudSat's blind zone, A_M is analyzed for different reflectivity classes (Fig. 3.12). Closest to the ground, with 90 %, light precipitation ($Z_M < 10$ dBZ) is the dominant contributor to A_M. These reflectivities strongly increase from 1.2 km altitude down to 500 m and less below. Z_M values between 10 and 20 dBZ equally contribute to A_M over all heights. Z_M values larger than 20 dBZ only occur below 400 m and contribute to A_M more strongly closer to the ground. The total precipitation amount has its maximum at 235 m height because it strongly increases below 1.2 km, probably due to formation of light precipitation, and slightly decreases down to 150 m due to sublimation. The increase in occurrence of higher-reflectivity classes just above the maximum height is likely related to aggregation.

In this study, with 90 %, light precipitation ($Z_M < 10$ dBZ) plays a more important role than for Ny-Ålesund, where it is 35 % (Maahn et al., 2014), while moderate and strong precipitation is greatly reduced. We also find a lower height of maximum precipitation (235 vs. 600 m) and less sublimation (3 vs 20 pp). This might be related to the generally higher latitudes and colder conditions encountered during the flights. Moreover, the recorded cloud types favor light precipita-

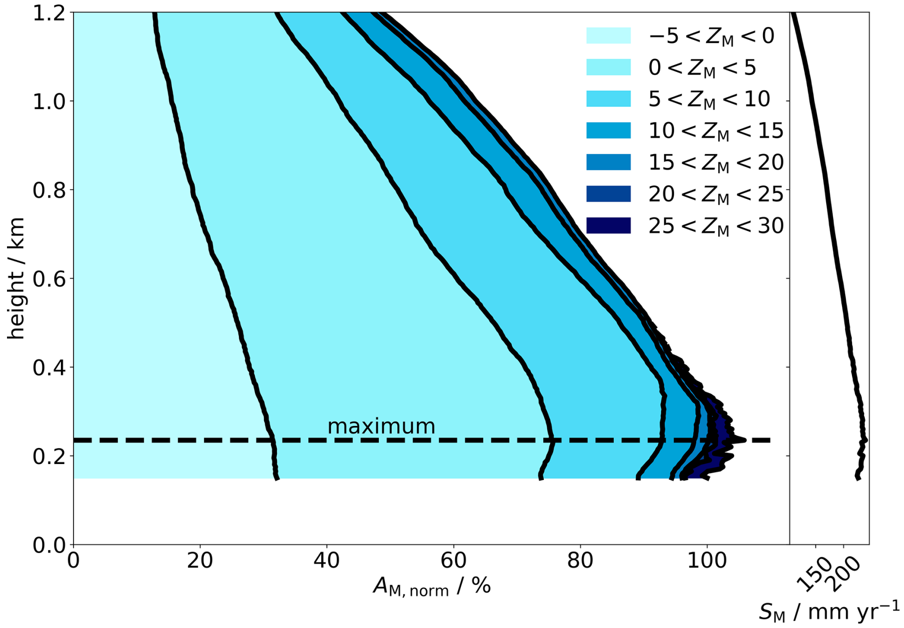

Figure 3.12: Contribution from different intervals of equivalent radar reflectivity obtained from the airborne radar MiRAC (Z_M) to the total precipitation amount over all campaigns (A_M) with height. $A_{\mathrm{M,\,norm}}$ is the integral over the snowfall rate (S_M) for a specific height, which is calculated for Z_M larger than -5 dBZ via the Z_e–S relation for three bullet rosettes following Maahn et al. (2014), normalized by A_M at 150 m, which is the nearest surface bin not affected by ground clutter. The dashed line at 235 m marks the height of maximal $A_{\mathrm{M,\,norm}}$. The profile of S_M with height is shown in the right column.

tion. In particular, many CAOs occurred throughout the campaigns (Fig. 3.3). At least 70 % of A_M is measured during CAOs for all heights and Z_M regimes. This ratio is higher at lower altitudes down to 250 m. During CAOs, the number of Z_M values larger than 5 dBZ is so low that these Z_M values do not enhance A_M. In summary, CAOs produce mainly light precipitation, dominating A_M.

3.6 CONCLUSIONS AND OUTLOOK

Many studies use CloudSat observations to investigate Arctic clouds (Liu et al., 2012; Mioche et al., 2015; Zygmuntowska et al., 2012) and snowfall (Lerber et al., 2022b). However, CloudSat CPR has a blind zone of about 1 km, a coarse spatial resolution, and a limited sensitivity, which impact its usefulness in the assessment of warm marine-boundary-layer clouds and precipitation (Lamer et al., 2020). Our study extends this investigation for the Arctic using finely spatially resolved airborne radar reflectivity measurements by MiRAC obtained during four campaigns that took place over different seasons.

The measurements, which cover more than 25 000 km, are used to forward-simulate CloudSat measurements. During four underflights, these forward-simulated and CloudSat radar reflectivities agree within 2 dB; thus the forward simulation is a good proxy for CloudSat observations. The cloud fraction obtained by MiRAC over all campaigns is on average 30 %, with lower values of about 15 % at 2.5 km and a maximum of 40 % close to the ground. CloudSat's limitations increase the forward-simulated cloud fraction at 720 m by 11 pp, which is 33 % of the MiRAC cloud fraction. However, there are compensating effects at play: CloudSat's horizontal resolution increases the cloud fraction by a maximum of 25 pp and its range resolution by a maximum of 20 pp, and its sensitivity decreases the cloud fraction by a maximum of 30 pp. The lower spatial resolution fills cloud gaps, stretches clouds by 240 m at the cloud top and bottom, and hence increases the cloud fraction of the forward-simulated observations more strongly the closer to the ground. Our finding that MiRAC and CloudSat radar reflectivities differ substantially below 1.5 km supports the conclusion of Lamer et al. (2020) that the CPR cloud mask might be too restrictive, such that airborne remote sensing is necessary to resolve fine cloud structures and the lowest kilometer of the atmosphere.

We aimed to identify the drivers for CloudSat's over- and underestimations: fewer discrepancies between the forward-simulated and MiRAC cloud fraction occurred over sea ice than over open water. With 16 pp, the forward simulations overestimate the MiRAC cloud fraction most strongly over water during cold-air outbreaks, mostly due to cloud top stretching. Northerly flows, mainly connected with CAOs, show the highest low-level cloud fraction and overestimation by CloudSat. Therefore, we suggest a correction for profiles below 1.5 km that show fractions above 30 % which is simply a function of cloud fraction. In this way, the overestimation can be corrected roughly with a residual uncertainty of 5 pp. Note that cloud fractions and CloudSat's performance might depend on flight tracks.

This study confirms the finding of Kulie et al. (2016) and Kulie and Milani (2018) that CloudSat observes mainly light snow events at high latitudes during CAOs. The previous studies highlight the until then unresolved blind zone limitations. This study resolves these caveats on snowfall occurrence and amount that lead to an underestimation of the total precipitation amount by 51 pp. This finding hampers efforts to quantify snowfall, especially light snowfall during CAOs, with the best available spaceborne instruments. Moreover, CloudSat's pulse length merges layers of multilayer clouds; thus the number of multilayer clouds obtained by MiRAC (48 %) reduces by a factor of 4 during the forward simulations.

Additionally, some interesting insights on Arctic low-level clouds have been revealed: cloud fractions over sea ice showed a rather constant vertical profile, while low-level cloud formation strongly enhances cloud fraction over water up to around 1 km. The cloud fractions obtained by MiRAC indicate that low-level strati appear at their lowest heights over sea ice. These strati were also frequently found below 150 m during a *Polarstern* cruise taking place simultaneously with ACLOUD (Griesche et al., 2020). These surface-coupled clouds have a strong radiative effect, but their spatial extent is mainly unknown due to the gaps in the current observation system. Hence, further measurements are needed to study them in more detail (Griesche et al., 2021).

To generalize our findings to the broader Arctic region, further air- or shipborne measurements such as MOSAiC campaign data, which cover a larger area, have to be studied. Moreover, winter- and summertime observations are needed to determine cloud occurrence year-round. To mimic CloudSat observations more accurately, the resolution adaption of the finely resolved radar measurements should comprise an across-track convolution in the future as well. Follow-on studies could test the performance of the EarthCARE CPR to detect Arctic low-level clouds and complement the study of Lamer et al. (2020) for warm marine-boundary-layer clouds. Compared to the CloudSat CPR, the EarthCARE CPR is more sensitive and has the same range resolution (500 m; Burns et al., 2016). Due to the higher sensitivity but remaining cloud stretching effect of about 250 m, we expect that it will observe more clouds than CloudSat.

3.7 APPENDIX A

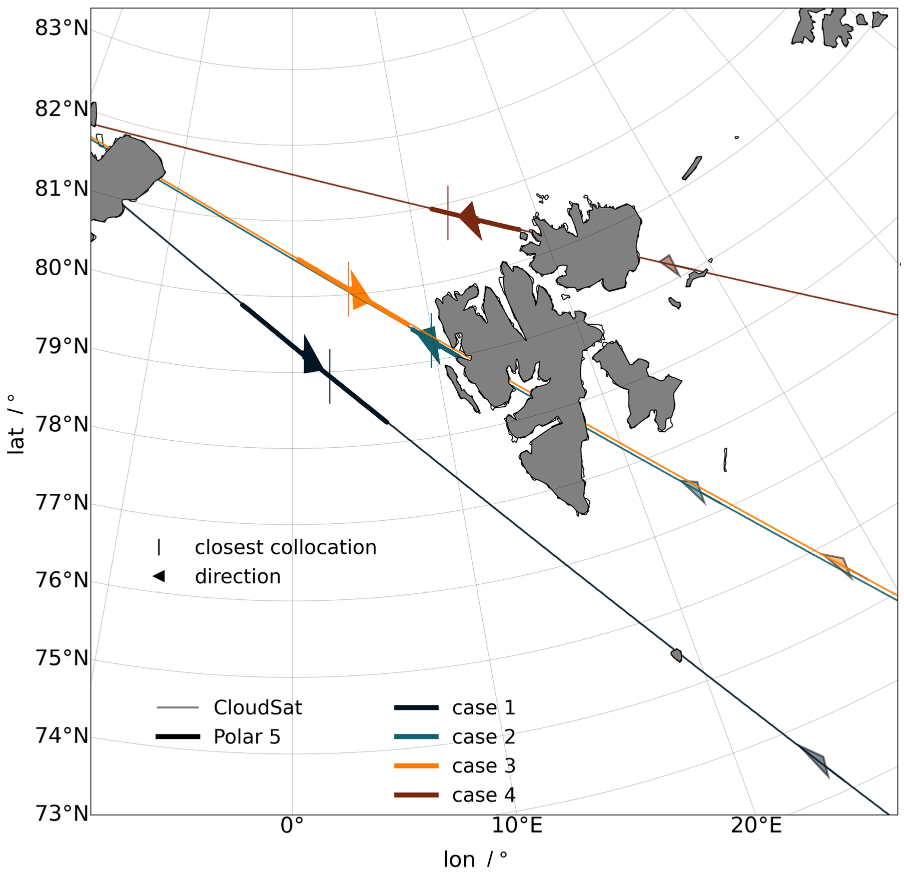

Figure 3.13: Map highlighting the tracks of CloudSat (light colors) and *Polar 5* (intense colors) during the four underflights (cases 1–4). The arrows and vertical lines indicate the flight direction of each platform and the location of the crossing, respectively.

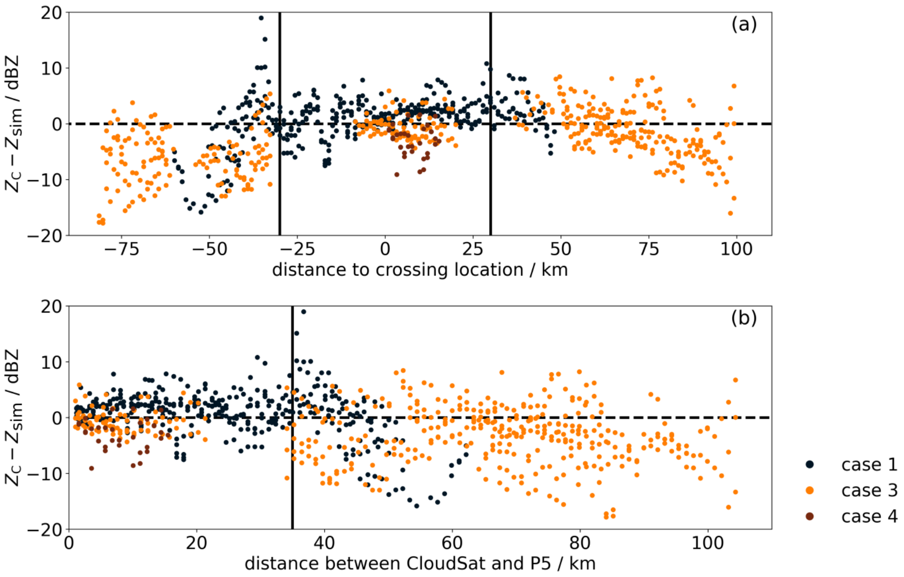

Figure 3.14: Dependence of the difference between the forward-simulated and CloudSat equivalent radar reflectivities ($Z_C - Z_{sim}$) over four underflights of *Polar 5* below CloudSat on distance to the crossing location **(a)** and distance between the platforms **(b)**. Note that CloudSat resolves no signals during case 2.

DATA AVAILABILITY

The MiRAC, AMALi, and AMSR2 ARTIST Sea Ice (ASI) sea ice concentration data (version 5.4; provided by the University of Bremen) are accessed via the ac3airborne intake catalog (Mech et al., 2022). The MiRAC measurements during ACLOUD (Mech et al., 2022a), AFLUX (Mech et al., 2022b), and MOSAiC-ACA (Mech et al., 2022c) as well as the cloud top heights from AMALi during ACLOUD (Kulla et al., 2021) and AFLUX (Kulla et al., 2021b) and the AMSR2 ASI observations (Melsheimer and Spreen, 2019) are stored on the PANGAEA database. Data that are not yet published are stored on the Nextcloud server of the (AC)^3 project. The marine cold-air-outbreak indices and circulation weather types are calculated from ERA5 reanalysis data (Hersbach et al., 2020).

COMPETING INTERESTS

At least one of the (co-)authors is a member of the editorial board of *Atmospheric Measurement Techniques*. The peer-review process was guided by an independent editor, and the authors also have no other competing interests to declare.

DISCLAIMER

ACKNOWLEDGEMENTS

We gratefully acknowledge the funding by the Deutsche Forschungsgemeinschaft (DFG, German Research Foundation) within the Transregional Collaborative Research Center (TRR 172) "ArctiC Amplification: Climate Relevant Atmospheric and SurfaCe Processes, and Feedback Mechanisms (AC)^3" (project number 268020496, subproject B03). We acknowledge the support from the Alfred Wegener Institute and *Polar 5* captains during the campaigns.

FINANCIAL SUPPORT

This research has been supported by the Deutsche Forschungsgemeinschaft (grant no. 268020496 – TRR 172).
This open-access publication was funded by Universität zu Köln.

REVIEW STATEMENT

This paper was edited by Stefan Kneifel and reviewed by two anonymous referees.

4

INITIAL DEVELOPMENT OF MARINE COLD AIR OUTBREAKS

This study addresses the second research question (Sect. 1.6.2) about how roll circulation and cloud properties change with fetch in the initial state of Marine Cold Air Outbreaks (MCAOs) and how this evolution is preconditioned by environmental conditions.

Schirmacher, I., S. Schnitt, M. Klingebiel, N. Maherndl, B. Kirbus, A. Ehrlich, M. Mech, and S. Crewell (2024a). "Clouds and precipitation in the initial phase of marine cold-air outbreaks as observed by airborne remote sensing." In: *Atmospheric Chemistry and Physics* 24.22, pp. 12823–12842. DOI: `10.5194/acp-24-12823-2024`

AUTHOR CONTRIBUTION

IS analyzed and visualized the data, wrote the paper, and developed the methodology, and together with SaS, MK, AE, and SC, the paper was conceptualized and results were discussed. MM and AE developed the flight strategy for the cloud street investigation. BK calculated the back trajectories. NM col- located the P5 and P6 measurements and computed the rime mass fraction. All authors contributed to manuscript revisions.

SUPPLEMENT

The supplement related to this article is available online at: https://acp.copernicus.org/articles/24/12823/2024/acp-24-12823-2024-supplement.pdf

CLOUDS AND PRECIPITATION IN THE INITIAL PHASE OF MARINE COLD AIR OUTBREAKS AS OBSERVED BY AIRBORNE REMOTE SENSING

ABSTRACT

Marine cold-air outbreaks (MCAOs) strongly affect the Arctic water cycle and, thus, climate through large-scale air mass transformations. The description of air mass transformations is still challenging, partly because previous observations do not resolve fine scales, particularly for the initial development of an MCAO, and due to a lack of information about the thermodynamical evolution starting over sea ice and continuing over open ocean and associated cloud microphysical properties. Therefore, we focus on the crucial initial development within the first 200 km over open water for two case studies in April 2022 during the HALO-(AC)^3 campaign (named after the *High Altitude and Long Range Research Aircraft* and Transregional Collaborative Research Centre ArctiC Amplification: Climate Relevant Atmospheric and SurfaCe Processes and Feedback Mechanisms (AC)^3). The two events, just 3 d apart, belong to a particularly long-lasting MCAO and occurred under relatively similar thermodynamic conditions. Even though both events were stronger than the climatological 75th percentile of that period, the first event was characterized by colder air masses from the central Arctic which led to an MCAO index twice as high compared to that of the second event.

The evolution and structure were assessed by flight legs crossing the Fram Strait multiple times at the same location, sampling perpendicularly to the cloud streets. Airborne remote sensing and in situ measurements were used to build statistical descriptions of the boundary layer, dynamics, clouds, and precipitation. For this purpose, we established a novel approach based solely on radar reflectivity measurements to detect roll circulation that forms cloud streets. The two cases exhibit different properties of clouds, riming, and roll circulations, though the width of the roll circulation is similar. For the stronger event, cloud tops are higher; more liquid-topped clouds exist; the liquid water path, mean radar reflectivity, precipitation rate, and precipitation occurrence have increased; and riming is active. The variability in rime mass has the same horizontal scale as the roll circulation, implying the importance of roll circulation on cloud microphysics and precipitation.

Boundary layer and cloud properties evolve with distance over open water, as seen by, e.g., cloud top height rising. In general, cloud streets form after traveling 15 km over open water. After 20 km, this

formation enhances cloud cover to just below 100 %. After around 30 km, precipitation forms, though for the weaker event, the development of precipitation is shifted to larger distances. Within our analysis, we developed statistical descriptions of various parameters (i) within the roll circulation and (ii) as a function of distance over open water. These detailed cloud metrics are particularly well suited for the evaluation of cloud-resolving models close to the sea ice edge to evaluate their representation of dynamics and microphysics.

4.1 INTRODUCTION

Marine cold-air outbreaks (MCAOs) are strong air mass transformations. During Arctic MCAOs, cold and dry air flows from the ice-covered central Arctic southward over the open ocean. There, cloud streets form that are clearly visible in satellite images and transform to cellular convection downstream under extreme surface heat fluxes (Brümmer, 1996). Especially over open ocean, cloud streets have important implications for the radiative surface energy budget due to their high albedo induced by liquid cloud tops (Geerts et al., 2022). Moreover, their long lifetimes affect precipitation evolution and characteristics (Abel et al., 2017) and, thus, the Arctic water cycle. Arctic MCAOs can also strongly influence the weather in the mid-latitudes (Turner and Marshall, 2011b).

The Arctic is a hot spot with respect to climate change, most pronounced by strong surface temperature increases and sea ice decline (Wendisch et al., 2023). Dahlke et al. (2022) also showed significant shifts in the occurrence of MCAOs, i.e., decreases in early winter and increases in late winter. These shifts are possibly caused by changes in synoptic circulation patterns and feedback mechanisms involving retreating sea ice. How MCAO characteristics will develop in the future will require improved modeling capabilities (Geerts et al., 2022) and a better process understanding of these air mass transformations, including cloud phase changes (Pithan et al., 2018). To resolve the mesoscale cloud organization in MCAOs, large-eddy simulations (LESs) are required. Yet, the transition between organizational states is especially difficult to model as initial conditions, turbulence, cloud microphysics, and large-scale flow interact. Furthermore, small-scale surface heterogeneity in the marginal sea ice zone (MIZ) is important for the formation of rolls (Gryschka et al., 2014), whereby the exposure of air to open water in the MIZ plays an important role (Spensberger and Spengler, 2021). LES studies also highlight the importance of mixed-phase microphysical processes in preconditioning the transition of cloud organization (Abel et al., 2017; Tornow et al., 2021). Model settings like the employed ice microphysical scheme and model resolution affect the timing of transformation that differs between the models, e.g., when the ice phase is permitted (Roode et al., 2019). Meanwhile, a higher resolution evokes roll convection at smaller distances to the sea ice edge and increases the precipitation amount (Spensberger and Spengler, 2021). So far, no consensus has been reached and progress is delayed by the lack of observations for models.

The first airborne in situ measurements during the Convection and Turbulence (KonTur) experiment (Brümmer et al., 1985, 1982; Markson, 1975); ARKTIS '88 (Brümmer et al., 1992), 1991, and 1993 (Brümmer, 1999); and Marginal Ice Zone Experiment (MIZEX; Walter and Overland, 1984) investigated the mesoscale roll convection inside the atmospheric boundary layer (ABL) that is strengthened by thermal instability when air flows from the sea ice over the open water (Atkinson and Wu Zhang, 1996). Brümmer (1996) and Müller et al. (1999) showed how the ABL was modified as a function of distance from the sea ice within the first 300 km under the influence of strong surface heat fluxes from open water. While cloud reflectance measurements by satellites have provided important insights into the geometrical appearance of MCAOs since their beginning, recent studies such as Murray-Watson et al. (2023), Wu and Ovchinnikov (2022), and Tornow et al. (2023) quantitatively studied cloud development in a quasi-Lagrangian way. Using back trajectories, they investigated cloud properties derived by the Moderate Resolution Imaging Spectroradiometer (MODIS) as a function of time since the air passed the sea ice edge. The liquid water path (LWP) and cloud top height (CTH) increase within the first 10 h, with the strongest increase in the initial MCAO phase, i.e., the first couple of hours. Further, they demonstrate that MCAO strength affects the development until 30 h after the air left the ice edge. However, due to retrieval limitations, they only considered liquid-dominated clouds, and no information on the vertical structure and precipitation is available. Based on CloudSat observations, Mateling et al. (2023) demonstrate the important role of snowfall from MCAOs, which produce the majority of snowfall in the North Atlantic. Yet, CloudSat sampling is limited by its blind zone of 1 km (Maahn et al., 2014; Schirmacher et al., 2023), and it is unclear whether differences with model precipitation result from model deficits or instrument limitation (Lerber et al., 2022a).

In summary, there is a clear need for high-resolution cloud observations within MCAOs. These are typically only available from ground-based remote sensing measurements at supersites. Therefore, the Cold-Air Outbreaks in the Marine Boundary Layer Experiment (COMBLE) in 2021–2022 (Geerts et al., 2022) established two ground stations at Andenes and Bear Island, Norway, providing important insights into cloud properties (Lackner et al., 2023; Mages et al., 2023) and supporting model evaluation (Geerts et al., 2022). As these stations were located about 1000 km away from the sea ice edge, only open and closed cellular convection was observed, whereas cloud streets were not.

In this study, we exploit detailed cloud observations taken during the initial MCAO phase close to the ice edge, where the rapid development of mixed-phase clouds occurred. We use airborne remote sensing observations that target model evaluation in a statistical sense and suggest suitable metrics for this. The measurements were performed during the HALO-(AC)^3 campaign (named after the *High Altitude and Long Range Research Aircraft* and Transregional Collaborative Research Centre ArctiC Amplification: Climate Relevant Atmospheric and SurfaCe Processes and Feedback Mechanisms (AC)^3; Wendisch et al., 2024) that took place over the Fram Strait where MCAOs occur frequently (Dahlke et al., 2022; Mateling et al., 2023; Papritz et al., 2015). We focus on a major MCAO event that remained active for more than 2 weeks (Walbröl et al., 2024). Within this period of northerly flow, two dedicated research flights were performed just 3 d apart, equipped with active and passive remote sensing instrumentation. The environmental conditions during the flights were similar but slightly different, particularly with respect to the cloud properties. Strait flight tracks crossed cloud streets multiple times perpendicularly to their elongated orientation to perform high-resolution measurements of cloud and precipitation properties which are not possible from a satellite (e.g., see LWP observations by MODIS; Fig. 4.1c, d). The data cover a fetch, i.e., the distance the air traveled over open water prior to the measurement, of up to about 150 km. From these unique measurements, we aim to answer the following questions:

1. What are the differences between the environmental conditions on both flight days, and what are their implications for cloud development?

2. Can we identify characteristic changes in cloud and precipitation properties perpendicular to the cloud street orientation, i.e., within the roll circulation?

3. How do roll circulation, clouds, and precipitation properties evolve with fetch in the initial MCAO phase, e.g., up to travel times of 4 h?

The paper is organized as follows: first, we introduce the airborne measurements and data (Sect. 4.2). Second, we describe the methodology that we developed to assign the fetch to each measurement using back-trajectory calculations (Sect. 4.3.1) and the identification algorithm to detect roll circulations from cloud radar measurements (Sect. 4.3.2). Section 4.4 describes the boundary layer and cloud development during the two flights (Sect. 4.4.1) and characterizes cloud properties within roll circulation (Sect. 4.4.3) and the development along fetch (Sect. 4.4.4). Finally, Sect. 4.5 concludes with the questions raised above and discusses pathways for future model evaluation.

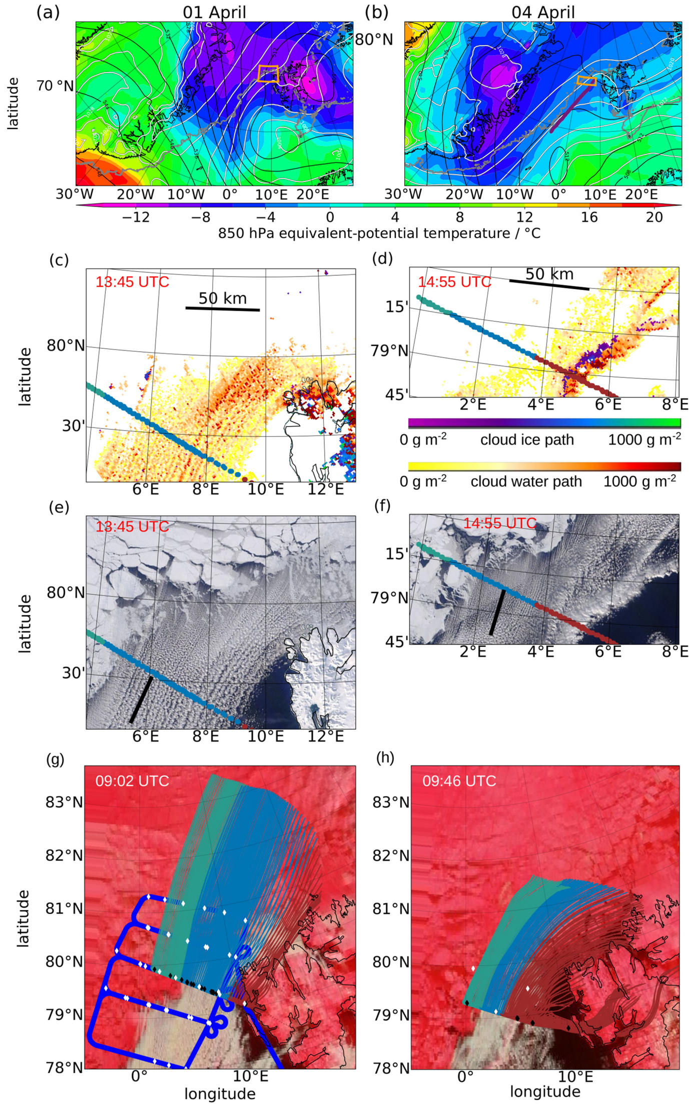

Figure 4.1: Overview of 1 (left) and 4 April 2022 (right). **(a, b)** Maps of mean sea level pressure (white contours), 500 hPa geopotential height (black contours), and 850 hPa equivalent potential temperature (shading) from ERA5 at 12:00 UTC with 15 % sea ice concentration (gray dots), the flight area (orange) shown in **(c)–(h)**, and the convergence line (purple) on 4 April. **(c, d)** Total cloud water path (NASA Worldview, 2023a; 1 km resolution) and **(e, f)** corrected reflectance (NASA Worldview, 2023c; 500 m resolution) of MODIS Terra on 1 April (13:45 UTC) and 4 April (14:15 UTC). Thick colored dots show the *P5* track, categorized by the measurement regime (Table 4.1). Black lines represent the orientation of the cloud streets. **(g, h)** Near-surface back trajectories for 12 h for the *P5* measurement locations (colored lines), dropsonde locations (diamonds) of *P5* (black) and *HALO* (white), and the flight path of *HALO* on 1 April 2022 (blue line). Background image from the Visible Infrared Imaging Radiometer Suite (VIIRS) (NASA Worldview, 2023b) at 09:02 UTC on 1 April and 09:46 UTC on 4 April.

4.2 DATA

Airborne measurements from the HALO-(AC)^3 campaign (Wendisch et al., 2021) manifest the backbone of this study. During this campaign, the *High Altitude and Long Range Research Aircraft* (*HALO*; Ziereis and Gläßer, 2006), the research aircraft *Polar 5* (*P5*), and the research aircraft *Polar 6* (*P6*; Wesche et al., 2016) operated in the North Atlantic sector of the Arctic at altitudes of around 10 km, 3 km, and below 3 km, respectively. This analysis mostly focuses on radar, radiometer, lidar, and dropsonde measurements from *P5* that probed MCAO events in their early phase. Dropsonde measurements from *HALO* and in situ observations from *P6* further support the analyses. We limit the analyses to measurements taken over the ocean and restrict the remote sensing measurements to straight flight segments that exceed a flight altitude of 2 km to observe clouds from aloft. The focus is on two *P5* flights, namely on 1 April 2022 (Fig. 4.1a) and 4 April 2022 (Fig. 4.1b). To investigate roll circulation, the flight paths crossed the cloud streets perpendicularly. *P5* probed along the same path going back and forth, yielding six legs on 1 April (09:08–14:20 UTC) and four legs on 4 April (10:06–14:22 UTC).

4.2.1 *Synoptic overview of cases*

On 1 and 4 April, the large-scale constellation of a high-pressure system over Greenland and a low-pressure system over Siberia led to advection of cold air from the central Arctic over the open ocean (Fig. 4.1a, b) and to cloud street formation (Fig. 4.1e, f). On 1 April, the center of the cold air at 850 hPa was located over Svalbard. A local near-surface low-pressure system southwest of Svalbard resulted in a near-surface northeasterly flow. With height, the flow turned northerly as indicated by the 500 hPa geopotential (Fig. 4.1a). On 4 April, contrarily, the cold air at 850 hPa height was shifted more to the west, and the flow at all heights aligned parallel to the sea ice edge over the Fram Strait (Fig. 4.1b). The easterly flow forced air to ascend over Svalbard, thereby causing a lee effect. Therefore, a larger cloud-free region west of the island appeared, and a convergence line parallel to the ice edge at the transition to the cloudy regime formed (Fig. 4.1f). However, note that the flow within our study area might deviate from the large-scale condition. On both days, the MCAO index was stronger than the 75th percentile of the climatology from 1979 to 2022 (Walbröl et al., 2024). While the synoptic conditions are similar for both cases, differences in flow directions led to different MCAO strengths which in turn precondition the evolution over water.

4.2.2 *Airborne instrumentation*

4.2.2.1 *Dropsondes*

Vaisala RD94 dropsondes were launched from *P5* and *HALO*. From *P5*, 18 and 14 sondes were launched on 1 and 4 April, respectively. They provide vertical profiles of potential temperature (θ; accuracy of 0.2 K), relative humidity (2 %), pressure (0.4 hPa), and horizontal wind components derived from GPS recordings (George et al., 2021; Vaisala, 2010).

4.2.2.2 *Airborne Mobile Aerosol Lidar (AMALi)*

The AMALi instrument on board *P5* measures profiles of backscattered intensities at 532 nm (parallel and perpendicular polarized) and 355 nm (not polarized; Stachlewska et al., 2010). The lidar measurements are processed with a vertical resolution of 7.5 m and temporal resolution of 1 s. Lidar backscatter is highly sensitive to hydrometeors, especially to liquid, which, in our case, is always supercooled. Cloud top height (CTH) is obtained for every profile that has consecutive heights with backscatter coefficients exceeding one of cloud-free sections by a factor of 5. The CTH is the maximum altitude of these consecutive heights. Further details can be found in Mech et al. (2022) and Schirmacher et al. (2023).

4.2.2.3 *Microwave Radar/radiometer for Arctic Clouds (MiRAC)*

The active component of the downward-looking airborne MiRAC (Mech et al., 2019) on board *P5* consists of a frequency-modulated continuous-wave (FMCW) radar that operates at 94 GHz. Additionally, a passive channel at 89 GHz accompanies the active measurements. Both measurements are taken at a 25° backward inclination. While the vertically resolved radar measurements are reconstructed to nadir measurements, the passive measurements are taken on a slanted path. MiRAC measures every second, corresponding to a horizontal resolution of the equivalent radar reflectivity (Z_e) of about 85 m at the ground in the flight direction for typical cruise altitudes of 3 km height and ground speeds of $80\,\mathrm{m\,s^{-1}}$. The radar measurements are quality-controlled and corrected for surface clutter and aircraft attitude (Mech et al., 2019). Sensitivity and the vertical resolution of the cloud radar depend on the chirp settings. During HALO-(AC)^3, the detection limit for the most distant ranges from *P5* of 3 km was around -45 dBZ and the vertical resolution was 4.5 m close to the aircraft and at most 13.5 m (Mech et al., 2022). The processing interpolated the vertical resolution to 5 m over the whole profile. A blind zone of 150 m above ground is omitted due to ground clutter (Schirmacher et al., 2023). The accuracy of Z_e is about 0.5 dBZ. Attenuation by water vapor (< 1 dBZ) and clouds (~ 0.6 dBZ) can potentially reduce this accuracy (Schirmacher et al., 2023).

The cloud top height is also derived from the radar profiles and corresponds to the height of the uppermost radar reflectivity signal above the noise level. Comparing this height with CTH derived from lidar allows us to assess the supercooled liquid layer thickness (LLT). Here, we exploit the fact that the lidar is more sensitive to the particle amount (liquid), whereas the radar is more sensitive to the particle size, i.e., ice particles (Ruiz-Donoso et al., 2020). Due to the limited vertical resolution of the instruments and resulting uncertainties in CTH, the CTH of the lidar has to exceed the CTH of the radar by at least 10 m for a profile to be defined as liquid topped and thus mixed-phase. For the calculation of the hydrometeor depth (D), we take the difference between the lidar CTH and the lowest radar signal within a continuous cloud layer. However, if a minor gap in the cloud profile occurs (i.e., the vertical distance between two layers is smaller than 50 m), we define only one layer from the lower cloud bottom to the upper cloud top.

We define profiles containing a Z_e value higher than -5 dBZ (Schirmacher et al., 2023) in the lowest 500 m (Shupe et al., 2008b) as precipitating. Using the Z_e–S relation for three bullet rosettes (Kulie and Bennartz, 2009), this value corresponds to a snowfall rate (S) of $0.07\,\mathrm{mm\,h^{-1}}$. This relation is also used to analyze S close to the ground at 150 m. Note that these S estimates are inaccurate since Z_e–S relations highly depend on ice habits, which are very variable within cloud streets (Maherndl et al., 2023; Moser et al., 2023).

The passive channel observes the brightness temperature (TB), which is primarily influenced by the emission of liquid clouds and the surface. Differences in TB between clear-sky and cloudy situations are used to retrieve LWP over the ocean via a regression approach (Ruiz-Donoso et al., 2020). Due to the unknown emissivity of sea ice, LWP is only derived over open ocean. Depending on atmospheric conditions, the maximum uncertainty is below $30\,\mathrm{g\,m^{-2}}$ (Ruiz-Donoso et al., 2020). While radar reflectivities are corrected to nadir profiles, TB and, thus, LWP measurements are measured along a slanted path (Mech et al., 2022). Due to the strong attenuation of the lidar backscatter close to the cloud top, we assume that most liquid resides in the uppermost few hundred meters of the cloud, which is in accordance with Shupe et al. (2008b). Therefore, LWP lags behind the radar observations in time. Based on geometric considerations, we shift the LWP measurements, assuming a daily average CTH for cloud streets. Since this average differs for both days, we shift the LWP measurements by different time periods, i.e., 16 and 19 s on 1 and 4 April, respectively, which results in an estimated maximum error of 4 s. As a result, a good agreement between LWP peaks and profiles of high Z_e is observed.

4.2.2.4 *In situ probes*

P6 was equipped with three in situ probes, namely the Cloud Droplet Probe (CDP; Lance et al., 2010), Cloud Imaging Probe (CIP; Baumgardner et al., 2011), and Precipitation Imaging Probe (PIP; Baumgardner et al., 2011). The CDP is a forward-scattering optical spectrometer that measures small cloud particles (2.8–50 µm). Larger cloud particles are observed by the CIP (15–960 µm) and PIP (103 µm–6.4 mm), which record shadow images of the cloud particles as particles pass through the sampling area (Moser et al., 2023). Rimed mass is calculated from images of the fractal particle shapes, as well as the continuous particle size distribution derived from combining CDP, CIP, and PIP observations. CIP and PIP data are processed similarly to those from previous campaigns (Mech et al., 2022).

4.2.2.5 *Collocation*

On both days, *P5* (remote sensing) and *P6* (in situ) were closely collocated. In the riming analyses, we use a data subset during which both aircraft flew on straight paths with a time difference between the collocated measurements of less than 5 min, a spatial distance between both platforms below 5 km, and a flight altitude of *P6* between 0.15 and 1.3 km. Thereby, we reduce the error caused by sampling different air masses with *P5* and *P6* and caused by sampling air masses with varying microphysical properties due to changing *P6* locations within the cloud vertical extent. On 1 April, 3971 s of collocated observations covers longitudes between 4.5 and 6.5° E, corresponding to 25–165 km of fetch. On 4 April, only 845 s of observations is collocated, located between 1.5 and 4.5° E and covering fetches between 55 and 165 km and mostly at around 80 km. On 1 April, seven collocated data segments exist with gaps of less than 5 s. These segments cover 39 min at a fetch of 60–140 km, with most measurements concentrated around 7° E.

4.2.3 *Satellite and reanalysis data*

For the sea ice concentration (SIC), we use a daily product that merges satellite observations from MODIS and the second Advanced Microwave Scanning Radiometer (AMSR2) at 1 km horizontal resolution (Ludwig et al., 2020). For the analysis, we interpolate the data to a $0.05° \times 0.05°$ latitude–longitude grid. The sea surface temperature (SST) is obtained from the Arctic Ocean – Sea and Ice Surface Temperature product based on observations from the Metop-A Advanced Very High Resolution Radiometer (AVHRR). The daily product (Copernicus Marine Service, 2023) has a spatial resolution of 0.05° and covers surface temperatures of the ocean, sea ice, and the MIZ. Using satellite SST and dropsonde temperature measurements over open water (Fig. 4.1g, h, black and white dots), we calculate the MCAO index from the difference between the potential temperature (θ) at the sea surface and 850 hPa altitude. Generally, the MCAO index is positive during a MCAO and describes its strength (Kolstad, 2017; Papritz et al., 2015). Over the ocean, we use the Coupled Ocean–Atmosphere Response Experiment (COARE) bulk air–sea flux algorithm (Fairall et al., 2003) to additionally calculate surface heat fluxes from satellite SST data and dropsonde observations at 10 m height.

The European Centre for Medium-Range Weather Forecasts (ECMWF) reanalysis product version 5 (ERA5; Hersbach et al., 2020) is used to analyze the large-scale environmental conditions and to compute back trajectories using Lagranto (Sprenger and Wernli, 2015). ERA5's temporal, horizontal, and vertical resolution is 1 h, 31 km, and 137 model levels from the surface up to the top of the atmosphere, respectively (Kirbus et al., 2024). Note that most *HALO* dropsondes have been assimilated into ERA5, leading to improved performance for our study cases.

4.3 ANALYSIS AND IDENTIFICATION APPROACHES

In the following, we describe two approaches we established for analyzing the airborne measurements: first, the quantification of fetch assigned to each measurement (Sect. 4.3.1) and, second, a novel method to identify roll circulation from airborne radar reflectivities only (Sect. 4.3.2).

4.3.1 *Trajectory calculations and fetch*

During MCAOs, the warm ocean alters thermodynamic ABL conditions of air masses initially formed in the central Arctic through turbulent surface heat and moisture fluxes (e.g., Brümmer, 1996) whenever SIC is below 100 %. We aim to quantify this influence of open water on ABL development. Since it is impossible to calculate integrated surface fluxes along the trajectories with our data, we derive the fetch for each airborne measurement. We follow Spensberger and Spengler (2021) and account for open water over the MIZ as well as leads in the ice. For flows unaffected by land masses, travel time over open water and fetch can be linearly converted and are both valid to study. The correlation coefficient between travel time and fetch is 0.99 for all $P5$ measurements that are not influenced by land masses and -0.5 for measurements influenced by Svalbard. Thus, the latter data have been removed from the analysis (see below).

We need to know the air masses' previous path to calculate fetch for each measurement. Therefore, we compute near-surface Lagrangian back trajectories using Lagranto (Sprenger and Wernli, 2015) with ERA5 wind fields as input. Specifically, we calculate back trajecto-

Table 4.1: Categorization of $P5$ airborne data.

Day	Description	Color	Location
1 April	influence by Svalbard	red	longitude $> 9.08°$ E
1 April	prior to cloud streets	green	fetch < 15 km
1 April	cloud streets	blue	remaining data
4 April	influence by Svalbard and convergence line	red	longitude $> 3.7°$ E
4 April	prior to cloud streets	green	longitude $< 1.7°$ E
4 April	cloud streets	blue	remaining data

ries for the previous 12 h for every flight minute and assign them to the observations within each minute. The trajectories originate from the horizontal location of $P5$ and 1000 hPa height, corresponding to roughly 300 m above the surface. To investigate the influence of the surface on the air masses, we take a near-surface starting point for the trajectories. Similar to Spensberger and Spengler (2021), we calculate the fetch for every back trajectory by integrating the ratio of open water obtained from MODIS–AMSR2 SIC data (Sect. 4.2.3) along the back-trajectory paths over the previous 12 h until measurement time (0 h):

$$\text{fetch} = \int_{s(12\,h)}^{s(0\,h)} (1 - \text{SIC}(s))\text{d}s. \tag{4.1}$$

Note that due to the resolution of ERA, neighboring trajectories are rather similar (Fig. 4.1g, h). Differences in fetches between two neighboring trajectories mainly come from differences in SIC along the trajectories. The median of the relative change between two adjacent fetches is 9.6 %.

To focus on cloud street characteristics during MCAO conditions, we limit the analysis to air masses that did not pass Svalbard at any time and that are not affected by the convergence line on 4 April (Table 4.1; Fig. 4.1c–h, non-red dots). The remaining measurements are classified as either "cloud streets" (Fig. 4.1c–h, blue) if radar reflectivities appear regularly or else as "prior to cloud streets" (Fig. 4.1c–h, green). The latter category includes samples taken over and close to sea ice that have fetches less than 15 km on 1 April and longitudes smaller than 1.7° E on 4 April (fetches of about 17 km; Table 4.1). On 4 April, longitude instead of fetch is used for classification as cloud streets over open ocean and cloud-free conditions over sea ice both have fetches of 17 km. Note that fetch includes contributions from the MIZ ($80\,\% < \text{SIC} < 100\,\%$) and open water.

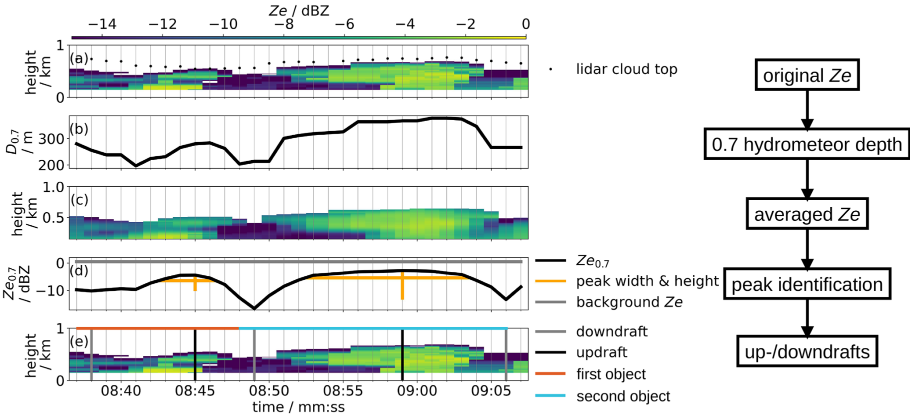

Figure 4.2: Visualization of roll cloud circulation identification. Time series (30 s) of the equivalent radar reflectivity Z_e profiles measured by MiRAC starting at 10:08:37 UTC on 1 April **(a)**, 0.7 of the hydrometeor depth ($D_{0.7}$, **b**), Z_e smoothed in space and time **(c)**, and smoothed Z_e at $D_{0.7}$ (**d**, black) with its peak width and height (**d**, orange) and the background Z_e (**d**, gray). The original Z_e observations (same as in **a**), detected up- (black) and downdrafts (gray), and circulation objects (blue, red) are shown in **(e)**. For comparison, cloud top height observed by the AMALi lidar is displayed (**a**, black dots). The shown time period covers fetches from 73 to 80 km and corresponds to a flight distance of 7 km.

4.3.2 *Roll circulation identification*

To identify roll circulation from radar measurements, we must rely on indirect information. Previous studies applied spectral analyses to observations of the three wind components, temperature, mixing ratio, and radiative fluxes (Brümmer et al., 1985; Brümmer, 1999; Brümmer et al., 1992; Walter and Overland, 1984). While vertical velocity cannot be extracted from the airborne Doppler measurements (Mech et al., 2022), we exploit the fact that cloud particles form to the largest extent at the location of the strongest updraft due to vertical motion. Here, frequent saturation with respect to ice occurs, facilitating the formation of cloud droplets and growth of both liquid and ice particles (Korolev and Field, 2008). In order to account for potential influences by dry entrainment at the cloud top (Klingebiel et al., 2015) or occurrence of precipitation (Morrison et al., 2012), we only consider measurements at the height of 0.7 of the hydrometeor depth (D; Sect. 4.2.2) for the identification of roll circulation. By using the radar reflectivity at this height ($Z_{e_{0.7}}$), we target the largest ice particles within the profile and minimize the influence of dry-air entrainment and supercooled liquid water droplets at the cloud top as well as precipitation at the bottom of D. We refer the reader to Appendix 4.6 for further discussion on the height selection, including a sensitivity analysis.

$Z_{e_{0.7}}$ serves as a proxy for vertical velocity. We assume that maxima in $Z_{e_{0.7}}$ represent updraft regions, while minima in $Z_{e_{0.7}}$ represent

Table 4.2: Conditions during 1 and 4 April. BLH and CTH stand for atmospheric boundary layer height, i.e., the inversion height of potential temperature, and cloud top height, respectively.

Parameter	Source	1 April	4 April
MCAO index	dropsondes	8.6 K	4.6 K
Cloud street orientation	MODIS	10° N	5° N
Cloud street wavelength	MODIS	2 km	1 km
Temperature at cloud top	dropsondes	< -20 °C	-20 to -10 °C
Median CTH of cloud streets	radar	700 m	300 m
Interquartile range of CTH of cloud streets	radar	530–790 m	250–375 m
BLH trend	dropsondes	$4.5\,\mathrm{m\,km^{-1}}$	$2.9\,\mathrm{m\,km^{-1}}$
Mixing ratio trend within 100 km fetch	dropsondes	< doubling	> doubling
Driver of wind shear	dropsondes	wind direction	wind speed
Cloud street profiles with precipitation	radar	67 %	35 %
Cloud street profiles with liquid-topped clouds	radar and lidar	86 %	71 %

downdraft regions of the roll circulation. For cloud-free areas, we define the downdraft in the area's center. The workflow of the circulation detection is summarized in Fig. 4.2. Appendix 4.6 further summarizes details, including Table 4.3 for a sensitivity analysis. Among different configurations, we selected the detection algorithm with the best ratio between determining peaks and ignoring noise. This automated peak detection depends only on the large-scale condition and, thus, might not determine every maximum of $Z_{e_{0.7}}$ considered by the human eye.

We only apply the detection algorithm to the cloud street regime as roll convection is invisible to the radar as long as no significant number of hydrometeors is present. According to our definition, the maximum updraft (maximum $Z_{e_{0.7}}$) is not necessarily centered between the two detected edges of our roll circulation object. The wavelength of the circulation λ is the distance between two identified adjacent downdrafts. The mesoscale circulation is described by the aspect ratio (AR), which is the ratio between λ and the CTH at the updraft position. In total, we identified 356 and 112 cloud circulation objects in the cloud street regime on 1 and 4 April, respectively.

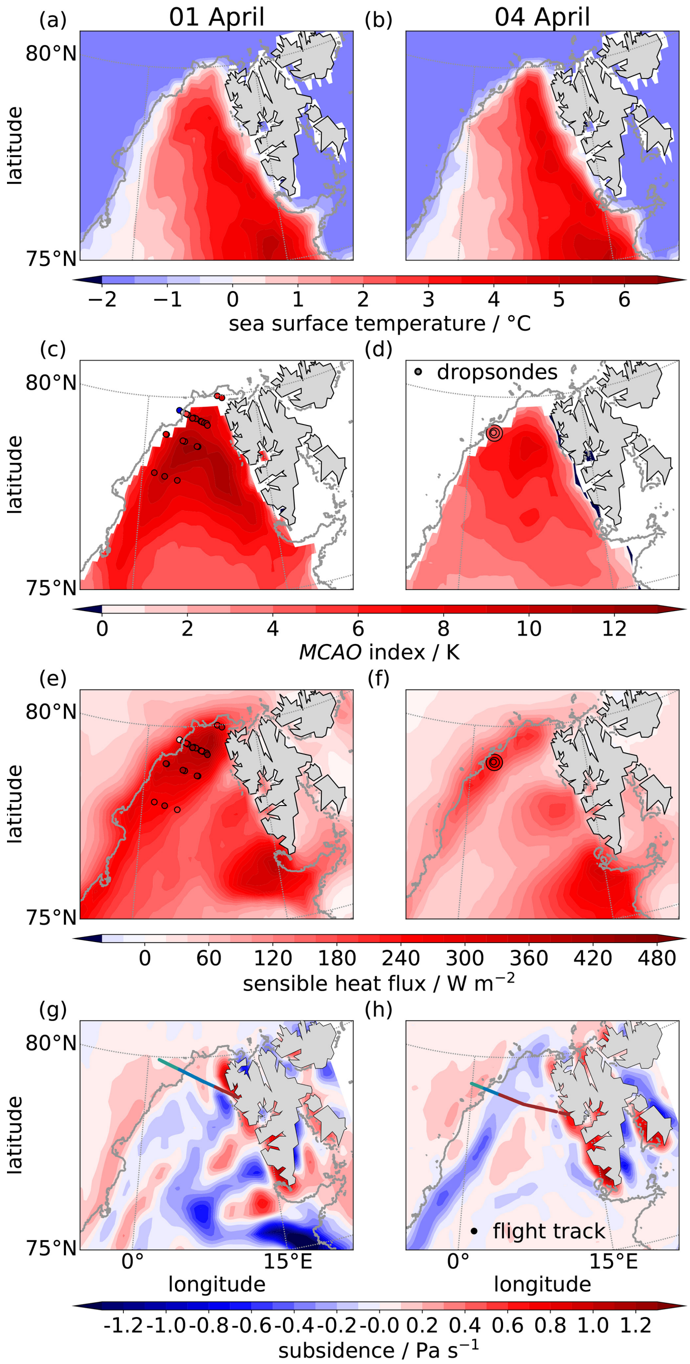

Figure 4.3: Overview of environmental conditions on 1 April (left) and 4 April (right). Maps of sea surface temperature **(a, b)**, the MCAO index **(c, d)**, sensible heat fluxes **(e, f)**, and subsidence at 925 **(g)** and 975 hPa **(h)** from ERA5 reanalysis data. Positive subsidence values indicate downward motion. MCAO indices **(c, d)** and sensible heat fluxes **(e, f)** from dropsonde observations are shown as circles. Flight tracks in **(g)** and **(h)** are color-coded according to the measurement categorization (Table 4.1). The gray lines indicate the 15 % sea ice concentration from ERA5.

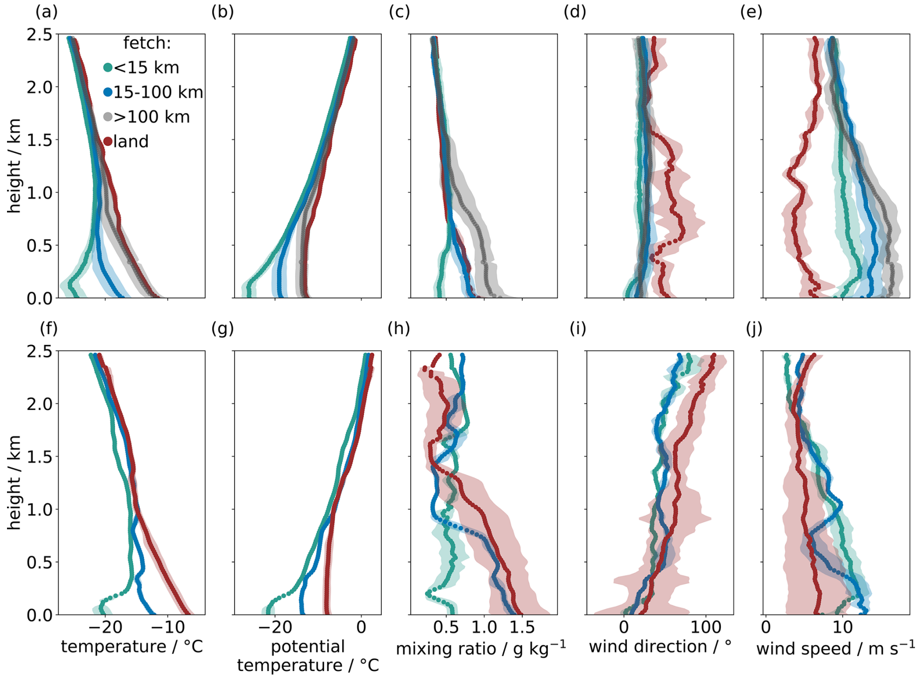

Figure 4.4: Averaged dropsonde profiles from *HALO* and *P5* of temperature **(a, f)**, potential temperature **(b, g)**, mixing ratio **(c, h)**, wind direction **(d, i)**, and speed **(e, j)** binned by fetch on 1 April (first row) and 4 April 2022 (second row). The shaded areas represent the standard deviation of each category. The color coding follows the categorization shown in Table 4.1. On 1 April, the number of dropsondes per category is 27 (< 15 km fetch; green), 14 (15–100 km and > 100 km fetch; dark and light blue), and 3 (land; red). On 4 April, the number is 3, 4, and 9, respectively.

4.4 VARIABILITY IN THERMODYNAMIC CONDITIONS AND CLOUD STREET PROPERTIES

In the following, we first investigate the boundary layer conditions (Sect. 4.4.1) and the preconditioning by riming (Sect. 4.4.2). We then statistically analyze cloud morphological and microphysical properties within the roll circulation object within the cloud street regime (Sect. 4.4.3), followed by an assessment of cloud and precipitation properties as a function of fetch within the first 170 km (4 h) of the MCAO development (Sect. 4.4.4).

4.4.1 *ABL conditioning*

First, we investigate how much the ABL conditions differ between the cases, including possible drivers. The influence of the ocean on the ABL through surface sensible and latent heat fluxes is more pronounced on 1 than 4 April (Fig. 4.3e, f). Dropsondes show maxima of 450 (225) W m^{-2} for sensible (latent) heat fluxes, respectively. Over the MIZ, fluxes decrease, and the ratio changes to a higher contribution of the sensible heat flux due to less evaporation over sea ice as also found by Li et al. (2020). Along the whole flight track, ERA5 shows that the sensible heat flux decreases much faster with distance from the sea ice edge on 4 than 1 April (Fig. 4.3e, f), even though oceanic conditions here represented by SST are similar (Fig. 4.3a, b). This indicates that the atmospheric conditions differ between the cases, which is especially confirmed for temperature by differences in MCAO fields (Fig. 4.3c, d). The MCAO index averaged over all dropsondes launched from *P5* is stronger on 1 than 4 April (8.6 K versus 4.6 K, Table 4.2). Note that although dropsondes were launched further away from sea ice on 1 April, ERA5 fields show roughly the same differences of a factor of 2 over both flight tracks. In accordance with Seethala et al. (2021), fluxes and MCAO indices from ERA5 generally correspond to dropsonde estimates, except over sea ice, where ERA5 seems to overestimate the fluxes. Finer spatial structures in both parameters are resolved in the dropsondes.

Cloud conditions on 1 April are characterized by cloud streets oriented by about 10° to the north (Fig. 4.1e, black line) and a wavelength of about 2 km with shorter distances between the separated streets close to sea ice. Note that this information is retrieved from MODIS sensors (bands 1, 3, and 4) that have a spatial resolution of at least 500 m. At the height of the median CTH, here 925 hPa, air subsides within the regimes of prior to cloud streets and cloud streets, respectively (Fig. 4.3g, green and blue track). Over the ocean, subsidence is generally reduced compared to over sea ice. The area of fetches between 75 and 120 km around 7° E is characterized by strong subsidence (Fig. 4.3a, c) throughout the entire atmospheric column (not shown) despite increasing SST and MCAO indices. This wave-like pattern is likely induced by wave effects originating from the Svalbard archipelago (Shestakova et al., 2022).

The thermodynamic state of the ABL is described by mean profiles of dropsondes released from *P5* and *HALO* over sea ice and open water. On 1 April, temperatures are lower than −20 °C throughout all altitudes over sea ice (fetch of < 15 km) and for parts over open water (Fig. 4.4a). Over sea ice, surface layers generally develop an inversion as air is cooled from the ground and warmed by subsidence from above. Profiles that were sampled by *HALO* dropsondes over sea ice exhibit a thin (< 250 m deep) ABL. Close to the sea ice edge, the depth of the ABL is similar to conditions over closed sea ice (Fig. 4.4b). The ABL is capped by a low-level jet at 250 m height (Fig. 4.4e) and has a low water vapor mixing ratio (0.5 g kg^{-1}; Fig. 4.4c). The mixing ratio indicates the low background vapor concentration of the polar air mass. With 28°, wind direction is constant with height, while the near-surface wind originates from 0° N regardless of surface properties (Fig. 4.4d). Over open water, temperatures and, thus, wind speeds within the neutrally stratified ABL increase with fetch. The boundary

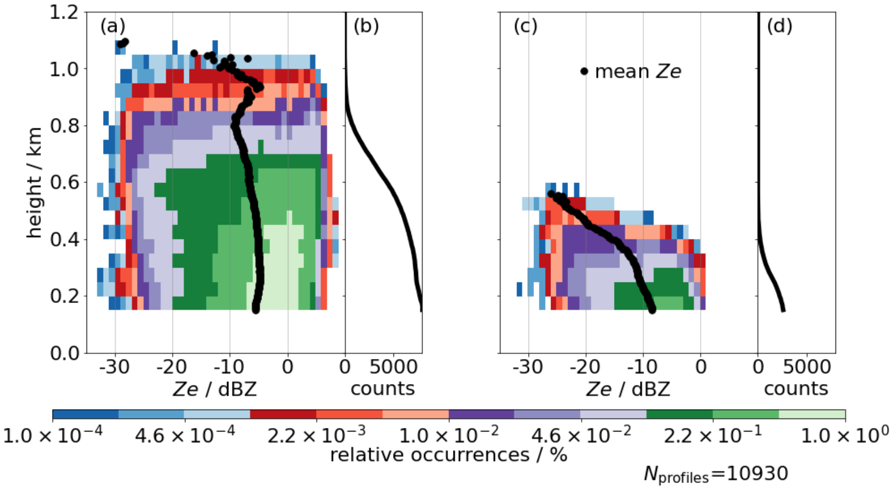

Figure 4.5: Contoured frequency by altitude diagram **(a, c)** and absolute counts per altitude **(b, d)** for all radar reflectivities (Z_e) obtained by MiRAC in the cloud street regime on 1 April **(a, b)** and 4 April **(c, d)**. Moreover, each averaged Z_e profile (black dots) and the total number of profiles ($N_{profiles}$) are displayed.

layer height (BLH), which is the inversion height of the potential temperature θ, doubles within the first 100 km (Fig. 4.4b). Mixing ratio increases with fetch due to strong surface heat fluxes and turbulent mixing of near-surface air.

On 4 April, the MODIS image shows cloud streets with an orientation of 5° to the north (Fig. 4.1f, black line) and a wavelength of about 1 km. Compared to conditions on 1 April, the air mass at CTH (975 hPa) ascends for fetches larger than 60 km (Fig. 4.3h). A wave effect is notable within the region affected by the lee effect but not for the analyzed data west of the convergence line. Warmer temperatures on 4 April reveal a difference in air mass between both days: all temperatures below 2 km height range within -20 to $-10\,°C$ (Fig. 4.4f). Free-tropospheric θ is higher by about 5 K on average compared to 1 April (Fig. 4.4b, g). Furthermore, mixing ratio of the polar air mass is slightly higher at all heights (Fig. 4.4c, h). Flow conditions differ compared to 1 April, even though a low-level jet also exists at 200 m over sea ice (Fig. 4.4j). A directional shear from northerly winds at the surface to westerly winds occurs at all heights and is strongest at the BLH (Fig. 4.4i). Although *HALO* dropsondes cannot detect a BLH in the central Arctic (81.3–87.0° N) as it is likely too shallow (not shown), the capping inversion is stronger over the sea ice close to its edge. On 4 April, this inversion weakens less with fetch compared to 1 April due to a layer of warm air above the BLH. Together with surface fluxes about half as high as those of ERA5 on 4 April (Fig. 4.3e, f), this results in a much weaker BLH increase rate averaged over all fetches (Table 4.2) and a reduction in wind speeds by $5\,\mathrm{m\,s^{-1}}$.

On both days, the radar profiles in the cloud street regime frequently (93 %) exhibit clouds. The diagrams of contoured frequency by altitude (Fig. 4.5) reveal the different cloud and precipitation characteristics of cloud streets between the days. CTH is twice as high on 1 as on 4 April, respectively. Furthermore, mean Z_e (black dots) is higher at all heights. On 1 April, values larger than -5 dBZ associated with the onset of snowfall occur at all heights. The shorter the fetch on 1 April, the stronger the decrease in the mean Z_e profile close to the surface (not shown). Thus, near-surface ice particles might experience stronger sublimation on 1 April when the mixing ratio is comparably small, and the relative humidity with respect to ice is below 100 % (not shown). On 4 April, Z_e rarely exceeds -5 dBZ even below 500 m, reducing the frequency of precipitation compared to 1 April (Table 4.2). Moreover, mean Z_e increases towards the surface, indicating the ongoing growth process of ice particles. On both days, most cloud streets are liquid topped (Table 4.2). Liquid-topped cloud streets are mainly characterized by a higher CTH compared to non-liquid-topped clouds (not shown).

In summary, the MCAO case on 1 April is stronger by a factor of 2 than that on 4 April due to colder and drier air masses (Table 4.2). Wind shear occurs during wind speed changes on 1 April and directional changes on 4 April, respectively. Contradicting the MCAO index, air subsides close to the surface in the cloud street regime at fetches around 100 km on 1 April due to a wave effect caused by Svalbard.

4.4.2 *Preconditioning by riming*

Ice growth affects the boundary layer evolution during MCAOs in several ways, e.g., by reducing cloud liquid water and triggering early and light precipitation, which then in turn cools and moistens the air below the cloud (Tornow et al., 2021). We evaluate the strength and variability in riming to investigate whether riming preconditions cloud microphysics and whether it impacts precipitation characteristics already in the initial state of MCAO evolution. We use a subset of in situ and remote sensing data during which *P5* and *P6* were collocated within the cloud street regime (Sect. 4.2). To determine the degree of riming, we calculate the normalized rime mass (M) defined as the rime mass divided by the mass of the size-equivalent spherical graupel particle. Following Maherndl et al. (2024a), two methods are applied. The combined method uses the closure of in situ particle size distributions and Z_e simulations obtained from running averages of in situ particle size distributions over 30 s. The in situ method relates M to in situ particle shape measurements only. The results of both retrievals are comparable. However, since the collocation of *P5* and *P6* measurements might be inaccurate, we only show results from

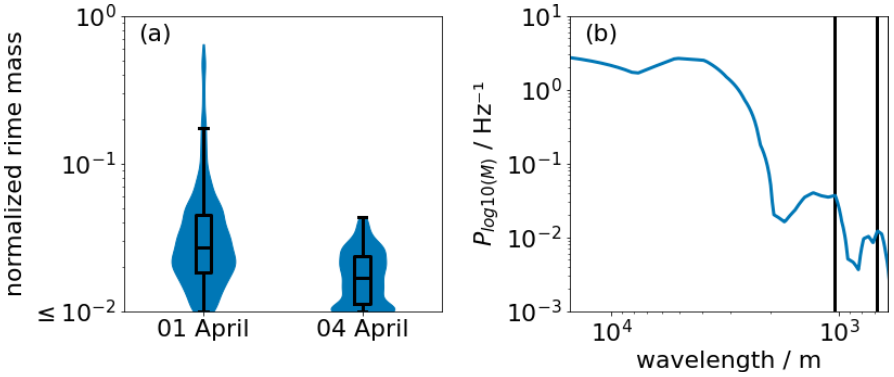

Figure 4.6: **(a)** Violin and box plot of the normalized rime mass (M) obtained by the in situ method for collocated cloud street flight data on 1 and 4 April. **(b)** Corresponding power spectrum of M on 1 April with black lines marking important local maxima of the spectrum.

the in situ method for which no matching is necessary. Note that our definition of updrafts might bias the following findings.

Considering particles with $M > 10^{-2}$ as rimed, more rimed particles exist on 1 April (97 %) than on 4 April (80 %), respectively. The median M of $10^{-1.6}$ on 1 April and $10^{-1.8}$ on 4 April (Fig. 4.6a) clearly reveals that riming is only significantly active in cloud streets on 1 April. In particular, normalized rime masses of $M > 10^{-1}$ only exist on 1 April. On this day, cloud top temperatures are colder than or at the low end of temperatures within the dendritic growth zone (DGZ; -20 to -10 °C). Hence, conditions are too cold for aggregation to be dominant (Chellini et al., 2022). On 4 April, contrarily, riming is not significant because cloud top temperatures lie within the DGZ, fostering aggregation.

The spatial variability in riming is investigated by linearly detrended and mean-centered power spectra of M obtained during seven collocated segments (Sect. 4.2). Edge effects are minimized by applying a Hann window for smoothing. Due to the units of variance, the power spectrum increases automatically for smaller wavelengths. The averaged power spectrum of M peaks at about 0.7 and 1.1 km (Fig. 4.6b). These values roughly correspond to the wavelength λ of cloud streets as seen in the MODIS images (Fig. 4.1; also see Sect. 4.4.4 below) and as derived from the roll circulation analyses below. For 1 April, we, hence, infer that riming is mainly present within the updraft regions of cloud streets. A more detailed comparison with λ of the roll circulation detected by the remote sensing measurements is performed in Sect. 4.4.4. We further analyze the effect of active riming, present on 1 April, on cloud microphysics in the following sections.

4.4.3 *Impact of roll circulation on cloud and precipitation properties*

Our measurement strategy across cloud streets allows us to detect individual roll circulation objects (Sect. 4.3.2). For the following statistical assessment, we refer to "clouds" as objects that have at least five successive radar measurements, resulting in 344 and 109 objects on 1 and 4 April, respectively. First, we investigate the location of their updraft center ($Z_{e_{0.7}}$) within the cloud. As explained before, these objects are not necessarily symmetric. However, most clouds form centered around the updraft of the circulation. Around 50 % of the time, maxima of $Z_{e_{0.7}}$ occur within the central tercile of the cloud, and only rarely are they within the tercile closest to the lateral cloud boundary (7 %).

To characterize how dynamics within roll circulations affect cloud and precipitation properties, circulation objects are composited for their relative distance to $Z_{e_{0.7}}$ (Fig. 4.7). More precisely, we group cloud properties into three regions according to their distance from the maximum updraft region ($Z_{e_{0.7}}$): the central updraft region, the region close to a cloud boundary, and the region in between.

On 1 April, the medians of several parameters show consistent behavior, although the variability, expressed by the interquartile distance, is high: CTH increases by 9 % from the cloud boundary to the location of the maximum updraft (Fig. 4.7a). In line with liquid formation within updrafts, LWP increases by 22 % (Fig. 4.7e). The mean of Z_e over each profile (82 %; Fig. 4.7g) and S (42 %; Fig. 4.7i) increases, supporting the assumption of enhanced ice production in updrafts. In contrast, a decrease in LLT (32 %; Fig. 4.7c) of 20 m can be seen, which exceeds the uncertainty of 10 m. We speculate that, here, updrafts carry ice particles to higher cloud regions. If so, the mixed-phase region would expand at the expense of the liquid layer and would enhance riming (Fig. 4.4.2). Potential riming occurrence would increase ice particle size, Z_e, and S in updrafts. The observed slight LWP increase in updrafts (Fig. 4.7e, f) could indicate that, in our study, condensation is more favored than the depletion of liquid.

Strong riming events might explain the frequently high extremes of S. Precipitation events not only intensify at updraft locations but also occur more frequently than at the cloud boundary (87 % compared to 55 % of the profiles, Fig. 4.7). On 1 April, we expect that most ice occurs at 0.6 of the hydrometeor depth for updraft positions as indicated by $Z_{e_{max}}$ (Fig. 4.7k). Large-rimed particles close to the cloud top might lift the height compared to the cloud boundary, where most ice is located within the lowest third of the hydrometeor depth.

On 4 April, the absolute increase in CTH (Fig. 4.7b) and mean Z_e (Fig. 4.7h) within the clouds is about half of that on 1 April. Moreover, S (Fig. 4.7j) and LLT (Fig. 4.7d) stay constant within the clouds. In all three categories, the normalized height at which ice occurrence is

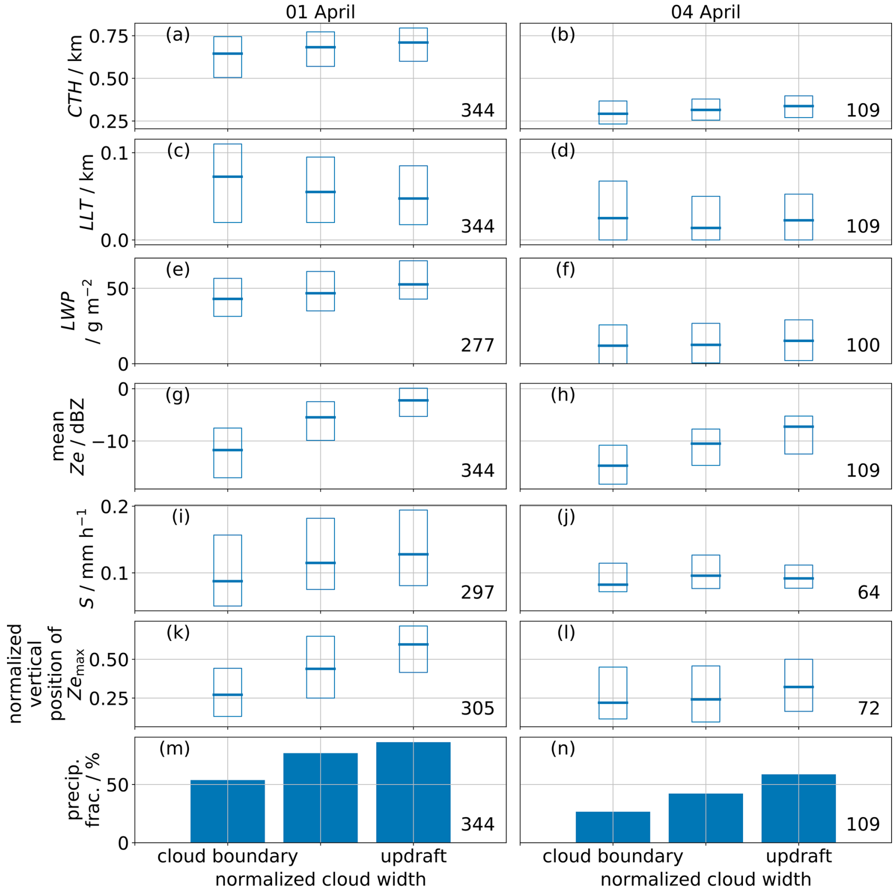

Figure 4.7: Average composites of cloud and precipitation properties within the normalized distance between the lateral cloud boundary and updraft (max $Z_{e_{0.7}}$) for circulation objects within the cloud street regime on 1 April (left column) and 4 April (right column): cloud top height (CTH; **a, b**), supercooled liquid layer thickness (LLT; **c, d**), liquid water path (LWP; **e, f**), mean radar reflectivity (Z_e) over each profile **(g, h)**, snowfall rate at 150 m (S; **i, j**), vertical position of the maximum Z_e for each profile normalized by the hydrometeor depth **(k, l)**, and fraction of precipitating profiles (precip. frac.; **m, n**). The median (horizontal line) and lower and upper quartile (box edges) are displayed at the boundary of the clouds, the updraft position, and in between. The total number of objects is given for every parameter separately.

highest is similar to cloud boundary conditions on 1 April (Fig. 4.7l). The smaller MCAO strength on 4 April seems to weaken the updraft motion and might, thus, suppress the rise in CTH and the lifting of ice into the liquid layer in updrafts. In updrafts, this might prevent riming, likely hampering an increase in S and mean Z_e as well as a lifting of the height level with the highest ice occurrence. While the absolute precipitation fraction is lower than on 1 April, e.g., reduced by 50 % at the cloud boundary, the relative increase in precipitation fraction from the object center to the boundary is similar (30 percentage points).

4.4.4 *Development along fetch*

To investigate how open water affects roll circulation and cloud properties, we analyze their evolution over all observed fetches (Fig. 4.8). The most prominent characteristic of an MCAO event is the rise in BLH driven by the strong heat fluxes as air flows over the relatively warm ocean. Already in the MIZ, evaporation and convection lead to the appearance of initial, still unorganized clouds in the regime of prior to cloud streets, although horizontal cloud cover is low (Fig. 4.8g). Within the cloud street regime, cloud cover increases rapidly and exceeds 90 % for fetches beyond 30 km. The comparison of BLH, derived from dropsondes, and closely located airborne measurements shows that CTH is generally only 8.5 m lower than BLH, which indicates that we can use CTH as a proxy for BLH. On both days, CTH increases steadily with fetch (Fig. 4.8a). Both the median CTH and CTH growth rate are reduced by more than half on 4 April compared to conditions on 1 April. A potential reason for this reduction might be a reduced buoyancy in the ABL, with warm air being advected above the boundary layer. Future modeling experiments could test this hypothesis, including lee effects on air mass development caused by the Svalbard archipelago. Interestingly, on 1 April, the linear increase in CTH levels at around 100 km fetch (2.5 h travel time). This area of fetch corresponds to an area of increased subsidence (see Fig. 4.3), capping cloud development. On 4 April, the CTH, cloud cover, and precipitation fraction decrease rapidly beyond fetches of 140 km. Corresponding trajectories are geographically close to trajectories excluded from the analysis due to land mass influences. We speculate that the Svalbard lee effect gains importance and increasingly suppresses cloud and precipitation formation despite coarse ERA5 subsidence values indicating rising air masses.

Next, we examine the dependency of circulation characteristics within the cloud street regime as function of fetch, specifically wavelength (λ) and aspect ratio (AR). Note that bins of fetch with less than 10 roll circulation objects, e.g., at fetches around 50 km, are removed as outliers from all following analyses of λ and AR (Fig. 4.8c, e). On 1 April, λ increases from roughly 1 to about 2 km at a fetch of 150 km (Fig. 4.8c), approaching the width of the cloud streets seen by MODIS (2 km; Sect. 4.4.1). For fetches larger than 60 km, AR is around 2 and remains rather constant with fetch. As discussed in Sect. 4.4.2 and Fig. 4.6b, the normalized rimed mass M follows a multi-modal power spectrum. Local maxima of 0.7 and 1.1 km, respectively, align with λ, suggesting that riming is enhanced in updraft regions of roll circulation objects. On 4 April, the measurements only revealed reliable circulation information for fetches smaller than 80 km. There, λ does not increase substantially with fetch and aligns with the cloud street width of the MODIS images (1 km; Sect. 4.4.1). Yet, the spread in λ val-

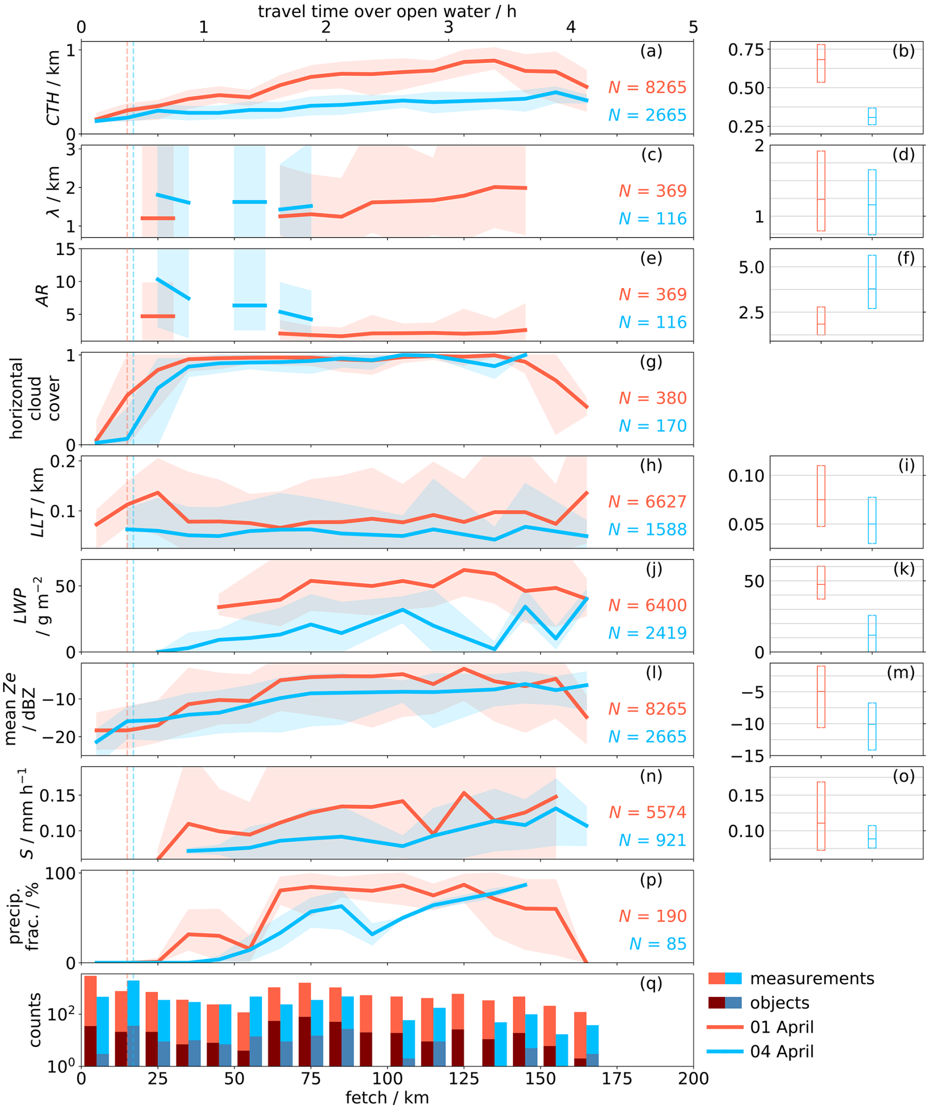

Figure 4.8: The left column shows the development of circulation, cloud, and precipitation characteristics with fetch on 1 (red) and 4 April (blue): cloud top height (CTH; **a, b**), wavelength of the circulation (λ; **c, d**), aspect ratio of the circulation (AR; **e, f**), horizontal cloud cover **(g)**, liquid layer thickness (LLT; **h, i**), liquid water path (LWP; **j, k**), mean radar reflectivity over each profile (mean Z_e; **l, m**), and snowfall rate at 150 m height (S; **n, o**), with precipitation fraction (precip. frac.; **p**) and number of measured profiles (light color) and identified cloud circulations (dark color) per fetch bin **(q)**. LLT, LWP, and S statistics are only calculated when a cloud/precipitation occurs. Lines and shades represent mean values and the 5th and 95th percentile, respectively. The vertical dashed lines indicate the regime change from prior to cloud streets to cloud streets (Sect. 4.3.1). On the right box plots show each distribution's median and interquartile range within the cloud street regime. The total number of measurements (N) is given for each parameter and day.

ues is high as roll convection is comparatively weaker at low fetches. This spread propagates to the derived AR distribution, which is characterized by a large interquartile range from 2.7 to 5.6. Beyond fetches of 60 km, where convection is stronger, variability is lower and AR slightly reduces with fetch. There, observed AR nearly doubles compared to conditions on 1 April. Brown (1972) relates larger AR to reduced available energy for convection. Heat fluxes observed at fetches of 60 km and beyond are indeed reduced on 4 April (Fig. 4.3e, f). In summary, median λ is similar on both days (around 1.2 km; Fig. 4.8d), while CTH on 1 April is increased by a factor of 2 compared to 4 April (Fig. 4.8b). Consequently, median AR on 1 April (Fig. 4.8f) is smaller than on 4 April (1.8 and 3.9, respectively).

We further analyze liquid layer thickness (LLT; Fig. 4.8h), LWP (Fig. 4.8j), mean Z_e (Fig. 4.8l), and S (Fig. 4.8n) to investigate how the exposure to open water influences cloud microphysics. All parameters except for LLT show a slight increase with fetch. Median LWP conditions differ substantially on both days as the median LWP reduces from 50 g m^{-2} on 1 April to 10 g m^{-2} on 4 April, respectively. While LWP ranges within the uncertainty limit of 30 g m^{-2} (see Sect. 4.2.2) for small fetches below 100 km, it steadily increases with fetch and exceeds the uncertainty limit for fetches larger 100 km. The median LLT of 75 (50) m on 1 (4) April points to the dominant presence of liquid-topped mixed-phase clouds. This finding is in agreement with the overall high occurrence of liquid layers of 86 % (71 %) for the respective days (see Table 4.2). We attribute the constant LLT with fetch to the fact that both liquid (LWP) and ice (approximated by mean Z_e) increase simultaneously, in turn keeping the LLT constant.

While the evolution of cloud microphysics with fetch is similar on both days, thermodynamic conditions modify the intensity of the parameters. On 4 April, characterized by overall warmer temperatures, clouds are more shallow. On this day, 90 % of the profiles containing liquid-topped cloud streets have an LLT of smaller than 100 m, which is more than on 1 April (70 %). Less supercooled liquid may reduce the number of liquid-topped cloud profiles (Table 4.2), LWP (Fig. 4.8k), and LLT (Fig. 4.8i). A potential mechanism could be that the warmer temperature, low amount of supercooled liquid, and weak MCAO index prevent riming, reducing snowfall rate and mean Z_e. This could potentially explain why snowfall occurs less frequently on 4 April. Moreover, the lack of riming in updrafts would reduce the variability in snowfall rate within each fetch bin. Lacking preconditioning by riming might delay the precipitation onset on 4 April by more than 10 km (Fig. 4.8p), which starts forming at fetches of 26 and 39 km on 1 and 4 April, respectively.

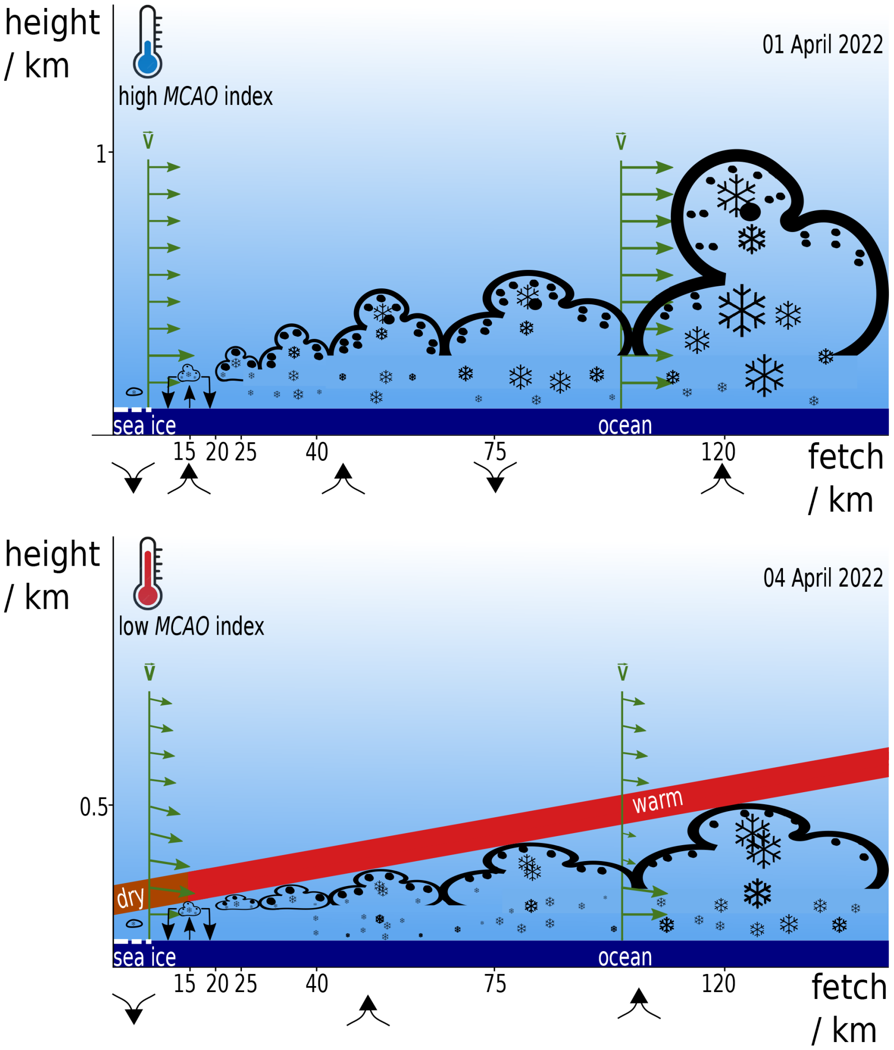

Figure 4.9: Sketch of the development of the roll circulation and microphysics of the associated cloud streets with fetch on 1 April (top) and 4 April (bottom). The arrows on the bottom indicate the direction of the near-surface vertical motion.

4.5 CONCLUSIONS

Our study investigates the evolution of thermodynamics, cloud and circulation morphology, cloud microphysics, and precipitation within air masses developing the first 170 km fetch (about 4 h of travel time) in a long-lasting cold-air outbreak in the Fram Strait. Airborne remote sensing and in situ observations were performed as part of the HALO-(AC)^3 campaign within two research flights just 3 d apart. A unique sampling strategy oriented perpendicularly to cloud streets provided the opportunity to statistically quantify finely resolved macro- and microphysical cloud and circulation properties in the initial MCAO phase. Specifically, two metrics were developed for this purpose. First, we make use of a novel approach to detect roll circulation from vertical radar profiles only, which allows for the analysis of cloud and precipitation parameters as a function of their position within the roll circulation. Second, we use back trajectories to analyze cloud and circulation development with fetch which allows us to draw a consistent picture of the MCAO development on 1 and 4 April 2022 (Fig. 4.9). Our findings answer the research questions posed in Sect. 4.1:

1. What are the differences between the environmental conditions on both flight days, and what are their implications for cloud development?
   Both MCAO events feature northerly winds advecting dry and cold air masses to the Fram Strait. The event on 1 April is characterized by colder air temperatures, leading to a doubling of the MCAO index and stronger heat fluxes compared to the 4 April case. The more active convection on 1 April deepens the boundary layer which causes higher cloud top heights that are aligned well with the boundary layer height. A rough scaling factor of 2 is observed in fluxes, the MCAO index, CTH, and LWP between both days. The Svalbard archipelago influenced the flow on both days, provoking a wave effect in the lee of Svalbard on 1 April, with subsiding air masses leading to reduced cloud top heights at 75 to 100 km fetch. On 4 April, lee effects caused an even stronger cloud-free zone west of the island, which led to a convergence zone and was not considered in the analysis.

   The difference in cloud top height between lidar and radar is used to detect the presence and derive the thickness of a supercooled liquid layer at the cloud top. Supercooled-liquid-topped mixed-phase clouds occurred 86 % and 71 % of the time on 1 and 4 April, respectively. With respect to cloud microphysics, the most prominent difference between both days is that riming is only significantly active during the cold and strong MCAO case on 1 April. This day also features a higher amount of supercooled liquid water with a median LWP of roughly $50\,\mathrm{g\,m^{-2}}$. Riming influences LLT, radar reflectivities, precipitation onset, and strength by producing larger ice particles. Regarding median properties, the cloud liquid layer thickness, liquid water path, and snowfall rate are again roughly lower by a factor of 2 for the weaker MCAO on 4 April.

2. Can we identify characteristic changes in cloud and precipitation properties perpendicular to the cloud street orientation, i.e., within the roll circulation?
   Yes, several hundred roll circulation objects were identified using cloud radar measurements performed on multiple legs perpendicular to the cloud street orientation. A composite analysis of these objects reveals that, on 1 April, several parameters show consistent trends from the updraft region towards cloud

boundaries, while, on 4 April, only radar reflectivity and cloud top height increase slightly in the respective updraft region. On 1 April, our data reveal the same frequency of the normalized rimed mass and updrafts within clouds. Thus, we speculate that the presence of significant riming on 1 April leads to the observed increases in snowfall rate, increases the height with most ice towards the updraft center, and impacts the observed LLT decrease towards the updraft as ice particles might be lifted into the pure liquid layer. Our statistical analysis of median cloud characteristics within the roll circulation and their variability (Fig. 4.7) could be used to test the performance of cloud parameterizations and better understand riming effects.

3. How do roll circulation, clouds, and precipitation properties evolve with fetch in the initial MCAO phase, e.g., up to travel times of 4 h?
   The analysis of our measurements as a function of fetch shows increasing the cloud top height, liquid water path, radar reflectivity, near-surface precipitation rate, horizontal cloud cover, and fraction of precipitating profiles with increasing fetch. Cloud streets form at around 15 km fetch and start precipitating at 25 to 40 km. We suspect that the later onset of precipitation on 4 April is attributed to the lack of riming in air masses with shorter fetches. The wavelength of the cloud streets λ slightly increases with fetch on 1 April, but the variability is rather high. The detected wavelength of around 1 km within the first 100 km of fetch aligns with the local maxima found in the spectral analysis of riming. Even though the airborne-derived results here generally coincide with MODIS-derived wavelengths, our analyses highlight the importance of high-resolution airborne measurements to evaluate satellite-derived products.

To answer the two last research questions, we established composite approaches to characterize the roll circulation (Fig. 4.7) and fetch (Fig. 4.8). These metrics can also be generated from cloud-resolving model output and be used to evaluate the model performance with respect to the representation of microphysics and dynamics in the initial phase of an MCAO. By considering the two cases with similar large-scale synoptic settings but differences with respect to microphysics, e.g., in LWP and riming, microphysical parameterization schemes can be evaluated. It will be particularly interesting to analyze whether these models successfully reproduce the observed factor of 2 in scaling found for several parameters between the two cases.

To study the impact of the sharpness of the MIZ and flow divergence on cloud evolution, more observations at a constant fetch over open water and at a variable fetch over the MIZ near the sea ice edge should be obtained in the future. Moreover, since the observed cloud top temperatures lie within the dendritic growth zone, aggregation is an important process to study, e.g., by dual-frequency radar observations (Chellini et al., 2022), in order to understand dominant precipitation-forming microphysical processes.

The Clouds over cOMPlEX environment (COMPEX) campaign planned for spring 2026 northwest of Svalbard will present the opportunity to better characterize the impact of the marginal sea ice zone (MIZ) on the air mass transformation. Flights within the MIZ and along the ice edge could increase the number of samples. Further, by enhancing our measurement suite with an airborne G-band radar, more information on cloud microphysics can be deduced.

4.6 APPENDIX A: PEAK DETECTION ALGORITHM AND SENSITIVITY

To detect up- and downdrafts, we solely use $Z_{e_{0.7}}$, which is the radar reflectivity at the height of 0.7 of the hydrometeor depth (D; Sect. 4.2.2). Figure 4.10 explains the choice of this height (red line). To understand the applied height and Z_e thresholds, one has to keep in mind that Z_e values larger $-5\,\mathrm{dBZ}$ (Schirmacher et al., 2023) and below 500 m (Shupe et al., 2008b) height are defined as precipitation. At 0.7 of the hydrometeor depth, most largest cloud particles occur, i.e., most maximum Z_e values per profile exceeding $-10\,\mathrm{dBZ}$ among all non-precipitating values (Fig. 4.10a, gray line). Most maximum Z_e values per profile among non-precipitating radar bins occur at the cloud bottom (Fig. 4.10a, black line). Nevertheless, this bottom near maximum is induced by very small Z_e values below $-10\,\mathrm{dBZ}$. Since we aim to detect updrafts at the selected height, we take the height where large particles ($> -10\,\mathrm{dBZ}$) occur most frequently. Moreover, with 98 %, most precipitation occurs below 0.7 of the hydrometeor depth (Fig. 4.10b, dashed black line). This finding is not sensitive to the $-5\,\mathrm{dBZ}$ threshold for precipitation (Fig. 4.10b, dashed gray line). Dry entrainment and liquid droplets seem rare at 0.7 of the hydrometeor depth since 91 % of the lowest Z_e values per profile lie above this altitude (Fig. 4.10b, solid black line). In conclusion, we take Z_e at the height of 0.7 of the hydrometeor depth to consider the largest ice particles within the profiles and minimize the influence of dry-air entrainment and supercooled liquid water droplets at the cloud top and precipitation at the bottom of the hydrometeor depth.

To find up- and downdraft regions using $Z_{e_{0.7}}$, we use the following method:

1. Determine 0.7 of D for every profile (Fig. 4.2b).
2. Average Z_e over 100 m in the vertical to reduce noise.
3. Smooth Z_e by averaging over 3 s to minimize noise detection (Fig. 4.2c).
4. Extract the smoothed $Z_{e_{0.7}}$ at 0.7 of D for each profile, which is the average between 0.65 and 0.75 times D (Fig. 4.2d, black line).
5. Derive the large-scale background $Z_{e_{back}}$ by averaging $Z_{e_{0.7}}$ over 500 s (~ 40 km; Fig. 4.2d, gray line).
6. Determine peaks in $Z_{e_{0.7}}$ using the Python package scipy.signal.find_peaks (Virtanen et al., 2020).
   If $Z_{e_{back}} \geqslant 0.67\,\mathrm{mm^6\,m^{-3}}$, find peaks for $Z_{e_{0.7}}$ with a prominence of at least $0.5\,\mathrm{mm^6\,m^{-3}}$ (difference between the height of the peak and its lowest contour line; Fig. 4.2d, vertical orange line)

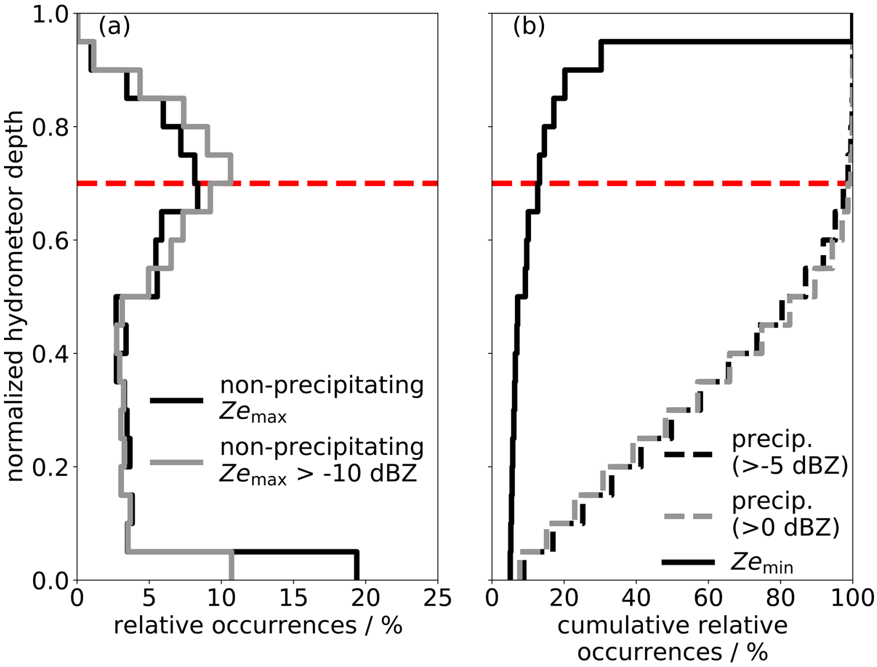

Figure 4.10: Relative occurrences of $Z_{e_{max}}$ among non-precipitating hydrometeors (**a**, solid black line) and of non-precipitating $Z_{e_{max}}$ that exceed -10 dBZ (**a**, solid gray line). Relative occurrence of precipitation defined by Z_e values larger than -5 dBZ (**b**, dashed black line) and larger than 0 dBZ (**b**, dashed gray line) and minimum Z_e of each radar profile (**b**, solid black line). The y axis is the normalized hydrometeor depth (0 = base, 1 = top). The height that is used to identify roll circulations is indicated by the red line.

and a width of at least 2.9 samples (about 230 m horizontal distance; Fig. 4.2d, horizontal orange line). Note that Fig. 4.2 shows Z_e in logarithmic space, while peaks are detected in linear space.

If $Z_{e_{back}} < 0.67\,\mathrm{mm^6\,m^{-3}}$, find peaks for $Z_{e_{0.7}}$ with a prominence of at least $0.1\,\mathrm{mm^6\,m^{-3}}$ and a width of at least 2.9 samples.

The detected peaks are defined as updrafts (Fig. 4.2e, vertical black lines). Here, we apply two different thresholds depending on $Z_{e_{back}}$ since the magnitude of the averaged Z_e and its peaks generally increase with fetch.

7. Find the minimum $Z_{e_{0.7}}$ between every two maxima (Fig. 4.2e, vertical gray line). If conditions between two cloud streets are cloud-free, we consider the downdraft location at the center of the cloud-free distance.

Table 4.3: Sensitivity of the steps of the algorithm applied to identify roll circulation objects. Relative changes in the number of objects in total; number of objects inside the cloud street regime; cloud top height (CTH) of cloud streets; and aspect ratio (AR) of the roll circulation to the results obtained by the applied configuration after adjusting, i.e., mostly doubling, parameters.

Modification	Total number of objects	Number of objects within cloud street regime	CTH	AR
III: average over 6 s	−17.8 %	−20 %	+24 %	+23 %
IV: 0.6 of hydrometeor depth	−1.8 %	−1 %	0 %	0 %
IV: 0.8 of hydrometeor depth	+3.4 %	0 %	0 %	0 %
VI: width of 5.8 samples	−31.3 %	−37 %	+59 %	+57 %
VI: if $Z_{e_{back}} \geqslant 0.67\,\mathrm{mm}^6\,\mathrm{m}^{-3}$, prominence of at least $0.2\,\mathrm{mm}^6\,\mathrm{m}^{-3}$	−9.8 %	−11 %	+10 %	+11 %
VI: if $Z_{e_{back}} < 0.67\,\mathrm{mm}^6\,\mathrm{m}^{-3}$, prominence of at least $1\,\mathrm{mm}^6\,\mathrm{m}^{-3}$	−9.3 %	−10 %	+10 %	+11 %

DATA AVAILABILITY

Processed radar, in situ, and dropsonde observations obtained during the HALO-(AC)^3 campaign are published by Ehrlich et al. (2024). The retrieved LWP data are currently being prepared for publication on PANGAEA. All airborne data are accessed via the ac3airborne module (Mech et al., 2022). The merged MODIS–AMSR2 sea ice concentration data are provided by the Institute of Environmental Physics at the University of Bremen (`https://data.seaice.uni-bremen.de/modis_amsr2/`, Ludwig and Spreen, 2023). Raw in situ data are stored at the German Aerospace Center and available on request. Back trajectories are calculated from ERA5 reanalysis data (Hersbach et al., 2017, 2020). ERA5 is available for pressure levels (Hersbach et al., 2023a) and single levels (Hersbach et al., 2023b). A Python implementation of the COARE 3.5 bulk air–sea flux algorithm is available in Ludovic et al. (2021). MODIS observations of the total water path can be found in NASA Worldview (2023a) (`https://go.nasa.gov/46vE70B`) and of corrected reflectance in NASA Worldview (2023c) (`https://go.nasa.gov/46o4aX0`). The corrected reflectance observed by VIIRS is available in NASA Worldview (2023b) (`https://go.nasa.gov/47mKJjr`).

COMPETING INTERESTS

The contact author has declared that none of the authors has any competing interests.

DISCLAIMER

SPECIAL ISSUE STATEMENT

This article is part of the special issue "HALO-(AC)^3 – an airborne campaign to study air mass transformations during warm-air intrusions and cold-air outbreaks". It is not associated with a conference.

ACKNOWLEDGEMENTS

We gratefully acknowledge the funding from the Deutsche Forschungsgemeinschaft (DFG, German Research Foundation; project no. 268020496) through the Transregional Collaborative Research Centre ArctiC Amplification: Climate Relevant Atmospheric and SurfaCe Processes and Feedback Mechanisms $(AC)^3$ (TR 172) (sub-project B03). We are grateful for the support from the Alfred Wegener Institute, Deutsches Zentrum für Luft- und Raumfahrt (DLR, German Aerospace Center), and aircraft crews during the HALO-$(AC)^3$ campaign. Moreover, we acknowledge the use of imagery from the NASA Worldview application (NASA Worldview, 2023a,b,c), part of the NASA Earth Observing System Data and Information System (EOSDIS). Furthermore, we thank the Institute of Environmental Physics at the University of Bremen for providing the merged MODIS–AMSR2 sea ice concentration dataset (Ludwig and Spreen, 2023). Many thanks go to the principal investigators (PIs): Stephan Borrmann, Johannes Schneider, and Veronika Pörtge. We are also grateful to Bjorn Stevens for discussing the flight strategy and cloud street investigation, Matt Shupe for discussing the roll circulation identification, and Vera Schemann for discussing future model evaluation efforts.

FINANCIAL SUPPORT

This research has been supported by the Deutsche Forschungsgemeinschaft (grant no. 268020496, TR 172).
This open-access publication was funded by Universität zu Köln.

REVIEW STATEMENT

This paper was edited by Markus Petters and reviewed by three anonymous referees.

5

SNOWFALL OVER THE FRAM STRAIT

This study addresses the third research question (Sect. 1.6.3) regarding the amount of snow falling over the Fram Strait during MCAOs and the limits of reanalyses in the representation of this snowfall.

Schirmacher, I., C. Pettersen, K. Ebell, and S. Crewell (2024b). *How much snow falls over the Fram Strait during marine cold air outbreaks: constraints derived from airborne radar observations*. (in prep.)

Currently, this work is under preparation and the future plan is to submit the manuscript.

AUTHOR CONTRIBUTION

All authors contributed to the conceptualization of the study. IS performed the analysis, visualization, writing, and methodology development. KE performed the undercatch correction for the gauge observations at Ny-Ålesund. All authors discussed the results and revised the manuscript.

HOW MUCH SNOW FALLS OVER THE FRAM STRAIT DURING MARINE COLD AIR OUTBREAKS: CONSTRAINTS DERIVED FROM AIRBORNE RADAR OBSERVATIONS

ABSTRACT

In the Arctic, the uncertainty of precipitation estimates is high because precipitation observations are rare and challenging. This holds especially true for marine cold air outbreaks during which low-level clouds produce light snow. The light snowfall is difficult to observe from spaceborne passive instruments. Moreover, spaceborne radar observations frequently miss low-level clouds and precipitation due to their roughly 1 km deep blind zone. Arctic marine cold air outbreaks are particularly common over the Fram Strait.

To constrain Arctic precipitation estimates, we retrieve snowfall rates for the Fram Strait region during marine cold air outbreaks. In doing so, we exploit airborne radar reflectivity observations obtained in the vicinity of Svalbard during three aircraft campaigns in the spring between 2017 and 2022. The data cover 45 h travel time, which corresponds to a distance of roughly 13.000 km, and span 190 km fetch. First, we deduce a radar reflectivity – snowfall rate (Z_e–S) relation for low-level mixed-phase clouds occurring under marine cold air outbreak conditions using collocated radar and precipitation gauge observations at Ny-Ålesund. Second, we apply the retrieved Z_e–S relation to the airborne radar observations obtained over the Fram Strait and reduce the temporal and spatial resolution to match the ones of the global ERA5 reanalysis. This enables a comparison with ERA5 and resampled regional reanalysis (CARRA) data.

On average, the observed snowfall rate over the Fram Strait during marine cold air outbreaks is 330 mm year^{-1}. Until 140 km fetch, the snowfall rates generally increase with fetch. At Ny-Ålesund, the snowfall occurrence is similar to the one over the ocean. However, snowfall events are occasionally intensified. Compared to common snowfall conditions between 1979 and 2022, the observations capture a 9 pp higher snowfall occurrence that is mostly very light snow and underrepresent high snowfall rates, which might be due to flight restrictions under these conditions. ERA5 overestimates the snowfall occurrence, particularly of light snow. Contrarily, CARRA underestimates the snowfall occurrence and underestimates medium and high snowfall rates over the whole Fram Strait. The observational data set can serve as a benchmark for future evaluations of models, reanalyses, or observations.

5.1 INTRODUCTION

In the Arctic, the uncertainty of precipitation estimates is high because the spatial and temporal coverage of accurate in situ and remote sensing observations is poor (Vihma et al., 2016). Ground-based observations are scarce. Spaceborne remote sensing instruments installed on polar orbiting satellites cannot observe precipitation in the central Arctic and struggle to capture light snowfall in general. Spaceborne visible imagery is constrained to polar day and, similarly to infrared imagery, fails to discriminate cloud and surface signals (Milani and Kidd, 2023). The latter holds also for light snowfall observed from spaceborne passive microwave remote sensing instruments (Milani and Kidd, 2023). Spaceborne radars have limitations in observing hydrometeors within their blind zone, i. e., the lowest kilometer of the atmosphere for CloudSat's cloud profiling radar (Schirmacher et al., 2023).

Within the Global Precipitation Climatology Project (GPCP) framework, an observational data product has been generated that merges ground-based gauges, spaceborne passive microwave, and spaceborne infrared and microwave sounder measurements. The data cover the entire Arctic from 1979 onwards (Adler et al., 2018). With the measurement techniques' limitations in mind, this data set is expected to be highly uncertain, especially for shallow and light snowfall (Maahn et al., 2014; Milani and Kidd, 2023; Schirmacher et al., 2023). It is even assumed that the GPCP data perform worse than reanalyses (Serreze et al., 2005) that are also affected by model limitations and the lack of reliable observations (Zhang et al., 2013).

Shallow and light snowfall dominates total snow accumulation, particularly during marine cold air outbreaks (MCAO; Mateling et al., 2023; Schirmacher et al., 2023), which are hence a blind spot for the assessment of precipitation (Lerber et al., 2022b). Arctic MCAOs frequently occur over the Fram Strait (Dahlke et al., 2022; Mateling et al., 2023; Papritz et al., 2015), where long-term precipitation rates thus range from 1 (Coupled Model Intercomparison Project Phase 5 and 6 (CMIP5, CMIP6) and GPCP; McCrystall et al., 2021) to 2 mm day^{-1} (fifth-generation global reanalysis (ERA5) and CloudSat; Lerber et al., 2022b; McCrystall et al., 2021).

During MCAOs, cold and dry air flows from the Arctic sea ice over the open ocean. Over the open water, cloud streets form with a width of the order of 1 km. With increasing travel distance over the open water, i. e., fetch, the cloud top heights (CTH) increase. However, Schirmacher et al. (2024a) showed that CTH was below 1 km height within 170 km fetch for two MCAO cases of different strengths. After being advected over the ocean for some tens of kilometers, precipitation sets in that, at least in some cases, intensifies with fetch (Schirmacher et al., 2024a).

Even though uncertainty is high, the long-term pattern of Arctic precipitation is similar among ERA5, CMIP5 and 6, GPCP, and CloudSat data (Edel et al., 2020; Lerber et al., 2022b; McCrystall et al., 2021). Precipitation rates are lowest over central Greenland and highest along the coast of Greenland, over the Greenland Sea, Barents Sea, and Fram Strait. Especially over the North Atlantic, cyclones that advect heat and moisture into the Arctic enhance precipitation rates (Lerber et al., 2022b).

The large variability in Arctic precipitation estimates causes different long-term precipitation trends among the data sets: models and reanalyses show an apparent increase in precipitation related to warming, which varies spatially and seasonally and is especially strong over the Arctic Ocean (Bintanja, 2018; IPCC, 2013; McCrystall et al., 2021; Vihma et al., 2016). Similarly, models and reanalyses have captured frequent phase changes from solid to liquid precipitation (Bintanja and Andry, 2017; Vihma et al., 2016). CMIP5 and 6 simulations show an Arctic-wide decrease in the ratio between snowfall and total precipitation occurrence with time, regardless of the season (McCrystall et al., 2021). The simulations predict a shift from a snow- to rain-dominated Arctic in autumn between 2055 and 2090 (McCrystall et al., 2021). The trend in precipitation amount obtained by models and reanalyses is in stark contrast to observations that show no clear trend (Boisvert and Stroeve, 2015; McCrystall et al., 2021; Vihma et al., 2016). Nevertheless, observations confirm an increase in rain fraction for the Atlantic sector of the Arctic (Łupikasza and Cielecka-Nowak, 2020), e. g., ground-based observations in Ny-Ålesund reported several periods of heavy rain in recent winters (Maturilli et al., 2013).

Arctic precipitation has substantial implications for the Arctic climate system (Oltmanns et al., 2019; Vihma et al., 2016; Zhang et al., 2013). This study thus aims to derive benchmark snowfall rate estimates over the Fram Strait during MCAOs, which vary widely between reanalyses and observations (Lerber et al., 2022b). The snowfall rates are retrieved from airborne radar observations obtained during several campaigns within the framework of the German Research Foundation project "ArctiC Amplification: Climate Relevant Atmospheric and SurfaCe Processes, and Feedback Mechanisms" ($(AC)^3$; Wendisch et al., 2023) that took place in the spring between 2017 and 2022.

Previous studies already derived several radar reflectivity – snowfall rate (Z_e–S) relations, which depend on the microphysical snow properties (Doviak and Zrnić, 2006), to derive snowfall for different crystal habits and observation locations (Kulie and Bennartz, 2009; Liu, 2008b; Matrosov, 2007; Schoger et al., 2021). To our knowledge, nevertheless, no Z_e–S relation exists for MCAOs over the Fram Strait. Thus, we first derive a Z_e–S relation from collocated radar and gauge measurements at Ny-Ålesund and apply it to the airborne radar observations.

The paper is organized as follows: first, we introduce the airborne measurements taken over the Fram Strait, the ground-based measurements from Ny-Ålesund, and reanalysis products (Sect. 5.2). Next, we derive the Z_e–S relation (Sect. 5.3) and provide a sensitivity study for this relation (Sect. 5.3.2). The precipitation estimates retrieved over the Fram Strait are presented in Sect. 5.4 and answer the following questions:

1. How large is the snowfall rate over the Fram Strait during MCAOs probed throughout the $(AC)^3$ campaigns, and do the measurements reveal spatial variability, e. g., compared to the well-equipped research station Ny-Ålesund, Svalbard? (Sect. 5.4.1)
2. How well is snowfall captured by the global reanalysis ERA5 and the Copernicus Arctic Regional Reanalysis (CARRA)? (Sect. 5.4.2)
3. Do the snowfall estimates retrieved during the campaigns represent typical MCAO conditions? (Sect. 5.4.3)

Finally, we conclude with the above questions and discuss future perspectives (Sect. 5.5).

5.2 DATA

This study aims to retrieve a Z_e–S relation that can be applied to airborne radar observations obtained over the Fram Strait during MCAOs (Sect. 5.2.1). To do so, we compare surface precipitation measurements from a precipitation gauge and radar observations both taken at Ny-Ålesund, Svalbard, during meteorological conditions similar to MCAO conditions (Sect. 5.2.2). After applying the relation to the airborne observations over the Fram Strait, we resample the retrieved estimates to ERA5 resolution, and compare them to ERA5 as well as resampled CARRA reanalyses data (Sect. 5.2.3).

5.2.1 *Airborne data*

Within the framework of $(AC)^3$ (Wendisch et al., 2023), airborne radar observations have been conducted during three aircraft campaigns: namely, the ACLOUD (Arctic CLoud Observations Using airborne measurements during polar Day; Ehrlich et al., 2019a; Wendisch et al., 2019) campaign in 2017, the AFLUX (Airborne measurements of radiative and turbulent FLUXes of energy and momentum in the Arctic boundary layer; Mech et al., 2022) campaign in 2019, and the HALO-$(AC)^3$ (High Altitude and LOng range research aircraft–$(AC)^3$;

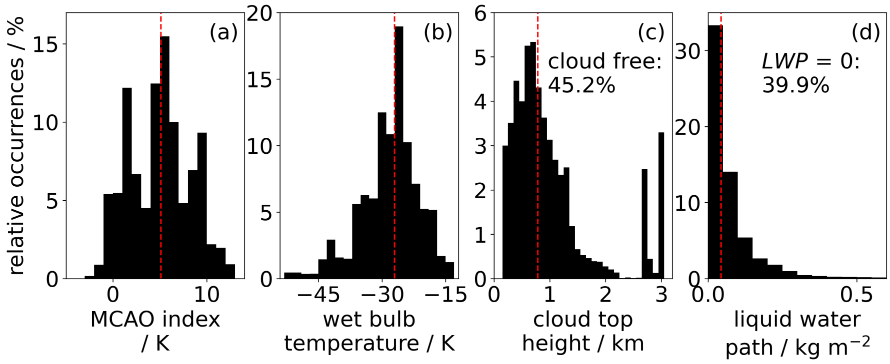

Figure 5.1: Conditions during the analyzed airborne observations. Only data over the open ocean are displayed. Marine cold air outbreak (MCAO) index from ERA5 (a), wet bulb temperature from ERA5 (b), observed cloud top height of the lowest cloud layer (c), and observed liquid water path (LWP; d). The median of each distribution (red dashed line) is highlighted. The total number of observations is 84,133, and the snowfall occurrence is 45.3 %.

Wendisch et al., 2024) campaign in 2022. The campaigns cover periods from March to June. During all campaigns, the Polar aircraft *P5* was based in Longyearbyen, Svalbard, and probed the Fram Strait.

On board *P5*, the Microwave Radar/radiometer for Arctic Clouds (MiRAC; Mech et al., 2019) was installed with a 25° backward inclination. The active module of MiRAC, i. e., MiRAC-A, consists of a downward-looking frequency-modulated continuous-wave (FMCW) radar that operates at 94 GHz (type RPG–FMCW–94–SP) with a sensitivity of at least -40 dBZ (Mech et al., 2019). The antenna of MiRAC-A was shortened compared to the original radar design, widening the half-power beamwidth (HPBW) to 0.85° (Mech et al., 2019). The vertical resolution of the radar observations is 4.5 m in the vicinity of the aircraft and not more than 27 m (Mech et al., 2019). Nadir profiles are constructed from the slant path measurements and vertically interpolated to a standard 5 m grid. Due to the radar's HPBW, its temporal resolution of 1 s, and the low flight speed of *P5*, each measurement covers roughly a distance of 110 m along the flight track. Radar reflectivities are not corrected for any attenuation that is generally small in the Arctic, e. g., below 1 and 0.6 dBZ for atmospheric water vapor and hydrometeors, respectively (Schirmacher et al., 2023). To exclude strong ground clutter effects, we only account for radar reflectivity profiles above 150 m altitude (Mech et al., 2019) that have been obtained along straight flight segments over the ocean and from a flight altitude above 2 km.

The passive channel of MiRAC measures brightness temperatures at 89 GHz, which are primarily influenced by the emission of liquid clouds and the surface. From differences in brightness temperatures between clear-sky and cloudy conditions, LWP is retrieved via a regression approach (Ruiz-Donoso et al., 2020). Due to the unknown emissivity of sea ice, LWP is derived only over open ocean. The uncertainty of LWP depends on atmospheric conditions and is below 30 $\mathrm{g\,m^{-2}}$ (Ruiz-Donoso et al., 2020). Contrarily to radar reflectivities, LWP is not adjusted to nadir profiles and is only available along slanted paths (Mech et al., 2022).

This study focuses only on snowfall by limiting the analysis to flight days with surface wet bulb temperatures continuously below -2°C along the flight track. To assess these air temperatures, we analyze measurements from dropsondes launched from *P5* at the height closest to the surface (George et al., 2021; Vaisala, 2010) and from ERA5 reanalysis at 1000 hPa.

To identify MCAO conditions, the MCAO index is calculated from the difference between potential temperatures at the surface and at 850 hPa height over the open water (Dahlke et al., 2022; Kolstad, 2017). We calculate the MCAO index from ERA5 reanalysis data using ocean skin temperature. We only consider flight days with a positive MCAO index averaged over the ice-free Fram Strait, i. e., all grid cells within 75–81.5°N and 9°W–16°E that have a sea ice concentration (SIC) of zero between 6 and 18 UTC.

Applying the above-mentioned selection criteria to the radar data results in a final data set that covers 45 hours (roughly 13,000 km distance) between March, April, and May. For the measurements over the open ocean, the MCAO index is by definition mostly positive (Fig. 5.1a), the median wet bulb temperature is -27°C (Fig. 5.1b), and the median cloud top height (CTH) is 0.8 km height (Fig. 5.1c). Note that the upper end of the CTH distribution is bounded by the flight altitude, which is, on average, 3 km. For multilayer clouds, i. e., cloud layers with a vertical gap of at least 90 m, only the lowest cloud layer is considered. With a median LWP of 43.5 $\mathrm{g\,m^{-2}}$, the clouds contain a substantial amount of cloud liquid (Fig. 5.1d). The radar signals further imply the presence of cloud ice, thus the probed clouds are mixed-phase clouds (MPC). Moreover, 45 % of the observed profiles indicate snowfall with rates of at least 0.01 $\mathrm{mm\,h^{-1}}$ at 150 m height.

5.2.2 *Ny-Ålesund*

We retrieve a Z_e–S relation adapted to MCAO conditions from observations obtained at the French-German AWIPEV research base (Neuber, 2006) in Ny-Ålesund, Svalbard, operated by the German Alfred Wegener Institute for Polar and Marine Research (AWI) and the French Polar Institute Paul-Émile Victor (IPEV). The data cover more than one year, lasting from 10.10.2021 to 31.12.2022. To concentrate on suitable meteorological conditions comparable to flight conditions, we focus on snowfall events from low-level MPCs, whose lowest cloud layer has a CTH below 2500 m (Chellini et al., 2023a), and filter the data using:

- temperature and wind observations from a measurement tower 180 m apart from the atmospheric observatory (Maturilli et al., 2013).
- CTH of the lowest cloud layer that is obtained analogous to CTH over the Fram Strait (Sect. 5.2.1) using the radar installed at the roof of the observatory building (Sect. 5.2.2.1).
- LWP from the passive microwave radiometer called Humidity And Temperature PROfiler (HATPRO) installed beside the radar (Chellini et al., 2023a).

Within this study, we furthermore use particle shape and size observations that are characterized by the Video In Situ Snowfall Sensor (VISSS) with a high resolution using two cameras installed at the ground near the atmospheric observatory (Maahn et al., 2024; Maahn and Maherndl, 2023).

5.2.2.1 *Radar*

At Ny-Ålesund, two radars of the model RPG–FMCW–94–SP consecutively obtained the analyzed radar reflectivities: the modified radar MiRAC-A that was also on board the *P5* and the unmodified JOYRAD-94. JOYRAD-94 was installed on the roof of the atmospheric observatory until 22.06.2022, followed by MiRAC-A. JOYRAD-94 has a beam width of 0.5° full-width half maximum (FWHM; Küchler et al., 2017). Both radars are operated with the same effective averaging time of 2 s and chirp settings, resulting in a sensitivity that is slightly better than -60 dBZ at the first radar bin at 102 m height (Chellini et al., 2023a). At Ny-Ålesund, Z_e is analyzed at the lowest available range gate at 102.2 m to observe snowfall conditions that are closest to the conditions at the surface. Up-looking radars are less influenced by near-surface ground clutter than down-looking radars. Additionally, Z_e observations at 150 m are investigated, which is the height of the lowest airborne range gate unaffected by ground clutter. Like the airborne radar observations, radar observations at Ny-Ålesund are not corrected for attenuation by hydrometeors and atmospheric gases. The radar data used in this study are available with a 6 s resolution and are processed and published by Chellini et al. (2023a).

5.2.2.2 *Precipitation gauge*

The precipitation gauge OTT Pluvio^2 L 400 measures the surface precipitation amount and intensity at AWIPEV, Ny-Ålesund, next to the measurement tower 180 m apart from the observatory (Ebell et al., 2024). It detects liquid and solid precipitation in mm water equivalent by weighing its bucket content, which has been collected over one hour, and gives an output every minute. The minimum amount for the gauge to detect precipitation is 0.05 mm (OTT, 2024), corresponding to a rate of 3 mm h^{-1} at the time step when the minimum detectable amount is exceeded. After reaching this threshold, the resolution is 0.6 mm h^{-1} (OTT, 2024). According to OTT (2024), Pluvio's measurement uncertainty of the precipitation rate per minute is ±1 %, corresponding to roughly ±0.3 mm h^{-1} for the highest amount measured. We use the non-real-time output that provides a more accurate precipitation estimate due to advanced filtering (OTT, 2024). Uncertainties in gauge observations frequently stem from wind-induced undercatch, mainly a function of wind speed and temperature. For solid precipitation at temperatures below -2°C, gauges catch only 80 % of the precipitation at wind speeds of 2 m s^{-1}, 40 % at 5 m s^{-1}, and 20 % at higher wind speeds (Wolff et al., 2015). To reduce undercatch and improve precipitation measurements (Nitu et al., 2018), a single Alter wind shield surrounds Pluvio at Ny-Ålesund. Moreover, we correct the data for undercatch following Wolff et al. (2015) using wind speed and temperature observations at 2 m height from the measurement tower close to the observatory. Kochendorfer et al. (2017) highlight the importance of this undercatch correction as it improves the 'bias' of the estimates and precipitation accumulation for averaging periods of 30 and 60 min. Since the correction factor rises with wind speed, the uncertainty range of the corrected precipitation estimate increases with stronger winds. Thus, we limit the analyzed wind speed conditions to below 4 m s^{-1} and the enhancement factor of corrected precipitation to below two. According to Kochendorfer et al. (2017), nevertheless, significant measurement errors persist after correcting for undercatch, likely due to measurement errors, the spatial variability of precipitation, and the variability in type, size, density, and fall speed of hydrometeors. This holds particularly true for heavily rimed particles that fall faster than unrimed particles.

5.2.3 *Reanalysis data*

We take the latest global reanalysis ERA5 and the novel, higher-resolved Arctic reanalysis CARRA to analyze their performance. ERA5 is based on the Integrated Forecasting System (IFS) model cycle 41r2 with a four-dimensional variational data assimilation scheme. Its horizontal and temporal resolution are 31 km and one hour, respectively (Hersbach et al., 2020). ERA5 distinguishes between large-scale and convective snowfall; however, we analyze the mean total snowfall amount, which includes both precipitation types. From the wind field, back trajectories are calculated for the airborne observations using Lagranto (Kirbus et al., 2024; Sprenger and Wernli, 2015). The trajectory calculations start at 10 hPa (~100 m) above ground. We use the open water fraction along these trajectories to calculate fetch by following Schirmacher et al. (2024a). Fetch is a proxy for the integrated turbulent fluxes from the ocean that influence the advected air along its track. For the calculation, we use spaceborne sea ice concentration (SIC) observations from a daily product with a 1 km horizontal resolution (Ludwig et al., 2020). For the ACLOUD campaign in 2017, this highly-resolved product is not available. Instead, a similar product with a 3.125 km resolution is used.

CARRA is based on the HARMONIE-AROME non-hydrostatic regional numerical weather prediction model that takes ERA5 output as boundary forcing (Yang et al., 2023). CARRA's horizontal resolution of 2.5 km is significantly finer than that of ERA5 (Yang et al., 2023). We use data from the western domain of CARRA that covers the Fram Strait. The snowfall amounts used in this study are from forecast runs. For every flight day, the forecast starts at 00:00 AM with a lead time of 3 h. Thus, we take the highest temporal resolution possible (3 h). As the difference in precipitation amount between the shortest and longer lead times is negligible after 6 h, we avoid spin-up problems for the times of the aircraft flights (Yang et al., 2023). The snowfall amount is the time integral of total solid precipitation since the starting time of the forecast and is converted to precipitation rate in mm h^{-1}. As for ERA5, the total snowfall flux in CARRA includes large-scale and convecve snowfall.

5.3 Z_e–S RELATION

The water equivalent snowfall rate (S) can be derived empirically from the radar reflectivity (Z_e) following a power law with the intercept parameter a and exponent parameter b (Doviak and Zrnić, 2006):

$$S = (\frac{1}{a} Z_e)^{\frac{1}{b}}. \quad (5.1)$$

This power law strongly depends on the microphysical properties of the observed snow particles (Doviak and Zrnić, 2006). Thus, previous studies derived various relations for different crystal habits and measurement locations through calculations or observations (Table 2.1). To our knowledge, no Z_e–S relation has been specifically deduced for MCAO conditions. We thus derive such a relationship using snowfall observations of low-level MPCs at Ny-Ålesund that occurred under conditions resembling MCAOs over the Fram Strait (Fig. 5.1).

The flowchart in Fig. 5.2 summarizes the derivation of the Z_e–S relation for Ny-Ålesund. Every minute, we take precipitation rates from Pluvio and allocate averaged radar reflectivities and meteorological parameters. Next, we only consider Z_e larger -15 dBZ as precipitation signals because lower values are assumed to be cloud signals with non-considerable snowfall rates (roughly 0.006mm h^{-1}). Further, we

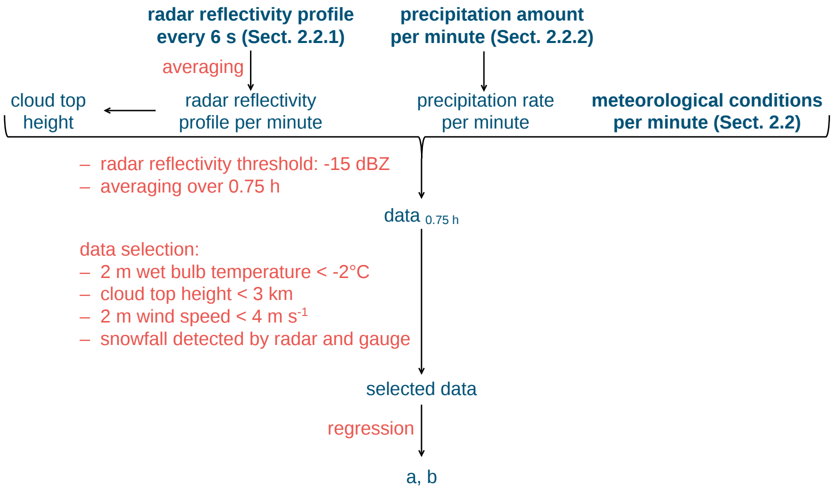

Figure 5.2: Flowchart summarizing the retrieval of the intercept parameter a and exponent parameter b of the Z_e–S relation (Eq. 5.1).

average the observations for several reasons: First, the instrument location of the radar and precipitation gauge is shifted by 180 m, and the sampling volumes differ. Through averaging, similar conditions should be captured at both sites (Grazioli et al., 2017). Second, Pluvio collects light precipitation over one hour and detects it when an amount of 0.05 mm is exceeded. Averaging helps to allocate light snowfall correctly. Third, averaging improves the precipitation accumulation (Sect. 5.2.2.2; Kochendorfer et al., 2017). Typical averaging times range from 30 to 60 min (Fujiyoshi et al., 1990; Grazioli et al., 2017; Kochendorfer et al., 2017; Rasmussen et al., 2003; Wiener et al., 2024; Wolff et al., 2015). Fujiyoshi et al. (1990) recommend an averaging time of 30 min for which their total snowfall was retrieved closest to the observed one. For our data, nevertheless, precipitation events in the radar and gauge data are frequently attributed to different time stamps for such a short averaging time. Thus, we decided on an averaging time of 0.75 h and manually sorted out heavy precipitation that occurs at averaging range edges and is attributed to different time stamps for the radar and Pluvio. A more in-depth discussion and sensitivity study of different averaging times is presented in Sect. 5.3.2.

Only a subset of these integrated low-level MPC observations is used for the regression calculation: Within the 0.75 h period,

1. the maximum 2 m wet bulb temperature has to be below -2°C to focus on snowfall only.

2. the maximum 2 m wind speed has to be smaller than $4\,\mathrm{m\,s^{-1}}$ to reduce inaccuracies in the undercatch correction (Sect. 5.2.2.2).

3. the maximum CTH has to be lower than 3 km to resemble CTHs arising during MCAOs over the Fram Strait (Fig. 5.1c).

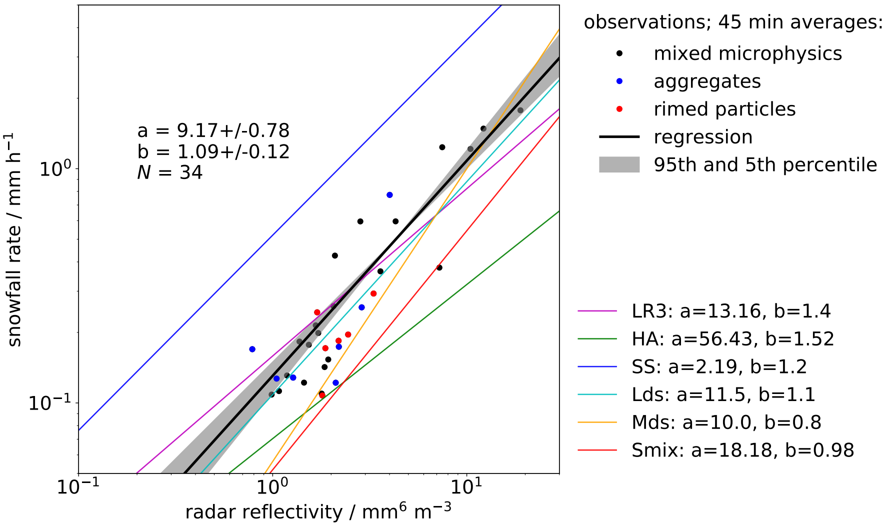

Figure 5.3: Z_e–S relation for low-level mixed-phase clouds at Ny-Ålesund under environmental conditions similar to marine cold air outbreak conditions over the Fram Strait. Observations averaged over 0.75 h (points), respective non-linear least square regression (black line), regression for the 5th and 95th percentile of the data (shade), and relations retrieved by previous studies (colored lines; Table 2.1). Periods with aggregates and rimed particles are highlighted in blue and red, respectively (Fig. 5.4). Intercept parameter a and exponent parameter b of the regressions (Eq. 5.1), and the total number of observations N are mentioned.

4. Pluvio and the radar have to detect snow to exclude cases during which Pluvio misses light snowfall due to its high detection limit (Sect. 5.2.2.2).

After applying the criteria above, the LWP distribution at Ny-Ålesund (not shown), which has a maximum of 0.5 kg m^{-2}, resembles the distribution derived from airborne measurements over the Fram Strait (Fig. 5.1d).

The analysis is based on 34 averaging periods (25.5 h). We obtain a Z_e–S relation by fitting the integrated radar reflectivities against the integrated precipitation rates in logarithmic space and applying a non-linear least square regression (Fig. 5.3, black line). The retrieved intercept parameter a is 9.18, and the exponent parameter b is 1.09. Both parameters are very similar to the findings by Liu (2008b) for dry snow consisting of mixed random oriented particle shapes, including nonspherical three, four, and six bullet rosettes, sectors, and dendrites (Table 2.1). Their relation is based on backscatter computations of ice particles and in situ measurements of particle size distributions.

Nevertheless, the scatter around the regression line is substantial (Fig. 5.3). Herein, for a given Z_e, S spans a range of values due to different crystal habits such as particle shape and size distribution. Nevertheless, the correlation coefficient r between the averaged ob-

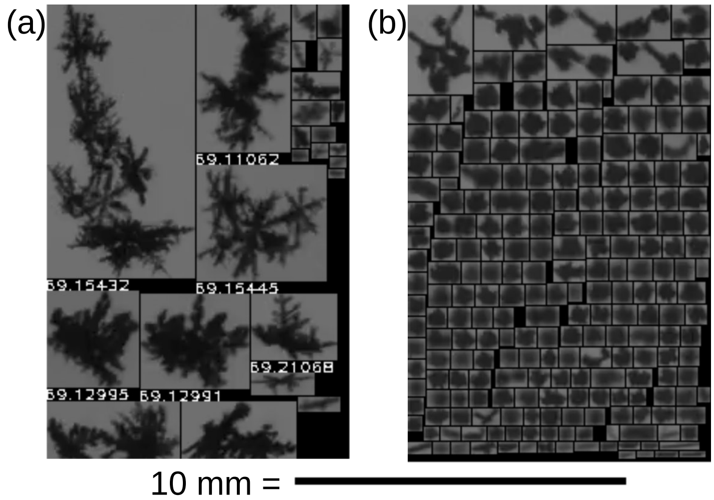

Figure 5.4: Aggregates (a) and rimed particles (b) detected by the Video In Situ Snowfall Sensor. Images are from Maahn and Maherndl (2023).

servations of S and Z_e is 0.93 high, and the RMSE concerning the fitting curve is relatively small with 0.15 mm h^{-1}.

To investigate whether different crystal habits cover different areas of the Z_e–S space, we identify averaging periods with mostly aggregated (Fig. 5.4a) or rimed particles (Fig. 5.4b) by visual inspections of images obtained by the VISSS (Sect. 5.2.2). The periods during which nearly solely rimed particles occurred form a distinct Z_e regime (Fig. 5.3). In contrast, the periods with aggregates span a wide range of Z_e. Compared to rimed particles that are relatively spherical, the cross-section of aggregates depends on their orientation and is thus more variable (Maahn et al., 2024; Maherndl et al., 2024a). The dependency of Z_e on the particle orientation for aggregates likely explains the aggregate's larger Z_e spread. Note that the uncertainty of S might be enhanced for rimed particles due to larger measurement errors stemming from higher fall speeds than other hydrometeors (Sect. 5.2.2.2; Kochendorfer et al., 2017).

5.3.1 *Retrieval test*

As a sanity check, we assess whether the retrieval reproduces the gauge observations at Ny-Ålesund within the observation period between October 2021 and December 2022 by comparing estimated snow accumulation. To do so, we apply the retrieved Z_e–S relation to the radar observations averaged over 0.75 h and set precipitation rates smaller than 0.01 mm h^{-1} equal to 0 mm h^{-1} to account for the accuracy of the gauge. This threshold is consistent with detection limits applied to models and observations in previous studies (Palerme et al., 2014; Roussel et al., 2023). For comparison, the lowest precipita-

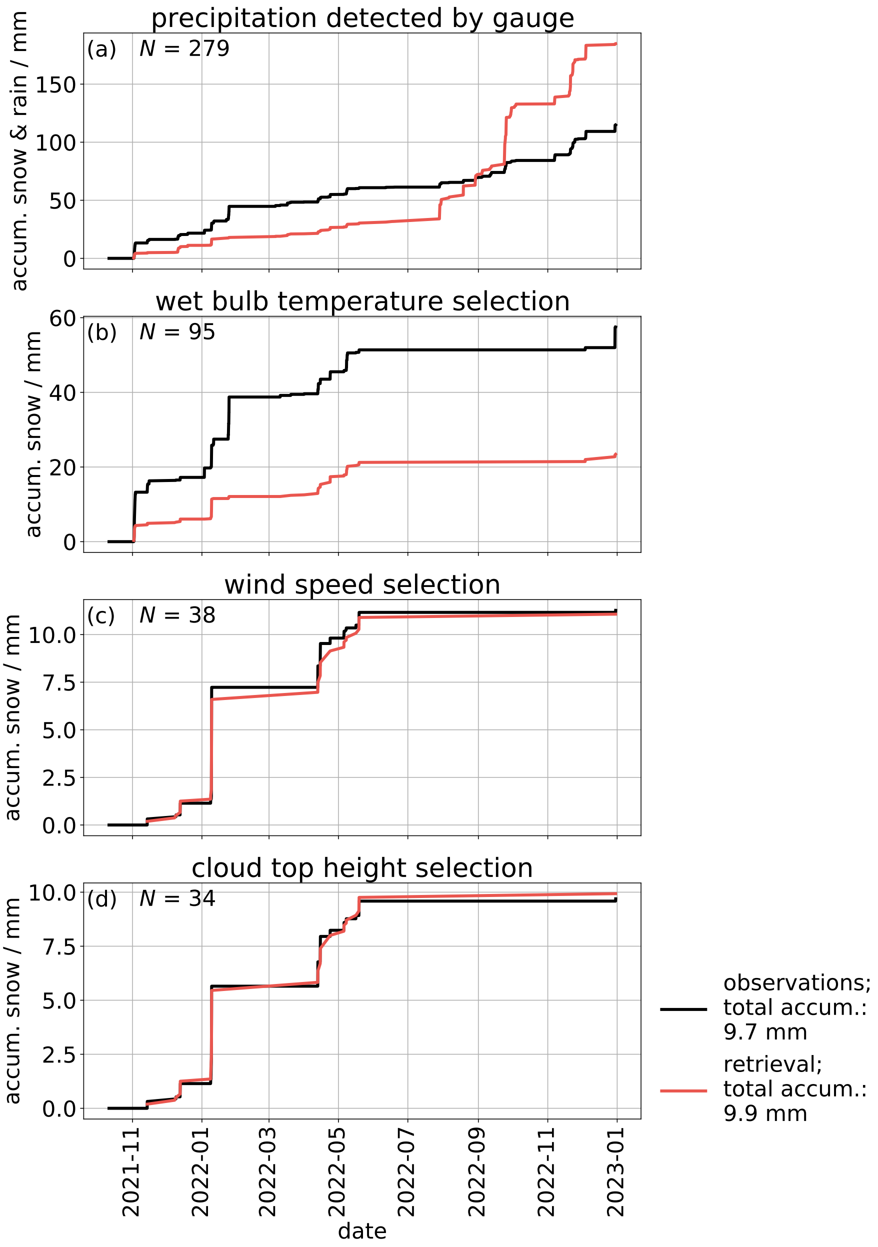

Figure 5.5: Accumulated surface precipitation observed by the gauge (black line) and retrieved by the Z_e–S relation (red line) during all observed averaging periods when precipitation was detected by the gauge (a), when also wet bulb temperatures were below -2°C (b), when also wind speeds were lower than $4\,\mathrm{m\,s^{-1}}$ (c), and when also cloud top heights were below 3 km (d). N highlights the total amount of averaging periods.

tion rate observed by the gauge at Ny-Ålesund over one minute is $0.04\,\mathrm{mm\,h^{-1}}$. We investigate the influence of each criterion applied to filter snowfall during MCAO conditions (Sect. 5.3) on the accumulated snow by selecting the calculated S consecutively.

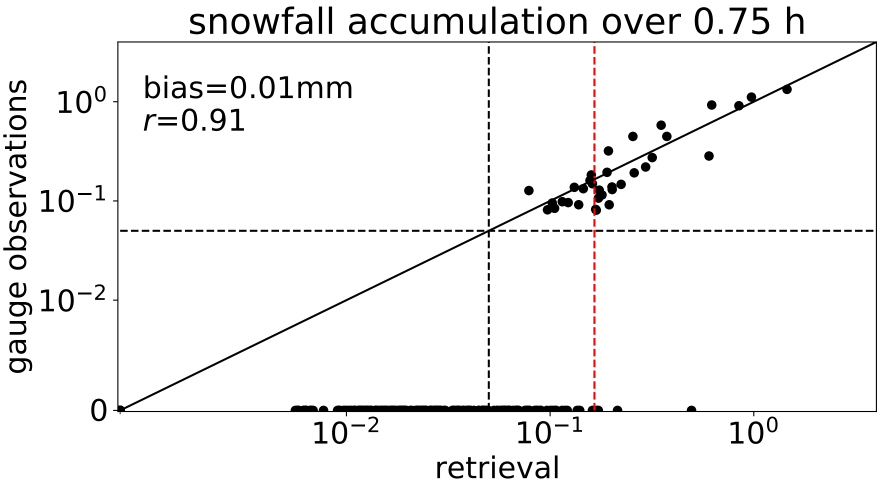

Figure 5.6: Comparison of observed and retrieved snowfall accumulation over 0.75 h periods. The bias of the retrieval, Pearson correlation coefficient r between observed and retrieved data, and line through origin are highlighted. The black dashed lines indicate the precipitation gauge's claimed minimum detectable precipitation amount, i. e. 0.05 mm over 1 h (Sect. 5.2.2.2). The red dashed line shows the minimum detectable precipitation amount according to our findings.

Over the entire period, the precipitation gauge detects 58 mm of snow within 71.25 h of snowfall and 57 mm of rain within 138 h of rainfall as defined by the temperature criterion (Fig. 5.5a, b). Because the uncertainty is higher under stronger winds, we only consider low wind speed conditions, drastically reducing total snowfall amount to roughly 11 mm (Fig. 5.5c). 86 % of this snowfall comes from clouds with top heights below 3 km (Fig. 5.5d).

The retrieval applies only to snowfall. Thus, the retrieved precipitation amount highly overestimates the observations, especially from August to December 2021, when temperatures indicate frequent rain (Fig. 5.5a). The retrieved snowfall amount is less than half of the observed (Fig. 5.5b). Under low wind speeds, the retrieval perfectly matches the observations (Fig. 5.5c). With a focus on clouds with CTHs below 3 km, retrieved (9.9 mm) and observed (9.7 mm) snow accumulations are still very similar (Fig. 5.5d). However, the minimum snowfall rate detected by the gauge (0.11 mm h^{-1}) is an order of magnitude larger than the one detected by the retrieval (0.01 mm h^{-1}; not shown).

The one-by-one comparison of the snow accumulation over 0.75 h periods shows a good agreement between observations and the retrieval (Fig. 5.6) with a high correlation (r=0.91) and very low high bias of the retrieval (0.01 mm). Such good scores are obtained even though the retrieval has a snowfall false detection rate compared to the gauge of 24 % (Table 5.1). Setting the detection limit of the

Table 5.1: Amount of analyzed snowfall observations at Ny-Ålesund separated by the retrieved and observed snowfall rate (S) averaged over 0.75 h. The value in the brackets highlights the number of periods during which the retrieved snowfall amount exceeds the claimed detection limit of the gauge (0.05 mm). These snowy periods should thus have been detected by the gauge as well.

		gauge observations	
		$S>0$	$S=0$
retrieval	S>0	34	190 (68)
	S=0	0	559

retrieval to the claimed limit of the gauge (0.05 mm collected over 1 h) already reduces the false detection rate from 24 to 9 %. However, we determined a detection limit of 0.165 mm over 0.75 h (Fig. 5.6, red line) below which retrieved snowfall detections during observed non-precipitating periods frequently go along with long-lasting, large-scale precipitation as indicated by the radar. The gauge does not detect any snowfall for consecutive averaging periods, which indicates a low sensitivity of the gauge. False detections by the retrieval of amounts larger than 0.165 mm (four events) are not induced by the low sensitivity of the gauge but rather stem from local snow events or events observed by the different instruments at consecutive periods. In conclusion, the retrieval reproduces gauge observations very well. Disagreements between snowfall accumulations stem from the gauge's low sensitivity or incorrect snowfall allocations but not from the retrieval per se. The relation can thus be applied to the airborne data over the Fram Strait.

5.3.2 *Sensitivity study*

We investigate uncertainties of the retrieved Z_e–S relation by performing five sensitivity studies (Table 5.2):

1. To account for the uncertainty of the gauge observations, we estimate a range of intercept parameters a and exponent parameters b by calculating a regression for the 95th and 5th percentile of the data (Fig. 5.3, gray shade). By definition, regressions with a between 9.17±0.78 and b between 1.09±0.12 cover 90 % of the data. The relative uncertainty of both parameters is roughly 10 %.

2. To account for Pluvio's accuracy (Sect. 5.2.2.2), we modify the observed data by adding Gaussian-distributed values between $\pm 0.3\,\mathrm{mm\,h^{-1}}$. The parameters of the Z_e–S relation lie within

the 90 % confidence interval of the data. Pluvio's uncertainty affects a by less than 4 % and b by 10 % relative to the retrieved parameters, leading to an underestimation of the retrieved total accumulation by 10 %.

3. To account for uncertainties due to the length of the averaging period, we apply different periods of 0.5, 1, 1.5, and 2 h. Contrary to the final relation, for which we manually exclude precipitation events captured by the radar and gauge on consecutive averaging periods, no such processing was done for the sensitivity study. Regressions for averaging times of 0.75, 1, and 1.5 h are very similar, while the regression parameters for 0.5 and 2 h differ by roughly 7 and 10–20 % compared to the 0.75 h averaging period, respectively (Table 5.2). The correlation coefficient between the observed and retrieved precipitation amounts is 0.91 for 0.75 h and reduces (increases) to 0.85 (0.97) for 30 min (2 h) averages. We decided against the 30-minute period because of the low correlation coefficient and against the 2-hour period because the regression parameters have not been reproduced by any other period and because the amount of periods with snowfall (18) is relatively low. We take the shortest remaining period to base our analysis on a large amount of data (34 periods with snowfall). An averaging period of 0.5 h (1 h) would result in 48 (33) snowfall periods.

4. Since the Doppler velocity spectra seem not to be affected by artifacts within the lowest range gates, we assume that artifacts in Z_e are negligible at the lowest range gate at 102 m height. Thus, we use the observations at 102 m height to retrieve the Z_e–S relation. To analyze whether changes in the microphysics below the lowest range gate of the airborne data and 102 m occur, we repeat the power law retrieval for Z_e obtained at 150 m height. Compared to the intercept and exponent parameters obtained by Z_e at 102 m, a and b are less than 4 % higher and lower at 150 m, respectively. The correlation coefficient between both precipitation rates is thus roughly 1.

5. Separate regressions for rimed and aggregated particles distinguished by mean Doppler velocity observations show no differences that hold over different averaging times tested within the framework of the sensitivity study. Thus, we decided to retrieve one Z_e–S relation for all data regardless of their microphysics.

Table 5.2: Sensitivity studies for the retrieved Z_e–S relation. Shown is the intercept parameter a and exponent parameter b of each Z_e–S relation, as well as the total snow accumulation over the selected period between October 2021 and December 2022 (Sect. 5.3).

name	condition	a	b	accumulation
retrieval		9.17	1.09	9.9 mm
sensitivity study 1	95th percentile	9.96	1.21	9.9 mm
sensitivity study 1	5th percentile	8.39	0.97	10.1 mm
sensitivity study 2	considering Pluvio's uncertainty	9.49	0.98	9.0 mm
sensitivity study 3	0.5 h averaging	8.50	1.15	10.5 mm
sensitivity study 3	1 h averaging	9.20	1.08	10.7 mm
sensitivity study 3	1.5 h averaging	9.10	1.12	11.5 mm
sensitivity study 3	2 h averaging	8.36	0.86	8.9 mm
sensitivity study 4	Z_e at 150 m height	9.51	1.06	9.9 mm

5.4 SNOWFALL RATES OVER THE FRAM STRAIT REGION DURING MCAOS

In the following sections, we analyze the snowfall rates over the Fram Strait calculated by applying the Z_e–S relation obtained for Ny-Ålesund to the airborne observations and setting the detection limit to 0.01 mm h^{-1}. To enable a comparison with previous studies and reanalysis products, we investigate S in mm year^{-1} and resample the observations to ERA5's temporal and spatial resolution, respectively. In Sect. 5.4.1, we present the observations and investigate the spatial variability of the snowfall rates by analyzing their fetch dependency and differences between the ocean and Ny-Ålesund. In Sect. 5.4.2, we investigate the representation of MCAO snowfall in reanalyses by comparing the retrieved estimates with ERA5 and CARRA products. In Sect. 5.4.3, we examine the representativeness of the observed snowfall rates concerning MCAO conditions over the Fram Strait.

5.4.1 *Snowfall rates and their spatial variability*

The temporal evolution of the snowfall rates observed during MCAOs over the Fram Strait indicates that the daily medians and interquartile ranges (IQR) of precipitation rates during such conditions are generally larger in spring than early summer (Fig. 5.7a). Note that the flight tracks during the different campaigns cover slightly different areas over the Fram Strait. Generally, data obtained during ACLOUD focus more on the southern and western parts of the investigated area, data from AFLUX mainly on the northern parts, while data from HALO-

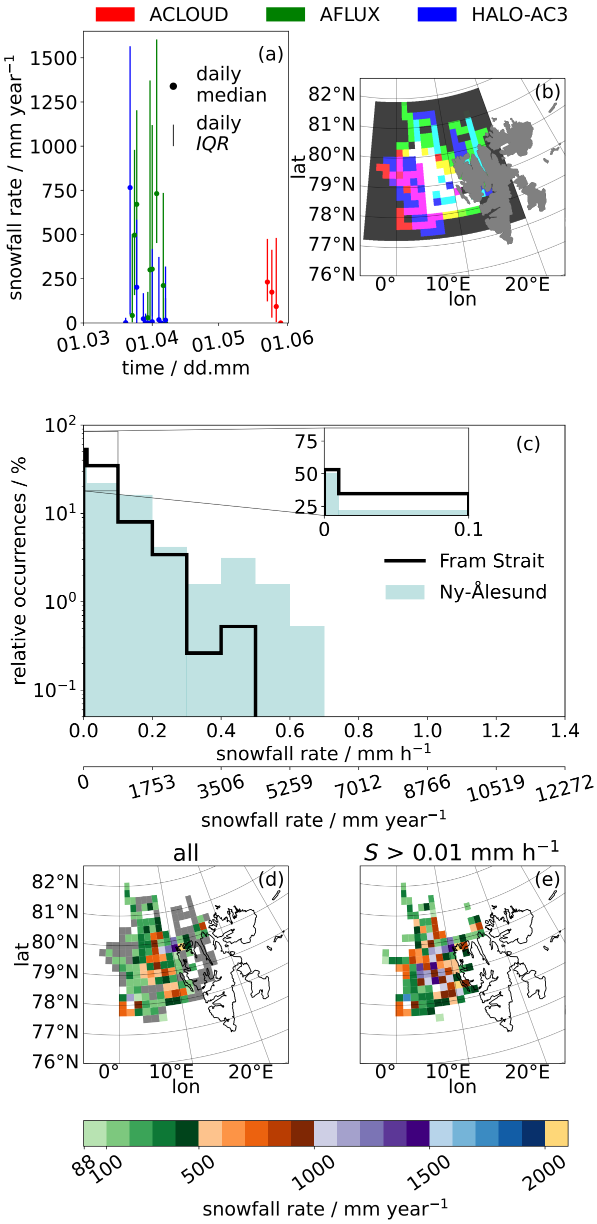

Figure 5.7: Observed snowfall rates over the Fram Strait during marine cold air outbreaks (MCAO). Temporal evolution of daily median values and interquartile ranges (IQR) during the ACLOUD (red), AFLUX (green), and HALO-(AC)³ (blue) campaign (a). RGB plot of the spatial frequency distribution of observations during ACLOUD (red), AFLUX (green), and HALO-(AC)³ (blue) at 31 km spatial resolution (b). Relative frequency distribution of the resampled (31 km, 1 h) snowfall rates over the Fram Strait (black) and of hourly rates for MCAOs between October 2021 and December 2022 at Ny-Ålesund (blue) (c). Spatial distribution for all observed resampled snowfall rates with snowfall rates below 0.01 mm h^{-1} in gray (d) and resampled rates exceeding 0.01 mm h^{-1} (e).

(AC)³ cover the whole area (Fig. 5.7b). Nevertheless, all campaigns cover the central Fram Strait.

Table 5.3: Mean snowfall rates over the Fram Strait. The averages include conditions without snowfall. The definition of the term 'climatology' is given in Sect. 5.4.3.

data	mean snowfall rate / mm year^{-1}
observations over Fram Strait during MCAOs	330
ERA5 along flight tracks during MCAOs	447
CARRA along flight tracks during MCAOs	143
ERA5 climatology	661
ERA5 climatology during MCAOs	476
observations at Ny-Ålesund during MCAOs between October 2021 and December 2022	666

Overall, the number of retrieved snowfall rates decreases with increasing rates (Fig. 5.7c, black). All observed snowfall rates are below 1 mm h^{-1} and thus classified as light precipitation (WMO, 1997). Nevertheless, we differentiate between light (< 0.1 mm h^{-1}), medium (0.1 – 0.3 mm h^{-1}), and heavy snowfall (> 0.3 mm h^{-1}) hereafter. Most of the resampled observations (53 %) detect no snowfall. Over all observations, the mean snowfall rate is 330 mm year^{-1} (Table 5.3), and the maximum rate is 4000 mm year^{-1}, corresponding to 0.46 mm h^{-1}. Note that the maximum rate holds for an approximately 30 km resolution. Considering snowfall events only, the mean snowfall rate increases to 700 mm year^{-1}. High precipitation rates contribute most to the total accumulation. Lasting 1 % of the measurement period, high snowfall rates would accumulate 11 % of the actual observed snow accumulation, while medium and light snowfall would accumulate approximately 5 and 1 % of the total accumulation.

We assess the spatial distribution of total snow accumulation by averaging the snowfall rates of all observations within each grid cell (Fig. 5.7d). The closer to the sea ice and the boundary of the measurement area, the more grid cells do not detect snowfall at all (gray cells). The overall snowfall rates are the lowest closer to the sea ice edge, and the highest over the central Fram Strait, directly west of the Svalbard archipelago. Among grid cells and times for which snowfall was detected ($S > 0.01$ mm h^{-1}), the snowfall pattern is similar (Fig. 5.7e). Nevertheless, some snowfall events close to sea ice, which are so rare that they do not enhance the overall snowfall rates (Fig. 5.7d), are intense (500–1000 mm year^{-1}; Fig. 5.7e).

The sea ice conditions under which the observations have been obtained differ due to the variety of years covered by the observations (Sect. 5.2.1). To analyze the influence of the open ocean and related

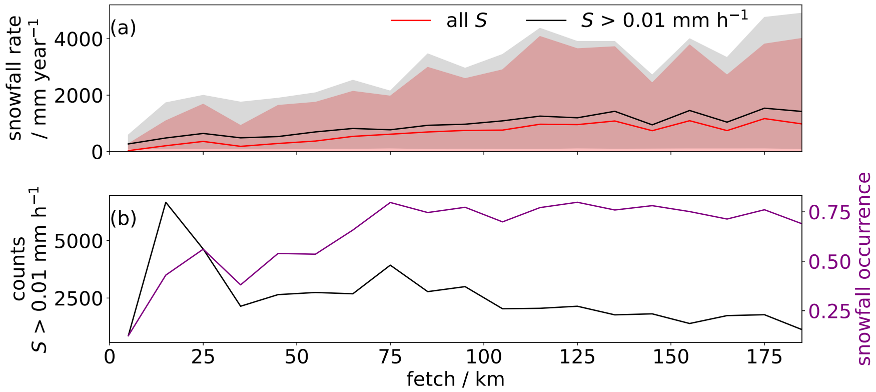

Figure 5.8: Snowfall rate dependency on fetch for all retrieved rates over the Fram Strait during marine cold air outbreaks (red) and respective rates above 0.01 mm h^{-1} (black) (a). The shades represent the 5th and 95th percentile of the data. Number of observations with snowfall rates above 0.01 mm h^{-1} (black) and detected snowfall occurrence (purple)(b).

surface heat fluxes on snowfall occurrence and intensity in depth, we investigate the dependence of snowfall on the travel distance over the open water, i. e., S along fetch (Fig. 5.8). We take S observations in their original resolution and only consider observations whose back trajectories did not pass the Svalbard archipelago to exclude potential lee effects. For the analyzed MCAO cases, these S estimates and their variability increase with fetch (Fig. 5.8a, red) for two reasons: The snowfall events intensify with fetch until 140 km fetch (Fig. 5.8a, black), particularly for the first 30 km fetch. Within the first 80 km of fetch, this intensification of snowfall is accompanied by an increase in snowfall occurrence (Fig. 5.8b, purple). For fetches beyond 80 km, snowfall occurrence is around 75 %, and the increase in S comes solely from the intensification of the already established events.

Next, we assess the spatial differences in snowfall rates during MCAOs stemming from the different conditions over the Fram Strait and at Ny-Ålesund (Fig. 5.7c). For Ny-Ålesund, we assess snowfall rates of low-level MPCs during MCAOs between October 2021 and December 2022. To obtain S, we apply the retrieved Z_e–S relation (Sect. 5.3) to the low-level MPC data set in its original temporal resolution (6 s, Sect. 5.2.2) and set the detection limit to 0.01 mm h^{-1}. To improve the comparability, we temporally resample the data over the Fram Strait and at Ny-Ålesund to the same resolution (1 h). Both data sets detect snowfall 50 % of the time (Fig. 5.7c). At Ny-Ålesund, nevertheless, the distribution is more positively skewed. Medium and heavy snowfall events occur more frequently at Ny-Ålesund and reach higher extreme rates than during the research flights over the Fram Strait. In contrast, the frequency of occurrence of light snowfall is reduced by 13 pp compared to over the Fram Strait. Thus, the mean snowfall rate at Ny-Ålesund is twice the rate over the Fram Strait (Table 5.3), leading to a higher total snow accumulation over a specific time at Ny-Ålesund.

Interestingly, high snowfall rates have been observed at Ny-Ålesund during different MCAO events under westerly to north-westerly wind directions (not shown). During MCAO events featuring these high snowfall rates, less intense snowfall was retrieved whenever the wind came more from the north (not shown). Under westerly to north-westerly wind directions, the fetch of the advected air is larger than for northerly winds when the air is advected over the Svalbard archipelago shortly before arriving at Ny-Ålesund. Thus, the finding that snowfall intensifies with fetch (Fig. 5.8a) likely applies to observations at Ny-Ålesund as well. However, further investigations are needed that also include orographic effects. In summary, westerly to north-westerly flows seem to intensify snowfall at Ny-Ålesund during MCAOs, resulting in larger snowfall rates than observed over the ocean.

5.4.2 *Snowfall comparison with reanalyses*

In this section, we investigate whether ERA5 and CARRA reanalysis represent the snowfall observations. To do so, we also resample the CARRA data to ERA5's spatial resolution and set CARRA's detection limit to 0.01 mm h^{-1}. Note that the temporal resolution is 1 h for ERA5 and the resampled observations and 3 h for CARRA. We compare the respective S distributions along the flight tracks and attribute differences between reanalyses and observations to limitations in the reanalyses.

The snowfall rate distribution of ERA5 and CARRA along the flight tracks differ (Fig. 5.9a). CARRA exhibits 42 pp fewer snowfall occurrences. Regardless of the snowfall intensity, ERA5 counts more relative occurrences than CARRA, especially for rates larger than 2300 mm year^{-1} that are not represented by CARRA at all.

Along the flight paths, ERA5 nicely represents the observed S distribution except for light rates (Fig. 5.9a). ERA5 misclassifies non-precipitating observations as slightly-precipitating and thus overestimates light snowfall by 43 pp and total snow accumulation along the flight paths by 34 %. Spatially, ERA5 mostly overestimates snowfall rates along the boundaries of the measurement area and underestimates the rates over the central Fram Strait (Fig. 5.9b). Thus, ERA5 underestimates snowfall rates in areas with high observed snowfall and vice versa (Fig. 5.7e).

Contrarily, CARRA slightly overestimates the relative occurrence of no snow by 10 pp compared to the observations and underestimates the relative occurrence of medium and high rates (Fig. 5.9a).

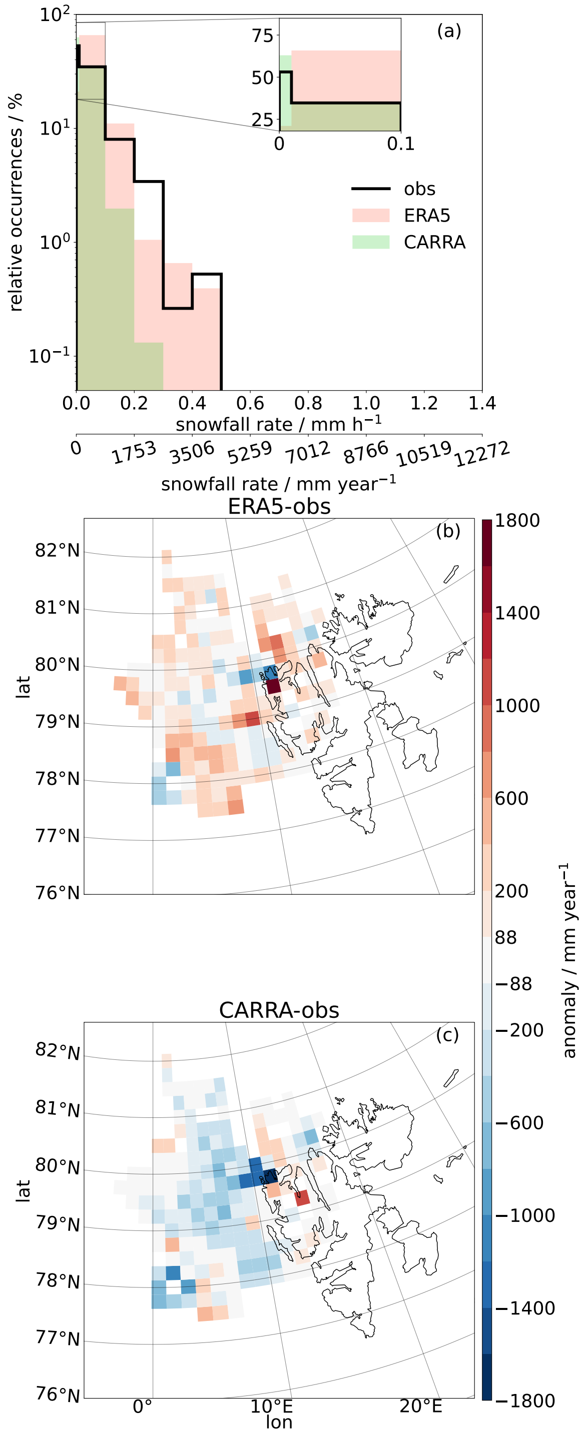

Figure 5.9: Snowfall rate estimates over the Fram Strait during marine cold air outbreaks from observations and reanalyses. Relative frequency distribution of snowfall rates from resampled (31 km, 1 h) observations over the Fram Strait (black), ERA5 reanalysis (red), and spatially resampled CARRA reanalysis (green) (a). Spatial distribution of the difference between estimates from reanalyses and resampled observations for ERA5 (b) and CARRA (c).

Therefore, CARRA underestimates total snow accumulation by 60 % relative to our observations. Spatially, CARRA underestimates the snowfall rates over the Fram Strait (Fig. 5.9c), rarely overestimates the rates at the boundary of the studied area, where the sample size is low (Fig. 5.7b), and resembles the observations close to the sea ice edge, probably due to highly-resolved sea ice concentrations within CARRA.

5.4.3 *Representativeness of the snowfall estimates*

Our observed mean snowfall rate (330 mm year^{-1}; Table 5.3) aligns approximately with the precipitation rate obtained over the Fram Strait by CMIP5 and 6, and GPCP observations (365 mm year^{-1}; McCrystall et al., 2021). However, our mean snowfall rate is about two to three times lower than corresponding ERA5 and CloudSat precipitation estimates (Lerber et al., 2022b; McCrystall et al., 2021). Contrarily to this study, the studies mentioned above assess precipitation rates over several years, including all kinds of meteorological conditions, and, despite the CloudSat observations, comprise rain and snowfall. This section investigates how the MCAO snowfall during the campaigns aligns with the long-term MCAO conditions over the Fram Strait.

We compare ERA5 data along the flight paths with the ERA5 snowfall rate climatology covering March, April, and May from 1979 until 2022. Herein, we first consider all snowfall events within the area over the Fram Strait (5°W – 10°E; 77.5 – 81.5°N) and second consider only events occurring during MCAOs. A comparison of the general (green) and MCAO (blue) ERA5 climatology indicates that under MCAO conditions, the maximum snowfall rate is less intense, and rates below 0.2 mm h^{-1} occur more frequently (Fig. 5.10a). However, the relative occurrence of snowfall is 8.5 pp higher during MCAOs. According to ERA5, snowfall occurs more frequently during MCAOs and is less intense than snowfall events in general. This agrees with findings from Mateling et al. (2023), who investigated CloudSat observations over the North Atlantic and found that, due to light snowfall, more snowfall is produced during MCAO compared to non-MCAO conditions. In ERA5, heavy snowfall over the northern North Atlantic sector is mainly attributed to cyclones and fronts (Lauer et al., 2023a). In our study, most high rates attributed to non-MCAO conditions occur in March and April. This is because, during AFLUX (ACLOUD), snow-dominated cyclones and fronts (rain-dominated atmospheric rivers) contributed most to the total precipitation (Lauer et al., 2023a).

During spring, snowfall rates are generally lower over the sea ice (below 700 mm year^{-1}) than over the open ocean and the Svalbard archipelago (roughly 1000 mm year^{-1}; Fig.5.10b). During MCAOs, rates are even lower over sea ice and land (Fig.5.10c, d). While souther-

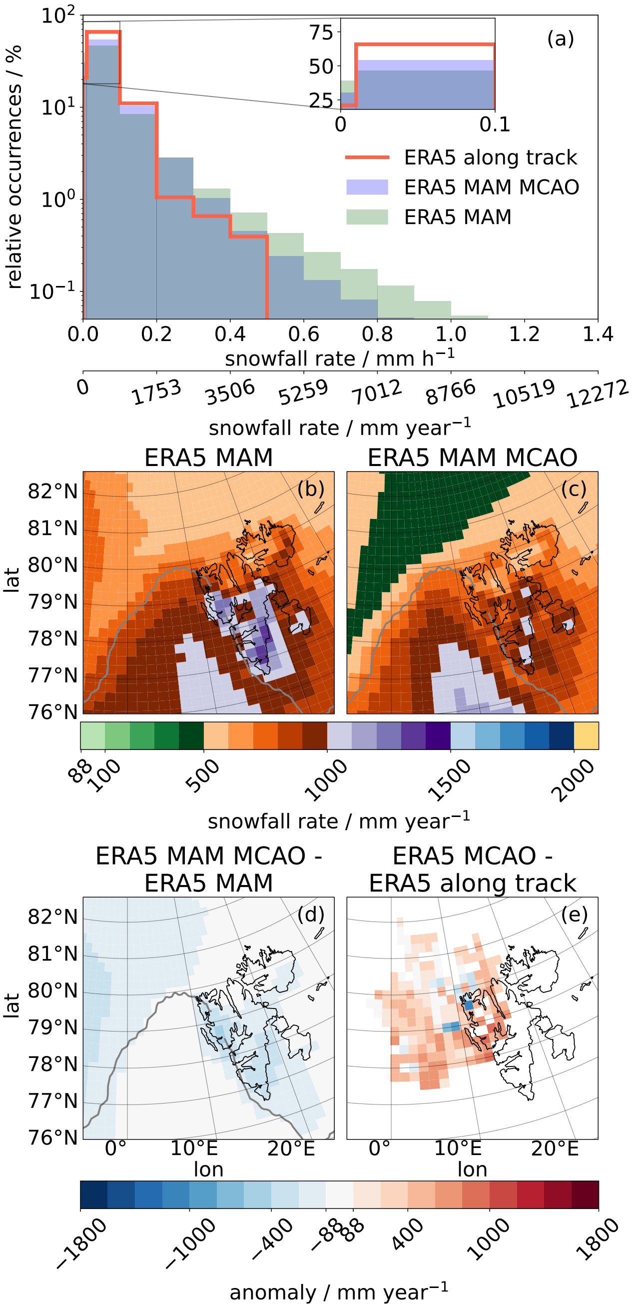

Figure 5.10: Snowfall rate estimates over the Fram Strait from ERA5 reanalysis. Relative frequency distribution of snowfall rates from ERA5 along the flight paths (orange), from ERA5 during March, April, and May between 1979 and 2022 (green), and from ERA5 during marine cold air outbreaks (MCAO) in March, April, and May between 1979 and 2022 (blue) (a). Spatial distribution of snowfall estimates from ERA5 during March, April, and May between 1979 and 2022 for all meteorological conditions (b), for MCAOs (c), and the respective difference (d). Spatial distribution of the difference between snowfall rates from the respective ERA5 MCAO climatology and ERA5 along the flight tracks (e).

ly flows from the open ocean transport more humid and warmer air over the sea ice that easily forms precipitation under the cold conditions over ice, the cold and dry airflow from the central Arctic reduces the snowfall rate during MCAOs. At first, surface heat fluxes from the open ocean moisten and warm the Arctic air, increasing snowfall rates. At least within the studied area, snowfall rates during MCAOs do not exceed general rates (Fig.5.10d).

The ERA5 climatology of snowfall during MCAOs in spring shows no snowfall for 30 % of the time, while along the tracks ERA5 shows no snowfall for 21 % of the time (Fig. 5.10a). Thus, ERA5 overestimates the snowfall occurrence along the tracks by 13 %. In particular, the light snowfall is overrepresented. However, the maximum snowfall rate of the ERA5 climatology is by a factor of more than seven larger than that along the tracks. The overestimation of snowfall occurrence and the underrepresentation of high snowfall rates along the tracks compared to the climatology result in similar mean snowfall rates. The mean snowfall rate along the tracks is only 6 % lower than the climatological one (Table 5.3). Spatially, the snowfall rates of the ERA5 climatology are higher than that of ERA5 along the tracks, almost over the entire Fram Strait, but most pronounced to the south (Fig.5.10e). The increasing difference with fetch is visible for all campaigns (not shown). All discrepancies between the ERA5 climatology during MCAOs in spring and ERA5 along the flight tracks arise due to exceptional weather conditions captured during the campaigns.

5.5 CONCLUSIONS AND OUTLOOK

In this study, we retrieve surface snowfall rates (S) for the Fram Strait region from airborne radar reflectivity observations (Z_e) obtained during marine cold air outbreaks (MCAO). To do so, we deduce a Z_e–S relation for low-level mixed-phase clouds (MPC) occurring under conditions similar to MCAO conditions over the Fram Strait. We derive the relation from observations from a 94 GHz radar and precipitation gauge at Ny-Ålesund. We also provide a sensitivity study for the retrieved relation, which considers observations averaged over 0.75 h. After applying the retrieved Z_e–S relation to the airborne observations over the Fram Strait, we can answer the research questions posed in Sect. 5.1:

1. How large is the snowfall rate over the Fram Strait during MCAOs probed throughout the (AC)³ campaigns, and do the measurements reveal spatial variability, e. g., compared to the well-equipped research station Ny-Ålesund, Svalbard?
   Averaged over all observations, the mean snowfall rate is 330 mm year^{-1}. The strength of S increases with fetch because, first, the precipitation events intensify until 140 km fetch, and second, the snowfall occurrence increases until 80 km fetch. At

Ny-Ålesund, the snowfall occurrence is similar to the one over the Fram Strait. Nevertheless, more intense snowfall occurs at Ny-Ålesund - especially during westerly to north-westerly flows, when the fetch of the advected air is presumably largest.

2. How well is snowfall captured by the global reanalysis ERA5 and the regional reanalysis CARRA?
   ERA5 (CARRA) overestimates (underestimates) the total snow accumulation along the flight tracks because of too much light (too few heavy) snowfall events. Even though CARRA has a higher resolution, it reproduces the observed mean snowfall rate worse than ERA5. Overall, CARRA underestimates snowfall rates over open ocean, whereas ERA5 generally underestimates heavy snowfall and overestimates light snowfall.

   The investigation of factors causing the differences between reanalyses and observations is beyond the scope of this study and should be tackled in future work. In particular, this study does not investigate the microphysical processes whose representations must be improved within the reanalyses in order to reduce the biases mentioned above. For ERA5 in particular, a too-smooth sea ice distribution in the marginal sea ice zone and a limited atmosphere-ocean exchange parametrization induce an overestimation of sensible heat fluxes at high sea ice fractions and vice versa (Renfrew et al., 2021). This presumably has a similar influence on snowfall rates.

3. Do the snowfall estimates retrieved during the campaigns represent typical MCAO conditions?
   The mean snowfall rate of the ERA5 climatology during MCAOs in spring and ERA5 along the flight tracks fit well; the rate along the flight tracks is only 6 % lower. However, there are likely two compensating effects at play. While ERA5 overestimates the snowfall occurrence along the tracks by 13 % due to an overrepresentation of light snow, it misses the very high snowfall rates due to flight restrictions. The ERA5 estimates along the tracks represent the observed flight conditions and enable a comparison with the ERA5 climatology, which suffers the same limitations stemming from the reanalysis.

Over the studied area covering the Fram Strait until 76°N, ERA5 snowfall rates during MCAOs in spring do not exceed rates occurring under further meteorological conditions. Further south, fetches increase, and snowfall rates during MCAOs might eventually exceed the general rates. This hypothesis should be studied using ERA5 data and verified by observations, e. g., from the Cold-Air Outbreaks in the Marine Boundary Layer Experiment (COMBLE) that comprises fetches around 1000 km (Geerts et al., 2022). In the future, our data set can be used to evaluate snowfall estimates from ERA6 and passive satellite retrievals (Camplani et al., 2024) over the Fram Strait during MCAOs.

DATA AVAILABILITY

The processed MiRAC-A radar observations obtained during ACLOUD (Mech et al., 2022a), AFLUX (Mech et al., 2022b), and HALO-(AC)³ (Mech et al., 2024), the dropsonde data obtained during ACLOUD (Ehrlich et al., 2019), AFLUX (Becker et al., 2020), MOSAiC-ACA (Becker et al., 2021), and HALO-(AC)³ (George et al., 2024), and the VISS images from Ny-Ålesund (Maahn and Maherndl, 2023) are published at PANGEA. The airborne data are accessed via the ac3airborne module (Mech et al., 2022). The radar and precipitation gauge data from Ny-Ålesund were processed by Chellini et al. (2023a) and are stored under Chellini et al. (2023b). The ERA5 snowfall climatology and back trajectories are calculated from ERA5 reanalysis data (Hersbach et al., 2017, 2020). ERA5 is available on pressure levels (Hersbach et al., 2023a) and single levels (Hersbach et al., 2023b). ERA5 snowfall data are accessed via Levante at DKRZ. The CARRA snowfall climatology is calculated using data at single levels (Schyberg et al., 2020). The merged MODIS-AMSR2 sea ice concentration data are provided by the Institute of Environmental Physics at the University of Bremen (Ludwig and Spreen, 2023).

COMPETING INTERESTS

The authors declare no competing interests.

ACKNOWLEDGEMENTS

We gratefully acknowledge the funding from the Deutsche Forschungsgemeinschaft (DFG, German Research Foundation; project no. 268020496) within the Transregional Collaborative Research Center TR 172 "ArctiC Amplification: Climate Relevant Atmospheric and SurfaCe Processes, and Feedback Mechanisms (AC)³". We are grateful for the support from the Alfred-Wegener-Institute, DLR, and aircraft crews during all campaigns. Many thanks to Benjamin Kirbus for providing the back trajectory calculations and Giovanni Chellini for processing the radar data at Ny-Ålesund.

6

CONCLUSIONS AND PERSPECTIVES

6.1 SUMMARY AND CONCLUSIONS

The aim of this thesis is to characterize and improve the understanding of Arctic low-level clouds and snowfall over the Fram Strait. Three research questions were posed at the beginning of this work and addressed by the presented studies using high-resolution airborne radar measurements obtained by the Microwave Radar/radiometer for Arctic Clouds (MiRAC) during four campaigns within the ArctiC Amplification: Climate Relevant Atmospheric and SurfaCe Processes, and Feedback Mechanisms ((AC)^3) project. In the following, brief answers to the questions are provided:

HOW LARGE IS THE LOW-LEVEL CLOUD FRACTION OVER THE FRAM STRAIT, AND HOW WELL CAN IT BE DERIVED FROM SATELLITE OBSERVATIONS?

The airborne observations are analyzed and used to forward-simulate CloudSat measurements that serve as a proxy for CloudSat observations. Hereafter, the hydrometeor fraction, which includes clouds and precipitation, is called the cloud fraction.

The vertically resolved cloud fraction below 2.5 km height obtained by MiRAC over all campaigns is on average 30 %, with lower values of about 15 % at 2.5 km and a maximum of 40 % close to the ground. Cloud fractions over sea ice show a relatively constant vertical profile, while low-level cloud formation strongly enhances cloud fraction over water up to around 1 km height. Northerly flows are mainly connected to Marine Cold Air Outbreaks (MCAOs) and thus show the highest low-level cloud fraction that also includes particularly light snow events.

Due to CloudSat limitations, the forward-simulated cloud fraction increases at 720 m altitude by 11 pp, which is 33 % of the MiRAC cloud fraction. Nevertheless, there are compensating effects at play: CloudSat's sensitivity decreases the cloud fraction by a maximum of 30 pp. CloudSat's horizontal resolution, however, increases the cloud fraction by a maximum of 25 pp and its range resolution, which stems from the long pulse length, by a maximum of 20 pp. CloudSat's lower spatial resolution fills cloud gaps and stretches clouds by about 240 m at their tops and bottoms. Both effects increase the cloud fraction of the forward-simulated observations stronger, the closer to the ground. Also, layers of multilayer clouds are merged, which reduces the number of multilayer clouds obtained by MiRAC (48 %) by a factor of 4 during the forward simulations. While the forward simulations represent MiRAC's cloud fraction over sea ice well, they overestimate MiRAC's cloud fraction by 16 pp strongest over water during MCAOs due to cloud top stretching.

This study also investigates CloudSat's blind zone limitations on snowfall occurrence and an underestimation of the total precipitation amount by 51 pp is found. This finding hampers efforts to quantify snowfall from space, especially light snowfall during MCAOs. In conclusion, MiRAC and CloudSat radar reflectivities differ substantially below 1.5 km, such that airborne remote sensing is necessary to resolve fine cloud structures and CloudSat's blind zone, especially during MCAOs. This is considered for the second study that answers the following question:

DO ENVIRONMENTAL CONDITIONS PRECONDITION MCAO EVOLUTION, AND HOW DO ROLL CIRCULATION AND CLOUD PROPERTIES CHANGE WITH FETCH IN THE INITIAL STATE OF MCAOs?

The evolution of thermodynamics, cloud and circulation morphology, cloud microphysics, and precipitation within the air during a long-lasting MCAO over the Fram Strait is studied within the first 170 km fetch, i. e., about 4 hours of travel time. The analysis is based on airborne remote sensing and in situ observations performed during the *High Altitude LOng range aircraft* (HALO)-(AC)^3 campaign on 1 and 4 April 2022. Roll circulations are detected by a novel approach using vertical radar profiles only, fetch is retrieved from calculated back trajectories, and composite approaches characterize both.

For both MCAO cases, environmental conditions precondition boundary layer and cloud characteristics slightly differently: both MCAO events feature northerly winds that advect dry and cold air over the Fram Strait. On 1 April, however, air temperatures are colder, doubling the MCAO index and heat fluxes compared to 4 April. The stronger convection on 1 April deepens the boundary layer and lifts the cloud top heights by a factor of two.

Another factor that preconditions the MCAO evolution is the Svalbard archipelago. On 1 April, the island provokes a wave effect in its lee with subsiding air masses that reduces cloud top heights at 75 to 100 km fetch. On 4 April, the lee effect causes an even larger cloud-free area and a convergence zone west of Svalbard.

Moreover, the occurrence of riming differs between the MCAO cases and might impact cloud and precipitation characteristics and evolution. Riming is only significantly active during the cold and strong MCAO case on 1 April. On this day, the median Liquid Water Path (LWP), supercooled liquid layer thickness at the cloud top, and precipitation strength are about two times higher, and precipitation onset is earlier. The local maximum found in the spectral analysis of riming equals the wavelength of roll clouds on 1 April. Thus, significant riming on 1 April might have occurred in updraft regions. Riming in updrafts would also explain the following modifications in updraft regions compared to the residual cloud: increased snowfall rates by producing larger ice particles, increased normalized height of maximum ice, and reduced liquid layer thickness as ice particles might be lifted into the pure liquid layer. Nevertheless, the relative occurrence of liquid-topped Mixed-Phase Clouds (MPCs) is higher on 1 April.

With increasing fetch, clouds evolve as follows: Cloud Top Height (CTH), LWP, equivalent radar reflectivity (Z_e), near-surface liquid-equivalent snowfall rate (S), horizontal cloud cover, and the fraction of precipitating profiles increase. Cloud streets form at around 15 km fetch and start precipitating at 25 to 40 km. The wavelengths of the roll circulations slightly increase with increasing fetch on 1 April. Nevertheless, the variability of the wavelengths is high at fetches below 60 km on both days, which leads to a decrease in the aspect ratio of the circulations, i. e., the ratio between circulation wavelength and CTH, within these fetches.

To study the evolution of S with fetch, a fixed Z_e–S relation assessing three bullet rosettes (Kulie and Bennartz, 2009) was applied to the radar observations. The retrieved S estimates are only rough estimates since Z_e–S relations highly depend on ice habits, which might be very variable within the studied MPCs.

The third study derives a specific Z_e–S relation for low-level MPCs under MCAO conditions for the Fram Strait, thus revealing more precise S estimates. The relation is derived from ground-based radar and precipitation gauge observations obtained at Ny-Ålesund and applied to airborne Z_e observations. These airborne observations have been obtained over the Fram Strait during campaigns within the $(AC)^3$ project in spring and early summer. The retrieved surface snowfall rates allow to answer the following question:

HOW MUCH SNOW FALLS OVER THE FRAM STRAIT DURING MCAOS, AND HOW WELL DO CURRENT REANALYSES CAPTURE THE OBSERVED SNOWFALL RATES?

Averaged over all observations, the mean snowfall rate of low-level MPCs during MCAOs is 330 mm year^{-1}. The strength of S increases with fetch because, first, the precipitation events intensify until 140 km fetch and, second, the fraction of snowfall observations increases until 80 km fetch. At Ny-Ålesund, the snowfall fraction is similar to the one over the Fram Strait. Nevertheless, more intense snowfall occurs at Ny-Ålesund, especially during westerly to north-westerly flows, when the fetch of the advected air is presumably at a maximum.

Snowfall estimates from the European Centre for Medium-range Weather Forecast (ECMWF) ReAnalysis version 5 (ERA5) (Copernicus Arctic Regional ReAnalysis (CARRA)) overestimate (underestimate) the total snow accumulation along the flight tracks because of too many light (too few heavy) snowfall events. ERA5 mostly overestimates the strength of the light snowfall and slightly underestimates the strength of the intense snowfall over the central Fram Strait. CARRA, however, underestimates most of the snowfall over open ocean.

Nevertheless, note that the observations do not represent typical snowfall conditions: Even though the ERA5 climatological mean snowfall rate during MCAOs in spring is only 6 % higher than the ERA5 mean snowfall rate along the flight tracks, there are two compensating effects at play: ERA5 has a 13 % higher snowfall occurrence along the tracks due to an overrepresentation of light snow and misses the high snowfall rates due to flight restrictions.

6.2 OUTLOOK

An improved understanding of low-level MPCs over the Fram Strait and the snowfall related to it is gained within the framework of this thesis. For each study, future steps are presented in the following that might answer unresolved questions or consider improvements to the applied methodologies. A recommendation that holds for all studies is to expand the conditions covered by the observations by including observations during summer and polar night.

In May 2024, the Earth Clouds, Aerosols and Radiation Explorer (EarthCARE) was launched, whose Cloud Profiling Radar (CPR) is the successor of CloudSat CPR (Illingworth et al., 2015; Wehr et al., 2023). The unique spaceborne Doppler capabilities on board raise new opportunities to sample not only cloud fraction and structure but also vertical motions within clouds and precipitation. The pulse length and thus range resolution (~500 m) and blind zone depth (~1 km) are the same for both CPR (Burns et al., 2016). Compared to the CloudSat CPR (Stephens et al., 2002, 2008; Tanelli et al., 2008), however, the EarthCARE CPR is more sensitive (-36 vs. -26 dBZ) and has a higher sampling rate (100 vs. 240 m; Burns et al., 2016). The different CPR specifications modify the cloud observations despite similar cloud conditions, which highlights the importance of being aware of the EarthCARE CPR limitations. Burns et al. (2016) already studied the limitations of EarthCARE in assessing marine stratus clouds: they suggest that the higher range sampling rate compared to CloudSat improves the detection within the blind zone by an order of magnitude. Moreover, they predict that the EarthCARE CPR range resolution leads to overestimating the cloud top heights by 100 m. However, this thesis found that CloudSat stretches cloud tops by 240 m for Arctic low-level clouds over the ocean. Since EarthCARE

CPR has the same range resolution and higher sensitivity compared to CloudSat, the cloud top stretching and thus cloud fraction overestimation by EarthCARE is assumed to be stronger compared to CloudSat and compared to EarthCARE observations of marine stratus clouds. This hypothesis should be tested during the upcoming airborne campaign COMPEX-EC (Clouds over cOMPlEX environment – EarthCARE) campaign in April 2025 that aims to validate EarthCARE observations.

In the future, the implications of EarthCARE's new payload on the assessed Arctic cloud fraction should be studied. To do so, the forward simulator applied in this thesis should be improved by implementing blind zone effects more accurately. The surface echo should be also simulated by the applied range weighting function (Lamer et al., 2020). This has already been implemented in the airborne reader of the 'orbital-radar' Python tool (Pfitzenmaier et al., 2024) that can be easily used for follow-up studies. Finally, the error raised by assuming a homogenous cloud field within the field of view across the track and by not considering an across-track convolution should be estimated in the future.

The second study presented in this thesis is a benchmark for future model evaluation studies about cloud street development during MCAOs. The developed composite approaches characterize the roll circulation and development along fetch. These metrics can also be generated from cloud-resolving model output. The results can be used to evaluate the representation of microphysics and dynamics during MCAOs in numerical models and to detect weak points in parametrization schemes. It is of particular interest whether these models successfully reproduce the different MCAO strengths and preconditioning conditions, such as the microphysics, i. e., LWP and riming, but similar cloud evolutions during the two studied MCAO events.

The aircraft observations of the two MCAO cases still provide unexplored information: for example, the flight paths feature several overpasses over the same locations. This has been exploited recently by Klingebiel et al. (2024), who studied the temporal evolution of cloud street properties. Nevertheless, an in-depth investigation of the temporal evolution of roll circulations, cloud macroscopic metrics such as wavelength or aspect ratio, and cloud microphysical properties needs to be included.

Still, questions remain that cannot be answered based on the conducted observations. The upcoming Clouds over cOMPlEX environment (COMPEX) campaign scheduled for spring 2025 northwest of Svalbard raises the opportunity to tackle these questions. The following unresolved research questions and proposed flight strategies should be considered during flight planning.

To answer whether cloud street evolution is already preconditioned over sea ice by e. g., sea ice inhomogeneities, further airborne observations over sea ice are required. Characterizing the impact of the sharpness of the Marginal Ice Zone (MIZ) on air mass transformation is particularly valuable - also for model comparison and evaluation studies (Spensberger and Spengler, 2021). Future flights should be conducted at constant fetch over open water, and at variable fetch over MIZ near the sea ice edge. According to the model study by Spensberger and Spengler (2021), also flow divergence affects cloud street and precipitation development. Especially over the Fram Strait, flow divergence is frequently induced by the Svalbard archipelago. However, the effect of divergence on cloud street evolution has yet to be studied by observations. Finally, the cloud top temperatures during the studied MCAO cases lie within the Dendritic Growth Zone (DGZ). Thus, aggregation would be another dominant precipitation-forming microphysical processes to study, e. g., by dual frequency radar observations (Chellini et al., 2022). The instantaneous deployment of a W– (94 GHz) and differential absorption G–band (167.3 and 174.7 GHz) radar during COMPEX will open possibilities to do so.

In the third study, snowfall rates are retrieved over the Fram Strait using a Z_e–S relation derived from precipitation gauge observations. These gauge observations have a low sensitivity and are prone to high uncertainties. Thus, deducing an improved relation using observations of the laser disdrometer Particle Size Velocity (PARSIVEL) might be reasonable - also to verify the applied relation. PARSIVEL observations include different measures of particle size, fall velocity, particle size distribution, and a particle shape description (Battaglia et al., 2010). From derived velocity and mass distributions and measured particle size distributions, S could be determined for Ny-Ålesund following Lerber et al. (2017). This method also allows to retrieve individual relations for different microphysical regimes that the particle shape measurements can distinguish.

Yet, only snowfall rates of low-level MPCs during MCAOs are retrieved for the Fram Strait. The data set could be expanded by retrieving a Z_e–S relation using radar data from Ny-Ålesund at 35 GHz and applying the new relation to radar observations obtained by MIRA-36 (Melchionna et al., 2008) on board HALO. MIRA-36 is part of the HALO Microwave Package (HAMP; Mech et al., 2014) and operates at 35.5 GHz. During HALO-(AC)^3, HALO covered areas between Kiruna, Sweden, and the North Pole. Thus, a snowfall data set derived from MIRA-36 observations would cover a larger area than the one derived from MiRAC observations on board *Polar 5* (P5). Contrarily to P5, HALO frequently probed warm air intrusions, providing the opportunity to retrieve snowfall estimates under meteorological conditions other than MCAOs. Retrieving snowfall estimates for warm air intrusions in the Arctic is crucial as local and heavy snowfall events are connected to these intrusions (Lauer et al., 2023b). Since Z_e–S relations strongly depend on cloud microphysics (Doviak and Zrnić, 2006), an optimal relation has to be retrieved for warm air intrusions at Ny-Ålesund, first.

The presented comparisons between observations and reanalyses indicate potential improvements in the representation of snowfall in reanalyses. Factors causing the differences between reanalyses and observations should be identified in future work. For ERA5 in particular, a too-smooth sea ice distribution in the MIZ and a limited atmosphere-ocean exchange parametrization induce an overestimation of sensible heat fluxes at high sea ice fractions and vice versa (Renfrew et al., 2021). This presumably has a similar influence on snowfall rates.

In the future, the retrieved snowfall estimates over the Fram Strait could also serve to evaluate further observations, models, or reanalyses. Currently, the ECMWF establishes the ERA6 reanalysis (Hersbach et al., 2022), which serves as the successor for ERA5 and comprises various improvements regarding spatial resolution (horizontal resolution of up to 14 km) and number of observations considered for data assimilation. It will be interesting to see whether the snowfall estimates improve and whether the location of mesoscale systems is resolved correctly. Imprecisely collocated mesoscale systems, which have not been explicitly resolved in ERA5, increase the potential to model poorer snowfall estimates.

Retrieving Arctic-wide snowfall from observations is a challenge that has been tackled by the spaceborne High lAtitude sNow Detection and Estimation aLgorithm for Advanced Technology Microwave Sounder (HANDEL-ATMS; Camplani et al., 2024). This snowfall retrieval is based on machine learning and uses passive ATMS and active CloudSat CPR observations as input and for testing, respectively. To evaluate HANDEL-ATMS, the spaceborne snowfall estimates should be collocated with the airborne estimates obtained in this thesis. Thus, the airborne snowfall estimates offer the opportunity to improve the spaceborne retrieval algorithm and to improve the accuracy of snowfall estimates that cover the entire Arctic.

BIBLIOGRAPHY

Abel, S. J., I. A. Boutle, K. Waite, S. Fox, P. R. A. Brown, R. Cotton, G. Lloyd, T. W. Choularton, and K. N. Bower (2017). “The Role of Precipitation in Controlling the Transition from Stratocumulus to Cumulus Clouds in a Northern Hemisphere Cold-Air Outbreak.” In: *Journal of the Atmospheric Sciences* 74.7, pp. 2293–2314. DOI: `10.1175/JAS-D-16-0362.1`.

Adler, R. F., M. R. P. Sapiano, G. J. Huffman, J.-J. Wang, G. Gu, D. Bolvin, L. Chiu, U. Schneider, A. Becker, E. Nelkin, P. Xie, R. Ferraro, and D.-B. Shin (2018). “The Global Precipitation Climatology Project (GPCP) Monthly Analysis (New Version 2.3) and a Review of 2017 Global Precipitation.” In: *Atmosphere* 9.4, p. 138. DOI: `10.3390/atmos9040138`.

Afargan-Gerstman, H., I. Polkova, L. Papritz, P. Ruggieri, M. P. King, P. J. Athanasiadis, J. Baehr, and D. I. V. Domeisen (2020). “Stratospheric influence on North Atlantic marine cold air outbreaks following sudden stratospheric warming events.” In: *Weather and Climate Dynamics* 1.2, pp. 541–553. DOI: `10.5194/wcd-1-541-2020`.

Akkermans, T., T. Böhme, M. Demuzere, S. Crewell, C. Selbach, T. Reinhardt, A. Seifert, F. Ament, and N. P. M. van Lipzig (2012). “Regime-dependent evaluation of accumulated precipitation in COSMO.” In: *Theoretical and Applied Climatology* 108.1, pp. 39–52. DOI: `10.1007/s00704-011-0502-0`.

Ansmann, A., M. Tesche, D. Althausen, D. Müller, P. Seifert, V. Freudenthaler, B. Heese, M. Wiegner, G. Pisani, P. Knippertz, and O. Dubovik (2008). “Influence of Saharan dust on cloud glaciation in southern Morocco during the Saharan Mineral Dust Experiment.” In: *Journal of Geophysical Research: Atmospheres* 113.D4, p. D04210. DOI: `10.1029/2007JD008785`.

Ansmann, A., K. Ohneiser, R. Engelmann, M. Radenz, H. Griesche, J. Hofer, D. Althausen, J. M. Creamean, M. C. Boyer, D. A. Knopf, S. Dahlke, M. Maturilli, H. Gebauer, J. Bühl, C. Jimenez, P. Seifert, and U. Wandinger (2023). “Annual cycle of aerosol properties over the central Arctic during MOSAiC 2019–2020 – light-extinction, CCN, and INP levels from the boundary layer to the tropopause.” In: *Atmospheric Chemistry and Physics* 23.19, pp. 12821–12849. DOI: `10.5194/acp-23-12821-2023`.

Atkinson, B. W. and J. Wu Zhang (1996). “Mesoscale shallow convection in the atmosphere.” In: *Reviews of Geophysics* 34.4, pp. 403–431. DOI: `10.1029/96RG02623`.

Bailey, H., A. Hubbard, E. S. Klein, K.-R. Mustonen, P. D. Akers, H. Marttila, and J. M. Welker (2021). “Arctic sea-ice loss fuels extreme European snowfall.” In: *Nature Geoscience* 14.5, pp. 283–288. DOI: `10.1038/s41561-021-00719-y`.

Barker, H. W., A. V. Korolev, D. R. Hudak, J. W. Strapp, K. B. Strawbridge, and M. Wolde (2008). “A comparison between CloudSat and aircraft data for a multilayer, mixed phase cloud system during the Canadian CloudSat-CALIPSO Validation Project.” In: *Journal of Geophysical Research: Atmospheres* 113.D8. DOI: `10.1029/2008JD009971`.

Barrett, A. I., R. J. Hogan, and R. M. Forbes (2017). “Why are mixed-phase altocumulus clouds poorly predicted by large-scale models? Part 1. Physical processes.” In: *Journal of Geophysical Research: Atmospheres* 122.18, pp. 9903–9926. DOI: `10.1002/2016JD026321`.

Battaglia, A., E. Rustemeier, A. Tokay, U. Blahak, and C. Simmer (2010). “PARSIVEL Snow Observations: A Critical Assessment.” In: *Journal of Atmospheric and Oceanic Technology* 27.2, pp. 333–344. DOI: `10.1175/2009JTECHA1332.1`.

Baumgardner, D., J. L. Brenguier, A. Bucholtz, H. Coe, P. DeMott, T. J. Garrett, J. F. Gayet, M. Hermann, A. Heymsfield, A. Korolev, M. Krämer, A. Petzold, W. Strapp, P. Pilewskie, J. Taylor, C. Twohy, M. Wendisch, W. Bachalo, and P. Chuang (2011). “Airborne instruments to measure atmospheric aerosol particles, clouds and radiation: A cook’s tour of mature and emerging technology.” In: *Atmospheric Research* 102.1, pp. 10–29. DOI: `10.1016/j.atmosres.2011.06.021`.

Beck, A., J. Henneberger, J. P. Fugal, R. O. David, L. Lacher, and U. Lohmann (2018). “Impact of surface and near-surface processes on ice crystal concentrations measured at mountain-top research stations.” In: *Atmospheric Chemistry and Physics* 18.12, pp. 8909–8927. DOI: `10.5194/acp-18-8909-2018`.

Becker, S., A. Ehrlich, M. Mech, C. Lüpkes, and M. Wendisch (2021). *Meteorological measurements by dropsondes released from POLAR 5 during MOSAiC-ACA 2020*. PANGEA [data set]. DOI: `10.1594/PANGAEA.933581`.

Becker, S., A. Ehrlich, J. Stapf, C. Lüpkes, M. Mech, S. Crewell, and M. Wendisch (2020). *Meteorological measurements by dropsondes released from POLAR 5 during AFLUX 2019*. PANGEA [data set]. DOI: `10.1594/PANGAEA.921996`.

Bennartz, R., M. D. Shupe, D. D. Turner, V. P. Walden, K. Steffen, C. J. Cox, M. S. Kulie, N. B. Miller, and C. Pettersen (2013). “July 2012 Greenland melt extent enhanced by low-level liquid clouds.” In: *Nature* 496.7443, pp. 83–86. DOI: `10.1038/nature12002`.

Bergeron, T. (1928). *Über die dreidimensional verknüpfende Wetteranalyse*. Vol. 6. 5. Geophys. Norv.

Bintanja, R. (2018). “The impact of Arctic warming on increased rainfall.” In: *Scientific Reports* 8.1, p. 16001. DOI: `10.1038/s41598-018-34450-3`.

Bintanja, R. and O. Andry (2017). "Towards a rain-dominated Arctic." In: *Nature Climate Change* 7.4, pp. 263–267. DOI: `10.1038/nclimate3240`.

Bintanja, R. and F. M. Selten (2014). "Future increases in Arctic precipitation linked to local evaporation and sea-ice retreat." In: *Nature* 509.7501, pp. 479–482. DOI: `10.1038/nature13259`.

Blanchard, Y., J. Pelon, E. W. Eloranta, K. P. Moran, J. Delanoë, and G. Sèze (2014). "A Synergistic Analysis of Cloud Cover and Vertical Distribution from A-Train and Ground-Based Sensors over the High Arctic Station Eureka from 2006 to 2010." In: *Journal of Applied Meteorology and Climatology* 53.11, pp. 2553–2570. DOI: `10.1175/JAMC-D-14-0021.1`.

Block, K., F. A. Schneider, J. Mülmenstädt, M. Salzmann, and J. Quaas (2020). "Climate models disagree on the sign of total radiative feedback in the Arctic." In: *Tellus A: Dynamic Meteorology and Oceanography* 72.1, pp. 1–14. DOI: `10.1080/16000870.2019.1696139`.

Boer, G. de, H. Morrison, M. D. Shupe, and R. Hildner (2011). "Evidence of liquid dependent ice nucleation in high-latitude stratiform clouds from surface remote sensors." In: *Geophysical Research Letters* 38.1. DOI: `10.1029/2010GL046016`.

Boisvert, L. N. and J. C. Stroeve (2015). "The Arctic is becoming warmer and wetter as revealed by the Atmospheric Infrared Sounder." In: *Geophysical Research Letters* 42.11, pp. 4439–4446. DOI: `10.1002/2015GL063775`.

Brown, R. A. (1972). "On the Inflection Point Instability of a Stratified Ekman Boundary Layer." In: *Journal of the Atmospheric Sciences* 29.5, pp. 850–859. DOI: `10.1175/1520-0469(1972)029<0850:OTIPIO>2.0.CO;2`.

Brümmer, B., S. Bakan, and H. Hinzpeter (1985). "Kontur: Observations of cloud streets and open cellular structures." In: *Dynamics of Atmospheres and Oceans* 9.3, pp. 281–296. DOI: `10.1016/0377-0265(85)90024-7`.

Brümmer, B., H. Schlünzen, and W. Bögel (1982). "Cloud Streets During KonTur." In: *Hamburger Geophysikalische Einzelschriften* 57, pp. 63–77.

Brümmer, B. (1996). "Boundary-layer modification in wintertime cold-air outbreaks from the Arctic sea ice." In: *Boundary-Layer Meteorology* 80.1-2, pp. 109–125. DOI: `10.1007/BF00119014`.

— (1997). "Boundary Layer Mass, Water, and Heat Budgets in Wintertime Cold-Air Outbreaks from the Arctic Sea Ice." In: *Monthly Weather Review* 125.8, pp. 1824–1837. DOI: `10.1175/1520-0493(1997)125<1824:BLMWAH>2.0.CO;2`.

— (1999). "Roll and Cell Convection in Wintertime Arctic Cold-Air Outbreaks." In: *Journal of the Atmospheric Sciences* 56.15, pp. 2613–

2636. DOI: 10.1175/1520-0469(1999)056<2613:RACCIW>2.0.CO;2.

Brümmer, B., B. Rump, and G. Kruspe (1992). "A cold air outbreak near Spitsbergen in springtime — Boundary-layer modification and cloud development." In: *Boundary-Layer Meteorology* 61.1, pp. 13–46. DOI: 10.1007/BF02033993.

Burns, D., P. Kollias, A. Tatarevic, A. Battaglia, and S. Tanelli (2016). "The performance of the EarthCARE Cloud Profiling Radar in marine stratiform clouds." In: *Journal of Geophysical Research: Atmospheres* 121.24, pp. 14,525–14,537. DOI: 10.1002/2016JD025090.

Cai, Z., Q. You, H. W. Chen, R. Zhang, Z. Zuo, D. Chen, J. Cohen, and J. A. Screen (2024). "Assessing Arctic wetting: Performances of CMIP6 models and projections of precipitation changes." In: *Atmospheric Research* 297, p. 107124. DOI: 10.1016/j.atmosres.2023.107124.

Campbell, J. R. and M. Shiobara (2008). "Glaciation of a mixed-phase boundary layer cloud at a coastal arctic site as depicted in continuous lidar measurements." In: *Polar Science* 2.2, pp. 121–127. DOI: 10.1016/j.polar.2008.04.004.

Camplani, A., D. Casella, P. Sanó, and G. Panegrossi (2024). "The High lAtitude sNowfall Detection and Estimation aLgorithm for ATMS (HANDEL-ATMS): a new algorithm for snowfall retrieval at high latitudes." In: *Atmospheric Measurement Techniques* 17.7, pp. 2195–2217. DOI: 10.5194/amt-17-2195-2024.

Castellani, B. B., M. D. Shupe, D. R. Hudak, and B. E. Sheppard (2015). "The annual cycle of snowfall at Summit, Greenland." In: *Journal of Geophysical Research: Atmospheres* 120.13, pp. 6654–6668. DOI: 10.1002/2015JD023072.

Cesana, G., D. E. Waliser, X. Jiang, and J.-L. F. Li (2015). "Multimodel evaluation of cloud phase transition using satellite and reanalysis data." In: *Journal of Geophysical Research: Atmospheres* 120.15, pp. 7871–7892. DOI: 10.1002/2014JD022932.

Cesana, G. V., O. Pierpaoli, M. Ottaviani, L. Vu, Z. Jin, and I. Silber (2024). "The correlation between Arctic sea ice, cloud phase and radiation using A-Train satellites." In: *Atmospheric Chemistry and Physics* 24.13, pp. 7899–7909. DOI: 10.5194/acp-24-7899-2024.

Chellini, G., R. Gierens, K. Ebell, T. Kiszler, P. Krobot, A. Myagkov, V. Schemann, and S. Kneifel (2023a). "Low-level mixed-phase clouds at the high Arctic site of Ny-Ålesund: a comprehensive long-term dataset of remote sensing observations." In: *Earth System Science Data* 15.12, pp. 5427–5448. DOI: 10.5194/essd-15-5427-2023.

Chellini, G., R. Gierens, K. Ebell, T. Kiszler, and S. Kneifel (2023b). *Low-level mixed-phase clouds at the high Arctic site of Ny-Ålesund: A comprehensive long-term dataset of remote sensing observations*. Zenodo [data set]. Version 1.0. DOI: 10.5281/zenodo.7803064.

Chellini, G., R. Gierens, and S. Kneifel (2022). “Ice Aggregation in Low-Level Mixed-Phase Clouds at a High Arctic Site: Enhanced by Dendritic Growth and Absent Close to the Melting Level.” In: *Journal of Geophysical Research: Atmospheres* 127.16. DOI: `10.1029/2022JD036860`.

Chellini, G. and S. Kneifel (2024). “Turbulence as a Key Driver of Ice Aggregation and Riming in Arctic Low-Level Mixed-Phase Clouds, Revealed by Long-Term Cloud Radar Observations.” In: *Geophysical Research Letters* 51.6, e2023GL106599. DOI: `10.1029/2023GL106599`.

Clough, S. A. and R. a. A. Franks (1991). “The evaporation of frontal and other stratiform precipitation.” In: *Quarterly Journal of the Royal Meteorological Society* 117.501, pp. 1057–1080. DOI: `10.1002/qj.49711750109`.

Cohen, J., J. A. Screen, J. C. Furtado, M. Barlow, D. Whittleston, D. Coumou, J. Francis, K. Dethloff, D. Entekhabi, J. Overland, and J. Jones (2014). “Recent Arctic amplification and extreme mid-latitude weather.” In: *Nature Geoscience* 7.9, pp. 627–637. DOI: `10.1038/ngeo2234`.

Condron, A. and I. A. Renfrew (2013). “The impact of polar mesoscale storms on northeast Atlantic Ocean circulation.” In: *Nature Geoscience* 6.1, pp. 34–37. DOI: `10.1038/ngeo1661`.

Connolly, P. J., C. Emersic, and P. R. Field (2012). “A laboratory investigation into the aggregation efficiency of small ice crystals.” In: *Atmospheric Chemistry and Physics* 12.4, pp. 2055–2076. DOI: `10.5194/acp-12-2055-2012`.

Copernicus Marine Service (2023). *Arctic Ocean - Sea and Ice Surface Temperature*.

Cotton, W. R., G. J. Tripoli, R. M. Rauber, and E. A. Mulvihill (1986). “Numerical Simulation of the Effects of Varying Ice Crystal Nucleation Rates and Aggregation Processes on Orographic Snowfall.” In: *Journal of Applied Meteorology and Climatology* 25.11, pp. 1658–1680. DOI: `10.1175/1520-0450(1986)025<1658:NSOTEO>2.0.CO;2`.

Crasemann, B., D. Handorf, R. Jaiser, K. Dethloff, T. Nakamura, J. Ukita, and K. Yamazaki (2017). “Can preferred atmospheric circulation patterns over the North-Atlantic-Eurasian region be associated with arctic sea ice loss?” In: *Polar Science* 14, pp. 9–20. DOI: `10.1016/j.polar.2017.09.002`.

Crosier, J., K. N. Bower, T. W. Choularton, C. D. Westbrook, P. J. Connolly, Z. Q. Cui, I. P. Crawford, G. L. Capes, H. Coe, J. R. Dorsey, P. I. Williams, A. J. Illingworth, M. W. Gallagher, and A. M. Blyth (2011). “Observations of ice multiplication in a weakly convective cell embedded in supercooled mid-level stratus.” In: *Atmospheric Chemistry and Physics* 11.1, pp. 257–273. DOI: `10.5194/acp-11-257-2011`.

Curry, J. A., P. V. Hobbs, M. D. King, D. A. Randall, P. Minnis, G. A. Isaac, J. O. Pinto, T. Uttal, A. Bucholtz, D. G. Cripe, H. Gerber, C. W. Fairall, T. J. Garrett, J. Hudson, J. M. Intrieri, C. Jakob, T. Jensen, P. Lawson, D. Marcotte, L. Nguyen, P. Pilewskie, A. Rangno, D. C. Rogers, K. B. Strawbridge, F. P. J. Valero, A. G. Williams, and D. Wylie (2000). "FIRE Arctic Clouds Experiment." In: *Bulletin of the American Meteorological Society* 81.1, pp. 5–30. DOI: `10.1175/1520-0477(2000)081<0005:FACE>2.3.CO;2`.

Curry, J. A. (1995). "Interactions among aerosols, clouds, and climate of the Arctic Ocean." In: *Science of The Total Environment*. Ecological Effects of Arctic Airborne Contaminants 160-161, pp. 777–791. DOI: `10.1016/0048-9697(95)04411-S`.

Curry, J. A., J. L. Schramm, W. B. Rossow, and D. Randall (1996). "Overview of Arctic Cloud and Radiation Characteristics." In: *Journal of Climate* 9.8, pp. 1731–1764. DOI: `10.1175/1520-0442(1996)009<1731:OOACAR>2.0.CO;2`.

Dahlke, S., N. E. Hughes, P. M. Wagner, S. Gerland, T. Wawrzyniak, B. Ivanov, and M. Maturilli (2020). "The observed recent surface air temperature development across Svalbard and concurring footprints in local sea ice cover." In: *International Journal of Climatology* 40.12, pp. 5246–5265. DOI: `10.1002/joc.6517`.

Dahlke, S., A. Solbès, and M. Maturilli (2022). "Cold Air Outbreaks in Fram Strait: Climatology, Trends, and Observations During an Extreme Season in 2020." In: *Journal of Geophysical Research: Atmospheres* 127.3, e2021JD035741. DOI: `10.1029/2021JD035741`.

Dickson, R., J. Lazier, J. Meincke, P. Rhines, and J. Swift (1996). "Long-term coordinated changes in the convective activity of the North Atlantic." In: *Progress in Oceanography* 38.3, pp. 241–295. DOI: `10.1016/S0079-6611(97)00002-5`.

Doviak, R. J. and D. S. Zrnić (2006). *Doppler Radar and Weather Observations*. Courier Corporation.

Eastman, R. and S. G. Warren (2010). "Interannual Variations of Arctic Cloud Types in Relation to Sea Ice." In: *Journal of Climate* 23.15, pp. 4216–4232. DOI: `10.1175/2010JCLI3492.1`.

Ebell, K., C. Buhren, R. Gierens, G. Chellini, M. Lauer, A. Walbröl, S. Dahlke, P. Krobot, and M. Mech (2024). *Multi-year precipitation characteristics based on in-situ and remote sensing observations at Ny-Ålesund, Svalbard*. DOI: `10.5194/egusphere-2024-3368`.

Ebell, K., T. Nomokonova, M. Maturilli, and C. Ritter (2020). "Radiative Effect of Clouds at Ny-Ålesund, Svalbard, as Inferred from Ground-Based Remote Sensing Observations." In: *Journal of Applied Meteorology and Climatology* 59.1, pp. 3–22. DOI: `10.1175/JAMC-D-19-0080.1`.

Edel, L., C. Claud, C. Genthon, C. Palerme, N. Wood, T. L'Ecuyer, and D. Bromwich (2020). "Arctic Snowfall from CloudSat Observations and Reanalyses." In: *Journal of Climate* 33.6, pp. 2093 –2109. DOI: `10.1175/JCLI-D-19-0105.1`.

Ehrlich, A., S. Crewell, A. Herber, M. Klingebiel, C. Lüpkes, M. Mech, S. Becker, S. Borrmann, H. Bozem, M. Buschmann, H.-C. Clemen, E. De La Torre Castro, H. Dorff, R. Dupuy, O. Eppers, F. Ewald, G. George, A. Giez, S. Grawe, C. Gourbeyre, J. Hartmann, E. Jäkel, P. Joppe, O. Jourdan, Z. Jurányi, B. Kirbus, J. Lucke, A. E. Luebke, M. Maahn, N. Maherndl, C. Mallaun, J. Mayer, S. Mertes, G. Mioche, M. Moser, H. Müller, V. Pörtge, N. Risse, G. Roberts, S. Rosenburg, J. Röttenbacher, M. Schäfer, J. Schaefer, A. Schäfler, I. Schirmacher, J. Schneider, S. Schnitt, F. Stratmann, C. Tatzelt, C. Voigt, A. Walbröl, A. Weber, B. Wetzel, M. Wirth, and M. Wendisch (2024). "A comprehensive in-situ and remote sensing data set collected during the HALO–(AC)^3 aircraft campaign." In: *Earth System Science Data Discussions* 2024, pp. 1–49. DOI: `10.5194/essd-2024-281`.

Ehrlich, A., J. Stapf, C. Lüpkes, M. Mech, S. Crewell, and M. Wendisch (2019). *Meteorological measurements by dropsondes released from POLAR 5 during ACLOUD 2017*. PANGEA [data set]. DOI: `10.1594/PANGAEA.900204`.

Ehrlich, A., J. Stapf, C. Lüpkes, M. Mech, S. Crewell, and M. Wendisch (2019a). *Meteorological measurements by dropsondes released from POLAR 5 during ACLOUD 2017*. PANGEA [data set]. DOI: `10.1594/PANGAEA.900204`.

Ehrlich, A., M. Wendisch, C. Lüpkes, M. Buschmann, H. Bozem, D. Chechin, H.-C. Clemen, R. Dupuy, O. Eppers, J. Hartmann, A. Herber, E. Jäkel, E. Järvinen, O. Jourdan, U. Kästner, L.-L. Kliesch, F. Köllner, M. Mech, S. Mertes, R. Neuber, E. Ruiz-Donoso, M. Schnaiter, J. Schneider, J. Stapf, and M. Zanatta (2019b). "A comprehensive in situ and remote sensing data set from the Arctic CLoud Observations Using airborne measurements during polar Day (ACLOUD) campaign." In: *Earth System Science Data* 11.4, pp. 1853–1881. DOI: `10.5194/essd-11-1853-2019`.

Etling, D. and R. A. Brown (1993). "Roll vortices in the planetary boundary layer: A review." In: *Boundary-Layer Meteorology* 65.3, pp. 215–248. DOI: `10.1007/BF00705527`.

Fabry, F. and I. Zawadzki (1995). "Long-Term Radar Observations of the Melting Layer of Precipitation and Their Interpretation." In: *Journal of the Atmospheric Sciences* 52.7, pp. 838–851. DOI: `10.1175/1520-0469(1995)052<0838:LTROOT>2.0.CO;2`.

Fairall, C. W., E. F. Bradley, J. E. Hare, A. A. Grachev, and J. B. Edson (2003). "Bulk Parameterization of Air–Sea Fluxes: Updates and Verification for the COARE Algorithm." In: *Journal of Climate* 16.4, pp. 571–591. DOI: `10.1175/1520-0442(2003)016<0571:BPOASF>2.0.CO;2`.

Faraday, M. R. (1850). “On certain conditions of freezing water.” In: *Journal of the Franklin Institute, of the State of Pennsylvania, for the Promotion of the Mechanic Arts; Devoted to Mechanical and Physical Science, Civil Engineering, the Arts and Manufactures, and the Recording of American and Other Patent Inventions (1828-1851)* 20.4, p. 283.

Fettweis, X., B. Franco, M. Tedesco, J. H. van Angelen, J. T. M. Lenaerts, M. R. van den Broeke, and H. Gallée (2013). “Estimating the Greenland ice sheet surface mass balance contribution to future sea level rise using the regional atmospheric climate model MAR.” In: *The Cryosphere* 7.2, pp. 469–489. DOI: `10.5194/tc-7-469-2013`.

Field, P. R., R. J. Cotton, K. McBeath, A. P. Lock, S. Webster, and R. P. Allan (2014). “Improving a convection-permitting model simulation of a cold air outbreak: Simulation of a Cold Air Outbreak.” In: *Quarterly Journal of the Royal Meteorological Society* 140.678, pp. 124–138. DOI: `10.1002/qj.2116`.

Field, P. R., R. Brožková, M. Chen, J. Dudhia, C. Lac, T. Hara, R. Honnert, J. Olson, P. Siebesma, S. De Roode, L. Tomassini, A. Hill, and R. McTaggart-Cowan (2017). “Exploring the convective grey zone with regional simulations of a cold air outbreak.” In: *Quarterly Journal of the Royal Meteorological Society* 143.707, pp. 2537–2555. DOI: `10.1002/qj.3105`.

Findeisen, W. (1938). “Die kolloidmeteorologischen Vorgänge bei der Niederschlagsbildung.” In: *Meteor* 55, pp. 121–133.

Fitch, K. E. and T. J. Garrett (2022). “Graupel Precipitating From Thin Arctic Clouds With Liquid Water Paths Less Than 50 g m$^-$2.” In: *Geophysical Research Letters* 49.1. DOI: `10.1029/2021GL094075`.

Fletcher, J. K., S. Mason, and C. Jakob (2016a). “A Climatology of Clouds in Marine Cold Air Outbreaks in Both Hemispheres.” In: *Journal of Climate* 29.18, pp. 6677–6692. DOI: `10.1175/JCLI-D-15-0783.1`.

Fletcher, J., S. Mason, and C. Jakob (2016b). “The Climatology, Meteorology, and Boundary Layer Structure of Marine Cold Air Outbreaks in Both Hemispheres*.” In: *Journal of Climate* 29.6, pp. 1999–2014. DOI: `10.1175/JCLI-D-15-0268.1`.

Fletcher, N. H. (1962a). “Surface structure of water and ice.” In: *The Philosophical Magazine: A Journal of Theoretical Experimental and Applied Physics* 7.74, pp. 255–269. DOI: `10.1080/14786436208211860`.

Fletcher, N. H. (1962b). *The Physics of Rainclouds*. Cambridge University Press.

Francis, J. A. and E. Hunter (2006). “New insight into the disappearing Arctic sea ice.” In: *Eos, Transactions American Geophysical Union* 87.46, pp. 509–511. DOI: `10.1029/2006EO460001`.

Francis, J. A. and S. J. Vavrus (2012). “Evidence linking Arctic amplification to extreme weather in mid-latitudes.” In: *Geophysical Research Letters* 39.6. DOI: `10.1029/2012GL051000`.

— (2015). “Evidence for a wavier jet stream in response to rapid Arctic warming.” In: *Environmental Research Letters* 10.1, p. 014005. DOI: 10.1088/1748-9326/10/1/014005.

Fujiyoshi, Y., T. Endoh, T. Yamada, K. Tsuboki, Y. Tachibana, and G. Wakahama (1990). “Determination of a Z-R Relationship for Snowfall Using a Radar and High Sensitivity Snow Gauges.” In: *Journal of Applied Meteorology and Climatology* 29.2, pp. 147–152. DOI: 10.1175/1520-0450(1990)029<0147:DOARFS>2.0.CO;2.

Gayet, J.-F., G. Mioche, A. Dörnbrack, A. Ehrlich, A. Lampert, and M. Wendisch (2009). “Microphysical and optical properties of Arctic mixed-phase clouds. The 9 April 2007 case study.” In: *Atmospheric Chemistry and Physics* 9.17, pp. 6581–6595. DOI: 10.5194/acp-9-6581-2009.

Geerts, B., S. E. Giangrande, G. M. McFarquhar, L. Xue, S. J. Abel, J. M. Comstock, S. Crewell, P. J. DeMott, K. Ebell, P. Field, T. C. J. Hill, A. Hunzinger, M. P. Jensen, K. L. Johnson, T. W. Juliano, P. Kollias, B. Kosovic, C. Lackner, E. Luke, C. Lüpkes, A. A. Matthews, R. Neggers, M. Ovchinnikov, H. Powers, M. D. Shupe, T. Spengler, B. E. Swanson, M. Tjernström, A. K. Theisen, N. A. Wales, Y. Wang, M. Wendisch, and P. Wu (2022). “The COMBLE Campaign: A Study of Marine Boundary Layer Clouds in Arctic Cold-Air Outbreaks.” In: *Bulletin of the American Meteorological Society* 103.5, E1371–E1389. DOI: 10.1175/BAMS-D-21-0044.1.

George, G., A. E. Luebke, M. Klingebiel, M. Mech, and A. Ehrlich (2024). *Dropsonde measurements from HALO and POLAR 5 during HALO-(AC)^3 in 2022*. PANGEA [data set]. DOI: 10.1594/PANGAEA.968891.

George, G., B. Stevens, S. Bony, R. Pincus, C. Fairall, H. Schulz, T. Kölling, Q. T. Kalen, M. Klingebiel, H. Konow, A. Lundry, M. Prange, and J. Radtke (2021). “JOANNE: Joint dropsonde Observations of the Atmosphere in tropical North atlaNtic meso-scale Environments.” In: *Earth Syst. Sci. Data* 13.11, pp. 5253–5272. DOI: 10.5194/essd-13-5253-2021.

Gierens, R., S. Kneifel, M. D. Shupe, K. Ebell, M. Maturilli, and U. Löhnert (2020). “Low-level mixed-phase clouds in a complex Arctic environment.” In: *Atmospheric Chemistry and Physics* 20.6, pp. 3459–3481. DOI: 10.5194/acp-20-3459-2020.

Goosse, H., J. E. Kay, K. C. Armour, A. Bodas-Salcedo, H. Chepfer, D. Docquier, A. Jonko, P. J. Kushner, O. Lecomte, F. Massonnet, H.-S. Park, F. Pithan, G. Svensson, and M. Vancoppenolle (2018). “Quantifying climate feedbacks in polar regions.” In: *Nature Communications* 9.1, p. 1919. DOI: 10.1038/s41467-018-04173-0.

Graversen, R. G., T. Mauritsen, M. Tjernström, E. Källén, and G. Svensson (2008). “Vertical structure of recent Arctic warming.” In: *Nature* 451.7174, pp. 53–56. DOI: 10.1038/nature06502.

Grazioli, J., C. Genthon, B. Boudevillain, C. Duran-Alarcon, M. Del Guasta, J.-B. Madeleine, and A. Berne (2017). "Measurements of precipitation in Dumont d'Urville, Adélie Land, East Antarctica." In: *The Cryosphere* 11.4, pp. 1797–1811. DOI: `10.5194/tc-11-1797-2017`.

Griesche, H. J., K. Ohneiser, P. Seifert, M. Radenz, R. Engelmann, and A. Ansmann (2021). "Contrasting ice formation in Arctic clouds: surface-coupled vs. surface-decoupled clouds." In: *Atmospheric Chemistry and Physics* 21.13, pp. 10357–10374. DOI: `10.5194/acp-21-10357-2021`.

Griesche, H. J., P. Seifert, A. Ansmann, H. Baars, C. Barrientos Velasco, J. Bühl, R. Engelmann, M. Radenz, Y. Zhenping, and A. Macke (2020). "Application of the shipborne remote sensing supersite OCEANET for profiling of Arctic aerosols and clouds during *Polarstern* cruise PS106." In: *Atmospheric Measurement Techniques* 13.10, pp. 5335–5358. DOI: `10.5194/amt-13-5335-2020`.

Gryschka, M. and S. Raasch (2005). "Roll convection during a cold air outbreak: A large eddy simulation with stationary model domain." In: *Geophysical Research Letters* 32.14. DOI: `10.1029/2005GL022872`.

Gryschka, M., J. Fricke, and S. Raasch (2014). "On the impact of forced roll convection on vertical turbulent transport in cold air outbreaks." In: *Journal of Geophysical Research: Atmospheres* 119.22, pp. 12–513.

Hallett, J. and S. C. Mossop (1974). "Production of secondary ice particles during the riming process." In: *Nature* 249.5452, pp. 26–28. DOI: `10.1038/249026a0`.

Hansen, B. B., K. Isaksen, R. E. Benestad, J. Kohler, Å. O. Pedersen, L. E. Loe, S. J. Coulson, J. O. Larsen, and O. Varpe (2014). "Warmer and wetter winters: characteristics and implications of an extreme weather event in the High Arctic." In: *Environmental Research Letters* 9.11, p. 114021. DOI: `10.1088/1748-9326/9/11/114021`.

Hao, M., Y. Luo, Y. Lin, Z. Zhao, L. Wang, and J. Huang (2019). "Contribution of atmospheric moisture transport to winter Arctic warming." In: *International Journal of Climatology* 39.5, pp. 2697–2710. DOI: `10.1002/joc.5982`.

Hartmann, M., K. Adachi, O. Eppers, C. Haas, A. Herber, R. Holzinger, A. Hünerbein, E. Jäkel, C. Jentzsch, M. van Pinxteren, H. Wex, S. Willmes, and F. Stratmann (2020). "Wintertime Airborne Measurements of Ice Nucleating Particles in the High Arctic: A Hint to a Marine, Biogenic Source for Ice Nucleating Particles." In: *Geophysical Research Letters* 47.13, e2020GL087770. DOI: `10.1029/2020GL087770`.

Haynes, J. M., R. T. Marchand, Z. Luo, A. Bodas-Salcedo, and G. L. Stephens (2007). "A Multipurpose Radar Simulation Package:

QuickBeam." In: *Bulletin of the American Meteorological Society* 88.11, pp. 1723–1728. DOI: 10.1175/BAMS-88-11-1723.

Henderson, D. S., T. L'Ecuyer, G. Stephens, P. Partain, and M. Sekiguchi (2013). "A Multisensor Perspective on the Radiative Impacts of Clouds and Aerosols." In: *Journal of Applied Meteorology and Climatology* 52.4, pp. 853–871. DOI: 10.1175/JAMC-D-12-025.1.

Henneberger, J., J. P. Fugal, O. Stetzer, and U. Lohmann (2013). "HOLIMO II: a digital holographic instrument for ground-based in situ observations of microphysical properties of mixed-phase clouds." In: *Atmospheric Measurement Techniques* 6.11, pp. 2975–2987. DOI: 10.5194/amt-6-2975-2013.

Hersbach, H., B. Bell, P. Berrisford, G. Biavati, A. Horányi, J. Muñoz Sabater, J. Nicolas, C. Peubey, R. Radu, I. Rozum, D. Schepers, A. Simmons, C. Soci, D. Dee, and J.-N. Thépaut (2023a). "ERA5 hourly data on pressure levels from 1940 to present." In: *Copernicus Climate Change Service (C3S) Climate Data Store (CDS)*. (last access: 29 August 2024) [data set]. DOI: 10.24381/cds.bd0915c6.

— (2023b). "ERA5 hourly data on single levels from 1940 to present." In: *Copernicus Climate Change Service (C3S) Climate Data Store (CDS)*. (last access: 29 August 2024) [data set]. DOI: 10.24381/cds.adbb2d47.

Hersbach, H., B. Bell, P. Berrisford, A. Horányi, J. M. Sabater, J. Nicolas, P. Poli, R. Radu, D. Schepers, A. Simmons, C. Soci, P. Laloyaux, A. O. Owono, R. Ribas, and M. Suttie (2022). *Characteristics of ERA5 and innovations for ERA6*. https://climate.copernicus.eu/sites/default/files/2022-09/S3_Hans_Hersbach_v1.pdf (last access: 26 October 2024).

Hersbach, H., B. Bell, P. Berrisford, S. Hirahara, A. Horányi, J. Muñoz-Sabater, J. Nicolas, C. Peubey, R. Radu, D. Schepers, A. Simmons, C. Soci, S. Abdalla, X. Abellan, G. Balsamo, P. Bechtold, G. Biavati, J. Bidlot, M. Bonavita, G. De Chiara, P. Dahlgren, D. Dee, M. Diamantakis, R. Dragani, J. Flemming, R. Forbes, M. Fuentes, A. Geer, L. Haimberger, S. Healy, R. J. Hogan, E. Hólm, M. Janisková, S. Keeley, P. Laloyaux, P. Lopez, C. Lupu, G. Radnoti, P. de Rosnay, I. Rozum, F. Vamborg, S. Villaume, and J.-N. Thépaut (2017). "Complete ERA5 from 1940: Fifth generation of ECMWF atmospheric reanalyses of the global climate." In: *Copernicus Climate Change Service (C3S) Data Store (CDS)*. (last access: 03 November 2023) [data set]. DOI: 10.24381/cds.143582cf.

— (2020). "The ERA5 global reanalysis." In: *Quarterly Journal of the Royal Meteorological Society* 146.730, pp. 1999–2049. DOI: 10.1002/qj.3803.

Hobbs, P. V. and A. L. Rangno (1985). "Ice Particle Concentrations in Clouds." In: *Journal of the Atmospheric Sciences* 42.23, pp. 2523–2549. DOI: 10.1175/1520-0469(1985)042<2523:IPCIC>2.0.CO;2.

Hobbs, P. V. and A. L. Rangno (1998). “Microstructures of low and middle-level clouds over the Beaufort Sea.” In: *Quarterly Journal of the Royal Meteorological Society* 124.550, pp. 2035–2071. DOI: `10.1002/qj.49712455012`.

Hong, G. (2007). “Radar backscattering properties of nonspherical ice crystals at 94 GHz.” In: *Journal of Geophysical Research: Atmospheres* 112.D22, p. D22203. DOI: `https://doi.org/10.1029/2007JD008839`.

Huang, Y., X. Dong, J. E. Kay, B. Xi, and E. A. McIlhattan (2021). “The climate response to increased cloud liquid water over the Arctic in CESM1: a sensitivity study of Wegener–Bergeron–Findeisen process.” In: *Climate Dynamics* 56.9, pp. 3373–3394. DOI: `10.1007/s00382-021-05648-5`.

IPCC (2013). “Climate Change 2013: The Physical Science Basis. Contribution of Working Group I to the Fifth Assessment Report of the Intergovernmental Panel on Climate Change.” In: *Cambridge University Press*. [Stocker, T.F., D. Qin, G.-K. Plattner, M. Tignor, S.K. Allen, J. Boschung, A. Nauels, Y. Xia, V. Bex and P.M. Midgley (eds.)], `https://www.ipcc.ch/site/assets/uploads/2018/02/WG1AR5_all_final.pdf`, p. 1535.

Ignatius, R. and M. Ortmeyer (2004). “The International Arctic Buoy Programme–monitoring the Arctic Ocean for forecasting and research.” In: *Arctic Research of the United States* 18, p. 21.

Illingworth, A. J., H. W. Barker, A. Beljaars, M. Ceccaldi, H. Chepfer, N. Clerbaux, J. Cole, J. Delanoë, C. Domenech, D. P. Donovan, S. Fukuda, M. Hirakata, R. J. Hogan, A. Huenerbein, P. Kollias, T. Kubota, T. Nakajima, T. Y. Nakajima, T. Nishizawa, Y. Ohno, H. Okamoto, R. Oki, K. Sato, M. Satoh, M. W. Shephard, A. Velázquez-Blázquez, U. Wandinger, T. Wehr, and G.-J. v. Zadelhoff (2015). “The EarthCARE Satellite: The Next Step Forward in Global Measurements of Clouds, Aerosols, Precipitation, and Radiation.” In: *Bulletin of the American Meteorological Society* 96.8, pp. 1311–1332. DOI: `10.1175/BAMS-D-12-00227.1`.

Intrieri, J. M., M. D. Shupe, T. Uttal, and B. J. McCarty (2002). “An annual cycle of Arctic cloud characteristics observed by radar and lidar at SHEBA.” In: *Journal of Geophysical Research: Oceans* 107.C10. DOI: `10.1029/2000JC000423`.

Intrieri, J. M. and M. D. Shupe (2004). “Characteristics and Radiative Effects of Diamond Dust over the Western Arctic Ocean Region.” In: *Journal of Climate* 17.15, pp. 2953–2960. DOI: `10.1175/1520-0442(2004)017<2953:CAREOD>2.0.CO;2`.

Isachsen, P. E., M. Drivdal, S. Eastwood, Y. Gusdal, G. Noer, and O. Saetra (2013). “Observations of the ocean response to cold air outbreaks and polar lows over the Nordic Seas.” In: *Geophysical Research Letters* 40.14, pp. 3667–3671. DOI: `10.1002/grl.50705`.

Kanji, Z. A., L. A. Ladino, H. Wex, Y. Boose, M. Burkert-Kohn, D. J. Cziczo, and M. Krämer (2017). "Overview of Ice Nucleating Particles." In: *Meteorological Monographs* 58.1, pp. 1.1–1.33. DOI: 10.1175/AMSMONOGRAPHS-D-16-0006.1.

Kanzow, T. (2023). "The Expedition PS131 of the Research Vessel POLARSTERN to the Fram Strait in 2022." In: *Reports on polar and marine research* 770. DOI: 10.57738/BzPM_0770_2023.

Karrer, M., A. Seifert, D. Ori, and S. Kneifel (2021). "Improving the representation of aggregation in a two-moment microphysical scheme with statistics of multi-frequency Doppler radar observations." In: *Atmospheric Chemistry and Physics* 21.22, pp. 17133–17166. DOI: 10.5194/acp-21-17133-2021.

Kay, J. E. and T. L'Ecuyer (2013). "Observational constraints on Arctic Ocean clouds and radiative fluxes during the early 21st century." In: *Journal of Geophysical Research: Atmospheres* 118.13, pp. 7219–7236. DOI: 10.1002/jgrd.50489.

Kirbus, B., I. Schirmacher, M. Klingebiel, M. Schäfer, A. Ehrlich, N. Slättberg, J. Lucke, M. Moser, H. Müller, and M. Wendisch (2024). "Thermodynamic and cloud evolution in a cold-air outbreak during HALO-(AC)^3: quasi-Lagrangian observations compared to the ERA5 and CARRA reanalyses." In: *Atmospheric Chemistry and Physics* 24.6, pp. 3883–3904. DOI: 10.5194/acp-24-3883-2024.

Kirschler, S., C. Voigt, B. E. Anderson, G. Chen, E. C. Crosbie, R. A. Ferrare, V. Hahn, J. W. Hair, S. Kaufmann, R. H. Moore, D. Painemal, C. E. Robinson, K. J. Sanchez, A. J. Scarino, T. J. Shingler, M. A. Shook, K. L. Thornhill, E. L. Winstead, L. D. Ziemba, and A. Sorooshian (2023). "Overview and statistical analysis of boundary layer clouds and precipitation over the western North Atlantic Ocean." In: *Atmospheric Chemistry and Physics* 23.18, pp. 10731–10750. DOI: 10.5194/acp-23-10731-2023.

Kiszler, T., K. Ebell, and V. Schemann (2023). "A Performance Baseline for the Representation of Clouds and Humidity in Cloud-Resolving ICON-LEM Simulations in the Arctic." In: *Journal of Advances in Modeling Earth Systems* 15.5, e2022MS003299. DOI: 10.1029/2022MS003299.

Kiszler, T., D. Ori, and V. Schemann (2024). "Microphysical processes involving the vapour phase dominate in simulated low-level Arctic clouds." In: *Atmospheric Chemistry and Physics* 24.17, pp. 10039–10053. DOI: 10.5194/acp-24-10039-2024.

Klein, S. A., R. B. McCoy, H. Morrison, A. S. Ackerman, A. Avramov, G. D. Boer, M. Chen, J. N. S. Cole, A. D. Del Genio, M. Falk, M. J. Foster, A. Fridlind, J.-C. Golaz, T. Hashino, J. Y. Harrington, C. Hoose, M. F. Khairoutdinov, V. E. Larson, X. Liu, Y. Luo, G. M. McFarquhar, S. Menon, R. A. J. Neggers, S. Park, M. R. Poellot, J. M. Schmidt, I. Sednev, B. J. Shipway, M. D. Shupe, D. A. Spangenberg, Y. C. Sud, D. D. Turner, D. E. Veron, K. V. Salzen,

G. K. Walker, Z. Wang, A. B. Wolf, S. Xie, K.-M. Xu, F. Yang, and G. Zhang (2009). “Intercomparison of model simulations of mixed-phase clouds observed during the ARM Mixed-Phase Arctic Cloud Experiment. I: single-layer cloud.” In: *Quarterly Journal of the Royal Meteorological Society* 135.641, pp. 979–1002. DOI: 10.1002/qj.416.

Klingebiel, M., A. Ehrlich, N. Risse, M. Gryschka, I. Schirmacher, S. Rosenburg, S. Doktorowski, M. Moser, E. Jäkel, M. Schäfer, H. Deneke, M. Mech, and M. Wendisch (2024). “Temporal Evolution of Cloud Properties in Arctic Cold Air Outbreak Cloud Streets Derived from Repeated Airborne Observations.” In: *Atmospheric Chemistry and Physics*. (in prep.)

Klingebiel, M., A. Ehrlich, E. Ruiz-Donoso, N. Risse, I. Schirmacher, E. Jäkel, M. Schäfer, K. Wolf, M. Mech, M. Moser, C. Voigt, and M. Wendisch (2023). “Variability and properties of liquid-dominated clouds over the ice-free and sea-ice-covered Arctic Ocean.” In: *Atmospheric Chemistry and Physics* 23.24, pp. 15289–15304. DOI: 10.5194/acp-23-15289-2023.

Klingebiel, M., A. de Lozar, S. Molleker, R. Weigel, A. Roth, L. Schmidt, J. Meyer, A. Ehrlich, R. Neuber, M. Wendisch, and S. Borrmann (2015). “Arctic low-level boundary layer clouds: in situ measurements and simulations of mono- and bimodal supercooled droplet size distributions at the top layer of liquid phase clouds.” In: *Atmospheric Chemistry and Physics* 15.2, pp. 617–631. DOI: 10.5194/acp-15-617-2015.

Kneifel, S., A. von Lerber, J. Tiira, D. Moisseev, P. Kollias, and J. Leinonen (2015). “Observed relations between snowfall microphysics and triple-frequency radar measurements.” In: *Journal of Geophysical Research: Atmospheres* 120.12, pp. 6034–6055. DOI: 10.1002/2015JD023156.

Knudsen, E. M., B. Heinold, S. Dahlke, H. Bozem, S. Crewell, I. V. Gorodetskaya, G. Heygster, D. Kunkel, M. Maturilli, M. Mech, C. Viceto, A. Rinke, H. Schmithüsen, A. Ehrlich, A. Macke, C. Lüpkes, and M. Wendisch (2018). “Meteorological conditions during the ACLOUD/PASCAL field campaign near Svalbard in early summer 2017.” In: *Atmospheric Chemistry and Physics* 18.24, pp. 17995–18022. DOI: 10.5194/acp-18-17995-2018.

Kochendorfer, J., R. Rasmussen, M. Wolff, B. Baker, M. E. Hall, T. Meyers, S. Landolt, A. Jachcik, K. Isaksen, R. Brækkan, and R. Leeper (2017). “The quantification and correction of wind-induced precipitation measurement errors.” In: *Hydrology and Earth System Sciences* 21.4, pp. 1973–1989. DOI: 10.5194/hess-21-1973-2017.

Kolstad, E. W. (2017). “Higher ocean wind speeds during marine cold air outbreaks.” In: *Quarterly Journal of the Royal Meteorological Society* 143.706, pp. 2084–2092. DOI: 10.1002/qj.3068.

Kolstad, E. W., T. J. Bracegirdle, and I. A. Seierstad (2009). "Marine cold-air outbreaks in the North Atlantic: temporal distribution and associations with large-scale atmospheric circulation." In: *Climate Dynamics* 33.2-3, pp. 187–197. DOI: `10.1007/s00382-008-0431-5`.

Komurcu, M., T. Storelvmo, I. Tan, U. Lohmann, Y. Yun, J. E. Penner, Y. Wang, X. Liu, and T. Takemura (2014). "Intercomparison of the cloud water phase among global climate models." In: *Journal of Geophysical Research: Atmospheres* 119.6, pp. 3372–3400. DOI: `10.1002/2013JD021119`.

Korolev, A., G. McFarquhar, P. R. Field, C. Franklin, P. Lawson, Z. Wang, E. Williams, S. J. Abel, D. Axisa, S. Borrmann, J. Crosier, J. Fugal, M. Krämer, U. Lohmann, O. Schlenczek, M. Schnaiter, and M. Wendisch (2017). "Mixed-Phase Clouds: Progress and Challenges." In: *Meteorological Monographs* 58, pp. 5.1 –5.50. DOI: `10.1175/AMSMONOGRAPHS-D-17-0001.1`.

Korolev, A. (2007). "Limitations of the Wegener–Bergeron–Findeisen Mechanism in the Evolution of Mixed-Phase Clouds." In: *Journal of the Atmospheric Sciences* 64.9, pp. 3372–3375. DOI: `10.1175/JAS4035.1`.

Korolev, A. and P. R. Field (2008). "The effect of dynamics on mixed-phase clouds: Theoretical considerations." In: *Journal of the Atmospheric Sciences* 65.1, pp. 66–86.

Korolev, A., I. Heckman, M. Wolde, A. S. Ackerman, A. M. Fridlind, L. A. Ladino, R. P. Lawson, J. Milbrandt, and E. Williams (2020). "A new look at the environmental conditions favorable to secondary ice production." In: *Atmospheric Chemistry and Physics* 20.3, pp. 1391–1429. DOI: `10.5194/acp-20-1391-2020`.

Korolev, A. and T. Leisner (2020). "Review of experimental studies of secondary ice production." In: *Atmospheric Chemistry and Physics* 20.20, pp. 11767–11797. DOI: `10.5194/acp-20-11767-2020`.

Kulie, M. S. and R. Bennartz (2009). "Utilizing Spaceborne Radars to Retrieve Dry Snowfall." In: *Journal of Applied Meteorology and Climatology* 48.12, pp. 2564–2580. DOI: `10.1175/2009JAMC2193.1`.

Kulie, M. S. and L. Milani (2018). "Seasonal variability of shallow cumuliform snowfall: A CloudSat perspective." In: *Quarterly Journal of the Royal Meteorological Society* 144.S1, pp. 329–343. DOI: `https://doi.org/10.1002/qj.3222`.

Kulie, M. S., L. Milani, N. B. Wood, S. A. Tushaus, R. Bennartz, and T. S. L'Ecuyer (2016). "A Shallow Cumuliform Snowfall Census Using Spaceborne Radar." In: *Journal of Hydrometeorology* 17.4, pp. 1261 –1279. DOI: `10.1175/JHM-D-15-0123.1`.

Kulla, B. S., M. Mech, N. Risse, and C. Ritter (2021). *Cloud top altitude retrieved from Lidar measurements during ACLOUD at 1 second resolution*. PANGEA [data set]. DOI: `10.1594/PANGAEA.932454`.

Kulla, B. S., M. Mech, N. Risse, and C. Ritter (2021b). *Cloud top altitude retrieved from Lidar measurements during AFLUX at 1 second resolution*. PANGEA [data set]. doi: `10.1594/PANGAEA.932455`.

Küchler, N., S. Kneifel, U. Löhnert, P. Kollias, H. Czekala, and T. Rose (2017). "A W-Band Radar–Radiometer System for Accurate and Continuous Monitoring of Clouds and Precipitation." In: *Journal of Atmospheric and Oceanic Technology* 34.11, pp. 2375–2392. doi: `10.1175/JTECH-D-17-0019.1`.

Lackner, C. P., B. Geerts, T. W. Juliano, L. Xue, and B. Kosovic (2023). "Vertical structure of clouds and precipitation during Arctic cold-air outbreaks and warm-air intrusions: Observations from COMBLE." In: *Journal of Geophysical Research: Atmospheres* 128.13, e2022JD038403.

Lamb, D. and J. Verlinde (2011). *Physics and Chemistry of Clouds*. Cambridge: Cambridge University Press. doi: `10.1017/CBO9780511976377`.

Lamer, K., P. Kollias, A. Battaglia, and S. Preval (2020). "Mind the gap – Part 1: Accurately locating warm marine boundary layer clouds and precipitation using spaceborne radars." In: *Atmospheric Measurement Techniques* 13.5, pp. 2363–2379. doi: `10.5194/amt-13-2363-2020`.

Lance, S., C. A. Brock, D. Rogers, and J. A. Gordon (2010). "Water droplet calibration of the Cloud Droplet Probe (CDP) and in-flight performance in liquid, ice and mixed-phase clouds during ARCPAC." In: *Atmospheric Measurement Techniques* 3.6, pp. 1683–1706. doi: `10.5194/amt-3-1683-2010`.

Landgren, O. A., I. A. Seierstad, and T. Iversen (2019). "Projected future changes in Marine Cold-Air Outbreaks associated with Polar Lows in the Northern North-Atlantic Ocean." In: *Climate Dynamics* 53.5, pp. 2573–2585. doi: `10.1007/s00382-019-04642-2`.

Lauer, M., A. Rinke, I. Gorodetskaya, M. Sprenger, M. Mech, and S. Crewell (2023a). "Influence of atmospheric rivers and associated weather systems on precipitation in the Arctic." In: *Atmospheric Chemistry and Physics* 23.15, pp. 8705–8726. doi: `10.5194/acp-23-8705-2023`.

Lauer, M., A. Rinke, I. Gorodetskaya, M. Sprenger, M. Mech, and S. Crewell (2023b). "Influence of atmospheric rivers and associated weather systems on precipitation in the Arctic." In: *Atmospheric Chemistry and Physics* 23.15, pp. 8705–8726. doi: `10.5194/acp-23-8705-2023`.

Lerber, A. von, M. Mech, A. Rinke, D. Zhang, M. Lauer, A. Radovan, I. Gorodetskaya, and S. Crewell (2022a). "Evaluating seasonal and regional distribution of snowfall in regional climate model simulations in the Arctic." In: *Atmospheric Chemistry and Physics* 22.11, pp. 7287–7317. doi: `10.5194/acp-22-7287-2022`.

Lerber, A. v., D. Moisseev, L. F. Bliven, W. Petersen, A.-M. Harri, and V. Chandrasekar (2017). "Microphysical Properties of Snow and Their Link to Ze–S Relations during BAECC 2014." In: *Journal of Applied Meteorology and Climatology* 56.6, pp. 1561–1582. DOI: `10.1175/JAMC-D-16-0379.1`.

Lerber, A. von, M. Mech, A. Rinke, D. Zhang, M. Lauer, A. Radovan, I. Gorodetskaya, and S. Crewell (2022b). "Evaluating seasonal and regional distribution of snowfall in regional climate model simulations in the Arctic." In: *Atmospheric Chemistry and Physics* 22.11, pp. 7287–7317. DOI: `10.5194/acp-22-7287-2022`.

Li, J., Y. Yi, P. Minnis, J. Huang, H. Yan, Y. Ma, W. Wang, and J. K. Ayers (2011). "Radiative effect differences between multi-layered and single-layer clouds derived from CERES, CALIPSO, and CloudSat data." In: *Journal of Quantitative Spectroscopy and Radiative Transfer* 112.2, pp. 361–375.

Li, X., S. K. Krueger, C. Strong, G. G. Mace, and S. Benson (2020). "Midwinter Arctic leads form and dissipate low clouds." In: *Nature Communications* 11.1, p. 206. DOI: `10.1038/s41467-019-14074-5`.

Lin, Y.-L., R. D. Farley, and H. D. Orville (1983). "Bulk Parameterization of the Snow Field in a Cloud Model." In: *Journal of Applied Meteorology and Climatology* 22.6, pp. 1065–1092. DOI: `10.1175/1520-0450(1983)022<1065:BPOTSF>2.0.CO;2`.

Liu, A. Q., G. W. K. Moore, K. Tsuboki, and I. A. Renfrew (2004). "A high-resolution simulation of convective roll clouds during a cold-air outbreak." In: *Geophysical Research Letters* 31.3. DOI: `10.1029/2003GL018530`.

Liu, G. (2008a). "A Database of Microwave Single-Scattering Properties for Nonspherical Ice Particles." In: *Bulletin of the American Meteorological Society* 89.10, pp. 1563–1570. DOI: `10.1175/2008BAMS2486.1`.

— (2008b). "Deriving snow cloud characteristics from CloudSat observations." In: *Journal of Geophysical Research: Atmospheres* 113.D8. DOI: `10.1029/2007JD009766`.

Liu, Y. (2022). "Impacts of active satellite sensors' low-level cloud detection limitations on cloud radiative forcing in the Arctic." In: *Atmospheric Chemistry and Physics* 22.12, pp. 8151–8173. DOI: `10.5194/acp-22-8151-2022`.

Liu, Y., J. R. Key, S. A. Ackerman, G. G. Mace, and Q. Zhang (2012). "Arctic cloud macrophysical characteristics from CloudSat and CALIPSO." In: *Remote Sensing of Environment* 124, pp. 159–173. DOI: `10.1016/j.rse.2012.05.006`.

Liu, Y., M. D. Shupe, Z. Wang, and G. Mace (2017). "Cloud vertical distribution from combined surface and space radar–lidar observations at two Arctic atmospheric observatories." In: *Atmospheric*

Chemistry and Physics 17.9, pp. 5973–5989. DOI: 10.5194/acp-17-5973-2017.

Lohmann, U., F. Lüönd, and F. Mahrt (2016). *An Introduction to Clouds: From the Microscale to Climate*. Cambridge University Press.

Lubin, D. and A. M. Vogelmann (2006). "A climatologically significant aerosol longwave indirect effect in the Arctic." In: *Nature* 439.7075, pp. 453–456. DOI: 10.1038/nature04449.

Ludovic, B., B. Byron, F. Christopher, T. Elizabeth, E. Jim, and P. Robert (2021). *Python implementation of the COARE 3.5 Bulk Air-Sea Flux algorithm*. Zenodo [code]. Version v1.1. DOI: 10.5281/zenodo.5110991.

Ludwig, V. and G. Spreen (2023). *modis_amsr2*. https://data.seaice.uni-bremen.de/modis_amsr2/ (last access: 20 October 2023) [data set].

Ludwig, V., G. Spreen, and L. T. Pedersen (2020). "Evaluation of a New Merged Sea-Ice Concentration Dataset at 1 km Resolution from Thermal Infrared and Passive Microwave Satellite Data in the Arctic." In: *Remote Sensing* 12.19, p. 3183. DOI: 10.3390/rs12193183.

Maahn, M., D. Moisseev, I. Steinke, N. Maherndl, and M. D. Shupe (2024). "Introducing the Video In Situ Snowfall Sensor (VISSS)." In: *Atmospheric Measurement Techniques* 17.2, pp. 899–919. DOI: 10.5194/amt-17-899-2024.

Maahn, M., C. Burgard, S. Crewell, I. V. Gorodetskaya, S. Kneifel, S. Lhermitte, K. Van Tricht, and N. P. M. van Lipzig (2014). "How does the spaceborne radar blind zone affect derived surface snowfall statistics in polar regions?" In: *Journal of Geophysical Research: Atmospheres* 119.24, pp. 13,604–13,620. DOI: 10.1002/2014JD022079.

Maahn, M. and N. Maherndl (2023). *Video In Situ Snowfall Sensor (VISSS) data for Ny-Ålesund (2021-2022)*. PANGEA [data set]. DOI: 10.1594/PANGAEA.958537.

Macke, A., J. Mueller, and E. Raschke (1996). "Single Scattering Properties of Atmospheric Ice Crystals." In: *Journal of the Atmospheric Sciences* 53.19, pp. 2813–2825. DOI: 10.1175/1520-0469(1996)053<2813:SSPOAI>2.0.CO;2.

Mages, Z., P. Kollias, Z. Zhu, and E. P. Luke (2023). "Surface-based observations of cold-air outbreak clouds during the COMBLE field campaign." In: *Atmospheric Chemistry and Physics* 23.6, pp. 3561–3574. DOI: 10.5194/acp-23-3561-2023.

Maherndl, N., M. Moser, J. Lucke, M. Mech, N. Risse, I. Schirmacher, and M. Maahn (2024a). "Quantifying riming from airborne data during the HALO-(AC)^3 campaign." In: *Atmospheric Measurement Techniques* 17.5, pp. 1475–1495. DOI: 10.5194/amt-17-1475-2024.

Maherndl, N., M. Moser, I. Schirmacher, A. Bansemer, J. Lucke, C. Voigt, and M. Maahn (2024b). "How does riming influence the observed spatial variability of ice water in mixed-phase clouds?" In: *EGUsphere* 2024, pp. 1–38. DOI: `10.5194/egusphere-2024-1214`.

Maherndl, N., M. Maahn, F. Tridon, J. Leinonen, D. Ori, and S. Kneifel (2023). "A riming-dependent parameterization of scattering by snowflakes using the self-similar Rayleigh–Gans approximation." In: *Quarterly Journal of the Royal Meteorological Society*, pp. 1–20. DOI: `10.1002/qj.4573`.

Marchand, R. (2018). *Level 2 GEOPROF Product Process Description and Interface Control Document, Product Version P1_R05, NASA JPL CloudSat project, document revision 0*. `https://www.cloudsat.cira.colostate.edu/cloudsat-static/info/dl/2b-geoprof/2B-GEOPROF_PDICD.P1_R05.rev0__0.pdf` (last access: 6 July 2022).

Markson, R. (1975). "Atmospheric Electrical Detection of Organized Convection." In: *American Association for the Advancement of Science*. 4194th ser. 188, pp. 1171 –1177. DOI: `10.1126/science.188.4194.1171`.

Mateling, M. E., C. Pettersen, M. S. Kulie, and T. S. L'Ecuyer (2023). "Marine Cold-Air Outbreak Snowfall in the North Atlantic: A CloudSat Perspective." In: *Journal of Geophysical Research: Atmospheres* 128.10. DOI: `10.1029/2022JD038053`.

Matrosov, S. Y. (1992). "Radar reflectivity in snowfall." In: *IEEE Transactions on Geoscience and Remote Sensing* 30.3, pp. 454–461.

Matrosov, S. Y. (2007). "Modeling Backscatter Properties of Snowfall at Millimeter Wavelengths." In: *Journal of the Atmospheric Sciences* 64.5, pp. 1727–1736. DOI: `10.1175/JAS3904.1`.

Matrosov, S. Y., C. Campbell, D. Kingsmill, and E. Sukovich (2009). "Assessing Snowfall Rates from X-Band Radar Reflectivity Measurements." In: *Journal of Atmospheric and Oceanic Technology* 26.11, pp. 2324–2339. DOI: `10.1175/2009JTECHA1238.1`.

Maturilli, M., A. Herber, and G. König-Langlo (2013). "Climatology and time series of surface meteorology in Ny-Ålesund, Svalbard." In: *Earth System Science Data* 5.1, pp. 155–163. DOI: `10.5194/essd-5-155-2013`.

Maturilli, M. and K. Ebell (2018). "Twenty-five years of cloud base height measurements by ceilometer in Ny-Ålesund, Svalbard." In: *Earth System Science Data* 10.3, pp. 1451–1456. DOI: `10.5194/essd-10-1451-2018`.

McCrystall, M. R., J. Stroeve, M. Serreze, B. C. Forbes, and J. A. Screen (2021). "New climate models reveal faster and larger increases in Arctic precipitation than previously projected." In: *Nature Communications* 12.1, p. 6765. DOI: `10.1038/s41467-021-27031-y`.

McFarquhar, G. M., G. Zhang, M. R. Poellot, G. L. Kok, R. McCoy, T. Tooman, A. Fridlind, and A. J. Heymsfield (2007). "Ice properties of single-layer stratocumulus during the Mixed-Phase Arctic

Cloud Experiment: 1. Observations." In: *Journal of Geophysical Research* 112.D24, p. D24201. DOI: `10.1029/2007JD008633`.

Mech, M., G. Marollo, D. Paul, N. Risse, and I. Schirmacher (2021). *Introduction — How_to_ac3airborne*. `https://igmk.github.io/how_to_ac3airborne/intro.html` (last access: 27 October 2024).

Mech, M., E. Orlandi, S. Crewell, F. Ament, L. Hirsch, M. Hagen, G. Peters, and B. Stevens (2014). "HAMP – the microwave package on the High Altitude and LOng range research aircraft (HALO)." In: *Atmospheric Measurement Techniques* 7.12, pp. 4539–4553. DOI: `10.5194/amt-7-4539-2014`.

Mech, M., A. Ehrlich, A. Herber, C. Lüpkes, M. Wendisch, S. Becker, Y. Boose, D. Chechin, S. Crewell, R. Dupuy, C. Gourbeyre, J. Hartmann, E. Jäkel, O. Jourdan, L.-L. Kliesch, M. Klingebiel, B. S. Kulla, G. Mioche, M. Moser, N. Risse, E. Ruiz-Donoso, M. Schäfer, J. Stapf, and C. Voigt (2022). "MOSAiC-ACA and AFLUX - Arctic airborne campaigns characterizing the exit area of MOSAiC." In: *Scientific Data* 9.1, p. 790. DOI: `10.1038/s41597-022-01900-7`.

Mech, M., L.-L. Kliesch, A. Anhäuser, T. Rose, P. Kollias, and S. Crewell (2019). "Microwave Radar/radiometer for Arctic Clouds (MiRAC): first insights from the ACLOUD campaign." In: *Atmospheric Measurement Techniques* 12.9, pp. 5019–5037. DOI: `10.5194/amt-12-5019-2019`.

Mech, M., N. Risse, S. Crewell, and L.-L. Kliesch (2022a). *Radar reflectivities at 94 GHz and microwave brightness temperature measurements at 89 GHz during the ACLOUD Arctic airborne campaign in early summer 2017 out of Svalbard*. PANGEA [data set]. DOI: `10.1594/PANGAEA.945988`.

— (2022b). *Radar reflectivities at 94 GHz and microwave brightness temperature measurements at 89 GHz during the AFLUX Arctic airborne campaign in spring 2019 out of Svalbard*. PANGEA [data set]. DOI: `10.1594/PANGAEA.944506`.

— (2022c). *Radar reflectivities at 94 GHz and microwave brightness temperature measurements at 89 GHz during the MOSAiC-ACA Arctic airborne campaign*. PANGEA [data set]. DOI: `10.1594/PANGAEA.944507`.

Mech, M., N. Risse, P. Krobot, D. Paul, I. Schirmacher, S. Schnitt, and S. Crewell (2024). *Radar reflectivities at 94 GHz and microwave brightness temperature measurements at 89 GHz during the HALO-AC3 Arctic airborne campaign*. PANGEA [data set]. DOI: `10.1594/PANGAEA.964977`.

Mech, M., N. Risse, P. Krobot, I. Schirmacher, S. Schnitt, and S. Crewell (2024a). *Microwave brightness temperature measurements during the HALO-AC3 Arctic airborne campaign in early spring 2022 out of Svalbard*. PANGEA [data set]. DOI: `10.1594/PANGAEA.964982`.

Mech, M., N. Risse, G. Marrollo, and D. Paul (2022). *Ac3airborne*. Zenodo [code]. DOI: `10.5281/zenodo.7305585`.

Mech, M., N. Risse, C. Ritter, I. Schirmacher, and J. H. Schween (2024b). *Cloud mask and cloud top altitude from the AMALi airborne lidar on Polar 5 during HALO-AC3 in spring 2022*. PANGEA [data set]. DOI: 10.1594/PANGAEA.964985.

Melchionna, S., M. Bauer, and G. Peters (2008). "A new algorithm for the extraction of cloud parameters using multipeak analysis of cloud radar data First application and preliminary results." In: *Meteorologische Zeitschrift*, pp. 613–620. DOI: 10.1127/0941-2948/2008/0322.

Melsheimer, C. and G. Spreen (2019). *AMSR2 ASI sea ice concentration data, Arctic, version 5.4 (NetCDF) (July 2012 - December 2019)*. PANGEA [data set]. DOI: 10.1594/PANGAEA.898399.

Meyer, M., I. Polkova, K. R. Modali, L. Schaffer, J. Baehr, S. Olbrich, and M. Rautenhaus (2021). "Interactive 3-D visual analysis of ERA5 data: improving diagnostic indices for marine cold air outbreaks and polar lows." In: *Weather and Climate Dynamics* 2.3, pp. 867–891. DOI: 10.5194/wcd-2-867-2021.

Milani, L. and C. Kidd (2023). "The State of Precipitation Measurements at Mid-to-High Latitudes." In: *Atmosphere* 14.11, p. 1677. DOI: 10.3390/atmos14111677.

Mioche, G., O. Jourdan, M. Ceccaldi, and J. Delanoë (2015). "Variability of mixed-phase clouds in the Arctic with a focus on the Svalbard region: a study based on spaceborne active remote sensing." In: *Atmospheric Chemistry and Physics* 15.5, pp. 2445–2461. DOI: 10.5194/acp-15-2445-2015.

Mioche, G., O. Jourdan, J. Delanoë, C. Gourbeyre, G. Febvre, R. Dupuy, M. Monier, F. Szczap, A. Schwarzenboeck, and J.-F. Gayet (2017). "Vertical distribution of microphysical properties of Arctic springtime low-level mixed-phase clouds over the Greenland and Norwegian seas." In: *Atmospheric Chemistry and Physics* 17.20, pp. 12845–12869. DOI: 10.5194/acp-17-12845-2017.

Mitchell, D. L. (1988). "Evolution of Snow-Size Spectra in Cyclonic Storms. Part I: Snow Growth by Vapor Deposition and Aggregation." In: *Journal of the Atmospheric Sciences* 45.22, pp. 3431–3451. DOI: 10.1175/1520-0469(1988)045<3431:EOSSSI>2.0.CO;2.

Mitchell, J. F. B., C. A. Senior, and W. J. Ingram (1989). "Co2 and climate: a missing feedback?" In: *Nature* 341.6238, pp. 132–134. DOI: 10.1038/341132a0.

Morrison, A. L., J. E. Kay, W. R. Frey, H. Chepfer, and R. Guzman (2019). "Cloud Response to Arctic Sea Ice Loss and Implications for Future Feedback in the CESM1 Climate Model." In: *Journal of Geophysical Research: Atmospheres* 124.2, pp. 1003–1020. DOI: 10.1029/2018JD029142.

Morrison, H. and J. O. Pinto (2006). "Intercomparison of Bulk Cloud Microphysics Schemes in Mesoscale Simulations of Springtime

Arctic Mixed-Phase Stratiform Clouds.” In: *Monthly Weather Review* 134.7, pp. 1880–1900. DOI: 10.1175/MWR3154.1.

Morrison, H., P. Zuidema, G. M. McFarquhar, A. Bansemer, and A. J. Heymsfield (2011). “Snow microphysical observations in shallow mixed-phase and deep frontal Arctic cloud systems.” In: *Quarterly Journal of the Royal Meteorological Society* 137.659, pp. 1589–1601. DOI: 10.1002/qj.840.

Morrison, H., G. de Boer, G. Feingold, J. Harrington, M. D. Shupe, and K. Sulia (2012). “Resilience of persistent Arctic mixed-phase clouds.” In: *Nature Geoscience* 5.1, pp. 11–17. DOI: 10.1038/ngeo1332.

Moser, M., C. Voigt, T. Jurkat-Witschas, V. Hahn, G. Mioche, O. Jourdan, R. Dupuy, C. Gourbeyre, A. Schwarzenboeck, J. Lucke, Y. Boose, M. Mech, S. Borrmann, A. Ehrlich, A. Herber, C. Lüpkes, and M. Wendisch (2023). *Microphysical and thermodynamic phase analyses of Arctic low-level clouds measured above the sea ice and the open ocean in spring and summer*. Tech. rep. 13, pp. 7257–7280. DOI: 10.5194/acp-23-7257-2023.

Mudryk, L., M. Santolaria-Otín, G. Krinner, M. Ménégoz, C. Derksen, C. Brutel-Vuilmet, M. Brady, and R. Essery (2020). “Historical Northern Hemisphere snow cover trends and projected changes in the CMIP6 multi-model ensemble.” In: *The Cryosphere* 14.7, pp. 2495–2514. DOI: 10.5194/tc-14-2495-2020.

Murray-Watson, R. J., E. Gryspeerdt, and T. Goren (2023). “Investigating the development of clouds within marine cold-air outbreaks.” In: *Atmospheric Chemistry and Physics* 23.16, pp. 9365–9383. DOI: 10.5194/acp-23-9365-2023.

Müller, G., B. Brümmer, and W. Alpers (1999). “Roll Convection within an Arctic Cold-Air Outbreak: Interpretation of In Situ Aircraft Measurements and Spaceborne SAR Imagery by a Three-Dimensional Atmospheric Model.” In: *Monthly Weather Review* 127.3, pp. 363–380. DOI: 10.1175/1520-0493(1999)127<0363:RCWAAC>2.0.CO;2.

NASA Worldview (2023a). *Cloud Water Path Terra / MODIS*. (last access: 21 November 2023).

— (2023b). *Corrected Reflectance (Bands M3-I3-M11) Suomi NPP/VIIRS*. (last access: 21 November 2023).

— (2023c). *Corrected Reflectance (True Color) Terra / MODIS*. (last access: 21 November 2023).

Narizhnaya, A. and A. Chernokulsky (2024). “Cloud Characteristics during Intense Cold Air Outbreaks over the Barents Sea Based on Satellite Data.” In: *Atmosphere* 15.3, p. 317. DOI: 10.3390/atmos15030317.

Neuber, R. (2006). “A Multi-Disciplinary Arctic Research Facility: From the Koldewey – Rabot – Corbel – Stations to the AWI-IPEV

Research Base on Spitsbergen." In: *Polarforschung* 73.2. https://epic.awi.de/id/eprint/14315/1/Neu2006a.pdf, pp. 117–123.

Nitu, R., Y.-A. Roulet, M. Wolff, M. E. Earle, A. Reverdin, C. D. Smith, J. Kochendorfer, S. Morin, R. Rasmussen, K. Wong, J Alastrué, L Arnold, B Baker, S Buisán, J. Collado, M Colli, B Collins, A Gaydos, H.-R Hannula, J Hoover, P Joe, A Kontu, T Laine, L Lanza, E Lanzinger, G. Lee, Y Lejeune, L Leppänen, E Mekis, J.-M. Panel, A Poikonen, S Ryu, F Sabatini, J Theriault, D Yang, C Genthon, F van den Heuvel, N Hirasawa, H Konishi, H Motoyoshi, S Nakai, K Nishimura, A Senese, and K Yamashita (2018). *WMO solid precipitation intercomparison experiment (SPICE)(2012-2015)*. Instruments and Observing Methods Report No. 131. https://library.wmo.int/idurl/4/56317. World Meteorological Organization.

OTT (2024). *Operating Instructions Precipitation gauge OTT Pluvio^2 L*. https://www.ott.com/download/operating-instructions-precipitation-gauge-ott-pluvio2-l-2/ (last access: 16 October 2024).

Oltmanns, M., F. Straneo, and M. Tedesco (2019). "Increased Greenland melt triggered by large-scale, year-round cyclonic moisture intrusions." In: *The Cryosphere* 13.3, pp. 815–825. DOI: 10.5194/tc-13-815-2019.

Onarheim, I. H., L. H. Smedsrud, R. B. Ingvaldsen, and F. Nilsen (2014). "Loss of sea ice during winter north of Svalbard." In: *Tellus A: Dynamic Meteorology and Oceanography* 66.1, p. 23933. DOI: 10.3402/tellusa.v66.23933.

Oue, M., M. Galletti, J. Verlinde, A. Ryzhkov, and Y. Lu (2016). "Use of X-Band Differential Reflectivity Measurements to Study Shallow Arctic Mixed-Phase Clouds." In: *Journal of Applied Meteorology and Climatology* 55.2, pp. 403–424. DOI: 10.1175/JAMC-D-15-0168.1.

Overland, J. E., M. Wang, J. E. Walsh, and J. C. Stroeve (2014). "Future Arctic climate changes: Adaptation and mitigation time scales." In: *Earth's Future* 2.2, pp. 68–74. DOI: 10.1002/2013EF000162.

Painemal, D., M. Clayton, R. Ferrare, S. Burton, D. Josset, and M. Vaughan (2019). "Novel aerosol extinction coefficients and lidar ratios over the ocean from CALIPSO–CloudSat: evaluation and global statistics." In: *Atmospheric Measurement Techniques* 12.4, pp. 2201–2217. DOI: 10.5194/amt-12-2201-2019.

Palerme, C., J. E. Kay, C. Genthon, T. L'Ecuyer, N. B. Wood, and C. Claud (2014). "How much snow falls on the Antarctic ice sheet?" In: *The Cryosphere* 8.4, pp. 1577–1587. DOI: 10.5194/tc-8-1577-2014.

Palerme, C., C. Claud, N. B. Wood, T. L'Ecuyer, and C. Genthon (2019). "How Does Ground Clutter Affect CloudSat Snowfall Retrievals Over Ice Sheets?" In: *IEEE Geoscience and Remote Sensing Letters* 16.3, pp. 342–346. DOI: 10.1109/LGRS.2018.2875007.

Pan, R., Q. Shu, Q. Wang, S. Wang, Z. Song, Y. He, and F. Qiao (2023). "Future Arctic Climate Change in CMIP6 Strikingly Intensified by NEMO-Family Climate Models." In: *Geophysical Research Letters* 50.4, e2022GL102077. DOI: `10.1029/2022GL102077`.

Papritz, L. and C. M. Grams (2018). "Linking Low-Frequency Large-Scale Circulation Patterns to Cold Air Outbreak Formation in the Northeastern North Atlantic." In: *Geophysical Research Letters* 45.5, pp. 2542–2553. DOI: `10.1002/2017GL076921`.

Papritz, L., S. Pfahl, H. Sodemann, and H. Wernli (2015). "A Climatology of Cold Air Outbreaks and Their Impact on Air–Sea Heat Fluxes in the High-Latitude South Pacific." In: *Journal of Climate* 28.1, pp. 342–364. DOI: `10.1175/JCLI-D-14-00482.1`.

Papritz, L. and T. Spengler (2017). "A Lagrangian Climatology of Wintertime Cold Air Outbreaks in the Irminger and Nordic Seas and Their Role in Shaping Air–Sea Heat Fluxes." In: *Journal of Climate* 30.8, pp. 2717–2737. DOI: `10.1175/JCLI-D-16-0605.1`.

Park, H., E. Watanabe, Y. Kim, I. Polyakov, K. Oshima, X. Zhang, J. S. Kimball, and D. Yang (2020). "Increasing riverine heat influx triggers Arctic sea ice decline and oceanic and atmospheric warming." In: *Science Advances* 6.45, eabc4699. DOI: `10.1126/sciadv.abc4699`.

Pasquier, J. T., J. Henneberger, F. Ramelli, A. Lauber, R. O. David, J. Wieder, T. Carlsen, R. Gierens, M. Maturilli, and U. Lohmann (2022). "Conditions favorable for secondary ice production in Arctic mixed-phase clouds." In: *Atmospheric Chemistry and Physics* 22.23, pp. 15579–15601. DOI: `10.5194/acp-22-15579-2022`.

Perovich, D. K., T. C. Grenfell, B. Light, and P. V. Hobbs (2002). "Seasonal evolution of the albedo of multiyear Arctic sea ice." In: *Journal of Geophysical Research: Oceans* 107.C10, SHE 20–1–SHE 20–13. DOI: `10.1029/2000JC000438`.

Petty, G. W. (2006). *A First Course in Atmospheric Radiation*. Sundog Publishing.

Pfitzenmaier, L., P. Kollias, N. Risse, I. Schirmacher, B. Puigdomenech Treserras, and K. Lamer (2024). "Orbital-Radar v1.0.0: A tool to transform suborbital radar observations to synthetic EarthCARE cloud radar data." In: *Geoscientific Model Development Discussions*, pp. 1–21. DOI: `10.5194/gmd-2024-129`.

Philipp, A., C. Beck, R. Huth, and J. Jacobeit (2016). "Development and comparison of circulation type classifications using the COST 733 dataset and software." In: *International Journal of Climatology* 36.7, pp. 2673–2691. DOI: `10.1002/joc.3920`.

Pithan, F., G. Svensson, R. Caballero, D. Chechin, T. W. l. Cronin, A. M. L. Ekman, R. Neggers, M. D. Shupe, A. Solomon, M. Tjernström, and M. Wendisch (2018). "Role of air-mass transformations in exchange between the Arctic and mid-latitudes." In: *Na-*

ture Geoscience 11.11, pp. 805–812. DOI: 10.1038/s41561-018-0234-1.

Prenni, A. J., P. J. Demott, D. C. Rogers, S. M. Kreidenweis, G. M. Mcfarquhar, G. Zhang, and M. R. Poellot (2009). "Ice nuclei characteristics from M-PACE and their relation to ice formation in clouds." In: *Tellus B* 61.2, pp. 436–448. DOI: 10.1111/j.1600-0889.2009.00415.x.

Prenni, A. J., J. Y. Harrington, M. Tjernström, P. J. DeMott, A. Avramov, C. N. Long, S. M. Kreidenweis, P. Q. Olsson, and J. Verlinde (2007). "Can Ice-Nucleating Aerosols Affect Arctic Seasonal Climate?" In: *Bulletin of the American Meteorological Society* 88.4, pp. 541–550. DOI: 10.1175/BAMS-88-4-541.

Protat, A., D. Bouniol, J. Delanoë, E. O'Connor, P. T. May, A. Plana-Fattori, A. Hasson, U. Görsdorf, and A. J. Heymsfield (2009). "Assessment of Cloudsat Reflectivity Measurements and Ice Cloud Properties Using Ground-Based and Airborne Cloud Radar Observations." In: *Journal of Atmospheric and Oceanic Technology* 26.9, pp. 1717–1741. DOI: 10.1175/2009JTECHA1246.1.

Protat, A., D. Bouniol, E. J. O'Connor, H. K. Baltink, J. Verlinde, and K. Widener (2011). "CloudSat as a Global Radar Calibrator." In: *Journal of Atmospheric and Oceanic Technology* 28.3, pp. 445–452. DOI: 10.1175/2010JTECHA1443.1.

Pruppacher, H. R. and J. D. Klett (1997). *Microphysics of Clouds and Precipitation: Second Revised and Enlarged Edition with an Introduction to Cloud Chemistry and Cloud Electricity*. Kluwer Academic Publishers.

Ramanathan, V., R. D. Cess, E. F. Harrison, P. Minnis, B. R. Barkstrom, E. Ahmad, and D. Hartmann (1989). "Cloud-Radiative Forcing and Climate: Results from the Earth Radiation Budget Experiment." In: *Science* 243.4887, pp. 57–63. DOI: 10.1126/science.243.4887.57.

Ramelli, F., J. Henneberger, R. O. David, A. Lauber, J. T. Pasquier, J. Wieder, J. Bühl, P. Seifert, R. Engelmann, M. Hervo, and U. Lohmann (2021). "Influence of low-level blocking and turbulence on the microphysics of a mixed-phase cloud in an inner-Alpine valley." In: *Atmospheric Chemistry and Physics* 21.6, pp. 5151–5172. DOI: 10.5194/acp-21-5151-2021.

Rasmussen, R., M. Dixon, S. Vasiloff, F. Hage, S. Knight, J. Vivekanandan, and M. Xu (2003). "Snow Nowcasting Using a Real-Time Correlation of Radar Reflectivity with Snow Gauge Accumulation." In: *Journal of Applied Meteorology and Climatology* 42.1, pp. 20–36. DOI: 10.1175/1520-0450(2003)042<0020:SNUART>2.0.CO;2.

Renfrew, I. A., C. Barrell, A. D. Elvidge, J. K. Brooke, C. Duscha, J. C. King, J. Kristiansen, T. L. Cope, G. W. K. Moore, R. S. Pickart, J. Reuder, I. Sandu, D. Sergeev, A. Terpstra, K. Våge, and A. Weiss (2021). "An evaluation of surface meteorology and fluxes over the Iceland and Greenland Seas in ERA5 reanalysis: The impact of sea ice distribution." In: *Quarterly Journal of the Royal Meteorological Society* 147.734, pp. 691–712. DOI: `10.1002/qj.3941`.

Renfrew, I. A., R. S. Pickart, K. Våge, G. W. K. Moore, T. J. Bracegirdle, A. D. Elvidge, E. Jeansson, T. Lachlan-Cope, L. T. McRaven, L. Papritz, J. Reuder, H. Sodemann, A. Terpstra, S. Waterman, H. Valdimarsson, A. Weiss, M. Almansi, F. Bahr, A. Brakstad, C. Barrell, J. K. Brooke, B. J. Brooks, I. M. Brooks, M. E. Brooks, E. M. Bruvik, C. Duscha, I. Fer, H. M. Golid, M. Hallerstig, I. Hessevik, J. Huang, L. Houghton, S. Jónsson, M. Jonassen, K. Jackson, K. Kvalsund, E. W. Kolstad, K. Konstali, J. Kristiansen, R. Ladkin, P. Lin, A. Macrander, A. Mitchell, H. Olafsson, A. Pacini, C. Payne, B. Palmason, M. D. Pérez-Hernández, A. K. Peterson, G. N. Petersen, M. N. Pisareva, J. O. Pope, A. Seidl, S. Semper, D. Sergeev, S. Skjelsvik, H. Søiland, D. Smith, M. A. Spall, T. Spengler, A. Touzeau, G. Tupper, Y. Weng, K. D. Williams, X. Yang, and S. Zhou (2019). "The Iceland Greenland Seas Project." In: *Bulletin of the American Meteorological Society* 100.9, pp. 1795–1817. DOI: `10.1175/BAMS-D-18-0217.1`.

Risse, N., G. Marrollo, D. Paul, and M. Mech (2022). *Ac3airborne - Flight-Phase-Separation*. Zenodo [code]. DOI: `10.5281/zenodo.7305558`.

Roode, S. R. de, T. Frederikse, A. P. Siebesma, A. S. Ackerman, J. Chylik, P. R. Field, J. Fricke, M. Gryschka, A. Hill, R. Honnert, S. K. Krueger, C. Lac, A. T. Lesage, and L. Tomassini (2019). "Turbulent Transport in the Gray Zone: A Large Eddy Model Intercomparison Study of the CONSTRAIN Cold Air Outbreak Case." In: *Journal of Advances in Modeling Earth Systems* 11.3, pp. 597–623. DOI: `10.1029/2018MS001443`.

Rose, T. (2022). "RPG-FMCW-94(35)-SP/DP 94 (35) GHz W(K)-band Doppler Cloud Radar Operation and Software Guide (Version 5.56)." In: *Radiometer Physics GmbH*. `https://www.radiometer-physics.de/download/PDF/Cloud%20Radar/RPG-FMCW-Operation%20and%20SW_Manual.pdf` (last access: 14 November 2024), p. 111.

Roussel, M.-L., V. Wiener, C. Genthon, E. Vignon, E. Bazile, C. Agosta, A. Berne, C. Durán-Alarcón, J.-L. Dufresne, and C. Claud (2023). "Assessing the simulation of snowfall at Dumont d'Urville, Antarctica, during the YOPP-SH special observing campaign." In: *Quarterly Journal of the Royal Meteorological Society* 149.753, pp. 1391–1406. DOI: `10.1002/qj.4463`.

Ruiz-Donoso, E., A. Ehrlich, M. Schäfer, E. Jäkel, V. Schemann, S. Crewell, M. Mech, B. S. Kulla, L.-L. Kliesch, R. Neuber, and M. Wendisch (2020). "Small-scale structure of thermodynamic phase in Arctic mixed-phase clouds observed by airborne remote sensing during a cold air outbreak and a warm air advection event."

In: *Atmospheric Chemistry and Physics* 20.9, pp. 5487–5511. DOI: 10.5194/acp-20-5487-2020.

Sandvik, A., M. Biryulina, N. G. Kvamstø, J. J. Stamnes, and K. Stamnes (2007). "Observed and simulated microphysical composition of arctic clouds: Data properties and model validation." In: *Journal of Geophysical Research: Atmospheres* 112.D5. DOI: 10.1029/2006JD007351.

Schirmacher, I., S. Schnitt, M. Klingebiel, N. Maherndl, B. Kirbus, A. Ehrlich, M. Mech, and S. Crewell (2024a). "Clouds and precipitation in the initial phase of marine cold-air outbreaks as observed by airborne remote sensing." In: *Atmospheric Chemistry and Physics* 24.22, pp. 12823–12842. DOI: 10.5194/acp-24-12823-2024.

Schirmacher, I., P. Kollias, K. Lamer, M. Mech, L. Pfitzenmaier, M. Wendisch, and S. Crewell (2023). "Assessing Arctic low-level clouds and precipitation from above – a radar perspective." In: *Atmospheric Measurement Techniques* 16.17, pp. 4081–4100. DOI: 10.5194/amt-16-4081-2023.

Schirmacher, I., C. Pettersen, K. Ebell, and S. Crewell (2024b). *How much snow falls over the Fram Strait during marine cold air outbreaks: constraints derived from airborne radar observations*. (in prep.)

Schoger, S. Y., D. Moisseev, A. v. Lerber, S. Crewell, and K. Ebell (2021). "Snowfall-Rate Retrieval for K- and W-Band Radar Measurements Designed in Hyytiälä, Finland, and Tested at Ny-Ålesund, Svalbard, Norway." In: *Journal of Applied Meteorology and Climatology* 60.3, pp. 273–289. DOI: 10.1175/JAMC-D-20-0095.1.

Schyberg, H., X. Yang, M. Køltzow, r. Amstrup B.and Bakketun, E. Bazile, J. Bojarova, J. E. Box, P. Dahlgren, S. Hagelin, M. Homleid, A. Horányi, J. Høyer, r. Johansson, M. Killie, H. Körnich, P. Le Moigne, M. Lindskog, T. Manninen, P. Nielsen Englyst, K. Nielsen, E. Olsson, B. Palmason, C. Peralta Aros, R. Randriamampianina, P. Samuelsson, R. Stappers, E. Støylen, S. Thorsteinsson, T. Valkonen, and Z. Wang (2020). "Arctic regional reanalysis on single levels from 1991 to present." In: *Copernicus Climate Change Service (C3S) Climate Data Store (CDS)*. (last access: 25 April 2024) [data set]. DOI: 10.24381/cds.713858f6.

Screen, J. A. (2021). "An ice-free Arctic: what could it mean for European weather?" In: *Weather* 76.10, pp. 327–328. DOI: 10.1002/wea.4069.

Screen, J. A. and I. Simmonds (2010). "The central role of diminishing sea ice in recent Arctic temperature amplification." In: *Nature* 464.7293, pp. 1334–1337. DOI: 10.1038/nature09051.

Seethala, C., P. Zuidema, J. Edson, M. Brunke, G. Chen, X.-Y. Li, D. Painemal, C. Robinson, T. Shingler, M. Shook, A. Sorooshian, L. Thornhill, F. Tornow, H. Wang, X. Zeng, and L. Ziemba (2021). "On Assessing ERA5 and MERRA2 Representations of Cold-Air Outbreaks Across the Gulf Stream." In: *Geophysical Research Let-*

ters 48.19, e2021GL094364. DOI: https://doi.org/10.1029/2021GL094364.

Seifert, A., J. Leinonen, C. Siewert, and S. Kneifel (2019). "The Geometry of Rimed Aggregate Snowflakes: A Modeling Study." In: *Journal of Advances in Modeling Earth Systems* 11.3, pp. 712–731. DOI: 10.1029/2018MS001519.

Serreze, M. C., A. P. Barrett, J. C. Stroeve, D. N. Kindig, and M. M. Holland (2009). "The emergence of surface-based Arctic amplification." In: *The Cryosphere* 3.1, pp. 11–19. DOI: 10.5194/tc-3-11-2009.

Serreze, M. C., A. P. Barrett, and F. Lo (2005). "Northern High-Latitude Precipitation as Depicted by Atmospheric Reanalyses and Satellite Retrievals." In: *Monthly Weather Review* 133.12, pp. 3407–3430. DOI: 10.1175/MWR3047.1.

Serreze, M. C., A. P. Barrett, and J. Stroeve (2012). "Recent changes in tropospheric water vapor over the Arctic as assessed from radiosondes and atmospheric reanalyses." In: *Journal of Geophysical Research: Atmospheres* 117.D10. DOI: 10.1029/2011JD017421.

Serreze, M. C. and R. G. Barry (2011). "Processes and impacts of Arctic amplification: A research synthesis." In: *Global and Planetary Change* 77.1, pp. 85–96. DOI: 10.1016/j.gloplacha.2011.03.004.

Shapiro, M. A., L. S. Fedor, and T. Hampel (1987). "Research aircraft measurements of a polar low over the Norwegian Sea." In: *Tellus A: Dynamic Meteorology and Oceanography* 39.4, pp. 272–306. DOI: 10.3402/tellusa.v39i4.11761.

Shestakova, A. A., D. G. Chechin, C. Lüpkes, J. Hartmann, and M. Maturilli (2022). "The foehn effect during easterly flow over Svalbard." In: *Atmospheric Chemistry and Physics* 22.2, pp. 1529–1548. DOI: 10.5194/acp-22-1529-2022.

Shupe, M. D. (2011). "Clouds at Arctic Atmospheric Observatories. Part II: Thermodynamic Phase Characteristics." In: *Journal of Applied Meteorology and Climatology* 50.3, pp. 645–661. DOI: 10.1175/2010JAMC2468.1.

Shupe, M. D., J. S. Daniel, G. de Boer, E. W. Eloranta, P. Kollias, C. N. Long, E. P. Luke, D. D. Turner, and J. Verlinde (2008a). "A FOCUS ON MIXED-PHASE CLOUDS: The Status of Ground-Based Observational Methods." In: *Bulletin of the American Meteorological Society* 89.10, pp. 1549–1562.

Shupe, M. D. and J. M. Intrieri (2004). "Cloud Radiative Forcing of the Arctic Surface: The Influence of Cloud Properties, Surface Albedo, and Solar Zenith Angle." In: *Journal of Climate* 17.3, pp. 616–628. DOI: 10.1175/1520-0442(2004)017<0616:CRFOTA>2.0.CO;2.

Shupe, M. D., P. Kollias, P. O. G. Persson, and G. M. McFarquhar (2008b). "Vertical Motions in Arctic Mixed-Phase Stratiform Clouds." In: *Journal of the Atmospheric Sciences* 65.4, pp. 1304–1322. DOI: 10.1175/2007JAS2479.1.

Shupe, M. D., S. Y. Matrosov, and T. Uttal (2006). “Arctic Mixed-Phase Cloud Properties Derived from Surface-Based Sensors at SHEBA.” In: *Journal of the Atmospheric Sciences* 63.2, pp. 697–711. DOI: 10.1175/JAS3659.1.

Shupe, M. D., D. D. Turner, V. P. Walden, R. Bennartz, M. P. Cadeddu, B. B. Castellani, C. J. Cox, D. R. Hudak, M. S. Kulie, N. B. Miller, R. R. Neely, W. D. Neff, and P. M. Rowe (2013). “High and Dry: New Observations of Tropospheric and Cloud Properties above the Greenland Ice Sheet.” In: *Bulletin of the American Meteorological Society* 94.2, pp. 169–186. DOI: 10.1175/BAMS-D-11-00249.1.

Shupe, M. D. et al. (2022). “Overview of the MOSAiC Expedition: Atmosphere.” In: *Elementa: Science of the Anthropocene* 10.1, p. 00060. DOI: 10.1525/elementa.2021.00060.

Solomon, A., M. D. Shupe, P. O. G. Persson, and H. Morrison (2011). “Moisture and dynamical interactions maintaining decoupled Arctic mixed-phase stratocumulus in the presence of a humidity inversion.” In: *Atmospheric Chemistry and Physics* 11.19, pp. 10127–10148. DOI: 10.5194/acp-11-10127-2011.

Spensberger, C. and T. Spengler (2021). “Sensitivity of Air-Sea Heat Exchange in Cold-Air Outbreaks to Model Resolution and Sea-Ice Distribution.” In: *Journal of Geophysical Research: Atmospheres* 126.5. DOI: 10.1029/2020JD033610.

Sprenger, M. and H. Wernli (2015). “The LAGRANTO Lagrangian analysis tool – version 2.0.” In: *Geoscientific Model Development* 8.8, pp. 2569–2586. DOI: 10.5194/gmd-8-2569-2015.

Stachlewska, I. S., R Neuber, A Lampert, C Ritter, and G Wehrle (2010). “AMALi – the Airborne Mobile Aerosol Lidar for Arctic research.” In: *Atmos. Chem. Phys.*, p. 17. DOI: 10.5194/acp-10-2947-2010.

Stapf, J., A. Ehrlich, and M. Wendisch (2021). “Influence of Thermodynamic State Changes on Surface Cloud Radiative Forcing in the Arctic: A Comparison of Two Approaches Using Data From AFLUX and SHEBA.” In: *Journal of Geophysical Research: Atmospheres* 126.5, e2020JD033589. DOI: 10.1029/2020JD033589.

Stephens, G. L., D. G. Vane, R. J. Boain, G. G. Mace, K. Sassen, Z. Wang, A. J. Illingworth, E. J. O’connor, W. B. Rossow, S. L. Durden, S. D. Miller, R. T. Austin, A. Benedetti, and C. Mitrescu (2002). “THE CLOUDSAT MISSION AND THE A-TRAIN: A New Dimension of Space-Based Observations of Clouds and Precipitation.” In: *Bulletin of the American Meteorological Society* 83.12, pp. 1771–1790. DOI: 10.1175/BAMS-83-12-1771.

Stephens, G. L., D. G. Vane, S. Tanelli, E. Im, S. Durden, M. Rokey, D. Reinke, P. Partain, G. G. Mace, R. Austin, T. L’Ecuyer, J. Haynes, M. Lebsock, K. Suzuki, D. Waliser, D. Wu, J. Kay, A. Gettelman, Z. Wang, and R. Marchand (2008). “CloudSat mission: Performance and early science after the first year of operation.” In: *Journal of*

Geophysical Research: Atmospheres 113.D8. doi: 10.1029/2008JD009982.

Storelvmo, T., I. Tan, and A. V. Korolev (2015). "Cloud Phase Changes Induced by CO2 Warming—a Powerful yet Poorly Constrained Cloud-Climate Feedback." In: *Current Climate Change Reports* 1.4, pp. 288–296. doi: 10.1007/s40641-015-0026-2.

Strong, C. and I. G. Rigor (2013). "Arctic marginal ice zone trending wider in summer and narrower in winter." In: *Geophysical Research Letters* 40.18, pp. 4864–4868. doi: 10.1002/grl.50928.

Stubenrauch, C. J., W. B. Rossow, S. Kinne, S. Ackerman, G. Cesana, H. Chepfer, L. D. Girolamo, B. Getzewich, A. Guignard, A. Heidinger, B. C. Maddux, W. P. Menzel, P. Minnis, C. Pearl, S. Platnick, C. Poulsen, J. Riedi, S. Sun-Mack, A. Walther, D. Winker, S. Zeng, and G. Zhao (2013). "Assessment of Global Cloud Datasets from Satellites: Project and Database Initiated by the GEWEX Radiation Panel." In: *Bulletin of the American Meteorological Society* 94.7, pp. 1031–1049. doi: 10.1175/BAMS-D-12-00117.1.

Sun, Z. and K. P. Shine (1994). "Studies of the radiative properties of ice and mixed-phase clouds." In: *Quarterly Journal of the Royal Meteorological Society* 120.515, pp. 111–137. doi: 10.1002/qj.49712051508.

Surussavadee, C. and D. Staelin (2006). "Comparison of AMSU Millimeter-Wave Satellite Observations, MM5/TBSCAT Predicted Radiances, and Electromagnetic Models for Hydrometeors." In: *IEEE Transactions on Geoscience and Remote Sensing* 44.10, pp. 2667–2678. doi: 10.1109/TGRS.2006.873275.

Surussavadee, C. and D. H. Staelin (2008). "Global Millimeter-Wave Precipitation Retrievals Trained With a Cloud-Resolving Numerical Weather Prediction Model, Part I: Retrieval Design." In: *IEEE Transactions on Geoscience and Remote Sensing* 46.1, pp. 99–108. doi: 10.1109/TGRS.2007.908302.

Takahashi, T., Y. Nagao, and Y. Kushiyama (1995). "Possible High Ice Particle Production during Graupel–Graupel Collisions." In: *Journal of the Atmospheric Sciences* 52.24, pp. 4523–4527. doi: 10.1175/1520-0469(1995)052<4523:PHIPPD>2.0.CO;2.

Tan, I. and T. Storelvmo (2016). "Sensitivity Study on the Influence of Cloud Microphysical Parameters on Mixed-Phase Cloud Thermodynamic Phase Partitioning in CAM5." In: *Journal of the Atmospheric Sciences* 73.2, pp. 709–728. doi: 10.1175/JAS-D-15-0152.1.

— (2019). "Evidence of Strong Contributions From Mixed-Phase Clouds to Arctic Climate Change." In: *Geophysical Research Letters* 46.5, pp. 2894–2902. doi: 10.1029/2018GL081871.

Tan, I., T. Storelvmo, and M. D. Zelinka (2016). "Observational constraints on mixed-phase clouds imply higher climate sensitivity." In: *Science* 352.6282, pp. 224–227. doi: 10.1126/science.aad5300.

Tanelli, S., S. L. Durden, E. Im, K. S. Pak, D. G. Reinke, P. Partain, J. M. Haynes, and R. T. Marchand (2008). "CloudSat's Cloud Profiling Radar After Two Years in Orbit: Performance, Calibration, and Processing." In: *IEEE Transactions on Geoscience and Remote Sensing* 46.11, pp. 3560–3573. DOI: 10.1109/TGRS.2008.2002030.

Terpstra, A., I. A. Renfrew, and D. E. Sergeev (2021). "Characteristics of Cold-Air Outbreak Events and Associated Polar Mesoscale Cyclogenesis over the North Atlantic Region." In: *Journal of Climate* 34.11, pp. 4567–4584. DOI: 10.1175/JCLI-D-20-0595.1.

Tetzlaff, A., C. Lüpkes, G. Birnbaum, J. Hartmann, T. Nygård, and T. Vihma (2014). "Brief Communication: Trends in sea ice extent north of Svalbard and its impact on cold air outbreaks as observed in spring 2013." In: *The Cryosphere* 8.5, pp. 1757–1762. DOI: 10.5194/tc-8-1757-2014.

Tomassini, L., P. R. Field, R. Honnert, S. Malardel, R. McTaggart-Cowan, K. Saitou, A. T. Noda, and A. Seifert (2017). "The "Grey Zone" cold air outbreak global model intercomparison: A cross evaluation using large-eddy simulations." In: *Journal of Advances in Modeling Earth Systems* 9.1, pp. 39–64. DOI: 10.1002/2016MS000822.

Tornow, F., A. S. Ackerman, and A. M. Fridlind (2021). "Preconditioning of overcast-to-broken cloud transitions by riming in marine cold air outbreaks." In: *Atmospheric Chemistry and Physics* 21.15, pp. 12049–12067. DOI: 10.5194/acp-21-12049-2021.

Tornow, F., A. S. Ackerman, A. M. Fridlind, G. Tselioudis, B. Cairns, D. Painemal, and G. Elsaesser (2023). "On the Impact of a Dry Intrusion Driving Cloud-Regime Transitions in a Midlatitude Cold-Air Outbreak." In: *Journal of the Atmospheric Sciences* 80.12, pp. 2881 – 2896. DOI: 10.1175/JAS-D-23-0040.1.

Turner, J. and G. J. Marshall (2011a). *Climate change in the polar regions*. (last access: 23 August 2024). Cambridge University Press.

— (2011b). *Climate change in the polar regions*. (last access: 23 August 2024). Cambridge University Press.

Ulaby, F. T. and D. G. Long (2014). *Microwave Radar and Radiometric Remote Sensing*. University of Michigan Press.

Uttal, T., J. A. Curry, M. G. McPhee, D. K. Perovich, R. E. Moritz, J. A. Maslanik, P. S. Guest, H. L. Stern, J. A. Moore, R. Turenne, A. Heiberg, M. C. Serreze, D. P. Wylie, O. G. Persson, C. A. Paulson, C. Halle, J. H. Morison, P. A. Wheeler, A. Makshtas, H. Welch, M. D. Shupe, J. M. Intrieri, K. Stamnes, R. W. Lindsey, R. Pinkel, W. S. Pegau, T. P. Stanton, and T. C. Grenfeld (2002). "Surface Heat Budget of the Arctic Ocean." In: *Bulletin of the American Meteorological Society* 83.2, pp. 255–276. DOI: 10.1175/1520-0477(2002)083<0255:SHBOTA>2.3.CO;2.

Vaisala (2010). *Vaisala Dropsonde RD94*. https://www.vaisala.com/sites/default/files/documents/RD94-Dropsonde-Datasheet-B210936EN-A-LoRes.pdf (last access: 31 October 2023).

Vasel, B., C. Schultz, R. Schnell, D. Stanitski, and B. Thomas (2020). “Arctic Report Card 2020: New Arctic Research Facility Opens Door to Science Collaborations.” In: DOI: 10.25923/24rn-c757.

Vihma, T., J. Screen, M. Tjernström, B. Newton, X. Zhang, V. Popova, C. Deser, M. Holland, and T. Prowse (2016). “The atmospheric role in the Arctic water cycle: A review on processes, past and future changes, and their impacts.” In: *Journal of Geophysical Research: Biogeosciences* 121.3, pp. 586–620. DOI: 10.1002/2015JG003132.

Virtanen, P., R. Gommers, T. E. Oliphant, M. Haberland, T. Reddy, D. Cournapeau, E. Burovski, P. Peterson, W. Weckesser, J. Bright, S. J. van der Walt, M. Brett, J. Wilson, K. J. Millman, N. Mayorov, A. R. J. Nelson, E. Jones, R. Kern, E. Larson, C. J. Carey, İ. Polat, Y. Feng, E. W. Moore, J. VanderPlas, D. Laxalde, J. Perktold, R. Cimrman, I. Henriksen, E. A. Quintero, C. R. Harris, A. M. Archibald, A. H. Ribeiro, F. Pedregosa, P. van Mulbregt, and SciPy 1.0 Contributors (2020). “SciPy 1.0: Fundamental Algorithms for Scientific Computing in Python.” In: *Nature Methods* 17, pp. 261–272. DOI: 10.1038/s41592-019-0686-2.

Vochezer, P., E. Järvinen, R. Wagner, P. Kupiszewski, T. Leisner, and M. Schnaiter (2016). “In situ characterization of mixed phase clouds using the Small Ice Detector and the Particle Phase Discriminator.” In: *Atmospheric Measurement Techniques* 9.1, pp. 159–177. DOI: 10.5194/amt-9-159-2016.

WMO (1997). “Expert meeting on automation of visual and subjective observations.” In: *Commission for Instruments and Methods of Observation*. final report. final report, pp. 14–16.

Waitz, F., M. Schnaiter, T. Leisner, and E. Järvinen (2022). *In situ observation of riming in mixed-phase clouds using the PHIPS probe*. DOI: 10.5194/acp-22-7087-2022.

Walbröl, A., J. Michaelis, S. Becker, H. Dorff, K. Ebell, I. Gorodetskaya, B. Heinold, B. Kirbus, M. Lauer, N. Maherndl, M. Maturilli, J. Mayer, H. Müller, R. A. J. Neggers, F. M. Paulus, J. Röttenbacher, J. E. Rückert, I. Schirmacher, N. Slättberg, A. Ehrlich, M. Wendisch, and S. Crewell (2024). “Contrasting extremely warm and long-lasting cold air anomalies in the North Atlantic sector of the Arctic during the HALO–$(\mathcal{AC})^3$ campaign.” In: *Atmospheric Chemistry and Physics* 24.13, pp. 8007–8029. DOI: 10.5194/acp-24-8007-2024.

Walter, B. A. and J. E. Overland (1984). “Observations of Longitudinal Rolls in a Near Neutral Atmosphere.” In: *Monthly Weather Review* 112.1, pp. 200–208. DOI: 10.1175/1520-0493(1984)112<0200:OOLRIA>2.0.CO;2.

Wang, P. K. and W. Ji (2000). "Collision Efficiencies of Ice Crystals at Low–Intermediate Reynolds Numbers Colliding with Supercooled Cloud Droplets: A Numerical Study." In: *Journal of the Atmospheric Sciences* 57.8, pp. 1001–1009. DOI: `10.1175/1520-0469(2000)057<1001:CEOICA>2.0.CO;2`.

Wang, Z., Q. Ding, R. Wu, T. J. Ballinger, B. Guan, D. Bozkurt, D. Nash, I. Baxter, D. Topál, Z. Li, G. Huang, W. Chen, S. Chen, X. Cao, and Z. Chen (2024). "Role of atmospheric rivers in shaping long term Arctic moisture variability." In: *Nature Communications* 15.1, p. 5505. DOI: `10.1038/s41467-024-49857-y`.

Wegener, A. (1911). *Thermodynamik der Atmosphäre*. J. A. Barth.

Wehr, T., T. Kubota, G. Tzeremes, K. Wallace, H. Nakatsuka, Y. Ohno, R. Koopman, S. Rusli, M. Kikuchi, M. Eisinger, T. Tanaka, M. Taga, P. Deghaye, E. Tomita, and D. Bernaerts (2023). "The EarthCARE mission – science and system overview." In: *Atmospheric Measurement Techniques* 16.15, pp. 3581–3608. DOI: `10.5194/amt-16-3581-2023`.

Weitkamp, C. (2005). *Lidar Range-Resolved Optical Remote Sensing of the Atmosphere*. Springer Science+Business Media.

Wendisch, M., S. Crewell, A. Ehrlich, A. Herber, B. Kirbus, C. Lüpkes, M. Mech, S. J. Abel, E. F. Akansu, F. Ament, C. Aubry, S. Becker, S. Borrmann, H. Bozem, M. Brückner, H.-C. Clemen, S. Dahlke, G. Dekoutsidis, J. Delanoë, E. De La Torre Castro, H. Dorff, R. Dupuy, O. Eppers, F. Ewald, G. George, I. V. Gorodetskaya, S. Grawe, S. Groß, J. Hartmann, S. Henning, L. Hirsch, E. Jäkel, P. Joppe, O. Jourdan, Z. Jurányi, M. Karalis, M. Kellermann, M. Klingebiel, M. Lonardi, J. Lucke, A. E. Luebke, M. Maahn, N. Maherndl, M. Maturilli, B. Mayer, J. Mayer, S. Mertes, J. Michaelis, M. Michalkov, G. Mioche, M. Moser, H. Müller, R. Neggers, D. Ori, D. Paul, F. M. Paulus, C. Pilz, F. Pithan, M. Pöhlker, V. Pörtge, M. Ringel, N. Risse, G. C. Roberts, S. Rosenburg, J. Röttenbacher, J. Rückert, M. Schäfer, J. Schaefer, V. Schemann, I. Schirmacher, J. Schmidt, S. Schmidt, J. Schneider, S. Schnitt, A. Schwarz, H. Siebert, H. Sodemann, T. Sperzel, G. Spreen, B. Stevens, F. Stratmann, G. Svensson, C. Tatzelt, T. Tuch, T. Vihma, C. Voigt, L. Volkmer, A. Walbröl, A. Weber, B. Wehner, B. Wetzel, M. Wirth, and T. Zinner (2024). "Overview: quasi-Lagrangian observations of Arctic air mass transformations – introduction and initial results of the HALO–$(\mathcal{AC})^3$ aircraft campaign." In: *Atmospheric Chemistry and Physics* 24.15, pp. 8865–8892. DOI: `10.5194/acp-24-8865-2024`.

Wendisch, M., D. Handorf, I. Tegen, R. Neggers, and G. Spreen (2021). "Glimpsing the Ins and Outs of the Arctic Atmospheric Cauldron." In: *Eos* 102. DOI: `https://doi.org/10.1029/2021EO155959`.

Wendisch, M. et al. (2023). "Atmospheric and Surface Processes, and Feedback Mechanisms Determining Arctic Amplification: A Review of First Results and Prospects of the (AC)3 Project." In: *Bulletin of the American Meteorological Society* 104.1, E208–E242. DOI: `10.1175/BAMS-D-21-0218.1`.

Wendisch, M., A. Macke, A. Ehrlich, C. Lüpkes, M. Mech, D. Chechin, K. Dethloff, C. B. Velasco, H. Bozem, M. Brückner, H.-C. Clemen, S. Crewell, T. Donth, R. Dupuy, K. Ebell, U. Egerer, R. Engelmann, C. Engler, O. Eppers, M. Gehrmann, X. Gong, M. Gottschalk, C. Gourbeyre, H. Griesche, J. Hartmann, M. Hartmann, B. Heinold, A. Herber, H. Herrmann, G. Heygster, P. Hoor, S. Jafariserajehlou, E. Jäkel, E. Järvinen, O. Jourdan, U. Kästner, S. Kecorius, E. M. Knudsen, F. Köllner, J. Kretzschmar, L. Lelli, D. Leroy, M. Maturilli, L. Mei, S. Mertes, G. Mioche, R. Neuber, M. Nicolaus, T. Nomokonova, J. Notholt, M. Palm, M. v. Pinxteren, J. Quaas, P. Richter, E. Ruiz-Donoso, M. Schäfer, K. Schmieder, M. Schnaiter, J. Schneider, A. Schwarzenböck, P. Seifert, M. D. Shupe, H. Siebert, G. Spreen, J. Stapf, F. Stratmann, T. Vogl, A. Welti, H. Wex, A. Wiedensohler, M. Zanatta, and S. Zeppenfeld (2019). "The Arctic Cloud Puzzle: Using ACLOUD/PASCAL Multiplatform Observations to Unravel the Role of Clouds and Aerosol Particles in Arctic Amplification." In: *Bulletin of the American Meteorological Society* 100.5, pp. 841–871. DOI: `10.1175/BAMS-D-18-0072.1`.

Wesche, C., D. Steinhage, and U. Nixdorf (2016). "Polar Aircraft Polar 5 and Polar 6 Operated by the Alfred-Wegener-Institute." In: *Journal of large-scale research facilities JLSRF* 2.0, p. 87. DOI: `10.17815/jlsrf-2-153`.

Wex, H., L. Huang, W. Zhang, H. Hung, R. Traversi, S. Becagli, R. J. Sheesley, C. E. Moffett, T. E. Barrett, R. Bossi, H. Skov, A. Hünerbein, J. Lubitz, M. Löffler, O. Linke, M. Hartmann, P. Herenz, and F. Stratmann (2019). "Annual variability of ice-nucleating particle concentrations at different Arctic locations." In: *Atmospheric Chemistry and Physics* 19.7, pp. 5293–5311. DOI: `10.5194/acp-19-5293-2019`.

Wiener, V., M.-L. Roussel, C. Genthon, E. Vignon, J. Grazioli, and A. Berne (2024). "A 7-year record of vertical profiles of radar measurements and precipitation estimates at Dumont d'Urville, Adélie Land, East Antarctica." In: *Earth System Science Data* 16.2, pp. 821–836. DOI: `10.5194/essd-16-821-2024`.

Winker, D. M., J. R. Pelon, and M. P. McCormick (2003). "The CALIPSO mission: spaceborne lidar for observation of aerosols and clouds." In: *Lidar Remote Sensing for Industry and Environment Monitoring III*. Ed. by U. N. Singh, T. Itabe, and Z. Liu. Vol. 4893. International Society for Optics and Photonics. SPIE, pp. 1 –11. DOI: `10.1117/12.466539`.

Winton, M. (2006). "Amplified Arctic climate change: What does surface albedo feedback have to do with it?" In: *Geophysical Research Letters* 33.3. DOI: `10.1029/2005GL025244`.

Wolff, M. A., K. Isaksen, A. Petersen-Øverleir, K. Ødemark, T. Reitan, and R. Brækkan (2015). "Derivation of a new continuous adjustment function for correcting wind-induced loss of solid precipitation: results of a Norwegian field study." In: *Hydrology and Earth System Sciences* 19.2, pp. 951–967. DOI: 10.5194/hess-19-951-2015.

Wood, N. B. (2011). "Estimation of snow microphysical properties with application to millimeter-wavelength radar retrievals for snowfall rate." https://www.proquest.com/dissertations-theses/estimation-snow-microphysical-properties-with/docview/889251913/se-2. PhD thesis. Colorado State University, p. 248.

Wood, N. B. and T. S. L'Ecuyer (2018). "Level 2C Snow Profile Process Description and Interface Control Document, Product Version P1 R05." In: *NASA JPL CloudSat project document revision 0*. https://www.cloudsat.cira.colostate.edu/cloudsat-static/info/dl/2c-snow-profile/2C-SNOW-PROFILE_PDICD.P1_R05.rev0_.pdf, 26 pp.

Woods, C., R. Caballero, and G. Svensson (2013). "Large-scale circulation associated with moisture intrusions into the Arctic during winter." In: *Geophysical Research Letters* 40.17, pp. 4717–4721. DOI: 10.1002/grl.50912.

Wu, P., R. Wood, and P. Stott (2005). "Human influence on increasing Arctic river discharges." In: *Geophysical Research Letters* 32.2. DOI: 10.1029/2004GL021570.

Wu, P. and M. Ovchinnikov (2022). "Cloud Morphology Evolution in Arctic Cold-Air Outbreak: Two Cases During COMBLE Period." In: *Journal of Geophysical Research: Atmospheres* 127.10. DOI: 10.1029/2021JD035966.

Xie, S., J. Boyle, S. A. Klein, X. Liu, and S. Ghan (2008). "Simulations of Arctic mixed-phase clouds in forecasts with CAM3 and AM2 for M-PACE." In: *Journal of Geophysical Research: Atmospheres* 113.D4. DOI: 10.1029/2007JD009225.

Yang, X., K. P. Nielsen, B. Amstrup, C. Peralta, J. Høyer, P. N. Englyst, H. Schyberg, M. Homleid, M. A. O. Køltzow, R. Randriamampianina, P. Dahlgren, E. Støylen, T. Valkonen, B. Palmason, S. Thorsteinsson, J. Bojarova, H. Körnich, M. Lindskog, J. Box, and K. Mankoff (2023). *C3S Arctic regional reanalysis – Full system documentation*. https://datastore.copernicus-climate.eu/documents/reanalysis-carra/CARRAFullSystemDocumentationFinal.pdf (last access: 09 August 2024) [data set].

Yau, M. K. and R. R. Rogers (1996). *A Short Course in Cloud Physics*. Elsevier.

Zelinka, M. D., D. A. Randall, M. J. Webb, and S. A. Klein (2017). "Clearing clouds of uncertainty." In: *Nature Climate Change* 7.10, pp. 674–678. DOI: 10.1038/nclimate3402.

Zeppenfeld, S., M. Van Pinxteren, M. Hartmann, M. Zeising, A. Bracher, and H. Herrmann (2023). "Marine carbohydrates in Arctic aerosol particles and fog – diversity of oceanic sources and atmospheric transformations." In: *Atmospheric Chemistry and Physics* 23.24, pp. 15561–15587. DOI: `10.5194/acp-23-15561-2023`.

Zhang, X., J. He, J. Zhang, I. Polyakov, R. Gerdes, J. Inoue, and P. Wu (2013). "Enhanced poleward moisture transport and amplified northern high-latitude wetting trend." In: *Nature Climate Change* 3.1, pp. 47–51. DOI: `10.1038/nclimate1631`.

Zhou, W., L. R. Leung, and J. Lu (2024). "Steady threefold Arctic amplification of externally forced warming masked by natural variability." In: *Nature Geoscience* 17.6, pp. 508–515. DOI: `10.1038/s41561-024-01441-1`.

Ziereis, H. and M. Gläßer (2006). "HALO - Global Player für die Atmosphärenforschung." In: *DLR Nachrichten* 115. `https://www.dlr.de/de/medien/publikationen/sonstige-publikationen/2011/global-player-fuer-die-atmosphaerenforschung-halo_86/@@download/file` (last access: 23 August 2024), pp. 32–36.

Zygmuntowska, M., T. Mauritsen, J. Quaas, and L. Kaleschke (2012). "Arctic Clouds and Surface Radiation – a critical comparison of satellite retrievals and the ERA-Interim reanalysis." In: *Atmospheric Chemistry and Physics* 12.14, pp. 6667–6677. DOI: `10.5194/acp-12-6667-2012`.

Łupikasza, E. B. and K. Cielecka-Nowak (2020). "Changing Probabilities of Days with Snow and Rain in the Atlantic Sector of the Arctic under the Current Warming Trend." In: *Journal of Climate* 33.7, pp. 2509–2532. DOI: `10.1175/JCLI-D-19-0384.1`.

ACKNOWLEDGEMENTS

First, I would like to thank my first supervisor Susanne Crewell for the opportunity to explore the fascinating field of Arctic clouds. Thank you for giving me the opportunity to go to the Arctic and fly over the sea ice just a few meters above the surface. That was a really great experience and a dream came true! Thank you for your feedback and guidance throughout my scientific work, but also for your understanding and support during times of personal difficulties!

I also thank Mario Mech, who was part of my doctoral committee, in particular for his technical assistance and his help with various day-to-day issues. Thanks also for being one of few people at the institute when I started my PhD during COVID, which made my first few months in Cologne much less lonely than they would have otherwise been.

I would like to acknowledge Manfred Wendisch, who was part of my doctoral committee and gave valuable feedback during my TAC meetings. Furthermore, I thank Heike Kalesse-Los for examining my PhD thesis.

Moreover, I am thankful that my fellow Phd students gave me all the emotional support, and motivated me whenever necessary. It was really fun to play table tennis and go to bistro with you. Special thanks go to Fiona, Jose, Jonathan, Paula, Melanie, Leonie, Tracy, and many more. A big thank you goes to Linnu, the greatest office mate: even though you defeated me in the ESC-bingo, you motivated me all the time and distracted me from work if further work was pointless. Additionally, I would like to thank Sabrina, Kerstin, and Claire for the scientific discussions and feedback on my work. Thanks, Sabrina, for taking the time to provide so much input on the second paper. Thank you Mario, Fiona, Melanie, and Flo for giving feedback regarding my thesis. Additionally, I would like to thank Dagmar, THE talent in getting bureaucracy done.

Thanks to Nils, Nina, Pavel, Sabrina, and Mario for the nice companionship during the campaign. Sabrina and Mario, I will never forget your invitations to the delicious self-cooked dinners. Luckily the campaign provided the opportunity to connect to people from different institutes. I really enjoyed the spirit within the $(AC)^3$ community.

I am especially grateful for the times I spent in Leipzig. Thanks, Marcus, for hosting me, and providing so much input and feedback on the second study! I really enjoyed the fruitful cooperation and the time with my very welcoming office mates, Christa and Marlen, who are also the most pleasant organization heros. And thanks to Johannes, Hanno, Benjamin, Sophie and all the others for the barbecue, the Feuerzangenbowle, accompanying me to the church service (sorry, Johannes I did not know that it would take ages....), and all the other fun stuff.

Furthermore, I am so lucky that I got to know Sabrina and Rosa: two very inspiring role models! And I am so happy that Lukas helped me to explore the science communication bubble and to figure out that I want to give this kind of stuff a try in the future. Of course thanks to the entire Podcast team for having so much fun, not only in front of the microphones.

Besides the science, many more people supported me during my journey. In particular, Caro, who is the best friend I ever had and who is always there for me! I also enjoyed the support, networking, and professional training within the Dr. Hans Riegel-Stiftung and Mint-Tank community. Then, there is my fabulous sister, who knows me better than I do and who believes in me. Thanks for the weekly phone calls that never lasted less than 6 hours! Last but not least, the greatest THANK YOU goes to Flo, who pushed me but also kept an eye on me all the time. Thanks for the encouraging words, the detailed scientific discussions, and the (mental) support. Without you I would never ever have finished this lifetime project!

Finally, I would like to thank my cello that I started practicing during the final phase of my Phd and that helped me calming down and tanking energy after exhausting working days. Thanks Paula, without you I would never have started playing the cello.

DECLARATION

„Hiermit versichere ich an Eides statt, dass ich die vorliegende Dissertation selbstständig und ohne die Benutzung anderer als der angegebenen Hilfsmittel und Literatur angefertigt habe. Alle Stellen, die wörtlich oder sinngemäß aus veröffentlichten und nicht veröffentlichten Werken dem Wortlaut oder dem Sinn nach entnommen wurden, sind als solche kenntlich gemacht. Ich versichere an Eides statt, dass diese Dissertation noch keiner anderen Fakultät oder Universität zur Prüfung vorgelegen hat; dass sie - abgesehen von unten angegebenen Teilpublikationen und eingebundenen Artikeln und Manuskripten - noch nicht veröffentlicht worden ist sowie, dass ich eine Veröffentlichung der Dissertation vor Abschluss der Promotion nicht ohne Genehmigung des Promotionsausschusses vornehmen werde. Die Bestimmungen dieser Ordnung sind mir bekannt. Darüber hinaus erkläre ich hiermit, dass ich die Ordnung zur Sicherung guter wissenschaftlicher Praxis und zum Umgang mit wissenschaftlichem Fehlverhalten der Universität zu Köln gelesen und sie bei der Durchführung der Dissertation zugrundeliegenden Arbeiten und der schriftlich verfassten Dissertation beachtet habe und verpflichte mich hiermit, die dort genannten Vorgaben bei allen wissenschaftlichen Tätigkeiten zu beachten und umzusetzen. Ich versichere, dass die eingereichte elektronische Fassung der eingereichten Druckfassung vollständig entspricht."

Köln, Dezember 2024

Imke Schirmacher

PUBLICATIONS

FIRST AUTHOR PUBLICATIONS

Schirmacher, I. et al. (2023). "Assessing Arctic low-level clouds and precipitation from above – a radar perspective." In: *Atmospheric Measurement Techniques* 16.17, pp. 4081–4100. DOI: `10.5194/amt-16-4081-2023`

Schirmacher, I. et al. (2024a). "Clouds and precipitation in the initial phase of marine cold-air outbreaks as observed by airborne remote sensing." In: *Atmospheric Chemistry and Physics* 24.22, pp. 12823–12842. DOI: `10.5194/acp-24-12823-2024`

Schirmacher, I. et al. (2024b). *How much snow falls over the Fram Strait during marine cold air outbreaks: constraints derived from airborne radar observations.* (in prep.)

CO-AUTHOR PUBLICATIONS

Klingebiel, M. et al. (2024). "Temporal Evolution of Cloud Properties in Arctic Cold Air Outbreak Cloud Streets Derived from Repeated Airborne Observations." In: *Atmospheric Chemistry and Physics*. (in prep.)
I conducted the airborne experimental work, processed and analyzed the data, and contributed to the interpretation of the findings and drafting of the manuscript.

Ehrlich, A. et al. (2024). "A comprehensive in-situ and remote sensing data set collected during the HALO–(AC)^3 aircraft campaign." In: *Earth System Science Data Discussions* 2024, pp. 1–49. DOI: `10.5194/essd-2024-281`
I conducted the Humidity And Temperature PROfiler (HATPRO), Microwave Radar/radiometer for Arctic Clouds (MiRAC), and Airborne Mobile Aerosol Lidar (AMALi) measurements, wrote Sect. 3.3.1 (the part about P5), 3.3.2, and 3.3.3, and revised the manuscript.

Maherndl, N. et al. (2024b). "How does riming influence the observed spatial variability of ice water in mixed-phase clouds?" In: *EGUsphere* 2024, pp. 1–38. DOI: `10.5194/egusphere-2024-1214`
I collected and processed AMALi data during HALO-(AC)^3, retrieved

the cloud top height product, and reviewed and edited the manuscript.

Pfitzenmaier, L. et al. (2024). "Orbital-Radar v1.0.0: A tool to transform suborbital radar observations to synthetic EarthCARE cloud radar data." In: *Geoscientific Model Development Discussions*, pp. 1–21. DOI: 10.5194/gmd-2024-129
I provided code for the Python tool, and edited and reviewed the paper.

Wendisch, M. et al. (2024). "Overview: quasi-Lagrangian observations of Arctic air mass transformations – introduction and initial results of the HALO–($\mathcal{AC}$)^3 aircraft campaign." In: *Atmospheric Chemistry and Physics* 24.15, pp. 8865–8892. DOI: 10.5194/acp-24-8865-2024
I provided Fig. 6 and text for Sect. 4.1.2, and contributed to the editing of the article and to the analysis and discussion of the results.

Kirbus, B. et al. (2024). "Thermodynamic and cloud evolution in a cold-air outbreak during HALO-(AC)^3: quasi-Lagrangian observations compared to the ERA5 and CARRA reanalyses." In: *Atmospheric Chemistry and Physics* 24.6, pp. 3883–3904. DOI: 10.5194/acp-24-3883-2024
I contributed to the conception and design of the study, supported the development of analysis methods, discussed the results, contributed to manuscript revision, and approved the final submitted version.

Walbröl, A. et al. (2024). "Contrasting extremely warm and long-lasting cold air anomalies in the North Atlantic sector of the Arctic during the HALO–($\mathcal{AC}$)^3 campaign." In: *Atmospheric Chemistry and Physics* 24.13, pp. 8007–8029. DOI: 10.5194/acp-24-8007-2024
I provided and analyzed Fig. 5 of the preprint, and reviewed the manuscript.

Maherndl, N. et al. (2024a). "Quantifying riming from airborne data during the HALO-(AC)^3 campaign." In: *Atmospheric Measurement Techniques* 17.5, pp. 1475–1495. DOI: 10.5194/amt-17-1475-2024
I collected the MiRAC data, collected and processed the AMALi data, retrieved the cloud top height product, and reviewed and edited the manuscript.

Klingebiel, M. et al. (2023). "Variability and properties of liquid-dominated clouds over the ice-free and sea-ice-covered Arctic Ocean." In: *Atmospheric Chemistry and Physics* 23.24, pp. 15289–15304. DOI: 10.5194/acp-23-15289-2023
I evaluated the accuracy of the retrieval results with radar observations, contributed to the interpretation of the results, and contributed to the writing and reviewing of the paper.

Mech, M. et al. (2021). *Introduction — How_to_ac3airborne*. https://igmk.github.io/how_to_ac3airborne/intro.html (last access: 27 October 2024)
I contributed to the editing of the website.

CO-AUTHOR DATA PUBLICATIONS

Mech, M. et al. (2024b). *Cloud mask and cloud top altitude from the AMALi airborne lidar on Polar 5 during HALO-AC3 in spring 2022*. PANGEA [data set]. DOI: 10.1594/PANGAEA.964985
Together with others, I processed the AMALi data, derived the cloud top height, and operated the AMALi during the campaign.

Mech, M. et al. (2024). *Radar reflectivities at 94 GHz and microwave brightness temperature measurements at 89 GHz during the HALO-AC3 Arctic airborne campaign*. PANGEA [data set]. DOI: 10.1594/PANGAEA.964977
I operated the MiRAC during the campaign.

Mech, M. et al. (2024a). *Microwave brightness temperature measurements during the HALO-AC3 Arctic airborne campaign in early spring 2022 out of Svalbard*. PANGEA [data set]. DOI: 10.1594/PANGAEA.964982
I operated the HATPRO during the campaign.

POPULAR SCIENCE PUBLICATIONS

Science Slam: Spannt den Sonnenschirm in der Arktis auf.
https://www.youtube.com/watch?v=X_7bdTYwapw&t=347s

FameLab: Highway in heaven: das Leben einer Wolke.
https://www.youtube.com/watch?v=dv79nb_oqHE&t=8s

Podcast: Konvergenzzone.
https://www.meteo-upas.de/wissenssammlung/podcast-konvergenzzone/

COLOPHON

This document was typeset using the typographical look-and-feel `classicthesis` developed by André Miede. The style was inspired by Robert Bringhurst's seminal book on typography "*The Elements of Typographic Style*". `classicthesis` is available for both LaTeX and LyX:

https://bitbucket.org/amiede/classicthesis/

Final Version as of March 3, 2025 (`classicthesis` version 4.2).